

**Photophysical Studies On Light Harvesting
Nanomaterials For Improved Solar Energy
Conversion**

**THESIS
SUBMITTED FOR THE DEGREE OF
DOCTOR OF PHILOSOPHY (SCIENCE)
IN
CHEMISTRY**

**BY
JAYITA PATWARI**

**DEPARTMENT OF CHEMISTRY
UNIVERSITY OF CALCUTTA**

2019

To My Parents

Acknowledgements

First and foremost, I would like to express my heartfelt gratitude to my research supervisor, Professor Samir Kumar Pal, for providing me the opportunity to work under his supervision. I really feel blessed and grateful to have such an exemplary mentor who has always been an inspiration to work hard and to be extremely focused, disciplined and passionate about work. This work would not have been possible without his valuable advice, constructive criticism and extensive discussions. I strongly believe that his thoughtful guidance, warm encouragement, innovative ideas and noble thoughts will continue to inspire me throughout my life. His constant enthusiasm, huge positive energy and unparalleled leadership quality will continue to influence my work and to orient my ideas in future also. Thank you very much sir for believing in my potential and for helping me to follow the way of my dreams.

I would like to thank Prof. Subhananda Chakrabarti of IIT Bombay, India, Dr. Chinmoy Bhattacharya of IEST Shibpur, India and Prof. Peter Lemmens of TU Braunschweig, Germany for fruitful collaborations. I am thankful to the lab members of my collaborating research groups: Dr. Hemant Ghadi, Dr. Sanjib Shyamal, Dr. Tuhin Khan for insightful discussions.

A special thanks to my senior Dr. Samim Sardar for helping me at the initial stage of my research work. I'd like to express my sincere thanks to all other lab seniors: Siddhi di, Susobhan da, Damayanti di, Priya di, Animesh da, Shreyasi di, Gulmi di, and Soumendra da for their assistance. I would like to thank Nivedita for her assistance in formatting and proof-reading of my thesis. My appreciation goes to my other colleagues and juniors: Harmit, Poulomi, Ramesh, Nur, Dipanjan, Tuhin da, Aniruddha, Probir da, Arpan, Arka, Suamita, Ria, Pritam, Dipsikha, Lopa, Oindrila, Amrita and each and every member of our group.

My time at S. N. Bose Centre was made enjoyable in large part due to my friends (Sumanti, Debolina, Sucheta di, Poonam di) and my music partners (Deba da, Anwasha, Shaili di) who actually became a part of my life for the last few years. I am also thankful to all my friends for their help and support I have received along the way at several instances. I must acknowledge all the excellent teachers I came across throughout my academic journey for all their blessings.

Last but not the least, a huge shout-out to my parents for their unconditional love, support, sacrifices and the values they have given to me which always helped me to choose the correct path at crisis time. I would like to specially thank my mother for tolerating all my tantrums, erratic behaviour and for supporting my work annoyances. This moment of accomplishment belongs to my parents as much as to me.

Dated:

*Department of Chemical, Biological and Macromolecular Sciences,
S. N. Bose National Centre for Basic Sciences,
Salt Lake, Kolkata 700106, India*

(Jayita Patwari)

CONTENTS

	Page
Chapter 1: Introduction	
1.1. Background	1
1.2. Nanomaterials in Light Harvesting: A Brief Overview	2
1.3. Scope of the Photophysical Investigation on Light Harvesting Nanomaterials for Improved Solar Energy Conversion	3
1.4. Objective	6
1.5. Summary of the Work Done	9
1.5.1. Photophysical Studies on Light Harvesting Nanomaterials for Improved Photovoltaic Application	9
1.5.1.1. Three in One Approach towards Efficient Organic Dye Sensitized Solar Cells: Aggregation Suppression, Panchromatic Absorption and Energy Transfer	9
1.5.1.2. Inversion of Activity in DSSC for TiO ₂ and ZnO Photo-anodes Depending on the Choice of Sensitizer and Carrier Dynamics	10
1.5.2. Photophysical Studies on Organic-Inorganic Hybrid Nanomaterials for Enhanced Photocatalytic Application	11
1.5.2.1. Ultrafast Dynamics in Co-sensitized Photocatalyst under Visible and NIR Light Irradiation	11
1.5.3. Photophysical Studies on NIR Light Harvesting Nanomaterials for Potential Device Application	12
1.5.3.1. Photo-induced Electronic Properties in Single Quantum Well System: Effect of Excitonic Lifetime	12

1.5.4.	Temperature Dependent Photophysical Studies on NIR Light Harvesting Nanomaterials	13
1.5.4.1.	<i>In Situ</i> Measurement of Temperature Dependent Picosecond Resolved Carrier Dynamics in Near Infrared (NIR) Sensitive Device on Action	13
1.5.4.2.	Optimizing Dot-in-a-well Infrared Detector Architecture for Achieving High Optical and Device Efficiency Corroborated with Theoretically Simulated Model	14
1.5.5.	Photophysical Studies on Light Harvesting Hybrid Nanomaterials in the Near Infrared Region (NIR) of Solar Radiation for Potential Environmental Cleaning Applications	15
1.5.5.1.	Exciton Dissociation in an NIR-Active Triohybrid Nanocrystal Leading to Efficient Generation of Reactive Oxygen Species	15
1.6.	Plan of thesis	16
	References	18

Chapter 2: An Overview of Experimental and Theoretical Tools and Systems

2.1.	Steady-state and Dynamical Tools	24
2.1.1.	Photoinduced Electron Transfer (PET)	24
2.1.2.	Förster Resonance Energy Transfer (FRET)	26
2.1.3.	Data Analysis of Time-Resolved Fluorescence Transients	29
2.1.4.	Dye-Sensitized Solar Cells (DSSC)	29
2.1.4.1.	Photocurrent–Voltage (I–V) Measurements	30
2.1.4.2.	Incident Photon-to-Current Conversion Efficiency	33

	(IPCE) Measurements	
2.1.4.3.	Photovoltage Decay Measurements	33
2.1.5.	Quantum Confinement Effect	34
2.1.5.1.	Effective Mass Approximation	35
2.1.6.	Diffuse Reflectance Spectroscopy	36
2.2.	Theoretical Modelling	36
2.2.1.	InAs/InGaAs Quantum Dots Parametric Equations	36
2.2.2.	Strain Equations	38
2.2.3.	Energy State Equations	39
2.2.4.	InGaAs Quantum Well Simulation	40
2.3.	Systems	40
2.3.1.	Quantum Confined Nanostructures	40
2.3.1.1.	GaAs/AlGaAs Quantum Well (QW)	41
2.3.1.2.	InAs/InGaAs/GaAs Dot-in-a-Well (DWELL)	41
2.3.1.3.	InAs/InGaAs/GaAs/AlGaAs Dot-in-a-Double-Well (DDWELL)	42
2.3.1.4.	PbS Colloidal Quantum Dot (QD)	43
2.3.2.	Molecular Probes	43
2.3.2.1.	3,7,12,17-Tetramethyl-8,13-divinyl-2,18- porphinedipropionic acid [Protoporphyrin IX, PP]	43
2.3.2.2.	Zinc Protoporphyrin (ZnPP)	44
2.3.2.3.	Cobalt Protoporphyrin (CoPP)	44
2.3.2.4.	Coumarin 343 (C343)	45
2.3.2.5.	3-N,3-N,6-N,6-N-Tetramethylacridine-3,6-diamine [Acridine Orange (AO)]	45
2.3.2.6.	2',7'-dichloro-3',6'-dihydroxy-3H-spiro[2-benzofuran- 1,9'-xanthen]-3-one [Dichlorofluorescein (DCFH)]	45
2.3.2.7.	Di-tetrabutylammonium cis-	46

	bis(isothiocyanato)bis(2,2'-bipyridyl-4,4'-dicarboxylato)ruthenium(II) (N719)	
2.3.2.8.	5-carboxy-2-[[3-[(2,3-dihydro-1,1-dimethyl-3-ethyl-1H-benzo[e]indol-2-ylidene)methyl]-2-hydroxy-4-oxo-2-cyclobuten-1-ylidene]methyl]-3,3-dimethyl-1-octyl-3H-indolium [Squaraine (SQ2)]	46
2.3.2.9.	10H-dibenzo-[b,e]-1,4-thiazine [Phenothiazine (PTZ)]	47
	References	48

Chapter 3: Instrumentation and Sample Preparation

3.1.	Instrumental Setups	54
3.1.1.	Steady-state UV-Vis Absorption and Emission Measurements	54
3.1.2.	Solid State Absorption Measurements in Retro-reflecting Mode	55
3.1.3.	Steady-state Absorption and Emission Measurements for UV-Vis-NIR Range	56
3.1.4.	Time-correlated Single Photon Counting (TCSPC) Technique	56
3.1.5.	Femtosecond-Resolved Transient Absorption Technique	57
3.1.6.	Customization of NIR TCSPC Setup	59
3.1.7.	Transmission Electron Microscopy (TEM)	61
3.1.8.	Cross-Sectional Transmission Electron Microscopy (XTEM)	62
3.1.9.	Low Temperature Steady-state Photoluminescence	63
3.1.10.	Low Temperature Photoluminescence Excitation (PLE)	63
3.1.11.	Fourier Transform Infrared (FTIR) Measurement	63

3.1.12.	Cyclic Voltammetry (CV)	65
3.1.13.	Electrochemical Impedance Spectroscopy (EIS)	66
3.1.14.	Capacitance-Voltage Measurements	67
3.1.15.	Solar Cell Characterization	68
3.1.16.	Fiber-Optic Coupled System for Photocatalytic Measurements	70
3.1.17.	Light Sources Used for Irradiation	72
3.1.18	Molecular Beam Epitaxy (MBE)	72
3.2.	Sample Preparation	74
3.2.1.	Chemicals Used	74
3.2.2.	Preparation of the Cocktail-dye Solutions	75
3.2.3.	Synthesis of the Co-sensitized Nanohybrids	76
3.2.4.	Methods for Photocatalysis Test	76
3.2.5.	Growth Technique of GaAs/ $Al_{0.27}Ga_{0.73}As$ Single Quantum Well (QW) Structures	77
3.2.6.	Fabrication of Capacitive Devices using QW Heterostructures	77
3.2.7.	Determination of Energy Levels of Quantum Well (QW) by Simulation	77
3.2.8.	Growth of the DWELL and DDWELL Heterostructures	78
3.2.9.	Fabrication and Characterization of the Photodetector Devices	78
3.2.10.	Synthesis of the PbS QD Based Hybrid Materials	79
3.2.11.	Preparation of Dichlorofluorescein and ROS Measurements	79
3.2.12.	Fabrication of Dye-Sensitized Solar Cells	79
	References	81

Chapter 4: Photophysical Studies on Light Harvesting Nanomaterials for Improved Photovoltaic Application

4.1.	Introduction	83
4.2.	Results and Discussion	87
4.2.1.	Three in One Approach towards Efficient Organic Dye Sensitized Solar Cells: Aggregation Suppression, Panchromatic Absorption and Energy Transfer	87
4.2.2.	Inversion of Activity in DSSC for TiO ₂ and ZnO Photo-anodes Depending on the Choice of Sensitizer and Carrier Dynamics	98
4.3.	Conclusion	110
	References	113

Chapter 5: Photophysical Studies on Organic-Inorganic Hybrid Nanomaterials for Enhanced Photocatalytic Application

5.1.	Introduction	121
5.2.	Results and Discussion	123
5.2.1.	Ultrafast Dynamics in Co-sensitized Photocatalyst under Visible and NIR Light Irradiation	123
5.3.	Conclusion	143
	References	144

Chapter 6: Photophysical Studies on NIR Light Harvesting Nanomaterials for Potential Device Application

6.1.	Introduction	150
6.2.	Results and Discussion	152
6.2.1.	Photo-induced Electronic Properties in Single Quantum Well System: Effect of Excitonic Lifetime	152

6.3.	Conclusion	162
	References	164
Chapter 7: Temperature Dependent Photophysical Studies on NIR Light Harvesting Nanomaterials		
7.1.	Introduction	169
7.2.	Results and Discussion	174
7.2.1.	<i>In Situ</i> Measurement of Temperature Dependent Picosecond Resolved Carrier Dynamics in Near Infrared (NIR) Sensitive Device on Action	174
7.2.2	Optimizing Dot-in-a-Well Infrared Detector Architecture for Achieving High Optical and Device Efficiency Corroborated with Theoretically Simulated Model	185
7.3.	Conclusion	202
	References	204
Chapter 8: Photophysical Studies on Light Harvesting Hybrid Nanomaterials in the Near Infrared Region (NIR) of Solar Radiation for Potential Environmental Cleaning Applications		
8.1.	Introduction	211
8.2.	Results and Discussion	214
8.2.1.	Exciton Dissociation in an NIR-Active Trio-hybrid Nanocrystal Leading to Efficient Generation of Reactive Oxygen Species	214
8.3.	Conclusion	227
	References	229
	List of Publications	234
	List of National/International Conferences	236

Chapter 1

Introduction

1.1. Background:

The population on earth has already surpassed seven billion and it is expected to reach nine billion by the middle of this century, which will eventually increase the energy requirement to almost double [1, 2]. In general, energy resources can be divided into three major categories: Fossil fuel, nuclear fuel and renewable ones. But till date the world's main energy economy is dependent only on non-renewable fossil fuels [3-6]. The overuse of oil, coal, and natural gas has caused serious issues to our environment due to the toxic gas emission. Additionally, the ever-increasing consumption of these non-renewable energy resources outpaces their regeneration rate, increasing the danger of complete exhaustion of fossil fuel sources on earth. Thus, it is an urgent need of mankind to deal with the energy crisis. Among all alternative and renewable energy sources, solar energy is the most abundant and eco-friendly source of energy. The total solar power that hits the Earth's surface is about 1×10^5 terawatts, which is around 1×10^4 times greater than the global consumption [7]. If only 0.1% of the solar energy that reaches the Earth's surface can be converted to electrical energy, with an average of 10% conversion efficiency, the amount would be enough to fulfil the energy requirement of the entire world. The solar energy conversion technology is growing tremendously in recent years. However, the high-cost of conventional silicon based photovoltaics, limits the competition with other sources. The need and desire to design cheap and renewable energy sources have triggered intensive research work in several other solar energy conversion technologies such as organic solar cells, dye sensitized solar cells (DSSC) and quantum dot sensitized solar cells (QDSSC). However, the inability of these

materials to absorb in the infrared (IR) region of solar light, which constitutes 52% of entire solar spectrum, causes the major energy loss mechanism. The same fundamental issue is true for conversion of solar energy to chemical energy also in the fields of photocatalysis and water splitting.

1.2. Nanomaterials in Light Harvesting: A Brief Overview:

Nanomaterials are defined as precisely miniaturized set of atoms and molecules where at least one dimension is less than approximately 100 nanometers. The growing research and technological interest in nanomaterials originates from the fact that unique material properties, compared to bulk, are generated at this length scale which are changeable upon varying size or shape. The family of nanomaterials have great diversity in their structural and optical properties. They exist in the form of nanoparticles, nanowires, nanopillars, nanotubes, nanocones, nanodomes, quantum dots and many more nanostructures [8, 9]. All these materials have very different physical properties, such as band-gap, absorption coefficient, surface/bulk recombination rate and different synthesis/fabrication approaches as well [10, 11]. Easy and cost effective synthesis procedure and the higher surface to volume ratio of nanomaterials lead to its application in different area such as photovoltaics, biomedicines, photocatalysis, sensing and environmental cleaning [12, 13].

Nanomaterials hold promising potency to enhance the light harvesting efficiency by improving both light trapping and photo-carrier collection. For the last few decades, semiconductor nanostructure materials such as TiO_2 , ZnO have been widely used in waste water purification and solar energy conversion [14-19]. Apart from the wide band gap semiconductor nanomaterials, some lower band gap nanoscale materials e.g. Fe_2O_3 , WO_3 , BiVO_4 , MoS_2 and metal chalcogenide quantum dots e.g. CdS , CdSe , PbS , PbSe , CdTe and some multi-junction III-V group compounds e.g. InAs , GaAs are receiving immense attention as they

possess the potential to overcome the limit of lower energy photon loss [20-23]. Designing nanomaterials and redistribution of energy levels can be done by combining multiple components such as polymer-semiconductor [24], dye-semiconductor [25] or semiconductor-semiconductor [26, 27] in order to increase the overall absorption window and to facilitate the charge separation. This strategy is raising a new class of light harvesting nanomaterials known as “Nanohybrids” which also have some extended application than the conventional nanomaterials.

1.3. Scope of the Photophysical Investigation on Light Harvesting Nanomaterials for Improved Solar Energy Conversion:

The behavior of materials and molecules in electronically excited states and the fate of the photogenerated carriers in the excited states are generally described by the so-called photophysical processes. Electron transfer (ET), hole transfer (HT) and energy transfer are key steps of many photochemical and photophysical processes occurring in light harvesting materials and devices [28-30]. For instance, photo-induced charge separation is the heart of natural photosynthesis process. An efficient conversion of solar light into electrical or chemical energy requires a series of step-wise carrier migration processes to create a long lived charge separated state. Besides the forward process of carrier dynamics in any light harvesting system, back recombination processes are also equally important to determine the overall efficiency and recyclability of the material. Mimicking the elementary steps of natural photosynthesis was the initial motivation of designing light harvesting artificial materials. However, going from simple mimics to actual functioning devices is not simple and requires a thorough understanding of all parameters controlling the separation and recombination of photo-induced charged carriers. In this context, different spectroscopic techniques provide the wide opportunity to identify the factors governing charge and energy transfer in

light harvesting nanomaterials. Hence, photophysical studies helps to improve the strategy of new material synthesis and device fabrication. Additionally, the formation of organic-inorganic and inorganic-inorganic hybrid nanomaterials allows a wide range of solar light absorption and an efficient charge separation. However, the activity of such multi-junction heterogeneous systems is critically dependent on the carrier dynamics occurring across the interfaces of the hybrid nanomaterials [31-33].

The key focus of this thesis is to investigate the photoinduced dynamical processes across the heterogeneous interface of novel nanomaterials and correlation of the fundamentals with different applications such as, efficient photocatalysis, photovoltaics, photo-induced capacitance, photodetectors and environment cleaning. Light harvesting hybrid nanomaterials used in DSSC and photocatalysis are related to ultrafast excited state charge transfer across the interface [34-37]. Thus, an accurate knowledge of creation, separation and recombination of photo-induced charge carriers across the interfaces is important to fully understand the microscopic mechanism related to technologically relevant processes. In one of our studies, we have explored the co-sensitization technique to increase the efficiency of DSSC using a visible absorbing dye Protoporphyrin IX (PPIX) and another NIR absorbing dye Squarine (SQ2) to emulate the solar spectra. Apart from achieving a panchromatic absorption, the study reveals the role of PPIX as an anti-aggregating agent of the other sensitizer SQ2 and increased photocurrent was also observed due to the energy transfer process from one sensitizer to the other. In another study, we have done a comparative study of the performance of TiO₂ and ZnO based photoanodes depending on organic sensitizer (C343) or metal based sensitizer N719. The fate of the light induced carriers both in forward and backward routes in a device has been investigated using spectroscopic tools to answer the long debated topic of lower efficiency in ZnO photoanodes compared to the TiO₂ counterpart. In addition to the photovoltaics,

we have also synthesized hybrid nanomaterials using multiple organic photosensitizers and an inorganic host nanoparticle (ZnO) for application in visible light as well as NIR light driven photocatalysis. Ultrafast photoinduced charge separation and charge recombination processes at the interfaces of the co-sensitized hybrid materials and their dependence on the core metal of the PPIX ring are also explored for efficient solar light harvesting. In this study, we found the ligand to metal charge transfer in one of the probes of FRET pair actually inhibits the efficiency of the energy transfer process and eventually affect the overall catalytic efficiency. In a recent study, we have explored the photoinduced carrier dynamics in a GaAs/AlGaAs single quantum well system depending on the varying well thickness. The photophysical study of the material has been used to investigate the light induced capacitance generated in such structures. Additionally, in these thesis we have focused on other NIR absorbing self-assembled quantum dot structures such as (InAs/InGaAs/GaAs dot-in-well (DWELL) and InAs/InGaAs/GaAs/AlGaAs dot-in-dual-well (DDWELL)) and on their carrier dynamics depending on varying temperature, external bias, excitation energy and emission wavelength as well. The possible 2D to 3D transition of the structures, possibility of formation of 2 dimensional electron gas (2D-GES) at the active condition has been predicted from these studies which correlates the fundamental carrier mechanism to the potential device performances in NIR region. Most importantly, for the first time we have demonstrated a trio hybrid material active in deeper NIR (~1470 nm) for potential environment cleaning applications via enhanced reactive oxygen species (ROS) generation. The concept of the trio hybrid material was to use simultaneously an electron transporting material (TiO_2 in our case) and a hole transporting material phenothiazine (PTZ) with PbS quantum dot in order to dissociate both the exciton at the same time so that the recombination centers can be diminished and consequently increasing the overall light harvesting efficiency.

The experimental tools used for studying the dynamical processes involve picosecond-resolved carrier relaxation dynamics in visible and NIR region, such as, photoinduced electron transfer (PET), photoinduced hole transfer (PHT) and Förster resonance energy transfer (FRET). The different experimental techniques employed for the structural and functional characterization of the light harvesting materials include steady-state UV-VIS absorption and fluorescence, diffuse reflectance spectroscopy, UV-VIS-NIR absorption and emission measurement, femtosecond resolved transient absorption, helium flow controlled closed cycle cryostat assisted low temperature photoluminescence (PL) and photoluminescence excitation (PLE), Fourier transform infrared spectroscopy (FTIR), cyclic voltammetry (CV), electrochemical impedance spectroscopy (EIS), capacitance (C) vs voltage (V) measurement, high-resolution transmission electron microscopy (HRTEM), cross-sectional transmission electron microscopy (XTEM). The DSSCs were fabricated and characterized by using photocurrent–voltage (I–V) measurements, incident photon-to-current conversion efficiency (IPCE) measurements and photovoltage decay measurements. A customized fiber optic coupled system is used for photocatalytic measurements. Molecular beam epitaxy (MBE) technique has been used to grow the self-assembled quantum dot heterostructures.

1.4. Objective:

The science of light harvesting nanomaterials is experiencing phenomenal growth and attracting huge interest as they are considered to be the potential mimics for photosynthetic systems [38, 39]. Efficient photovoltaic devices are based on the impressive material properties of hybrid nanomaterials which have either inorganic-inorganic or inorganic-organic interfaces [40]. Efficient transfer of electrons, holes or electronic energy across the semiconductor interface is the key factor for the efficiency of converting light energy into photovoltaics [15], photocatalysis [41] and environmental cleaning [42] as well. Therefore, a basic

understanding of the mechanisms and dynamics of these ultrafast charge transfer processes is essential from the perspective of developing efficient light-harvesting assemblies (LHAs) and for their large-scale industrialization. But, so far the efficiency of solar energy converting devices are largely limited by the poor photon to current conversion in the near-infrared or NIR spectral region [43-45]. Thus, in this thesis our primary objective was to focus on NIR light harvesting materials and to study their unique photophysical properties using different experimental techniques in order to extend their application towards enhanced light harvesting.

Dye Sensitized Solar Cell (DSSC) has attracted attention in the fields of alternative energy resources [46, 47]. The commonly used photosensitizers in DSSC are Ruthenium based organometallic dyes. The high cost and toxicity of the organometallic dyes are considered as disadvantages. Thus, our aim was to use stable, nontoxic, metal free and low cost organic dyes in DSSC. However, in spite of having very high molar extinction coefficient, the relatively narrow absorption band of organic dyes limits their efficiency. Thus, in one of our studies, we have co-sensitized the photoanodes using multiple sensitizers together to achieve a panchromatic absorption window. We have chosen near infrared (NIR) absorbing dye Squaraine (SQ2) and visible absorbing dye Protoporphyrin IX (PPIX) for a co-sensitized DSSC and detail photo-physical studies have been carried out to explore the dynamical processes occurring between these two dyes after the attachment to TiO_2 surface. In this work, we have also solved the aggregation problem of SQ2 sensitizer [48] on the photoanode surface by using the other sensitizer as an anti-aggregating agent. In another study, we have addressed a long debated issue of DSSC that why the ZnO photoanodes always show poor performance than TiO_2 . We have done a comparative study using ultrafast dynamics and device characteristics to reinvestigate the age old problem with a

new perspective. Organic sensitizer C343 and ruthenium based sensitizer N719 has been used for the comparative study.

In the case of photocatalyst designing, the NIR harvesting is an important factor as IR light ensure longer working hour and deeper penetration. We have extended the idea of co-sensitization to design a photocatalyst based on ZnO nanoparticles which will be active both under visible and NIR light irradiation. Different photophysical interaction occurring between the metalloporphyrins and squaraine on the ZnO surface was explored by investigating the ultrafast dynamical events at the organic-inorganic interfaces of the hybrids.

Self-assembled Quantum Dots (QD) and Quantum Well (QW) systems are also widely accepted NIR harvesting material in terms of device application. In one of our study, we have focused on the explanations of the significant increase in capacitance observed in GaAs/AlGaAs single QW upon light irradiation and this phenomena is correlated to the carrier escape lifetime from the excited state. We have also investigated the detail carrier dynamics of InAs/InGaAs/GaAs dot-in-well (DWELL) and InAs/InGaAs/GaAs/AlGaAs dot-in-dual-well (DDWELL) structures depending on the changes of their specific layer thickness or growth parameters. Thermal escape and carrier capture are two competing phenomena which controls the exact operability condition of the devices in such quantum confined nanostructures. Thus, an external bias dependent TRPL study was also done for the DDWELL at active condition of the device. The carrier holding capacity of a particular energy state is directly related to the predominance of the thermionic current and tunnelling current component of these devices. Ultrafast carrier dynamics study in these self-assembled quantum confined structures is essential to determine the optimum growth condition and structural parameters also. All the dynamical behaviour of the photo-induced carriers at these inorganic-inorganic interfaces have been studied to find out the structural, optical and dynamical properties of the QDs and to correlate them with device performances.

Solar energy conversion using colloidal quantum dots (QD) involves absorption of photon to generate an electron-hole pair which is known as exciton. The formation of exciton is followed by dissociation through extraction of either the hole or the electron [49]. This charge separation process is supposed to be faster than the back recombination of exciton leading to regeneration of the ground state of the QD. Precise knowledge of the chemical and electronic factors which controls the rate of exciton dissociation in QDs is therefore essential for enabling rational design of efficient light harvesting material which incorporate QDs. We have introduced a new triohybrid (PbS_TiO₂_PTZ) material by incorporating an NIR absorbing QD PbS with the large band gap semiconductor TiO₂ and oxidizing molecule phenothiazine (PTZ) to simultaneously separate the electron and hole from the QD. The coherent exciton separation technique was giving better light harvesting due to destruction of the back recombination centres.

1.5. Summary of the Work Done:

1.5.1. Photophysical Studies on Light Harvesting Nanomaterials for Improved Photovoltaic Application:

1.5.1.1. Three in One Approach towards Efficient Organic Dye Sensitized Solar Cells: Aggregation Suppression, Panchromatic Absorption and Energy Transfer [50]: In this study, protoporphyrin IX (PPIX) and squaraine (SQ2) have been used in a co-sensitized dye-sensitized solar cell (DSSC) to apply their high absorption coefficients in the visible and NIR region of the solar spectrum and to probe the possibility of Förster resonance energy transfer (FRET) between the two dyes. FRET from the donor PPIX to acceptor SQ2 was observed from detailed investigation of the excited-state photophysics of the dye mixture, using time-resolved fluorescence decay measurements. The electron transfer time scales from the dyes to TiO₂ have also been characterized for each dye. The current - voltage

(*I-V*) characteristics and the wavelength-dependent photocurrent measurements of the co-sensitized DSSCs reveal that FRET between the two dyes increase the photocurrent as well as the efficiency of the device. From the absorption spectra of the co-sensitized photoanodes, PPIX was observed to be efficiently acting as a co-adsorbent and to reduce the dye aggregation problem of SQ2. It has further been proven by a comparison of the device performance with a chenodeoxycholic acid (CDCA) added to a SQ2-sensitized DSSC. Apart from increasing the absorption window, the FRET induced enhanced photocurrent and the anti-aggregating behavior of PPIX towards SQ2 are crucial points that improve the performance of the co-sensitized DSSC.

1.5.1.2. Inversion of Activity in DSSC for TiO₂ and ZnO Photo-anodes Depending on the Choice of Sensitizer and Carrier Dynamics [51]:

In this study, we have demonstrated an inversion in the efficiency of TiO₂ and ZnO based dye sensitized solar cells for an organic sensitizer C343 and another Ru based sensitizer N719. Despite of faster electron injection from sensitizer C343 to TiO₂ than ZnO, the later shows a better photovoltaic efficiency. The higher photocurrent in C343-ZnO has been mechanistically justified by slower back electron recombination and higher dye loading obtained from open circuit potential decay, electrochemical impedance spectroscopy and absorption spectra of the sensitized photoanodes. The similar positive features are there for N719-ZnO system also. Still TiO₂-N719 performs much better than ZnO-N719 in terms of device efficiency. We have found a signature of H-type aggregate formation of N719 dye on the ZnO photoanode surface which shows a higher energy absorption peak than the monomeric form of the dye in the diffuse reflectance mode absorption spectra of the photoanodes. These type of aggregates are unable to inject electrons into the semiconductor rather the dye aggregates can pull back the electrons from the CB of the ZnO and eventually undergoes ground state recombination. Ultrafast transient absorption spectroscopy and wavelength

dependent photo-current spectra provides further insight into the effect of the dye aggregates on the photo-excited carrier dynamics which essentially reduces the light harvesting efficiency.

1.5.2. Photophysical Studies on Organic-Inorganic Hybrid Nanomaterials for Enhanced Photocatalytic Application:

1.5.2.1. Ultrafast Dynamics in Co-sensitized Photocatalyst under Visible and NIR Light Irradiation [52]: Co-sensitization to achieve a broad absorption window is a widely accepted technique in light harvesting nanohybrid synthesis. Protoporphyrin (PPIX) and squaraine (SQ2) are two organic sensitizers absorbing in the visible and NIR wavelength regions of solar spectrum, respectively. In the present study, we have sensitized zinc oxide (ZnO) nanoparticles using PPIX and SQ2 simultaneously for their potential use in broad-band solar light harvesting in photocatalysis. Förster resonance energy transfer (FRET) from PPIX to SQ2 in close proximity to the ZnO surface has been found to enhance visible light photocatalysis. In order to confirm the effect of intermolecular FRET in the photocatalysis, the excited state lifetime of the energy donor dye PPIX has been modulated by inserting d^{10} (Zn^{II}) and d^7 (Co^{II}) metal ions in the central position of the dye (PP(Zn) and PP(Co)). In the case of PP(Co)-SQ2, extensive photo-induced ligand to metal charge transfer counteracts the FRET efficiency while efficient FRET has been observed for the PP(Zn)-SQ2 pair. This observation has been justified by the comparison of the visible light photocatalysis of the respective nanohybrids with several control studies. We have also investigated the NIR photocatalysis of the co-sensitized nanohybrids which reveals that reduced aggregation of SQ2 due to co-sensitization of PPIX increases the NIR photocatalysis. However, core-metalation of PPIX reduces the NIR photocatalytic efficacy, most probably due to excited state charge transfer from SQ2 to the metal

centre of the PP(Co)/PP(Zn) through the conduction band of the host ZnO nanoparticles.

1.5.3. Photophysical Studies on NIR Light Harvesting Nanomaterials for Potential Device Application:

1.5.3.1. Photo-induced Electronic Properties in Single Quantum Well System:

Effect of Excitonic Lifetime [53]: In the present study, we have established a correlation between the photo-induced electronic phenomena and excited state lifetime of the photo generated carriers in double barrier $\text{Al}_{0.3}\text{Ga}_{0.7}\text{As}/\text{GaAs}$ quantum well (QW) structures. The excited state lifetime was measured experimentally by picosecond time resolved photoluminescence spectroscopy for two samples with different well widths (5.3 nm and 16.5 nm). The faster nonradiative decay time of the narrower well can be attributed to the facile escape of electrons from well to barrier due to lower associated energy compared to that of the thicker well which resembles the simulated results of the energy level distribution. The proposed mechanism of carrier escape is further proven from the higher value of unconventional excitonic capacitance value in the thicker well, measured by impedance spectroscopy. The dependence of photo-induced capacitance on well thickness is explained by lifetime of the excited carriers in this study. Dependence of the photo-generated capacitance (C) on externally applied bias voltage (V) was also studied to quantitatively establish a proportional relation between the carrier holding capacity of the well and the excitonic lifetime. The higher accumulation of charge and lower ground state energy of the thicker well is evident from the higher tunnelling current found for the same in the photocurrent (I) versus voltage (V) measurement. Thus, the escape of electrons from the well to barrier is the key factor affecting the photo generated charge accumulation and its holding capacity which in turn influences the device performances.

1.5.4. Temperature Dependent Photophysical Studies on NIR Light Harvesting Nanomaterials:

1.5.4.1. *In Situ* Measurement of Temperature Dependent Picosecond Resolved Carrier Dynamics in Near Infrared (NIR) Sensitive Device on Action [54]: The carrier dynamics study of emerging near infrared (NIR) absorbing materials is an essential need to develop device technology towards enhanced NIR light harvesting. In this study, we have documented the design of an indigenously developed time correlated single photon counting (TCSPC) system working in the NIR (900 nm- 1700 nm) spectral region. The system is compatible to study transient photoluminescence of device samples under tunable bias voltages. The liquid nitrogen cooling and electrical heating of the sample chamber provides additional flexibility of temperature dependent study starting from -196 °C to 400 °C. As a model system to study, we have chosen a multi-layer InAs/InGaAs/GaAs/AlGaAs dot in dual well (DDWELL) device sample as the thin film quantum dot heterostructures are of huge relevance in various NIR harvesting devices. We have investigated the detail carrier dynamics of the device sample using the transient photoluminescence upon varying temperature (80 K to 300 K), varying emission energy and different bias voltages (0 V-15 V). The critical temperature (160 K) and critical bias (12 V) of achieving longest excited state lifetime has been mechanistically explained using various competing photophysical phenomena such as hole diffusion, energy relaxation etc. The emission wavelength dependent study at below and above critical temperature further provides an insight into the dominance of carrier capture and thermal escape at the two different temperature zone. Along with the detail understanding of the carrier dynamics, the results can be helpful to get an idea of the electrical stability of the device and the operability temperature as well. The reasonable good resolution of the NIR TCSPC system and considerable good results ensure the future application of the same for other devices also.

1.5.4.2. Optimizing Dot-in-a-well Infrared Detector Architecture for Achieving High Optical and Device Efficiency Corroborated with Theoretically Simulated Model [55]: Dot-in-a-well (DWELL) heterostructures have been extensively researched in quantum dot based infrared photo-detectors as it offers tuning of detection peak wavelength, low dark current and a higher operating temperature with optimized quantum well thickness. In this paper, we have correlated experimentally observed opto-electronic properties of three different InAs quantum dots in DWELL configuration with varying ternary capping ($\text{In}_{0.15}\text{Ga}_{0.85}\text{As}$ - Strain reducing ternary alloy) thickness from 4 to 8 nm to the proposed simulation model for achieving high efficiency in device performance. Low temperature (8 K) photoluminescence (PL) spectra exhibits a blue shift of around 24 nm along with a decrease in intensity as the capping thickness increases above 6 nm. Decrease in full width at half maximum (FWHM) value for PL peak was observed as the capping thickness is increased from 6 to 8 nm. These are attributed to formation of InGaAs quantum wells via dots sublimation process. Presence of InGaAs wells for 8 nm capped sample was confirmed using low temperature photoluminescence measurement at 2.54 W/cm^2 and photoluminescence excitation (PLE). Time resolved photoluminescence spectroscopy gave further insight into the carrier dynamics of the grown structures and confirms undesirable quantum well formation in 8 nm capped sample. Improved optical characteristics with formation of defect-free structure having larger quantum dot was achieved in 6 nm capped sample affirmed using transmission electron microscopy images. Low dark current density with high confinement energy was achieved from 6 nm capped DWELL structure. Dominant spectral response peak was obtained at $7.56 \mu\text{m}$ from all the samples. A concentration-dependent theoretical strain model using the Schrödinger equation was developed to calculate the potential, ground-state and inter-sub band energy-levels. It was validated by comparing experimentally achieved PL and PLE peaks along with spectral response peaks. The theoretical model was used to calculate

the energy levels corresponding to conduction and valence bands for InGaAs well and indium concentration in the well was obtained to be around 30%. Similarly, concentration dependent 2D to 3D transition for $\text{In}_x\text{Ga}_{1-x}\text{As}$ ($0 \leq x \leq 1$) quantum dots formation was modelled using People-Bean relation which matches with the proposed simulation.

1.5.5. Photophysical Studies on Light Harvesting Hybrid Nanomaterials in the Near Infrared Region (NIR) of Solar Radiation for Potential Environmental Cleaning Applications:

1.5.5.1. Exciton Dissociation in an NIR-Active Trio hybrid Nanocrystal Leading to Efficient Generation of Reactive Oxygen Species [56]: Lead sulfide (PbS) colloidal quantum dots (QDs) are emerging materials for fundamental studies because of their potential application in near infrared (NIR) light harvesting technologies. However, inefficient electron separation, facile charge recombination and defect state trapping of photoexcited carriers are reported as limitations of the PbS QDs to achieve efficient energy conversion. In the present study, we have synthesized a trio hybrid by assembling a semiconductor titanium dioxide (TiO_2), an organic oxidizing molecule phenothiazine (PTZ) and PbS QDs. The trio hybrid along with the PbS_ TiO_2 and PbS_PTZ hybrids have been characterized and the attachments of different components are verified by spectroscopic and microscopic techniques. The interfacial dynamics of the photoexcited carriers in the PbS_ TiO_2 and PbS_PTZ hybrids have been investigated separately using steady-state and time-resolved photoluminescence (TRPL) measurements. The photo-induced electron transfer (PET) from PbS QD to the conduction band (CB) of TiO_2 and photo induced hole transfer (PHT) from the valence band (VB) of QD to the highest occupied molecular orbital (HOMO) of PTZ have been observed and correlated mechanistically to the energy level alignments obtained from cyclic voltammetric (CV) analysis. The PTZ molecule is also found to act as a surface

defect passivator of the PbS QD. Finally, simultaneous exciton dissociation and reduced back recombination phenomena have been correlated with a higher reactive oxygen species (ROS) generation activity of the trio hybrid than the other two, under IR light irradiation. Thus, a detailed investigation of carrier dynamics and a mechanism of higher NIR light activity for a novel nano hybrid is explored and analyzed which could be beneficial for NIR catalysis or antibacterial activities.

1.6. Plan of Thesis:

The plan of the thesis is as follows:

Chapter 1: This chapter gives a brief introduction to the scope and motivation behind the thesis work. A brief summary of the work done is also included in this chapter.

Chapter 2: This chapter provides a brief overview of the steady-state, dynamical, theoretical tools and the structural aspects of the quantum confined nanostructures, dyes and fluorescent probes used in the experiments.

Chapter 3: Details of instrumentation, data analysis and experimental procedures have been discussed in this chapter.

Chapter 4: In this chapter, the fundamental electron and energy transfer processes in dye sensitized wide band gap semiconductors are investigated for improved photovoltaic application. The near infrared (NIR) absorbing dye Squarine (SQ2) and visible absorbing dye Protoporphyrin IX (PPIX) are being used to fabricate a co-sensitized dye sensitized solar cells (DSSC) using a TiO₂ photoanode. We have also done a comparative study to rationalize the efficiency inversion of ZnO and TiO₂ DSSC depending on the choice of sensitizer. Organic sensitizer C343 and ruthenium based sensitizer N719 are used for comparison.

Chapter 5: The co-sensitization of ZnO NPs by multiple dyes has been investigated for enhanced photocatalytic application under visible and NIR light

irradiation. Different metaloporphyrin systems and their interaction with the NIR dye SQ2 on ZnO surface is elaborated in this chapter.

Chapter 6: In this chapter, the changes in carrier dynamics of NIR absorbing $\text{Al}_{0.3}\text{Ga}_{0.7}\text{As}/\text{GaAs}$ quantum well (QW) structures has been investigated depending on varying well thickness in order to get an mechanistic explanation of the huge photo-induced capacitance in QW based devices.

Chapter 7: In this chapter, we have employed temperature dependent, excitation energy dependent and varying bias dependent time resolved photoluminescence technique in NIR region to study the excited state dynamical processes in multilayer $\text{InAs}/\text{InGaAs}/\text{GaAs}/\text{AlGaAs}$ dot-in-double-well (DDWELL) device sample. Temperature dependent NIR TCSPC technique has also been used to understand the concentration dependent 2D to 3D transition in an $\text{InAs}/\text{InGaAs}/\text{GaAs}$ Dot-in-a-Well (DWELL) structure depending on the thickness of the InGaAs layer for potential application in photodetector.

Chapter 8: In this chapter, a new NIR active triohybrid material using PbS quantum dot, electron transporting semiconductor TiO_2 and a hole transporting molecule phenothiazine (PTZ) has been synthesized and the dynamical processes at the interfaces of the hybrid are evaluated in order to generate enhanced reactive oxygen species (ROS) for potential environmental cleaning application.

References

- [1] S.Y. Tee, K.Y. Win, W.S. Teo, L.D. Koh, S. Liu, C.P. Teng, M.Y. Han, Recent progress in energy-driven water splitting, *Adv. Sci.*, 4 (2017) 1600337.
- [2] G. Chen, J. Seo, C. Yang, P.N. Prasad, Nanochemistry and nanomaterials for photovoltaics, *Chem. Soc. Rev.*, 42 (2013) 8304-8338.
- [3] K. Kalyanasundaram, M. Grätzel, Themed issue: nanomaterials for energy conversion and storage, *J. Mater. Chem. C*, 22 (2012) 24190-24194.
- [4] A.J. Nozik, J. Miller, Introduction to solar photon conversion, *Chem. Rev.*, 110 (2010) 6443-6445.
- [5] R. Luna-Rubio, M. Trejo-Perea, D. Vargas-Vázquez, G. Ríos-Moreno, Optimal sizing of renewable hybrids energy systems: A review of methodologies, *Sol. Energy*, 86 (2012) 1077-1088.
- [6] G. Müller-Fürstenberger, M. Wagner, Exploring the environmental Kuznets hypothesis: Theoretical and econometric problems, *Ecol. Econ.*, 62 (2007) 648-660.
- [7] Y. Shang, S. Hao, C. Yang, G. Chen, Enhancing solar cell efficiency using photon upconversion materials, *Nanomaterials*, 5 (2015) 1782-1809.
- [8] R. Yu, Q. Lin, S.-F. Leung, Z. Fan, Nanomaterials and nanostructures for efficient light absorption and photovoltaics, *Nano energy*, 1 (2012) 57-72.
- [9] B. Wu, Y. Kuang, X. Zhang, J. Chen, Noble metal nanoparticles/carbon nanotubes nanohybrids: synthesis and applications, *Nano Today*, 6 (2011) 75-90.
- [10] W.K. Choi, T.H. Liew, H.G. Chew, F. Zheng, C.V. Thompson, Y. Wang, M.H. Hong, X.D. Wang, L. Li, J. Yun, A combined top-down and bottom-up approach for precise placement of metal nanoparticles on silicon, *Small*, 4 (2008) 330-333.
- [11] X. Wang, J. Zhuang, Q. Peng, Y. Li, A general strategy for nanocrystal synthesis, *Nature*, 437 (2005) 121.
- [12] J. Gao, H. Gu, B. Xu, Multifunctional magnetic nanoparticles: Design, synthesis, and biomedical applications, *Acc. Chem. Res.*, 42 (2009) 1097-1107.

- [13] A.H. Lu, E.e.L. Salabas, F. Schüth, Magnetic nanoparticles: synthesis, protection, functionalization, and application, *Angew. Chem.*, 46 (2007) 1222-1244.
- [14] A. Fujishima, K. Honda, Electrochemical photolysis of water at a semiconductor electrode, *Nature*, 238 (1972) 37-38.
- [15] B. O'Regan, M. Grätzel, A low-cost, high-efficiency solar cell based on dye-sensitized colloidal TiO₂ films, *Nature*, 353 (1991) 737-740.
- [16] N. Serpone, A.V. Emeline, Semiconductor photocatalysis-past, present, and future outlook, *J. Phys. Chem. Lett.*, 3 (2012) 673-677.
- [17] O. Legrini, E. Oliveros, A.M. Braun, Photochemical processes for water treatment, *Chem. Rev.*, 93 (1993) 671-698.
- [18] M.A. Fox, M.T. Dulay, Heterogeneous photocatalysis, *Chem. Rev.*, 93 (1993) 341-357.
- [19] M.R. Hoffmann, S.T. Martin, W. Choi, D.W. Bahnemann, Environmental applications of semiconductor photocatalysis, *Chem. Rev.*, 95 (1995) 69-96.
- [20] C. Ratanatawanate, A. Chyao, K.J. Balkus Jr, S-nitrosocysteine-decorated PbS QDs/TiO₂ nanotubes for enhanced production of singlet oxygen, *J. Am. Chem. Soc.*, 133 (2011) 3492-3497.
- [21] M. Mishra, D.-M. Chun, α -Fe₂O₃ as a photocatalytic material: A review, *Appl. Catal., A*, 498 (2015) 126-141.
- [22] S. Selvarajan, A. Suganthi, M. Rajarajan, K. Arunprasath, Highly efficient BiVO₄/WO₃ nanocomposite towards superior photocatalytic performance, *Powder Technol.*, 307 (2017) 203-212.
- [23] T. Bora, H.H. Kyaw, J. Dutta, Zinc oxide-zinc stannate core-shell nanorod arrays for CdS quantum dot sensitized solar cells, *Electrochim. Acta*, 68 (2012) 141-145.
- [24] S. Sardar, P. Kar, H. Remita, B. Liu, P. Lemmens, S.K. Pal, S. Ghosh, Enhanced charge separation and FRET at heterojunctions between semiconductor nanoparticles and conducting polymer nanofibers for efficient solar light harvesting, *Sci. Rep.*, 5 (2015) 17313.

- [25] S. Sardar, S. Chaudhuri, P. Kar, S. Sarkar, P. Lemmens, S.K. Pal, Direct observation of key photoinduced dynamics in a potential nano-delivery vehicle of cancer drugs, *Phys. Chem. Chem. Phys.*, 17 (2015) 166-177.
- [26] B.-R. Hyun, Y.-W. Zhong, A.C. Bartnik, L. Sun, H.D. Abruna, F.W. Wise, J.D. Goodreau, J.R. Matthews, T.M. Leslie, N.F. Borrelli, Electron injection from colloidal PbS quantum dots into titanium dioxide nanoparticles, *ACS nano*, 2 (2008) 2206-2212.
- [27] X. Guo, W. Song, C. Chen, W. Di, W. Qin, Near-infrared photocatalysis of β -NaYF₄: Yb³⁺, Tm³⁺@ZnO composites, *Phys. Chem. Chem. Phys.*, 15 (2013) 14681-14688.
- [28] M. Gilbert, B. Albinsson, Photoinduced charge and energy transfer in molecular wires, *Chem. Soc. Rev.*, 44 (2015) 845-862.
- [29] M.S. Azzaro, M.C. Babin, S.K. Stauffer, G. Henkelman, S.T. Roberts, Can exciton-delocalizing ligands facilitate hot hole transfer from semiconductor nanocrystals?, *J. Phys. Chem. C*, 120 (2016) 28224-28234.
- [30] J.I. Basham, G.K. Mor, C.A. Grimes, Förster resonance energy transfer in dye-sensitized solar cells, *ACS Nano*, 4 (2010) 1253-1258.
- [31] P.V. Kamat, Manipulation of charge transfer across semiconductor interface. A criterion that cannot be ignored in photocatalyst design, *J. Phys. Chem. Lett.*, 3 (2012) 663-672.
- [32] S. Lian, D.J. Weinberg, R.D. Harris, M.S. Kodaimati, E.A. Weiss, Subpicosecond photoinduced hole transfer from a CdS quantum dot to a molecular acceptor bound through an exciton-delocalizing ligand, *ACS nano*, 10 (2016) 6372-6382.
- [33] J.B. Sambur, B.A. Parkinson, CdSe/ZnS core/shell quantum dot sensitization of low index TiO₂ single crystal surfaces, *J. Am. Chem. Soc.*, 132 (2010) 2130-2131.
- [34] S.G. Kumar, L.G. Devi, Review on modified TiO₂ photocatalysis under UV/visible light: Selected results and related mechanisms on interfacial charge carrier transfer dynamics, *J. Phys. Chem. A*, 115 (2011) 13211-13241.

- [35] J. Nieto-Pescador, B. Abraham, L. Gundlach, Photoinduced ultrafast heterogeneous electron transfer at molecule-semiconductor interfaces, *J. Phys. Chem. Lett.*, 5 (2014) 3498-3507.
- [36] H. Lee, H.C. Leventis, S.J. Moon, P. Chen, S. Ito, S.A. Haque, T. Torres, F. Nüesch, T. Geiger, S.M. Zakeeruddin, PbS and CdS quantum dot-sensitized solid-state solar cells: "Old concepts, new results", *Adv. Funct. Mater.*, 19 (2009) 2735-2742.
- [37] L.-H. Yu, J.-Y. Xi, K.C. Lo, L.J. Antrobus, D.L. Phillips, W.K. Chan, Transient absorption of N719 and its electron transfer kinetics on ZnO nanoparticles surface, *J. Inorg. Organomet. Polym. Mater.*, 25 (2015) 169-175.
- [38] S. Chu, A. Majumdar, Opportunities and challenges for a sustainable energy future, *Nature*, 488 (2012) 294.
- [39] X. Chen, C. Li, M. Grätzel, R. Kostecki, S.S. Mao, Nanomaterials for renewable energy production and storage, *Chem. Rev.*, 41 (2012) 7909-7937.
- [40] R. Asahi, T. Morikawa, T. Ohwaki, K. Aoki, Y. Taga, Visible-light photocatalysis in nitrogen-doped titanium oxides, *Science*, 293 (2001) 269-271.
- [41] A. Fujishima, K. Honda, Electrochemical photolysis of water at a semiconductor electrode, *Nature*, 238 (1972) 37.
- [42] J. Schneider, M. Matsuoka, M. Takeuchi, J. Zhang, Y. Horiuchi, M. Anpo, D.W. Bahnemann, Understanding TiO₂ photocatalysis: Mechanisms and materials, *Chem. Rev.*, 114 (2014) 9919-9986.
- [43] P. Brogdon, H. Cheema, J.H. Delcamp, Near-infrared-absorbing metal-free organic, porphyrin, and phthalocyanine sensitizers for panchromatic dye-sensitized solar cells, *ChemSusChem*, 11 (2018) 86-103.
- [44] S. Lade, A. Zahedi, A revised ideal model for AlGaAs/GaAs quantum well solar cells, *Microelectron. J.*, 35 (2004) 401-410.
- [45] F. Tutu, P. Lam, J. Wu, N. Miyashita, Y. Okada, K.-H. Lee, N. Ekins-Daukes, J. Wilson, H. Liu, InAs/GaAs quantum dot solar cell with an AlAs cap layer, *Appl. Phys. Lett.*, 102 (2013) 163907.

- [46] M. Grätzel, Recent advances in sensitized mesoscopic solar cells, *Acc. Chem. Res.*, 42 (2009) 1788-1798.
- [47] M. Grätzel, Dye-sensitized solar cells, *J. Photochem. Photobiol. C*, 4 (2003) 145-153.
- [48] S. Das, K.G. Thomas, K. Thomas, V. Madhavan, D. Liu, P.V. Kamat, M. George, Aggregation behavior of water soluble bis(benzothiazolylidene) squaraine derivatives in aqueous media, *J. Phys. Chem.*, 100 (1996) 17310-17315.
- [49] K.E. Knowles, M.D. Peterson, M.R. McPhail, E.A. Weiss, Exciton dissociation within quantum dot-organic complexes: Mechanisms, use as a probe of interfacial structure, and applications, *J. Phys. Chem. C*, 117 (2013) 10229-10243.
- [50] J. Patwari, S. Sardar, B. Liu, P. Lemmens, S.K. Pal, Three-in-one approach towards efficient organic dye-sensitized solar cells: aggregation suppression, panchromatic absorption and resonance energy transfer, *Beilstein J. Nanotechnol.*, 8 (2017) 1705-1713.
- [51] J. Patwari, S. Shyamal, T. Khan, H. Ghadi, C. Bhattacharya, S. Chakrabarti, S.K. Pal, Inversion of activity in DSSC for TiO₂ and ZnO photo-anodes depending on the choice of sensitizer and carrier dynamics, *J. Lumin.*, 207 (2019) 169-176.
- [52] J. Patwari, A. Chatterjee, S. Sardar, P. Lemmens, S.K. Pal, Ultrafast dynamics in co-sensitized photocatalysts under visible and NIR light irradiation, *Phys. Chem. Chem. Phys.*, 20 (2018) 10418-10429.
- [53] J. Patwari, H. Ghadi, S. Sardar, J. Singhal, B. Tongbram, S. Shyamal, C. Bhattacharya, S. Chakrabarti, S.K. Pal, Photo-induced electronic properties in single quantum well system: effect of excitonic lifetime, *Mater Res Express* 4 (2017) 016301.
- [54] J. Patwari, A. Chatterjee, H. Ghadi, H. Sharma, S. Chakrabarti, S.K. Pal, *In situ* measurement of temperature dependent picosecond resolved carrier dynamics in near infrared (NIR) sensitive device on action, *Rev. Sci. Instrum.*, 90 (2019) 043909.
- [55] H. Ghadi, J. Patwari, P. Murkute, D. Das, P. Singh, S. Dubey, M. Bhatt, A. Chatterjee, A. Balgarkashi, S. Pal, Optimizing dot-in-a-well infrared detector

architecture for achieving high optical and device efficiency corroborated with theoretically simulated model, *J. Alloys Compd.*, 751 (2018) 337-348.

[56] J. Patwari, H. Joshi, H. Mandal, L. Roy, C. Bhattacharya, P. Lemmens, S.K. Pal, Exciton dissociation in an NIR-active trio hybrid nanocrystal leading to efficient generation of reactive oxygen species, *Phys. Chem. Chem. Phys.*, 21 (2019) 10667-10676

Chapter 2

An Overview of Experimental and Theoretical Tools and Systems

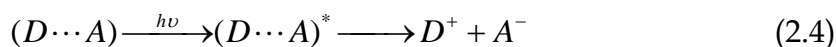
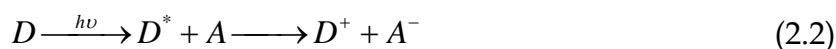
In order to investigate the dynamical processes involved in the light harvesting materials, different steady-state and dynamical tools have been employed. These include photoinduced electron transfer (PET), Förster resonance energy transfer (FRET), photocurrent–voltage (I–V) characterization, incident photon to current conversion efficiency measurement, photovoltage decay measurement of photovoltaic solar cells, an overview of quantum confinement effect and diffuse reflectance spectroscopy. In this chapter, a brief discussion about these tools has been provided. A brief overview of the various systems which are being used, has also been discussed.

2.1. Steady-state and Dynamical Tools:

2.1.1. Photoinduced Electron Transfer (PET): PET can be described as the movement of an electron caused by the absorption of light from an electron-rich species (D) to an electron deficient species (A), as shown in equation 2.1.



The first law of photochemistry tells us that a photoinduced process must be initiated by the absorption of light. In PET, the absorbing species can either be a donor, the acceptor, or a ground-state complex between the donor and acceptor, often referred to as a charge transfer complex. These possibilities are shown in equations 2.2–2.4.



Transport of charges or excitons are commonly seen as fundamental processes in many optoelectronic devices as well as biological systems. The creation, diffusion, and annihilation of excitons and the mobility of charges are some of the key processes in many devices that interconvert electric and light energies [1, 2]. PET is an important process in many biochemical systems, such as those in respiration and photosynthesis [3, 4]. To gain a deep understanding for these systems, it is important to describe the rates of these processes with a few empirically derived parameters [5, 6]. Therefore, it has become increasingly important to develop computational techniques that allow us to calculate the rate of charge or energy transport. In our systems the apparent rate constants, k_{nr} , were determined for the nonradiative processes by comparing the lifetimes of donor in the absence (τ_0) and in the presence (τ) of an acceptor, using equation 2.5 [7].

$$k_{nr} = 1/\langle\tau\rangle - 1/\langle\tau_0\rangle \quad (2.5)$$

This thesis demonstrates several PET processes, particularly in light-harvesting materials and discusses the consequences of various interfacial electron transfer processes. In heterogeneous photocatalysis, the photoinduced charge separation in the photocatalyst is necessary and several strategies have been employed to facilitate the charge separation. In dye/quantum dot-sensitized solar cells (DSSC/QDSC), a series of charge transfer processes had to occur cooperatively so that the electrical output can be harnessed efficiently. These include (i) electron injection from excited dye/QD into metal oxides, (ii) electron transport to the collecting electrode surface, (iii) hole transfer to the redox couple, and (iv) regeneration of the redox couple at the counter electrode. A major force that counteracts these favourable processes (i–iv) is the charge recombination of electrons at the electrolyte interface. The matching of the band energies of the two semiconductors facilitates desired functionality either to induce electron–hole recombination (e.g., light-emitting diodes) or to improve charge separation by driving electrons and holes in two different nanoparticles (e.g., QDSC). In each

instance where semiconductor nanocrystals are implemented into a practical device, PET reactions are intimately involved, and they dictate overall functionality. This thesis focuses on the recent progresses made in understanding the kinetics and mechanistic aspects of various PET processes at the semiconductor interface and their role in optimization of solar cell performance.

2.1.2. Förster Resonance Energy Transfer (FRET): FRET is an electrodynamic phenomenon involving the nonradiative transfer of the excited state energy from the donor dipole (D) to an acceptor dipole (A) in the ground state (Figure 2.1a). Basically, FRET is of two types: (i) homo-molecular FRET and (ii) hetero-molecular FRET. In the former case the same fluorophore acts both as energy donor and acceptor, while in the latter case two different molecules act as donor and acceptor.

Each donor-acceptor (D-A) pair participating in FRET is characterized by a distance known as Förster distance (R_0) i.e., the D-A separation at which energy transfer is 50% efficient. The rate of resonance energy transfer (k_T) from donor to an acceptor is given by [8],

$$k_T = \frac{1}{\tau_D} \left(\frac{R_0}{r} \right)^6 \quad (2.6)$$

where τ_D is the lifetime of the donor in the absence of acceptor and r is the donor to acceptor (D-A) distance. The rate of transfer of donor energy depends upon the extent of overlap of the emission spectrum of the donor with the absorption spectrum of the acceptor ($J(\lambda)$), the quantum yield of the donor (Q_D), the relative orientation of the donor and acceptor transition dipoles (κ^2) and the distance between the donor and acceptor molecules (r) (Figure 2.1b). In order to estimate FRET efficiency of the donor and hence to determine distances between donor-acceptor pairs, the methodology described below is followed [8]. R_0 is given by,

$$R_0 = 0.211 \left[\kappa^2 n^{-4} Q_D J(\lambda) \right]^{1/6} \quad (\text{in } \text{Å}) \quad (2.7)$$

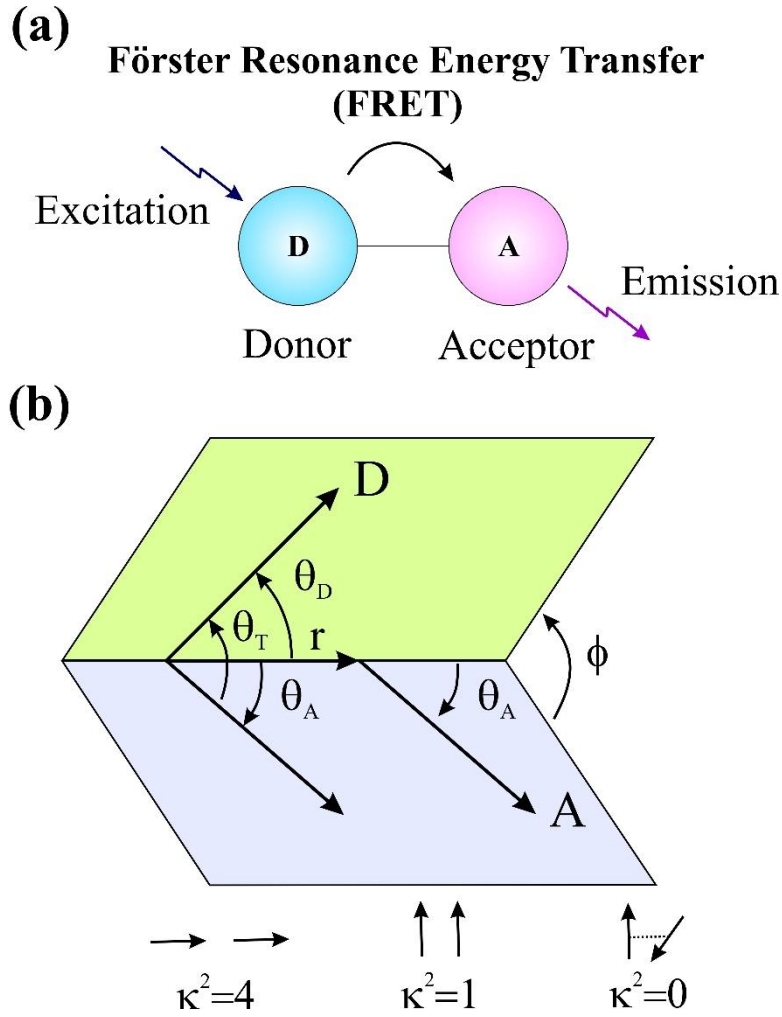


Figure 2.1. (a) Schematic illustration of the FRET process. (b) Dependence of the orientation factor κ^2 on the directions of the emission and absorption dipoles of the donor and acceptor, respectively.

where n is the refractive index of the medium, Q_D is the quantum yield of the donor and $J(\lambda)$ is the overlap integral. κ^2 is defined as,

$$\kappa^2 = (\cos \theta_T - 3 \cos \theta_D \cos \theta_A)^2 = (\sin \theta_D \sin \theta_A \cos \varphi - 2 \cos \theta_D \cos \theta_A)^2 \quad (2.8)$$

where θ_T is the angle between the emission transition dipole of the donor and the absorption transition dipole of the acceptor, θ_D and θ_A are the angles between these dipoles and the vector joining the donor and acceptor and φ is angle between the planes of the donor and acceptor (Figure 2.1b). κ^2 value can vary from 0 to 4. For collinear and parallel transition dipoles, $\kappa^2 = 4$; for parallel dipoles, $\kappa^2 = 1$; and for perpendicularly oriented dipoles, $\kappa^2 = 0$. For donor and acceptors that randomize

by rotational diffusion prior to energy transfer, the magnitude of κ^2 is assumed to be 2/3. However, in systems where there is a definite site of attachment of the donor and acceptor molecules, to get physically relevant results, the value of κ^2 has to be estimated from the angle between the donor emission and acceptor absorption dipoles [9]. $J(\lambda)$, the overlap integral, which expresses the degree of spectral overlap between the donor emission and the acceptor absorption, is given by,

$$J(\lambda) = \frac{\int_0^{\infty} F_D(\lambda) \varepsilon_A(\lambda) \lambda^4 d\lambda}{\int_0^{\infty} F_D(\lambda) d\lambda} \quad (2.9)$$

where $F_D(\lambda)$ is the fluorescence intensity of the donor in the wavelength range of λ to $\lambda+d\lambda$ and is dimensionless. $\varepsilon_A(\lambda)$ is the extinction coefficient (in $M^{-1}cm^{-1}$) of the acceptor at λ . If λ is in nm, then $J(\lambda)$ is in units of $M^{-1} cm^{-1} nm^4$.

Once the value of R_0 is known, the efficiency of energy transfer can be calculated. The efficiency of energy transfer (E) is the fraction of photons absorbed by the donor which are transferred to the acceptor and is defined as,

$$E = \frac{k_T(r)}{\tau_D^{-1} + k_T(r)} \quad (2.10)$$

$$\text{Or, } E = \frac{R_0^6}{r^6 + R_0^6} \quad (2.11)$$

For D-A systems decaying with multiexponential lifetimes, E is calculated from the amplitude weighted lifetimes $\langle \tau \rangle = \sum_i \alpha_i \tau_i$ of the donor in absence (τ_D) and presence (τ_{DA}) of the acceptor as,

$$E = 1 - \frac{\tau_{DA}}{\tau_D} \quad (2.12)$$

The D-A distances can be measured using equations (2.11) and (2.12).

2.1.3. Data Analysis of Time-Resolved Fluorescence Transients: Curve fitting of the time-resolved fluorescence transients was carried out using a nonlinear least square fitting procedure to a function (2.13) comprised of convolution of the IRF

$$(X(t) = \int_0^t E(t')R(t - t')dt') \quad (2.13)$$

($E(t)$) with a sum of exponentials (2.14) with pre-exponential factors (B_i),

$$(R(t) = A + \sum_{i=1}^N B_i e^{-t/\tau_i}) \quad (2.14)$$

characteristic lifetimes (τ_i) and a background (A). Relative concentration in a multiexponential decay is expressed as (2.15).

$$c_n = \frac{B_n}{\sum_{i=1}^N B_i} \times 100 \quad (2.15)$$

The average lifetime (amplitude-weighted) of a multiexponential decay is expressed as,

$$\tau_{av} = \sum_{i=1}^N c_i \tau_i \quad (2.16)$$

2.1.4. Dye-Sensitized Solar Cells (DSSC): DSSC [10-13] is potentially inexpensive alternatives to traditional semiconductor solar cells. The essential components of a DSSC are semiconductor metal oxides attached to sensitizing dyes (mostly, ruthenium) and an electrolyte medium (iodine-based). A schematic of the interior and operating principle of a DSSC is shown in Figure 2.2. The typical basic configuration is as follows: at the heart of the device is the metal oxide layer (mostly ZnO/TiO₂), which is deposited on a fluorine doped tin oxide (FTO) coated glass substrate. Attached to the surface of the nanocrystalline film is a monolayer of the charge transfer dyes/QDs. Photoexcitation of the latter results in the injection of an electron into the conduction band of the oxide, leaving the dye in its oxidized state. The dye is restored to its ground state by electron transfer from the electrolyte, usually an organic solvent containing the iodide/triiodide (I⁻/I₃⁻) redox system.

The regeneration of the sensitizer by iodide intercepts the recapturing of the conduction band electron by the oxidized dye. The I_3^- ions formed by oxidation of I^- diffuse a short distance ($\sim 60 \mu\text{m}$) through the electrolyte to the cathode, which is coated with a thin layer of platinum catalyst, where the regenerative cycle is completed by electron transfer to reduce I_3^- to I^- .

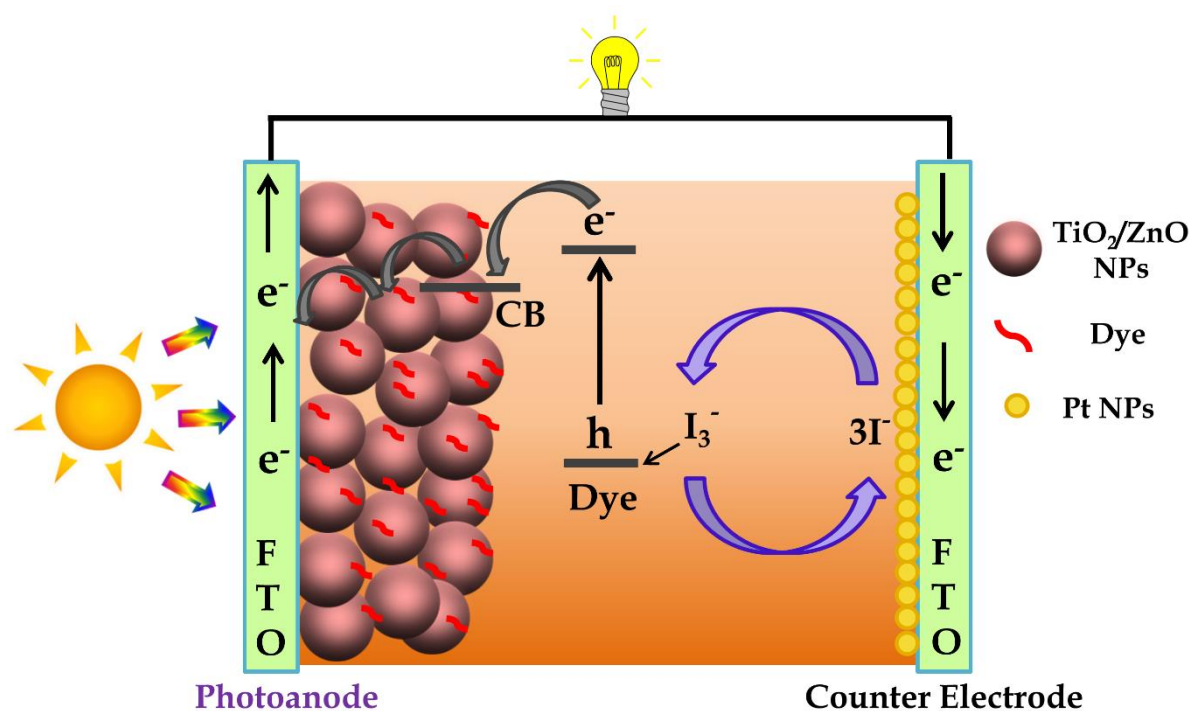


Figure 2.2. Schematic representation of a DSSC showing different charge migration processes.

In order to quantitatively measure the efficacy of a DSSC, photocurrent–voltage (I – V or J – V) measurements under simulated sunlight, incident photon-to-current conversion efficiency (IPCE) under monochromatic light and photovoltage decay measurement under dark condition following a brief illumination of light are important.

2.1.4.1. Photocurrent–Voltage (I – V) Measurements: Many solar cell parameters can be obtained from current-voltage (I – V) measurements of a cell. The I – V characteristics measurement can be done using a Source-Measure Units (SMUs), which can source and measure both current and voltage. A DSSC can be represented

by an equivalent electric circuit shown in Figure 2.3, where, I_L is the photocurrent, R_S is the series resistance (describes the resistances of the materials) and R_{sh} the shunt resistance.

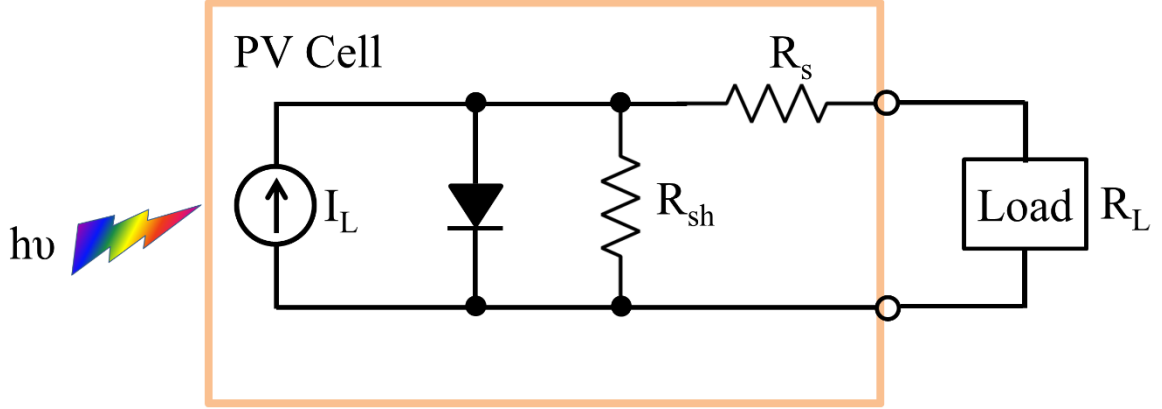


Figure 2.3. Idealized equivalent electric circuit of a DSSC.

A. Short-Circuit Current (I_{sc} or J_{sc}): The current equals the short-circuit current when the applied bias potential is zero:

$$I = I_{ph} - I_s \left[\exp\left(\frac{V + I.R_s}{\eta.V_{th}}\right) - 1 \right] \quad (2.17)$$

B. Open-Circuit Voltage (V_{oc}): When no current is flowing through the cell the potential equals the open-circuit potential, using equation 2.18 one can find:

$$V_{oc} = \eta.V_{th} \ln\left(\frac{I_{ph}}{I_c} + 1\right) \quad (2.18)$$

C. Maximum Power Output (P_{max}): The power delivered from a solar cell at a certain potential equals the product of the current at this potential times the potential:

$$P(V) = I(V).V \quad (2.19)$$

To obtain a graphic representation of the power, one has to vary the potential between V_{oc} and 0. The point where the power is maximum (P_{max}) corresponds to

the peak power point (PPP) for the I - V curve. These are the optimal current and potential conditions (I_m , V_m) for the operating cell.

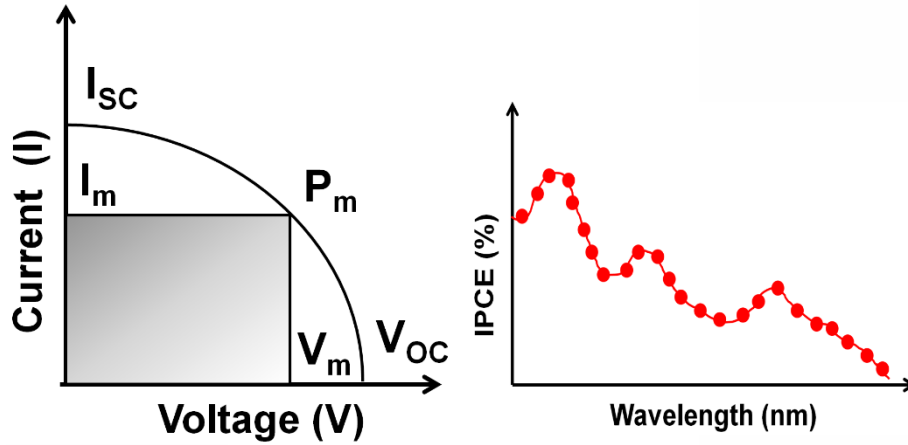


Figure 2.4. Schematic representation of conventional I - V characteristic diagram (left). Typical IPCE characteristic diagram of a DSSC (right).

D. Fill Factor (FF): The FF quantifies the quality of the solar cell, which is the ratio of actual power output ($V_m \times I_m$) versus its 'dummy' power output ($V_{oc} \times I_{sc}$) of a solar cell, as shown in equation 2.20:

$$FF = \frac{V_m I_m}{V_{oc} I_{sc}} \quad (2.20)$$

The FF lies between 0.6 and 0.85 for an efficient DSSC. These values are influenced by the values of the series and the shunt resistances. To obtain high FF values the shunt resistance has to be as small as possible and the series resistance as high as possible.

E. Photo-conversion Efficiency (η): The overall photo-conversion efficiency is given by the following equation:

$$\eta = \frac{V_m I_m}{P_{in}} = \frac{V_{oc} I_{sc} FF}{P_{in}} \quad (2.21)$$

It expresses the ratio of produced power and the incoming power (P_{in}). The experimental conditions have been fixed worldwide, in order to compare results coming from different places. A power density value of 100 mW/cm², at air mass 1.5 global (AM 1.5 G) condition has been set for the incident solar radiation, and the temperature of the cell should be 25 °C. The AM is the ratio of the path-length of incoming sunlight through the atmosphere when the sun is at an angle to the zenith, and the path-length when the Sun is at the zenith.

2.1.4.2. Incident Photon-to-Current Conversion Efficiency (IPCE) Measurements:

The sensitivity of a solar cell varies with the wavelength of the incoming light. The IPCE value corresponds to the photocurrent density produced in the external circuit under monochromatic illumination of the cell divided by the photon flux that strikes the cell. From such an experiment the IPCE as a function of wavelength can be calculated from:

$$IPCE(\lambda) = \frac{n_{electrons}(\lambda)}{n_{photons}(\lambda)} = \frac{I(\lambda)/e}{P_{in}(\lambda)/h\nu} = \frac{I(\lambda)}{\lambda P_{in}(\lambda)} \cdot \frac{hc}{\nu} \quad (2.22)$$

$$\text{Or, } IPCE\% = [1240 \times J_{sc}(\text{A/cm}^2)] / [\lambda(\text{nm}) \times P(\text{W/cm}^2)] \times 100 \quad (2.23)$$

where, $I(\lambda)$ is the current given by the cell at wavelength λ , $P_{in}(\lambda)$ the incoming power at wavelength λ and I_p is the incident light power striking the device. IPCE values provide practical information about the monochromatic quantum efficiencies of a solar cell. Figure 2.4 (right) shows a typical IPCE spectrum of a standard DSSC.

2.1.4.3. Photovoltage Decay Measurements: The open circuit voltage of a DSSC generated under illumination is equivalent to the separation between the quasi-Fermi level of electrons in the TiO₂ film and the rest potential of the counter electrode, which remains in equilibrium with the redox couple. The forward

electron injection from sensitizer to TiO₂ is terminated upon stopping the illumination, thus discharging of electrons occurs through the back electron transfer or recombination with the oxidized electrolytes. The open circuit voltage decay reflects the timescales for the recombination processes.

2.1.5. Quantum Confinement Effect: The band gap of a semiconductor is defined as the difference between the highest energy level of the valence band and the lowest energy level of the conduction band [13]. When a semiconductor is excited by a photon with sufficient energy two quasiparticles are created (a hole h⁺ with the mass m^{*_h} and a positive charge +e and an electron e⁻ with the mass m^{*_e} and the negative charge -e). The concept of quasiparticles is used in theory to replace a consideration of a large number of interacting particles by a small number of non-interacting quasiparticles. These quasiparticles are described as elementary excitations of a system of a number of real particles. In our case, the electron in the conduction band represents the primary elementary excitation of the electron subsystem of the crystal. The hole represents an ensemble of electrons in the valence band from which one electron was removed (e.g. to the conduction band). In reality, the electron and the hole as charged particles do interact *via* the Coulomb potential and form a third quasiparticle the so called exciton, which corresponds to a hydrogen-like bound state of an electron-hole pair and is therefore characterized by the exciton Bohr radius a_B [14]:

$$a_B = \frac{4\pi\epsilon_0\epsilon_r\hbar^2}{e^2} \left(\frac{1}{m_e^*} + \frac{1}{m_h^*} \right) \quad (2.24)$$

The exciton Bohr radius is considerably larger than the respective value for a hydrogen atom because the values for the effective masses for the electron and the hole are smaller than the effective mass of the electron at rest m_0 , and the dielectric constant ϵ in a semiconductor several times larger than 1 which is the value for vacuum. Typical values for a_B for common semiconductors range in the interval from 1-10 nm. As a result of the creation of an exciton and a free e-h pair, the

absorption spectrum of direct band gap semiconductor monocrystals contains a pronounced resonance peak at the energy,

$$h\nu = E_g - Ry^* \quad (2.25)$$

with ν the frequency and the Rydberg energy being,

$$Ry^* = \frac{e^2}{2\epsilon a_B} \quad (2.26)$$

when the Rydberg energy is smaller than kT ($kT \ll Ry^*$).

When the radius of a particle approaches a_B the exciton in the particles experience a spatial confinement and can only exist in the particle when it is in a state of higher energy which leads to an increase in the energy gap of the semiconductor. As a result of such a quantum confinement an exciton in a nanocrystal has to be considered as a particle in a box, so its kinetic energy becomes quantized and the energy bands split into discrete levels. This is the origin of the name quantum dots for such particles [14]. This quantum confinement can be explained by the effective mass approximation [15].

2.1.5.1. Effective Mass Approximation: The effective mass approximation calculates the size-dependent band gap of the quantum dots, mechanism, with the particle in a box approach and uses the effective masses of electron and hole in the term for the kinetic energy, which leads to the following result [13]:

$$E = E_g + \frac{\pi^2 \hbar^2}{2m_0 r^2} \left(\frac{1}{m_e^*} + \frac{1}{m_h^*} \right) - \frac{1.8e^2}{4\pi\epsilon_0\epsilon_r} - 0.25 \frac{e^4}{8\pi^2\epsilon_0^2\epsilon_r^2\hbar} \left(\frac{1}{m_e^*} + \frac{1}{m_h^*} \right) \quad (2.27)$$

The first term is the bulk band gap energy, the second is the kinetic energy of both the electron and the hole in a spherical box, the third term is their Coulomb attraction and the last one corresponds to the correlation between two particles. When r tends to high values E approaches E_g .

2.1.6. Diffuse Reflectance Spectroscopy: Reflectance spectroscopy is very closely related to UV/Vis spectroscopy, as both of these techniques use visible light to excite valence electrons to empty orbitals. The difference in these techniques is that in UV/Vis spectroscopy one measures the relative change of transmittance of light as it passes through a solution, whereas in diffuse reflectance, one measures the relative change in the amount of reflected light off of a surface. A solution that is completely clear and colorless has essentially 100% transmission of all visible wavelengths of light, which means that it does not contain any dissolved components that have (allowed) electronic transitions over that energy range. By the same line of reasoning, a white powder effectively reflects 100% of all visible wavelengths of light that interacts with it. However, if the material has electronic energy levels that are separated by energy in the visible region, then it may absorb some of light energy to move electrons from the filled energy level (valence band) into this empty level (conduction band). This causes a relative decrease in the amount of light at that particular energy, relative to a reference source. In other words, the % transmission/reflectance will decrease.

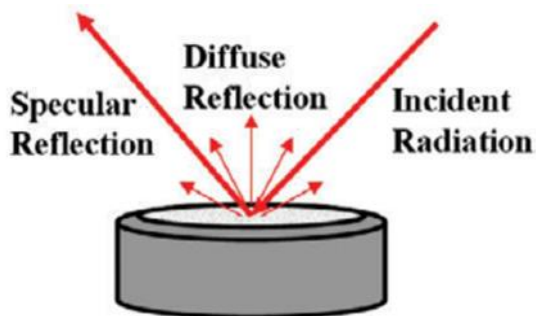


Figure 2.5. Schematic representation of the diffuse reflection from a solid sample. The diffuse light can be collected for spectroscopic studies.

2.2. Theoretical Modelling:

2.2.1. InAs/InGaAs Quantum Dots Parametric Equations: A concentration dependent strain model is developed to simulate the InAs/InGaAs DWELL structure. The different parameters of InGaAs depend on the concentration of In (c) and are depicted as follows,

$$E_g = 0.475c^2 - 1.575c + 1.52 \quad (2.28)$$

$$m_e = 0.04c + 0.665(1 - c) \quad (2.29)$$

As shown in Figure 2.6, QDs are considered to be of truncated pyramidal structure. The dimensions for InAs QDs are considered from TEM images. The effect of increasing the capping thickness of In_{0.15}Ga_{0.85}As on the transition energies is studied. The observed conduction band profile are shown in Figure 2.7.

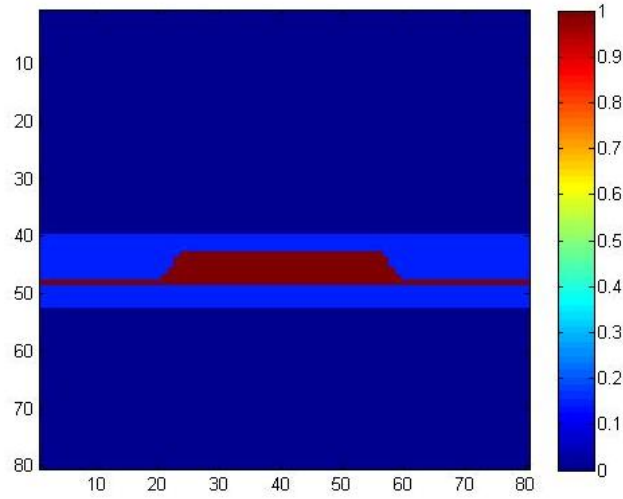


Figure 2.6. Truncated Pyramidal Structure of Quantum Dot in a Well for DWELL structure.

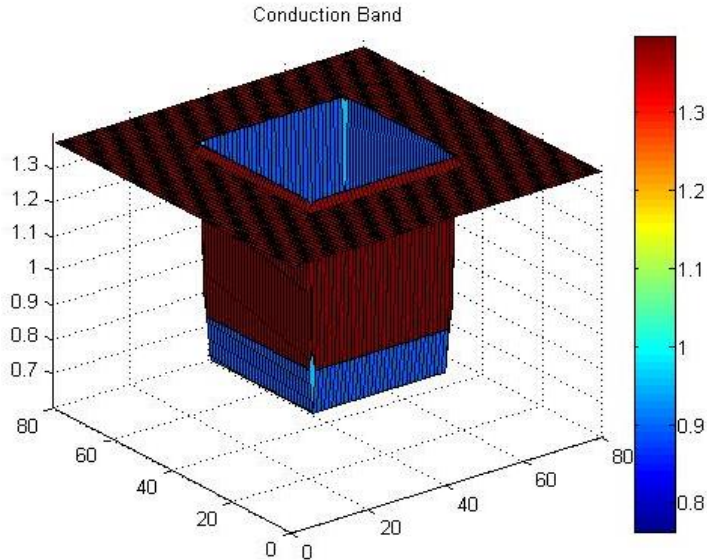


Figure 2.7. Conduction Band Diagram for DWELL structure.

2.2.2. Strain Equations: The methodology for the calculation of strain [16] and energy levels remains the same, irrespective of capping. We calculate strain using equation 2.

$$\epsilon = \frac{a_x - a_0}{a_0} \quad (2.30)$$

Here, a_x and a_0 represent the lattice constant of the epitaxial layer and substrate, respectively. The various parameters used in the strain model are concentration dependent and are calculated from the equations 2.31-2.36, The elastic coefficient [17] is calculated as follows:

$$c_{11} = (12.23 - 3.9c_{in}) * 10^{11} \text{ dynes/cm}^2 \quad (2.31)$$

$$c_{12} = (5.71 - 1.18c_{in}) * 10^{11} \text{ dynes/cm}^2 \quad (2.32)$$

The hydrostatic pressure coefficient [17] is expressed as follows:

$$\frac{dE_g}{dP} = (11.3 - 1.1c_{in}) \text{ eV/bal} \quad (2.33)$$

The effect on the confinement caused by the hydrostatic component of strain can be expressed as follows:

$$S_{\perp} = -2a(1 - \frac{c_{12}}{c_{11}})\epsilon \quad (2.34)$$

Here, "a" is the hydrostatic deformation potential expressed as follows:

$$a = -\frac{1}{3}(c_{11} + 2c_{12}) \frac{dE_g}{dP} \quad (2.35)$$

The conduction band (CB) offset and valence band (VB) offset using Andersons rule is in a 66/34 ratio for InGaAs. Strain potential is obtained from equation 2.36.

$$V = \Delta E * S_{\perp} \quad (2.36)$$

Here, ΔE is the offset in the respective bands.

2.2.3. Energy State Equations: Schrödinger's equation (equation 2.37) was employed to calculate energy levels of the heterostructure for both electrons and holes.

$$H\psi = -\frac{\hbar^2}{2} \nabla \cdot \left(\frac{1}{m^*} \nabla \psi \right) + V\psi = E\psi \quad (2.37)$$

The finite-difference approximation has been used with the Dirichlet boundary conditions imposed on the wavefunction, resulting in an eigenvalue problem, where the Hamiltonian is the matrix formed by the calculations presented before, and energies are obtained as its eigenvalues. The potential described in the Schrodinger equation above accounts only the lattice formed potential; however, to handle electronic interaction among carriers, we need to solve the Poisson equation 2.38.

$$\nabla^2 V = \frac{\rho}{\epsilon} \quad (2.38)$$

Linear interpolation of permittivity is possible using Vegard's law and the electrostatic energy was calculated using equation 2.39.

$$E_{coul} = \int \rho V d\tau \quad (2.39)$$

All the calculated energies are added and the photoluminescence E_{PL} energy peak obtained is as follows,

$$E_{PL} = E_{coul} + E_{conf}^e + E_{conf}^h \quad (2.40)$$

Here, E_{conf}^e and E_{conf}^h represent the electron and hole confinement energies, respectively.

In the simulation, we have defined band gap as the separation between the bottom CB to the top of VB (heavy hole branch). Strain causes deviation in the potential values of energy levels as it acts as a perturbation and hence lifts the degeneracy among the light and heavy holes. The band gap decreases as the heavy hole branch moves up keeping the conduction band minima to be fixed. As a result

of the spatial variation in strain strength in the sample, this band gap decrease is detectable at the edges as strain attains its maximum. In other words, the greater the strain, the lesser is the band gap. Hence, at low temperature, strain is considerably strong, band gap reduces; hence, CB exhibits a dip at the edges [18].

2.2.4. InGaAs Quantum Well Simulation: As the capping thickness is increased beyond 6 nm, the dissolution of dots predominates leading to the formation of InGaAs well. The well is formed with a concentration gradient of In from the center (InAs dots, In-100%) to the periphery (In-15%) of the capping layer. The theoretical model was modified to compute the energy band of the InGaAs Well with varying In concentration. The experimental data was compared with the theoretical model and the percentage of In in the InGaAs well was calculated. For the theoretical model the average In concentration in the well is calculated instead of the concentration gradient in the well.

In this model, we use the finite difference method for calculating the Hamiltonian matrix and the corresponding Eigen values while taking into account the effective mass differences at the interface. We discretize the position variable x into a lattice of points such that the spacing between the points is equal to a . The representation becomes exact only in the limit $a \rightarrow 0$ but as long as ' a ' is smaller than the spatial scale on which ψ varies, it is expected to be reasonably accurate.

The thickness of the InGaAs wells formed is considered to be 6 nm for sample A, 8 nm for sample B and 10 nm for sample C including the 2 nm pseudo-morphic InGaAs layer below the dot layer. Same parametric equations as InAs QDs are used in InGaAs well.

2.3. Systems:

2.3.1. Quantum Confined Nanostructures: The quantum confinement effect, which occurs when the size of a particle is small (usually <10 nm) compared to the wavelength of its electron. This effect influences the optical and electronic

properties and the bandgap of the material. When the movement of an electron or hole is restricted in any dimension, the energy band is discretized to energy states. The discreteness of possible energy states that the particle can occupy is evident if the confinement of a particle to a region of space is on the order of (or smaller than) the particle's de Broglie wavelength. In contrast to the continuous absorption spectrum of a bulk semiconductor, this discrete structure of the energy states leads to a discrete absorption spectrum. According to the number of spatial dimensions along which the particles are confined, quantum-confined structures can be classified as quantum wells (QWs; confinement along one dimension-1D), quantum wires (confinement along two dimensions-2D), and quantum dots (QDs; confinement along three dimensions-3D). We have used quantum well (QW), self-assembled or epitaxial QDs and colloidal QDs as well in our studies for NIR light harvesting. In this section, we will discuss about the different quantum confined structures that have been used in the course of study.

2.3.1.1. GaAs/AlGaAs quantum well (QW): Quantum wells is formed when a smaller band gap semiconductor material such as gallium arsenide (GaAs) is sandwiched between two layers of a wider bandgap material like aluminium arsenide (AlGaAs). A potential well of discrete energy states are generated which leads to distinct and structured optical transitions. These structures are grown by molecular beam epitaxy (MBE) with monolayer level control on the layer thickness.

2.3.1.2. InAs/InGaAs/GaAs Dot-in-a-Well (DWELL): The dots-in-a-well (DWELL) architecture has received considerable academic attention in the last decade [19-21]. A typical DWELL structure (Figure 2.6) consists of InAs QDs placed between two asymmetric InGaAs capping layer and surrounded by a GaAs capping. For device application, this design offers the advantages of tuning the detection peak wavelength, low dark current, and high operating temperature. Additionally, the quality of the dot highly dependent on the thickness of the well in which the dot is embedded as the well act as a strain reducing layer for the dot. On the contrary,

after a certain thickness limit, this strain reducing layer may cause the dot sublimation.

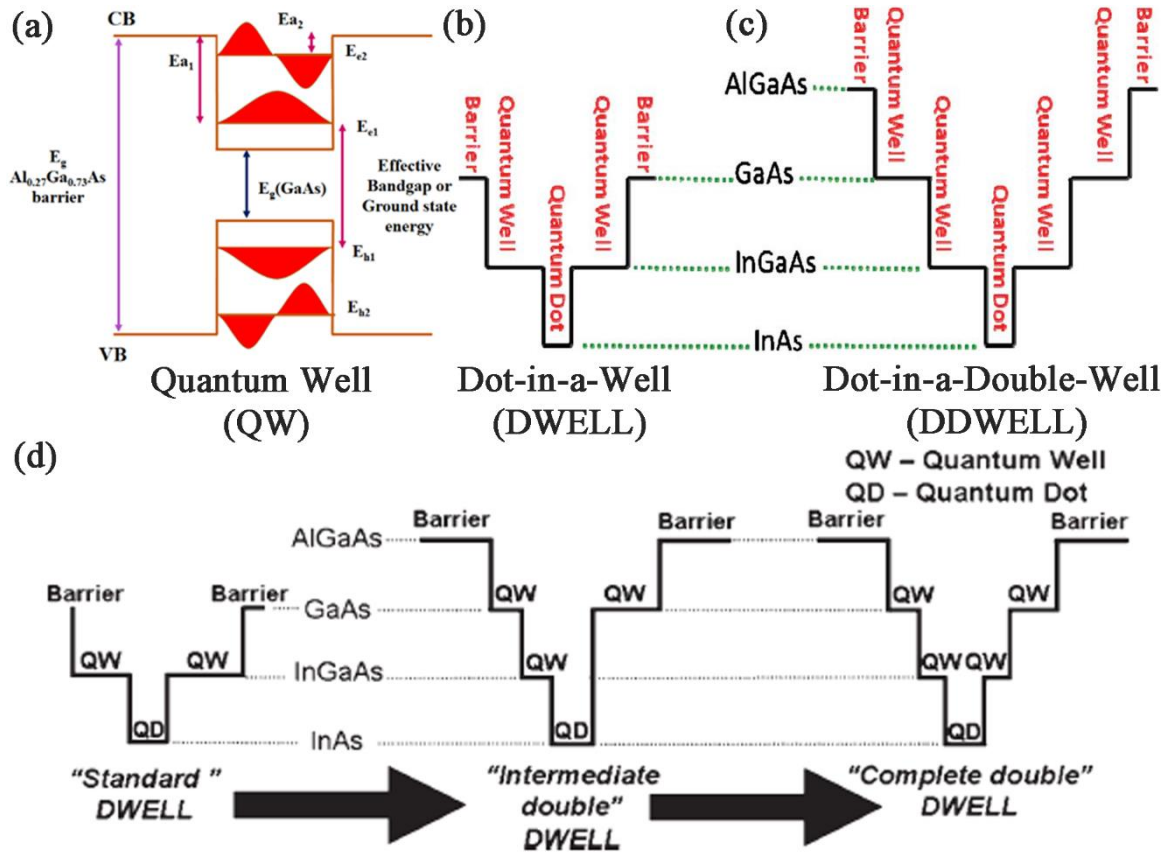


Figure 2.6. Schematic representation of the energy diagram of (a-c) all quantum confined heterostructures used, (d) Progression of structure from DWELL to intermediate DDWELL and finally to complete DDWELL [22, 23].

2.3.1.3. InAs/InGaAs/GaAs/AlGaAs Dot-in-a-Double-Well (DDWELL): More recently, technologies in DWELL devices have been further advanced by embedding InAs QDs in InGaAs and GaAs double wells with AlGaAs barriers, leading to a less strained InAs/InGaAs/GaAs/AlGaAs heterostructure. These lower strain quantum dots-in-a-double-well devices exhibit lower dark current than the previous generation DWELL devices while still demonstrating spectral tunability. The DDWELL heterostructures are advantageous than the dot in the single well or simple dots due to reduced strain between the multiple stacks. Thus, the DDWELL structure is better choice for device fabrication. But at the same time

due to increased number of interfaces the carrier loss possibilities are also more. The schematic band diagram of the active layer of a DDWELL sample and the step by step growth procedure has been represented in Figure 2.6.

2.3.1.4. PbS Colloidal Quantum Dot (QD): Among all the lead chalcogenide colloidal nanocrystals (NCs), lead sulfide quantum dots (PbS QDs) are the most promising material for solution processable optoelectronics. PbS is a class of IV-VI semiconductor NC which have attracted a huge scientific attention in recent years due to its large exciton Bohr radius (18 nm) and strong quantum confinement effects. PbS QDs are a suitable choice for diode laser, light-emitting diodes, infrared detector, photovoltaics and incoherent up/down conversion of infrared light [23] applications due to their interesting electrical and optical properties such as band gap tunability, strong absorption over a broad wavelength region spanning the near and short wavelength infrared (NIR 700-1000 nm and SWIR 1000-1600 nm) which extends its applications beyond the band gap of silicon. Large dipole moment, enhanced multiple exciton generation (MEG) and low-cost solution processability are some other interesting feature of this quantum dot [24, 25].

2.3.2. Molecular Probes: In this section, we will discuss about the different probe molecules that have been used in the course of study.

2.3.2.1. 3,7,12,17-Tetramethyl-8,13-divinyl-2,18-porphinedipropionic acid [Protoporphyrin IX, PP]: PP is an important precursor to biologically essential prosthetic groups such as heme, cytochrome c, and chlorophylls. PP is a very well-known cancer drug and efficient hydrophobic photosensitizer (PS) [26]. PPIX exhibits an intense Soret band absorption at 406 nm (S_0-S_2 transition), together with four weaker Q-bands at 506, 542, 577, and 630 nm (S_0-S_1 transition) [27, 28]. PP is a very well-known photosensitizer (PS) for photodynamic therapies, energy harvesting application [28, 29].

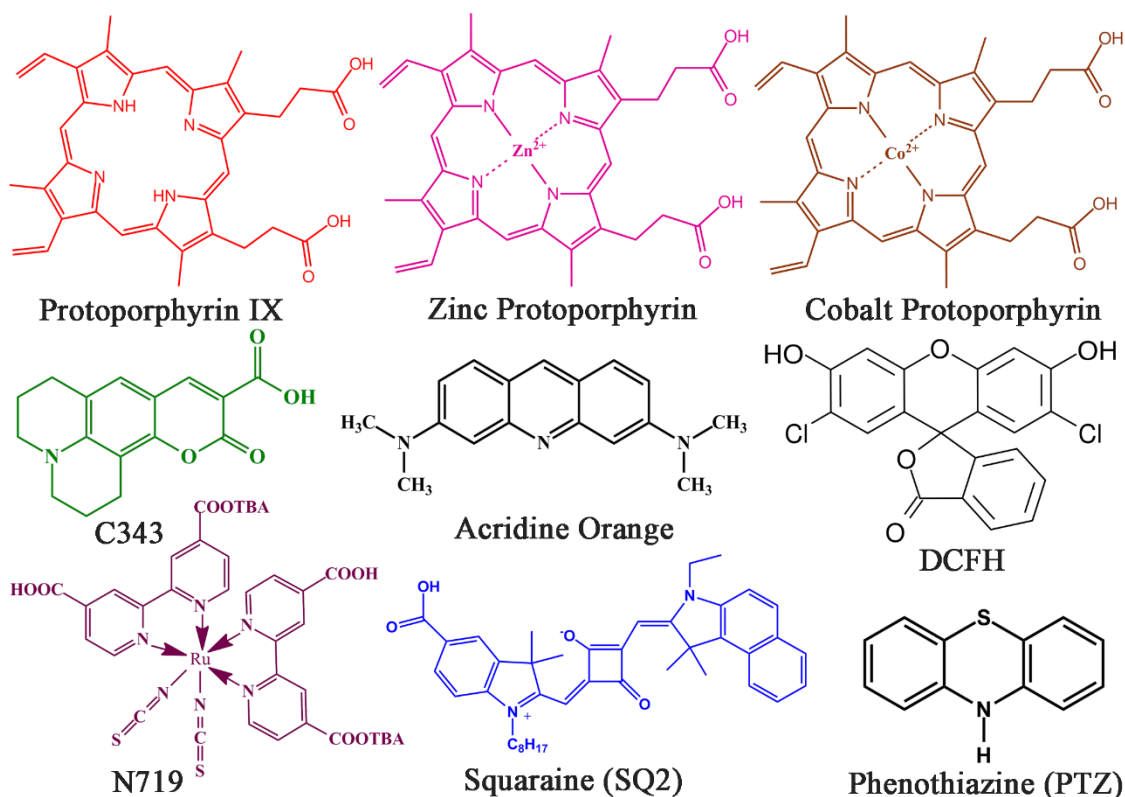


Figure 2.7. Schematic representation of the molecular probes used.

2.3.2.2. Zinc Protoporphyrin (ZnPP): ZnPP (structure shown in Figure 2.7) is a regular metalloporphyrin which contains a closed-shell d^{10} metal ion Zn (II) at the core of the protoporphyrin moiety. In ZnPP, the $d\pi$ (dxz , dyz) metal-based orbitals are relatively low in energy. For PP(Zn) the Soret band maxima appears at 421 nm and the two prominent Q bands appear at 547 nm and 584 nm [30]. The decrease in the number of Q bands upon core metalation can be assigned to the increase in molecular symmetry from D_{2h} to D_{4h} [31]. Zinc porphyrin structures has widely been used in electrocatalysis and other light harvesting applications [32].

2.3.2.3. Cobalt Protoporphyrin (CoPP): Cobalt porphyrin (CoPP) is a 'Hypsoporphyrin' complexes having the d^7 Co^{2+} ion at the central core of the protoporphyrin ring. It play significant roles in many biological and catalytic systems [33-35]. In the case of PP(Co), the B band maxima is at 423 nm and the Q (1,0), Q (0,0) peaks are at 535 nm and 568 nm. The diversity of the functions of CoPP

system is due to the variety of valence states of cobalt metals that bind in the “pocket” of the porphyrin ring system. Co(II) porphyrin resembles the naturally occurring cobalt-containing coenzyme vitamin B12. Like the other hypso-porphyrin systems, in CoPP also there is a significant metal $d\pi$ to porphyrin π^* orbital interaction (metal to ligand π -backbonding) which leads to an increased porphyrin π to π^* energy separation.

2.3.2.4. Coumarin 343 (C343): C343 is an ideal system for studying electron transfer into metal oxides, as it is known to undergo fast electron injection [36, 37] with ~80–90% efficiency [37, 38]. C343 and its derivatives have been successfully used in organic DSSCs [39-41], where the carboxyl group of C343 binds directly to the metal ions on the surface of the nanoparticles [42]. They also have large extinction coefficient though absorption spectrum shows a sharp peak at ~442 nm ($4.4 \times 10^4 \text{ M}^{-1} \text{ cm}^{-1}$) [43].

2.3.2.5. 3-N,3-N,6-N,6-N-Tetramethylacridine-3,6-diamine [Acridine Orange (AO)]: Acridine orange (AO) is a heterocyclic dye containing nitrogen atoms, which is widely used in the fields of printing and dyeing, leather, printing ink and lithography [44]. The organic dye AO (Figure 2.7) absorbs in the visible region and is being used as a nucleic acid-selective fluorescent cationic dye. It has also been used extensively in biological stains. Toxicological investigations indicate that aminoacridine has mutagenic potential. The release of this colored wastewater in the ecosystem is a dramatic source of water pollution, eutrophication and perturbation in aquatic life [45]. Therefore, a method of treating wastewater containing AO is highly desirable method to detect the efficiency of a photocatalyst.

2.3.2.6. 2',7'-dichloro-3',6'-dihydroxy-3H-spiro[2-benzofuran-1,9'-xanthen]-3-one [Dichlorofluorescein (DCFH)]: Dichlorofluorescein (DCFH) is a probe which belong to the organic compounds of fluorescein family. DCFH is trapped within cells and can be oxidized to dichlorofluorescein (DCF) which has an intense green

fluorescence. The molecular structure of DCFH is shown in Figure 2.7. Dichlorofluorescein (DCFH) is non-fluorescent which convert to fluorescent dichlorofluorescein (DCF) upon oxidation through reacting with reactive oxygen species (ROS). This quantifies amount of ROS as well as cellular oxidative stress.

2.3.2.7. Di-tetrabutylammonium cis-bis(isothiocyanato)bis(2,2'-bipyridyl-4,4'-dicarboxylato)ruthenium(II) (N719): Metal complexes, in particular the Ru(II) complexes, have been investigated intensively for DSSC application because of their broad absorption spectra, large value of extinction coefficient ($1.4 \times 10^4 \text{ M}^{-1} \text{ cm}^{-1}$) [46], and favorable photovoltaic properties. N719 (Figure 2.7) consists of a central Ru(II) ion with ancillary ligands having four anchoring groups (COOH). Light absorption in the visible part of the solar spectrum is due to a metal to ligand charge transfer (MLCT) process. The central metal ion is therefore a crucial part of the overall properties of the complexes. Ancillary ligands (bipyridines) can be tuned by different substituents (alkyl, aryl, heterocycle, etc.) to change the photophysical and electrochemical properties and thus improve the photovoltaic performance. Anchoring groups are employed to link the dye with the semiconductor and facilitate the injection of the excited electron into the conduction band of the semiconductor. One can modify any part of the complex to tune the energy levels of the MLCT states and to optimize electron injection and dye regeneration kinetics.

2.3.2.8. 5-carboxy-2-[[3-[(2,3-dihydro-1,1-dimethyl-3-ethyl-1H-benzo[e]indol-2-ylidene)methyl]-2-hydroxy-4-oxo-2-cyclobuten-1-ylidene]methyl]-3,3-dimethyl-1-octyl-3H-indolium [Squaraine (SQ2)]: Squaraine SQ2 (Figure 2.7) is a condensation product of electron-rich substrate and squaric acid derivatives, with a four-membered squaraine ring present into the polymethine chain structure consist of absorption maxima in longer wavelength region [47, 48]. SQ2 impose greater light-absorption ability (molar extinction co-efficient $319\ 000 \text{ M}^{-1} \text{ cm}^{-1}$) at low-energy region ($\sim 665 \text{ nm}$ absorption maxima) and higher photo-stability with respect to other available commercial dyes. Due to the extended absorption in the near

infra-red (NIR) region, SQ2 is considered as an important photoactive materials in the field of organic photovoltaic devices [49], dye sensitized solar cell (DSSC) [50], biomedical imaging and photomedicine [48].

2.3.2.9. 10H-dibenzo-[b,e]-1,4-thiazine [Phenothiazine (PTZ)]: Phenothiazine (PTZ) [51-55], is a well-known heterocyclic organic compound having the chemical formula $S(C_6H_4)_2NH$. It is related to the thiazine-class of heterocyclic compounds. PTZ (Figure 2.7) can act as an electron-donating unit due to the presence of the electron-rich sulfur and nitrogen heteroatoms. PTZ is widely reported to be a very good hole acceptor because of its low oxidation potential (+0.76 V vs SCE) [56]. PTZ has been used as a probe for hole transfer dynamics in DNA [57, 58] and quantum dots [59] as well. Derivatives of phenothiazine are used in the field of medicinal chemistry, pest management, advanced batteries and fuel cells. It is able to form charge-transfer salts with many acceptors.

References

- [1] H. Spanggaard, F.C. Krebs, A brief history of the development of organic and polymeric photovoltaics, *Sol. Energy Mater. Sol. Cells*, 83 (2004) 125-146.
- [2] Y. Shirota, H. Kageyama, Charge carrier transporting molecular materials and their applications in devices, *Chem. Rev.*, 107 (2007) 953-1010.
- [3] H.B. Gray, J.R. Winkler, Electron tunneling through proteins, *Q. Rev. Biophys.*, 36 (2003) 341-372.
- [4] G. McLendon, R. Hake, Interprotein electron transfer, *Chem. Rev.*, 92 (1992) 481-490.
- [5] H. Bassler, Charge transport in disordered organic photoconductors: A monte carlo simulation study, *Phys. Status Solidi B*, 175 (1993) 15-56.
- [6] V.M. Kenkre, J.D. Andersen, D.H. Dunlap, C.B. Duke, Unified theory of the mobilities of photoinjected electrons in naphthalene, *Phys. Rev. Lett.*, 62 (1989) 1165-1168.
- [7] J.H. Bang, P.V. Kamat, Quantum dot sensitized solar cells. A tale of two semiconductor nanocrystals: CdSe and CdTe, *ACS Nano*, 3 (2009) 1467-1476.
- [8] J.R. Lakowicz, Principles of fluorescence spectroscopy, 2nd ed., *Kluwer Academic/Plenum*, New York, 2006.
- [9] D. Banerjee, S.K. Pal, Simultaneous binding of minor groove binder and intercalator to dodecamer DNA: Importance of relative orientation of donor and acceptor in FRET, *J. Phys. Chem. B*, 111 (2007) 5047-5052.
- [10] B. O'regan, M. Grätzel, A low-cost, high-efficiency solar cell based on dye-sensitized colloidal TiO₂ films, *Nature*, 353 (1991) 737-740.
- [11] M. Grätzel, Photoelectrochemical cells, *Nature*, 414 (2001) 338-344.
- [12] M. Grätzel, Conversion of sunlight to electric power by nanocrystalline dye-sensitized solar cells, *J. Photochem. and Photobiol. A*, 164 (2004) 3-14.
- [13] P.E. Lippens, M. Lannoo, Calculation of the band gap for small CdS and ZnS crystallites, *Phys. Rev. B*, 39 (1989) 10935-10942.

- [14] S.V. Gaponenko, Optical properties of semiconductor nanocrystals, *Cambridge University Press*, Cambridge, 1998.
- [15] L.E. Brus, Electron-electron and electron-hole interactions in small semiconductor crystallites: The size dependence of the lowest excited electronic state, *J. Chem. Phys.*, 80 (1984) 4403.
- [16] H. Ghadi, N. Sehara, P. Murkute, S. Chakrabarti, Minimization of material inter-diffusion for thermally stable quaternary-capped InAs quantum dot via strain modification, *Superlattice. Microst.*, 105 (2017) 117-131.
- [17] K. Nishi, H. Saito, S. Sugou, J.-S. Lee, A narrow photoluminescence linewidth of 21 meV at 1.35 μm from strain-reduced InAs quantum dots covered by $\text{In}_{0.2}\text{Ga}_{0.8}\text{As}$ grown on GaAs substrates, *Appl. Phys. Lett.*, 74 (1999) 1111-1113.
- [18] M. Srujan, K. Ghosh, S. Sengupta, S. Chakrabarti, Presentation and experimental validation of a model for the effect of thermal annealing on the photoluminescence of self-assembled InAs/GaAs quantum dots, *J. Appl. Phys.*, 107 (2010) 123107.
- [19] J. Urayama, T.B. Norris, J. Singh, P. Bhattacharya, Observation of phonon bottleneck in quantum dot electronic relaxation, *Phys. Rev. Lett.*, 86 (2001) 4930.
- [20] H. Ghadi, S. Sengupta, S. Shetty, A. Manohar, A. Balgarkashi, S. Chakrabarti, N.B. Pendyala, S.L. Prajapati, A. Kumar, Comparison of three design architectures for quantum dot infrared photodetectors: InGaAs-capped dots, dots-in-a-well, and submonolayer quantum dots, *IEEE T Nanotechnol*, 14 (2015) 603-607.
- [21] H. Ghadi, S. Adhikary, A. Agarwal, S. Chakrabarti, Tuning in spectral response due to rapid thermal annealing on dot-in-a-well infrared photodetectors, *Superlattice. Microst.*, 65 (2014) 106-112.
- [22] Y.D. Sharma, M. Kutty, R. Shenoi, A.V. Barve, S. Myers, J. Shao, E. Plis, S. Lee, S. Noh, S. Krishna, Investigation of multistack InAs/InGaAs/GaAs self-assembled quantum dots-in-double-well structures for infrared detectors, *J. Vac. Sci. Technol., B: Nanotechnol. Microelectron.: Mater., Process., Meas., Phenom.*, 28 (2010) C3G1-C3G7.

- [23] J.R. Andrews, S.R. Restaino, S.W. Teare, Y.D. Sharma, W.-Y. Jang, T.E. Vandervelde, J.S. Brown, A. Reisinger, M. Sundaram, S. Krishna, Comparison of quantum dots-in-a-double-well and quantum dots-in-a-well focal plane arrays in the long-wave infrared, *IEEE Trans. Electron Devices*, 58 (2011) 2022-2027.
- [24] J.R. Caram, S.N. Bertram, H. Utzat, W.R. Hess, J.A. Carr, T.S. Bischof, A.P. Beyler, M.W. Wilson, M.G. Bawendi, PbS nanocrystal emission is governed by multiple emissive states, *Nano letters*, 16 (2016) 6070-6077.
- [25] H. Beygi, S.A. Sajjadi, A. Babakhani, J.F. Young, F.C. van Veggel, Surface chemistry of as-synthesized and air-oxidized PbS quantum dots, *Appl. Surf. Sci.*, 457 (2018) 1-10.
- [26] W.E. Grant, A. MacRobert, S.G. Bown, C. Hopper, P.M. Speight, Photodynamic therapy of oral cancer: photosensitisation with systemic aminolaevulinic acid, *Lancet*, 342 (1993) 147-148.
- [27] E. Balasubramaniam, P. Natarajan, Photophysical properties of protoporphyrin IX and thionine covalently attached to macromolecules, *J. Photochem. Photobiol*, 103 (1997) 201-211.
- [28] H. Ding, B.D. Sumer, C.W. Kessinger, Y. Dong, G. Huang, D.A. Boothman, J. Gao, Nanoscopic micelle delivery improves the photophysical properties and efficacy of photodynamic therapy of protoporphyrin IX, *J. Control. Release*, 151 (2011) 271-277.
- [29] A. Kathiravan, V. Raghavendra, R.A. Kumar, P. Ramamurthy, Protoporphyrin IX on TiO₂ electrode: A spectroscopic and photovoltaic investigation, *Dyes Pigm.*, 96 (2013) 196-203.
- [30] J. Patwari, A. Chatterjee, S. Sardar, P. Lemmens, S.K. Pal, Ultrafast dynamics in co-sensitized photocatalysts under visible and NIR light irradiation, *Phys. Chem. Chem. Phys.*, 20 (2018) 10418-10429.
- [31] M. Prushan, Absorption and fluorescence spectroscopy of tetraphenylporphyrin and metallo-tetraphenylporphyrin, (2005). DOI: <http://www1.lasalle.edu/~prushan/Abs%20and%20Fluor%20of%20TPPH2.pdf>.

- [32] Y. Wu, J. Jiang, Z. Weng, M. Wang, D.L. Broere, Y. Zhong, G.W. Brudvig, Z. Feng, H. Wang, Electroreduction of CO₂ catalyzed by a heterogenized Zn-porphyrin complex with a redox-innocent metal center, *ACS Cent. Sci*, 3 (2017) 847-852.
- [33] J. Shen, R. Kortlever, R. Kas, Y.Y. Birdja, O. Diaz-Morales, Y. Kwon, I. Ledezma-Yanez, K.J.P. Schouten, G. Mul, M.T. Koper, Electrocatalytic reduction of carbon dioxide to carbon monoxide and methane at an immobilized cobalt protoporphyrin, *Nat. Commun*, 6 (2015) 8177.
- [34] S.G. Tullius, M. Nieminen-Kelhä, R. Buelow, A. Reutzel-Selke, P.N. Martins, J. Pratschke, U. Bachmann, M. Lehmann, D. Southard, S. Iyer, Inhibition of ischemia/reperfusion injury and chronic graft deterioration by a single-donor treatment with cobalt-protoporphyrin for the induction of heme oxygenase-1, *Transplantation*, 74 (2002) 591-598.
- [35] D.V. Stynes, H.C. Stynes, B.R. James, J.A. Ibers, Thermodynamics of ligand and oxygen binding to cobalt protoporphyrin IX dimethyl ester in toluene solution, *J. Am. Chem. Soc.*, 95 (1973) 1796-1801.
- [36] N.A. Anderson, T. Lian, Ultrafast electron transfer at the molecule-semiconductor nanoparticle interface, *Ann. Rev. Phys. Chem.*, 56 (2005) 491-591.
- [37] J.M. Rehm, G.L. McLendon, Y. Nagasawa, K. Yoshihara, J. Moser, M. Grätzel, Femtosecond electron-transfer dynamics at a sensitizing dye-semiconductor (TiO₂) interface, *J. Phys. Chem.*, 100 (1996) 9577-9578.
- [38] O. Enea, J. Moser, M. Grätzel, Achievement of incident photon to electric current conversion yields exceeding 80% in the spectral sensitization of titanium dioxide by coumarin, *J. Electroanal. Chem.*, 259 (1989) 59-65.
- [39] K. Hara, K. Sayama, Y. Ohga, A. Shinpo, S. Suga, H. Arakawa, A coumarin-derivative dye sensitized nanocrystalline TiO₂ solar cell having a high solar-energy conversion efficiency up to 5.6%, *Chem. Commun.*, (2001) 569-570.
- [40] X. Zhang, J.J. Zhang, Y.Y. Xia, Molecular design of coumarin dyes with high efficiency in dye-sensitized solar cells, *J. Photochem. Photobiol. A*, 194 (2008) 167-172.

- [41] V. Kandavelu, H.S. Huang, J.L. Jian, T.C.K. Yang, K.L. Wang, S.T. Huang, Novel iminocoumarin dyes as photosensitizers for dye-sensitized solar cell *Sol. Energy*, 83 (2009) 574-581.
- [42] W.R. Duncan, O.V. Prezhdo, Theoretical studies of photoinduced electron transfer in dye-sensitized TiO₂, *Annu. Rev. Phys. Chem.*, 58 (2007) 143-184.
- [43] G.A. Reynolds, K.H. Drexhage, New coumarin dyes with rigidized structure for flashlamp-pumped dye lasers, *Optics Commun.*, 13 (1975) 222-225.
- [44] Y. Xie, F. Chen, J. He, J. Zhao, H. Wang, Photoassisted degradation of dyes in the presence of Fe³⁺ and H₂O₂ under visible irradiation, *J. Photochem. Photobiol. A Chem.*, 136 (2000) 235-240.
- [45] M. Faisal, M.A. Tariq, M. Muneer, Photocatalysed degradation of two selected dyes in UV-irradiated aqueous suspensions of titania, *Dyes Pigm.*, 72 (2007) 233-239.
- [46] M.K. Nazeeruddin, F.D. Angelis, S. Fantacci, A. Selloni, G. Viscardi, P. Liska, S. Ito, B. Takeru, M. Grätzel, Combined experimental and DFT-TDDFT computational study of photoelectrochemical cell ruthenium sensitizers, *J. Am. Chem. Soc.*, 127 (2005) 16835-16847.
- [47] S. Sreejith, P. Carol, P. Chithra, A. Ajayaghosh, Squaraine dyes: a mine of molecular materials, *J. Mater. Chem.*, 18 (2008) 264-274.
- [48] J.-H. Yum, P. Walter, S. Huber, D. Rentsch, T. Geiger, F. Nüesch, F. De Angelis, M. Grätzel, M.K. Nazeeruddin, Efficient far red sensitization of nanocrystalline TiO₂ films by an unsymmetrical squaraine dye, *J. Amer. Chem. Soc.*, 129 (2007) 10320-10321.
- [49] G. Chen, H. Sasabe, Y. Sasaki, H. Katagiri, X.-F. Wang, T. Sano, Z. Hong, Y. Yang, J. Kido, A series of squaraine dyes: effects of side chain and the number of hydroxyl groups on material properties and photovoltaic performance, *Chem. Mater.*, 26 (2014) 1356-1364.
- [50] H. Choi, P.K. Santra, P.V. Kamat, Synchronized energy and electron transfer processes in covalently linked CdSe-squaraine dye-TiO₂ light harvesting assembly, *ACS nano*, 6 (2012) 5718-5726.

- [51] S.A. Jenekhe, L. Lu, M.M. Alam, New conjugated polymers with donor-acceptor architectures: synthesis and photophysics of carbazole-quinoline and phenothiazine-quinoline copolymers and oligomers exhibiting large intramolecular charge transfer, *Macromolecules*, 34 (2001) 7315-7324.
- [52] A. Higuchi, H. Inada, T. Kobata, Y. Shirota, Amorphous molecular materials: Synthesis and properties of a novel starburst molecule, 4, 4', 4''-Tri (N-phenothiazinyl) triphenylamine, *Adv. Mater.*, 3 (1991) 549-550.
- [53] R.Y. Lai, X. Kong, S.A. Jenekhe, A.J. Bard, Synthesis, cyclic voltammetric studies, and electrogenerated chemiluminescence of a new phenylquinoline-biphenothiazine donor-acceptor molecule, *J. Am. Chem. Soc.*, 125 (2003) 12631-12639.
- [54] X. Kong, A.P. Kulkarni, S.A. Jenekhe, Phenothiazine-based conjugated polymers: synthesis, electrochemistry, and light-emitting properties, *Macromolecules*, 36 (2003) 8992-8999.
- [55] D.-H. Hwang, S.-K. Kim, M.-J. Park, J.-H. Lee, B.-W. Koo, I.-N. Kang, S.-H. Kim, T. Zyung, Conjugated polymers based on phenothiazine and fluorene in light-emitting diodes and field effect transistors, *Chem. Mater.*, 16 (2004) 1298-1303.
- [56] M.T. Tierney, M.W. Grinstaff, Synthesis and characterization of fluorenone-, anthraquinone-, and phenothiazine-labeled oligodeoxynucleotides: 5'-probes for DNA redox chemistry, *J. Org. Chem.*, 65 (2000) 5355-5359.
- [57] T. Takada, K. Kawai, M. Fujitsuka, T. Majima, Direct observation of hole transfer through double-helical DNA over 100 Å, *Proc. Natl. Acad. Sci.*, 101 (2004) 14002-14006.
- [58] M.T. Tierney, M. Sykora, S.I. Khan, M.W. Grinstaff, Photoinduced electron transfer in an oligodeoxynucleotide duplex: Observation of the electron-transfer intermediate, *J. Phys. Chem. B*, 104 (2000) 7574-7576.
- [59] J. Huang, Z. Huang, S. Jin, T. Lian, Exciton dissociation in CdSe quantum dots by hole transfer to phenothiazine, *J. Phys. Chem. C*, 112 (2008) 19734-19738.

Chapter 3

Instrumentation and Sample Preparation

In this chapter, the details of instrumental setup and sample preparation techniques used in our studies have been described.

3.1. Instrumental Setups:

3.1.1. Steady-state UV-Vis Absorption and Emission Measurements: Steady-state UV-Vis absorption and emission spectra were measured with Shimadzu UV-2600 spectrophotometer and Horiba Fluorolog, respectively. Schematic ray diagrams of these two instruments are shown in Figures 3.1 and 3.2.

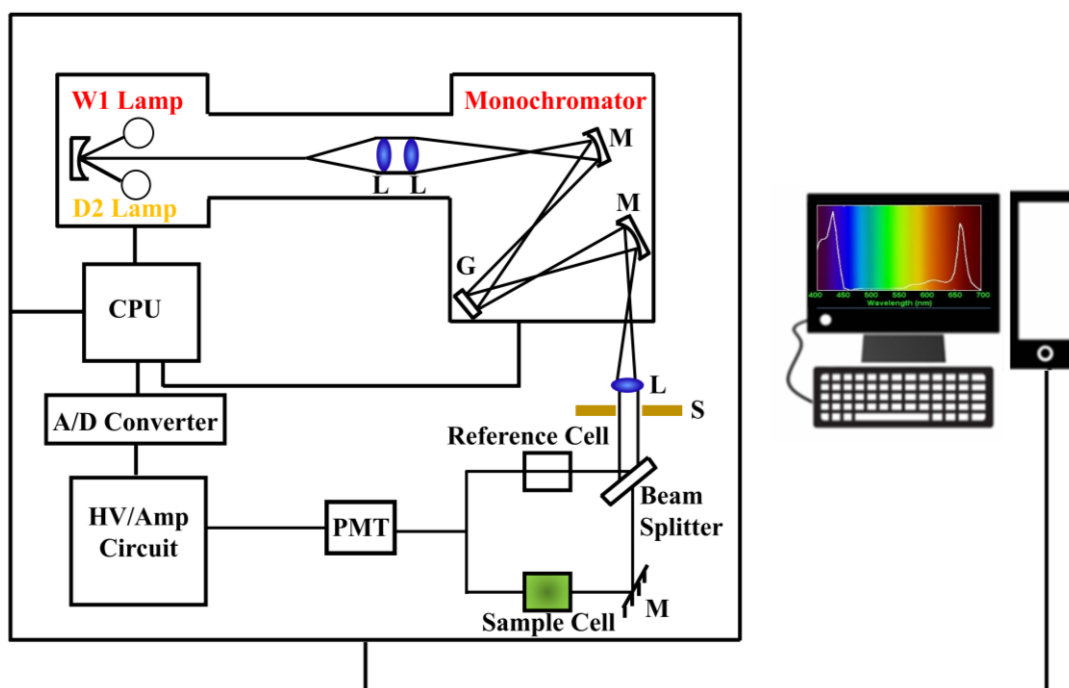


Figure 3.1. Schematic ray diagram of an absorption spectrophotometer. Tungsten halogen (W1) and deuterium lamps (D2) are used as light sources in the visible and UV regions, respectively. M, G, L, S, PMT designate mirror, grating, lens, shutter and photomultiplier tube, respectively. CPU, A/D converter and HV/amp indicate central processing unit, analog to digital converter and high-voltage/amplifier circuit, respectively.

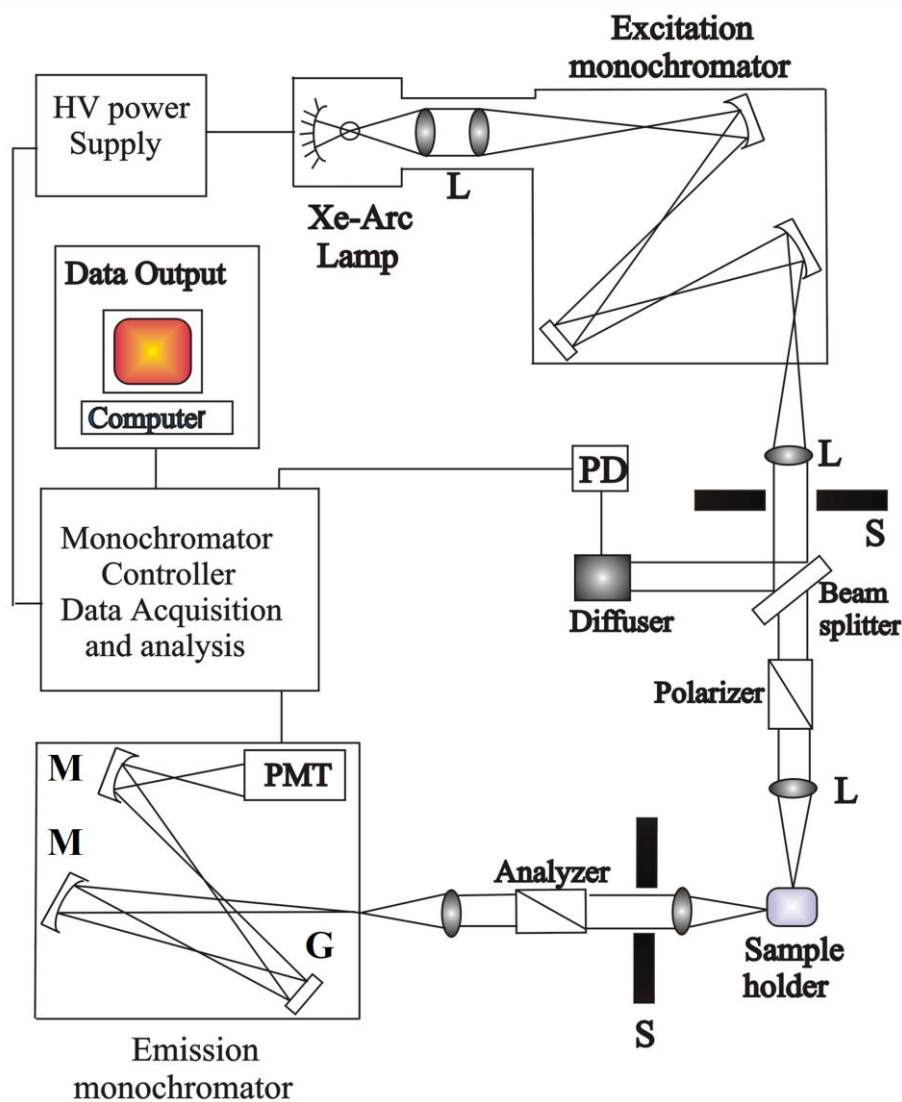


Figure 3.2. Schematic ray diagram of an emission spectrofluorimeter. M, G, L, S, PMT and PD represent mirror, grating, lens, shutter, and photomultiplier tube and reference photodiode, respectively.

3.1.2. Solid State Absorption Measurements in Retro-reflecting Mode: The retro-reflecting mode absorption spectra of the photo-anodes and nano-hybrids were recorded in a custom made set up using either StellarNet™ spectrograph in diffuse reflection technique at wavelength resolution of 0.5 nm or using STS-VIS-L10-400-SMA spectrograph with wavelength resolution of 0.47 nm. For the transmission and collection of light, lab-grade optical fiber probe from Ocean Optics was used in this customized set-up. The block diagram of the spectrograph is shown in Figure 3.3.

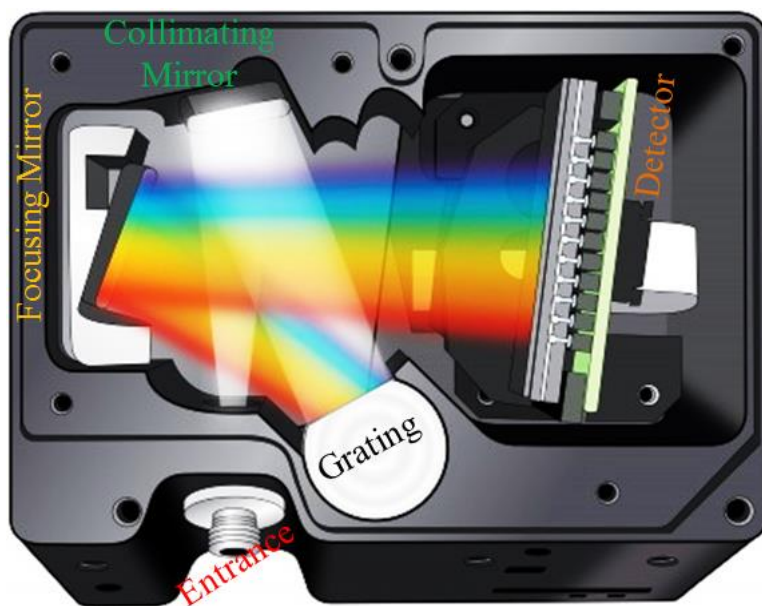


Figure 3.3. Basic internal ray diagram of CCD array detector based STS-VIS and StellarNet™ spectrographs.

3.1.3. Steady-state Absorption and Emission Measurements for UV-Vis-NIR

Range: The absorption and steady-state emission for IR absorbing samples were done using a Perkin Elmer (Lambda 950) UV-VIS-NIR spectrophotometer and a Horiba, Jobin Yvon FL1057 UV-VIS-NIR spectrofluorometer respectively. The NIR absorption spectra of these samples were taken in transmission mode in solvent toluene keeping the samples in micro-cuvettes of 2 micron path length.

3.1.4. Time-correlated Single Photon Counting (TCSPC) Technique:

All the picosecond-resolved fluorescence transients were recorded using TCSPC technique. The schematic block diagram of a TCSPC system is shown in Figure 3.4. TCSPC setup from Edinburgh instruments, U.K., was used during fluorescence decay acquisitions. Lasers used for the excitation source was of Pico-quant. The instrument response functions (IRFs) of the laser sources at different excitation wavelengths varied between 70 ps to 80 ps. The fluorescence from the sample was detected by a photomultiplier after dispersion through a grating monochromator [1]. For all transients, the polarizer in the emission side was adjusted to be at 54.70 (magic angle) with respect to the polarization axis of excitation beam.

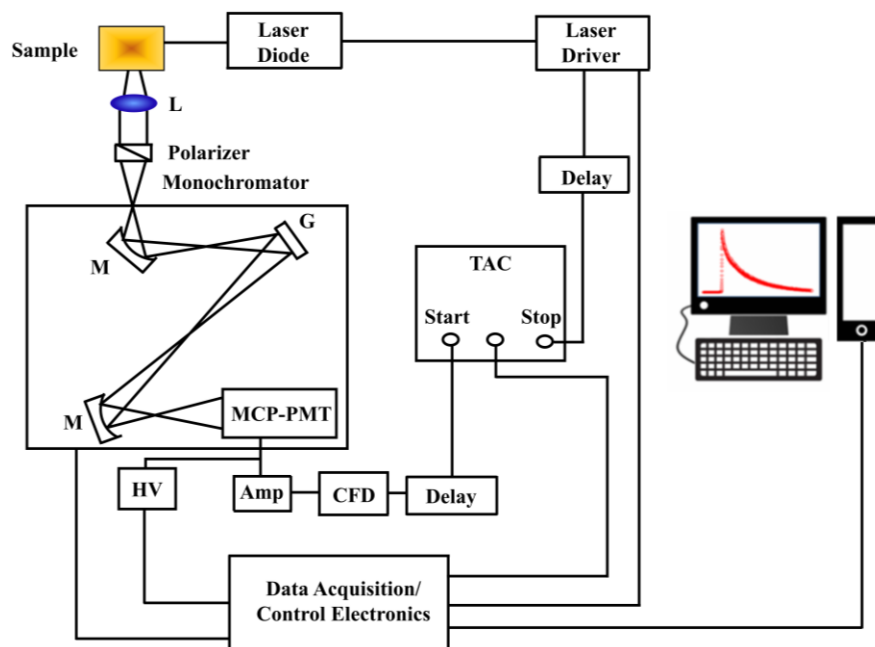


Figure 3.4. Schematic ray diagram of a time correlated single photon counting (TCSPC) spectrophotometer. A signal from microchannel plate photomultiplier tube (MCP-PMT) is amplified (Amp) and connected to start channel of time to amplitude converter (TAC) via constant fraction discriminator (CFD) and delay. The stop channel of the TAC is connected to the laser driver via a delay line. L, M, G and HV represent lens, mirror, grating and high voltage source, respectively.

3.1.5. Femtosecond-Resolved Transient Absorption Technique: For pump-probe experiment (ExciPro, CDP, Russia) output of a regenerative amplifier (Libra, Coherent, USA) is used to generate both the pump and probe light. A portion of the amplified 800 nm light is fed to optical parametric amplifier (TOPAS-C, Light Conversion, Lithonia) to generate variable excitation wavelength in and another portion to generate white light continuum (WLC) for the probe light. Whole experimental setup is explained briefly (Figure 3.5). 1.75 W output of a second harmonic Nd: YVO4 laser (Verdi, Coherent, USA) is used to pump the mode-locked Ti: sapphire laser (Vitesse, Coherent, USA) peaked at 800 nm (80 MHz, 100 fs, 330 mW), which acts as a seed for the amplifier. A portion of the seed light is first passed through a stretcher (to minimize peak power) and then fed to Ti: Sapphire crystal in the regenerative amplifier. For the amplification of the seed light, a 20W second harmonic Q-Switched Nd: YLF laser (Evolution, Coherent, USA) with a repetition rate of 1 kHz, and pulse duration of 200 ns is used as a

pump. After sufficient amplification (~15 round trips) the amplified 800 nm light is passed through a compressor to get back ~100 fs light. Around 1.6 W (of 4.2 W) light is fed to the OPA to get the desired wavelength for pumping the sample. 400 nm pump light was generated by bypassing the OPA and effecting a second harmonic generation of the 800 nm light.

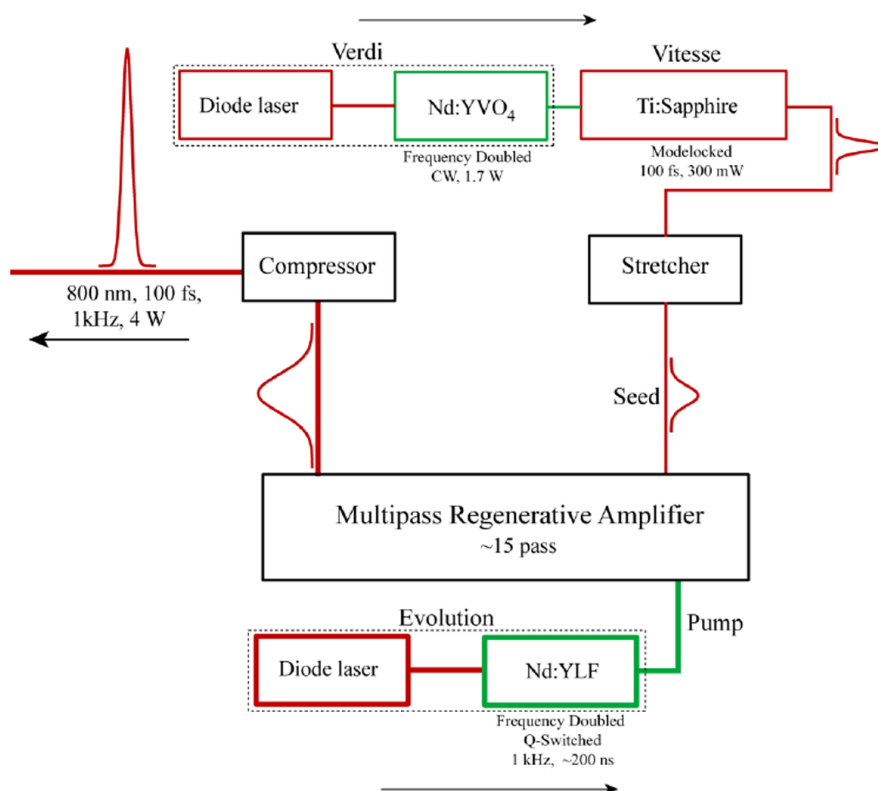


Figure 3.5. Diagram of Libra including Verdi, Vitesse and Evolution.

For transient absorption measurement (Figure 3.6) few mW of around 200 mW of the other portion of the 800 nm light is focused on 2 mm thick translating CaF₂ crystal to get WLC (350-800 nm). The probe light is split into probe and reference part to eliminate shot to shot fluctuation [2]. A magic angle condition is maintained to eliminate rotational anisotropy. The pump intensity is adjusted by using variable neutral density filter. Maximum power used at the sample is 1 mW which corresponds to per pulse power of 2 μ J. Both the pump and probe light is focused on the sample housed in a rotating disk. The transmitted light is collected by an optical fiber connected to a spectrometer (Horiba CP140-

104) coupled with CMOS detector. A chirp correction file is generated by measuring the coherent signal of the solvent [3, 4]. The dynamics are found to be independent of the pump intensity at the range worked with.

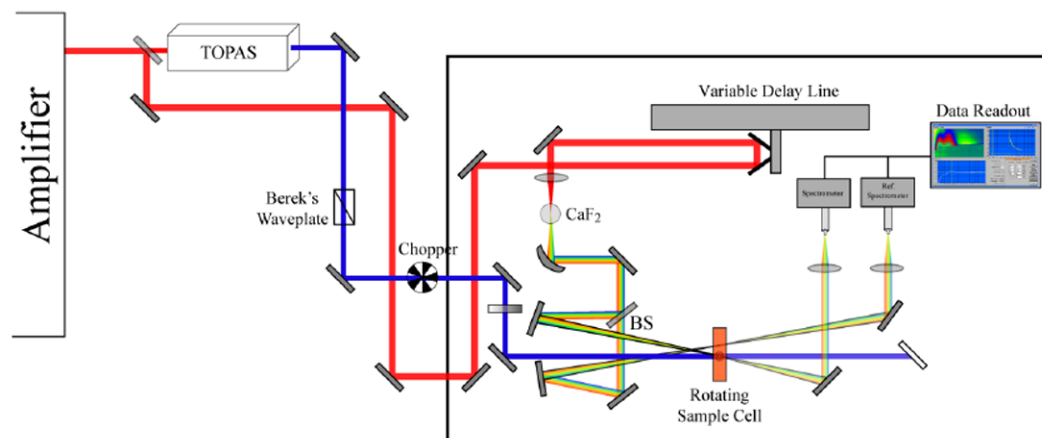


Figure 3.6. Schematic ray diagram of femtosecond transient absorption spectrophotometer.

For our experiment, the pump pulse of 400 nm wavelength (2 mJ per pulse) was used in this measurement and probe pulses was a white light continuum (450–800 nm). All transient absorption experiments were conducted at room temperature. The observed transients were fitted using a nonlinear least squares fitting procedure (software SCIENTIST) to a function composed of the convolution of the instrument response function with a sum of exponentials. The purpose of this fitting is to obtain the decays in an analytic form suitable for further data analysis.

3.1.6. Customization of NIR TCSPC Setup: The block diagram of the customized near infrared (NIR) time correlated single photon counting (TCSPC) system is shown in Figure 3.7. The sample was mounted on the stage lead of a vertically placed microscope compatible cryo stage of Linkam Scientific Instruments (LTS420E-PB4). The temperature controller software LKS10043 is able to tune the temperature from -196 °C to 400 °C. The software controlled liquid nitrogen flow around the stage lead is used for cooling. On the other hand, electrical heating is

used to increase the temperature of the stage and that too is controlled by the same software. There is a temperature sensor which sense the accurate temperature of the stage and gives the feedback to the software. According to the difference between the target temperature and the present temperature of the stage, the software interfaces either the nitrogen flow to the stage or electrical heating. The minimum step of temperature is 0.01 °C for the stage. The details of the stage can be found in the website of Linkam Scientific Instruments as well. There were

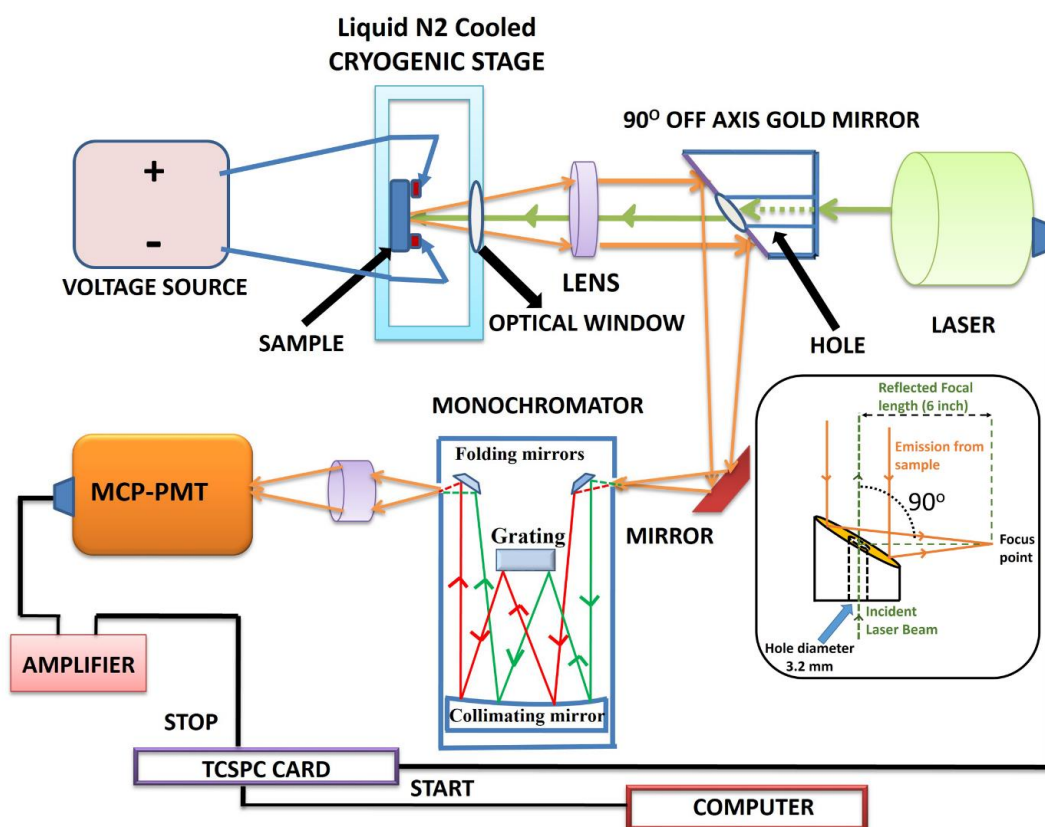


Figure 3.7. Box diagram of the custom made cryo assisted NIR TCSPC experimental set up along with external voltage source for device sample. The inset shows the ray diagram of the 90° off axis gold mirror.

four pin probes within the stage to provide electrical bias to the sample. The pin probes were connected to a tunable DC voltage source using external cables. The excitation laser of 2 mm beam diameter was passed through the central hole (3.2 mm diameter) of a 90° off axis gold coated parabolic mirror and focused on the

sample using a plano-convex lens of 25.4 mm focal length at a spot size of 10 micron. The diverged emission was then collected through an optical window on the stage and has been collimated by the same plano-convex lens. Then, the collimated light was focused on the entry slit of a monochromator using a 90° off axis gold coated parabolic mirror (Thorlab, model number MPD269V_M01) and another reflecting mirror in the optical path. Parabolic mirrors are able to focus collimated light without any spherical aberration on the axis of incident collimated light. Off-axis parabolic mirror is the side section of a parent parabolic mirror. Collimated light incident to an off-axis parabolic mirror is focused to a particular point at a specific angle with respect to the incident light. For an 90° off-axis parabolic mirror, the angle between the collimated beam and the reflected converging light is 90°.

The ray diagram of the 90° off axis gold coated mirror is represented at the inset of Figure 3.7 and the details can be found at the website of Thorlab as well. The diverging light coming from the exit slit was again focused on the detector using a set of coupled plano-convex lens. All optical components (lenses and mirrors) including the 90° off axis gold coated mirror were purchased from Thorlab. The monochromator used in the signal collection path was purchased from Optometrics (Model 05) which has a blazing wavelength at 1.2 micrometer. For the detection of the signal a Hamamatsu Microchannel Plate Photomultiplier Tube (MCP-PMT) with a model number of R3809U-69 has been used. The wavelength response range of the detector is from 900 nm to 1700 nm. The TCSPC card used in the system is SPC-130 module of Becker & Hickl and the transient photoluminescence data was fitted using Micromath Scientist software using the deconvolution by iterative reconvolution method.

3.1.7. Transmission Electron Microscopy (TEM): A FEI TecnaiTF-20 field-emission high-resolution TEM (Figure 3.8) equipped with energy dispersive X-ray (EDAX) spectrometer was used to characterize the microscopic structures of

samples and to analyze their elemental composition. The sizes of the nanostructures were determined from the TEM images obtained at 200 kV acceleration voltage of the microscope. Samples for TEM were prepared by placing a drop of the colloidal solution on a carbon-coated copper grid and allowing the film to evaporate overnight at room-temperature.

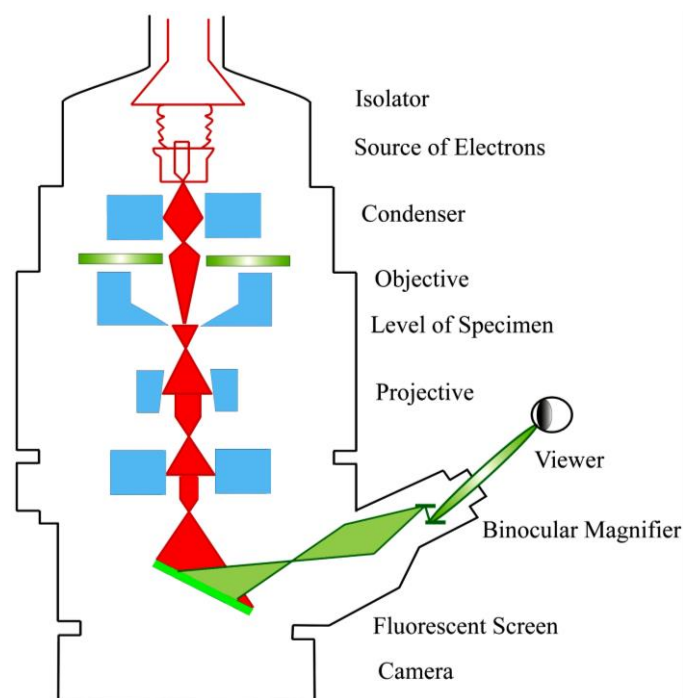


Figure 3.8. Schematic diagram of a typical transmission electron microscope (TEM). After the transmission of electron beam through a specimen, the magnified image is formed either in the fluorescent screen or can be detected by a CCD camera.

3.1.8. Cross-sectional Transmission Electron Microscopy (XTEM): Cross-sectional transmission electron microscopy (XTEM) was used to explore the morphology of the quantum well samples and to get an idea about the exact well thicknesses. Cross-sectional transmission microscopy (XTEM) samples were prepared by a destructive technique that involved cleaving, grinding, polishing, and Ar⁺ beam ion milling for high electron transparency. For this purpose, the area of interest of the precise disc center was dimpled down to 20 μm. The samples were loaded inside a precision ion milling system (PIPs) for further thinning. The PIP was carried out at a low Ar⁺ beam angle of 3.5° and at a pressure of 9×10⁻⁵ Torr with

an acceleration voltage of 4 kV until the samples were perforated. We reduced the incidence beam angle to 2° with 2.0 kV and milled the samples for a longer period till a reddish diffracted spot was visible at the edges of the perforated region of the CBQD sample. XTEM images were carried out on JEOL JEM 2010F electron microscope system operating at 200 kV.

3.1.9. Low Temperature Steady-state Photoluminescence: Photoluminescence measurements at 8-300 K were performed in a Helium flow controlled closed cycle cryostat was used to perform PL measurements. The mounted samples were excited with a green continuous wave laser of wavelength 532 nm and variable laser power. A high pass filter (645 nm) was used to pass only specific range of wavelength. A liquid nitrogen cooled InGaAs array detector was used to detect the emitted luminescence signal along the normal direction. This signal was obtained after dispersion by a 600 g/mm grating in a 750 mm focal length spectrometer.

3.1.10. Low Temperature Photoluminescence Excitation (PLE): In Photoluminescence excitation spectroscopy, emission wavelength was fixed to ground state achieved from PL spectrum and the excitation wavelength is varied to observe higher energy peak from single dot. Halogen lamp as a light source was used for irradiating sample kept in He- closed cycle cryostat (8 - 300 K). The incident light was dispersed through 0.75 nm monochromator and the obtained PLE signal was sampled using chopper and lock in amplifier (to reduce noise). This signal was through a 0.75 nm monochromator and collected in InGaAs detector. The input side monochromator grating was fixed at 600 g/mm and output side to 300 g/mm.

3.1.11. Fourier Transform Infrared (FTIR) Measurement: FTIR spectroscopy is a technique that can provide very useful information about functional groups in a sample. An infrared spectrum represents the fingerprint of a sample with

absorption peaks which correspond to the frequencies of vibrations between the bonds of the atoms making up the material. Because each different material is a unique combination of atoms, no two compounds produce the exact same infrared spectrum. Therefore, infrared spectroscopy can result in a positive identification (qualitative analysis) of every different kind of material. In addition, the size of the peaks in the spectrum is a direct indication of the amount of material present. The two-beam Michelson interferometer is the heart of FTIR spectrometer. It consists of a fixed mirror (M4), a moving mirror (M5) and a beam-splitter (BS1), as illustrated in Figure 3.9. The beam-splitter is a laminate material that reflects and transmits light equally. The collimated IR beam from the source is partially transmitted to the moving mirror and partially reflected to the fixed mirror by the beam-splitter. The two IR beams are then reflected back to the beam-splitter by the mirrors. The detector then sees the transmitted beam from the fixed mirror and reflected beam from the moving mirror, simultaneously. The two combined beams

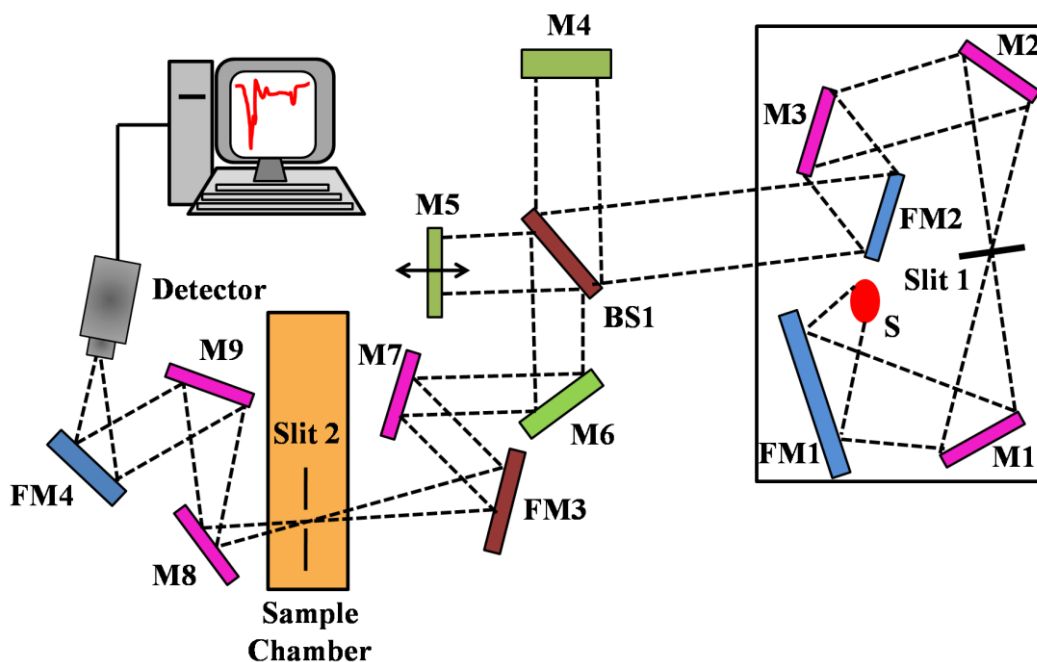


Figure 3.9. Schematic of Fourier Transform Infrared (FTIR) spectrometer. It is basically a Michelson interferometer in which one of the two fully-reflecting mirrors is movable, allowing a variable delay (in the travel-time of the light) to be included in one of the beams. M, FM and BS1 represent the mirror, focussing mirror and beam splitter, respectively. M5 is a moving mirror.

interfere constructively or destructively depending on the wavelength of the light (or frequency in wavenumbers) and the optical path difference introduced by the moving mirror. The resulting signal is called an interferogram which has the unique property that every data point (a function of the moving mirror position) which makes up the signal has information about every infrared frequency which comes from the source. Because the analyst requires a frequency spectrum (a plot of the intensity at each individual frequency) in order to make identification, the measured interferogram signal cannot be interpreted directly. A means of “decoding” the individual frequencies is required. This can be accomplished *via* a well-known mathematical technique called the Fourier transformation. This transformation is performed by the computer which then presents the user with the desired spectral information for analysis. FTIR measurements were performed on a JASCO FTIR-6300 spectrometer (transmission mode). For the FTIR measurements, powdered samples were mixed with KBr powder and pelletized. The background correction was made using a reference blank of KBr pellet.

3.1.12. Cyclic Voltammetry (CV): CV is a useful technique for studying electrochemical reactions. In case of CV, the voltage is swept between two potential values (V_1 and V_2) at a fixed rate, however now when the voltage reaches V_2 from V_1 , the scan is reversed and the voltage is swept back to V_1 . The current response is plotted as a function of the applied potential. Electrochemical experiments were performed using a CH analyser potentiostat (CHI1110C). A three electrode system consisting of a platinum working electrode, a platinum counter electrode and a reference electrode were employed. All the potentials reported in this thesis are referenced to the Ag/Ag⁺ couple. Electrolyte is usually added to the sample solution to ensure sufficient conductivity. The solvent, electrolyte, and material composition of the working electrode will determine the potential range that can be accessed during the experiment. The schematic presentation of the CV set up is shown in Figure 3.10.

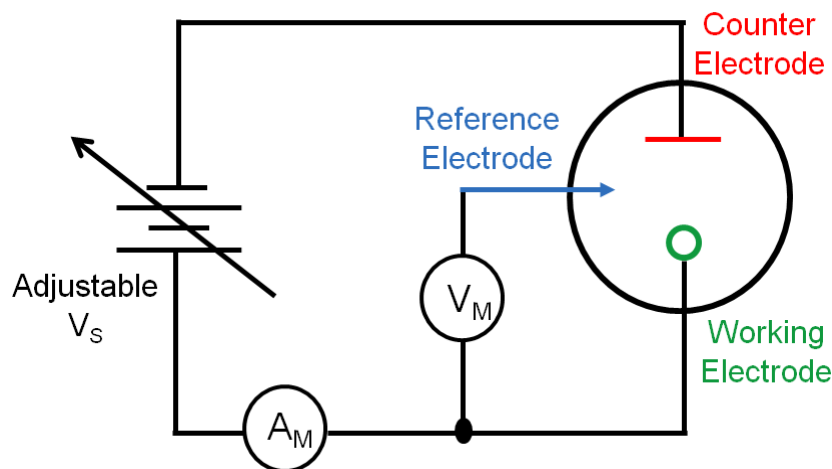


Figure 3.10. Schematic diagram of a simplified measurement circuit for performing cyclic voltammetry (CV).

A typical electrochemical measurement circuit made up of an electrochemical cell, an adjustable voltage source (V_s), an ammeter (A_M) and a voltmeter (V_M). The three electrodes of the electrochemical cell are the working electrode (WE), reference electrode (RE) and the counter (or auxiliary) electrode (CE). The voltage source (V_s) for the potential scan is applied between the working electrode and the counter electrode. The potential (E) between the reference electrode and the working electrode is measured with the voltmeter and the overall voltage (V_s) is adjusted to maintain the desired potential at the working electrode with respect to the reference electrode. The resulting current (i) flowing to or from the working electrode is measured with the ammeter (A_M).

3.1.13. Electrochemical Impedance Spectroscopy (EIS): Electrochemical Impedance Spectroscopy (EIS) is a powerful technique to investigate the electronic and ionic processes in dye sensitized solar cells (DSSC). Electrochemical impedance is usually measured by applying an AC potential to an electrochemical cell and then measuring the current through the cell. An important advantage of EIS over other techniques is the possibility of using tiny ac voltage amplitudes exerting a very small perturbation on the system. A Nyquist plot can be made by plotting the real part of the transfer function on the X-axis and the imaginary part

on the Y-axis. The Nyquist diagram for DSSC features typically three semicircles that in the order of increasing frequency are attributed to the Nernst diffusion within the electrolyte, the electron transfer at the oxide/electrolyte interface and the redox reaction at the platinum counter electrode. From applying appropriate equivalent circuits, the transport rate and lifetime of the electron in the mesoscopic film are derived. Electrochemical impedance spectroscopy (EIS) were performed on an electrochemical workstation CHI650E (CH instruments) with a frequency range from 100 kHz to 0.1 Hz in the open circuit condition. The schematic presentation of the EIS set up is shown in Figure 3.11. All impedance measurements were carried out under a bias illumination of 100 mW/cm². The obtained spectra were fitted using the CHI650E software in terms of appropriate equivalent circuits.

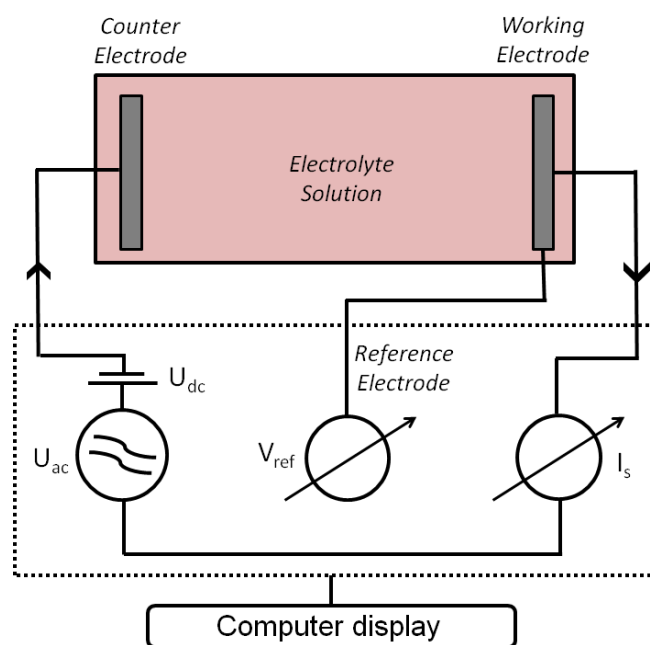


Figure 3.11. Schematic diagram of a simplified measurement circuit for performing Electrochemical Impedance Spectroscopy (EIS).

3.1.14. Capacitance-Voltage Measurements: Capacitance-voltage (C-V) profiling is a well-documented technique for characterizing the devices based on semiconductor junctions. In this experiment, the applied bias is varied, and the corresponding capacitance is measured. The capacitance measured at different

interval is plotted as a function of applied voltage. The technique uses either a Schottky barrier i.e. a metal–semiconductor junction or a conventional p–n junction. A depletion region is created at the different junctions upon applied bias. Depletion region is can be empty of electrons and holes, but it contains some ionized donors and electrically active trap states. This region containing ionized charges shows capacitor like behavior. Upon application of varying voltage to the junction, the depletion width also varies. The changes in the width of the depletion region upon the applied voltage provides information on the characteristics of the junction, such as the doping profile and defect state densities. For our studies, the Capacitance Voltage (CV) experiments were carried out on an electrochemical workstation CHI650E (CH instruments). The frequency was kept at 1000 Hz during the measurements. The active areas of the samples were illuminated under 100 mW/cm² condition, using 300W Xe lamp source (Excillitus, USA), during the measurements.

3.1.15. Solar Cell Characterization: The characterization of DSSCs involves the electrical current–voltage (I–V) characteristics, incident photon to current conversion efficiency (IPCE) measurements and photovoltage decay measurements. The current density–voltage characteristics of the cells were recorded by a Keithley multimeter under irradiance of 100 mW cm⁻² (AM 1.5 simulated illuminations, Photo Emission Tech). The electrical circuit used to measure the I–V characteristics of the solar cells is shown in Figure 3.12. The short-circuit current (I_{SC}) and open-circuit voltage (V_{OC}) of the solar cells were determined from their respective I–V characteristic curves. The fill factor (FF) and efficiency (η) of the solar cells were calculated by using equations 2.24 and 2.25, respectively.

The IPCE of the DSSCs was measured by using a homemade setup with a Bentham monochromator and dual light (deuterium and xenon) sources. The monochromatic light was allowed to fall on the solar cells and the respective

current from the solar cell at every incident wavelength of light was measured. Finally, the IPCE was calculated by using equation 2.27. The set up used to measure the IPCE of the solar cells is shown in Figure 3.13. The photo-current (J_{sc}) vs wavelength (λ) was recorded by measuring short-circuit photocurrent (J_{sc}) at different wavelengths (λ) using standard Bentham PVE300 set up.

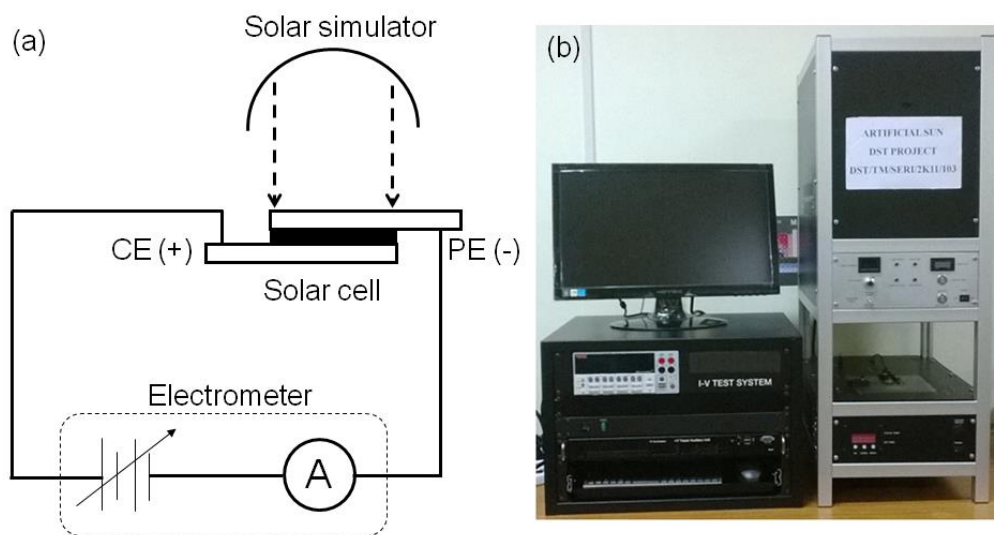


Figure 3.12. (a) Electrical setup and (b) photograph of the solar simulator used for the solar cell characterization.

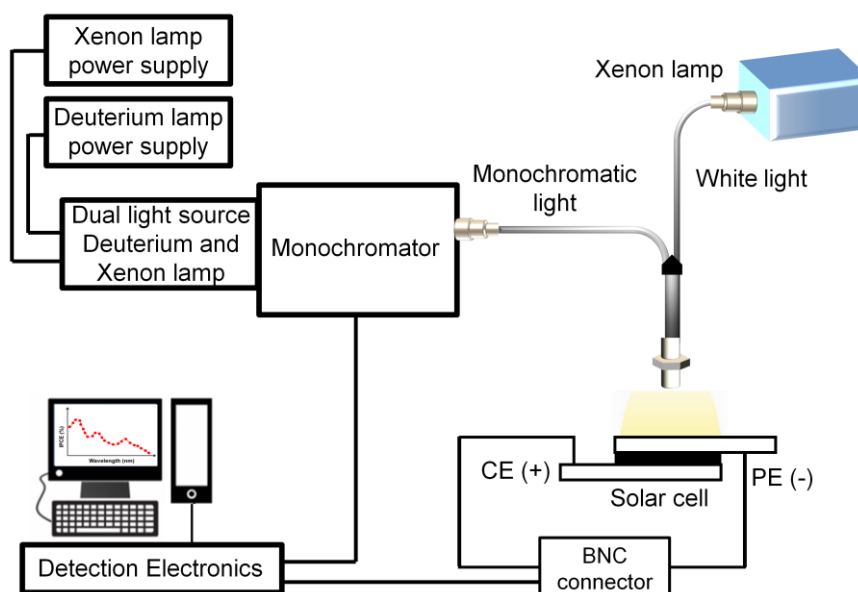


Figure 3.13. Schematic diagram of a simplified measurement circuit for performing IPCE measurements.

Photovoltage decay measurements were carried out after illuminating the cells under 1 Sun condition. The photovoltage decays after switching off the irradiation were monitored by an oscilloscope (Owon) through computer interface as shown in Figure 3.14. The decays were fitted with exponential decay functions using Origin software.

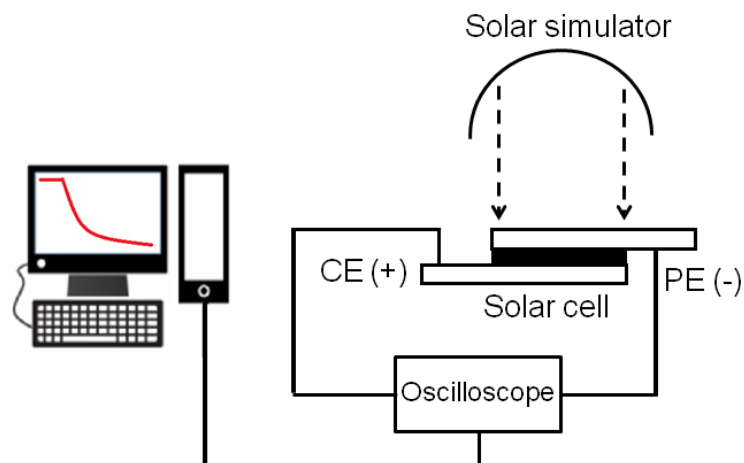


Figure 3.14. Schematic diagram of the photovoltage decay measurement setup.

3.1.16. Fiber-Optic Coupled System for Photocatalytic Measurements: Increased sensitivity in the signal detection in the presence of strong ambient light in our experimental setup lies on the confocal geometry of the excitation and detection sides [5]. As shown in the schematic ray-diagram of the experimental setup (Figure 3.15) the excitation fiber (400 μm core diameter) carrying laser light is connected to an optical coupler (Ocean Optics, USA, model: 74-UV) in order to focus excitation light at the middle of a sample holder, which is an all-side polished quartz-cuvette from Starna cells (U.S.A). The numerical aperture (NA) of the excitation fiber (NA=0.45) and focal length of the optical coupling lens (0.5 cm) systems are to achieve out-of-focus rejection by two strategies: firstly by illuminating a single point of the specimen at any one time with a focused beam, so that illumination intensity drops off rapidly above and below the plane of focus and secondly by the use of optical fiber as a collecting unit with similar coupling lens so that light emitted away from the point in the specimen being illuminated is

blocked from reaching the detector. The collection fiber is arranged in 'I' geometry and connected with the commercially available CCD based miniaturized spectrograph (Ocean Optics, USA, model: HR4000) in order to measure absorption of the sample of interest. More flexibility in the measurement can also be achieved by using Shimadzu spectrophotometer (UV-2600) or Jobin Yvon (Fluoromax-3) fluorimeter to measure absorption and photoluminescence, respectively.

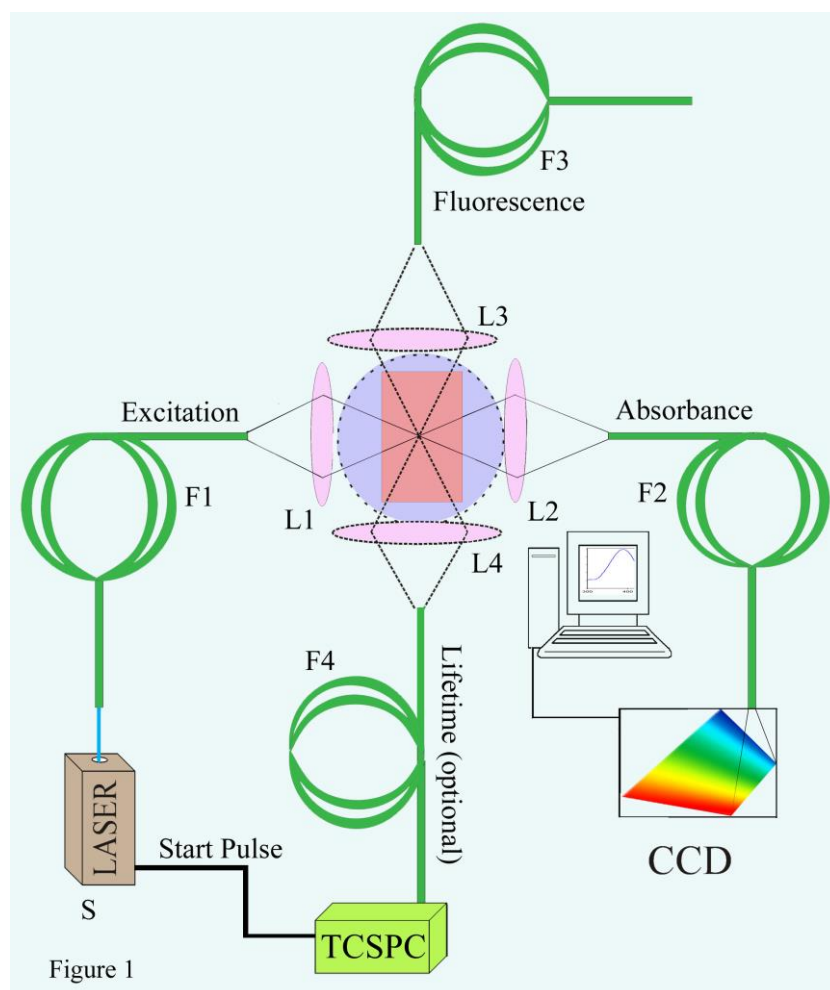


Figure 3.15. Schematic diagram of the universal setup. S is the source, F1-F4 are the optical fibers, L1-L4 are the fiber coupler lenses, the violate circle represents the ambient light around the sample (reddish rectangle). CCD is the photo-signal detector, connected with computer.

In order to establish the fact that the absorption of a sample can be measured in presence of strong ambient light effectively, we have placed the quartz cell containing test sample on a home-made UV bath (8W).

3.1.17. Light Sources Used for Irradiation: The NIR catalysis was performed using a tungsten-halogen lamp with a 650 nm high pass filter. The intensity of this particular lamp was measured to be 31200 Lux. The visible light induced catalysis was performed by irradiating the sample with a mercury lamp of 7800 Lux, using a 395 nm high pass filter. The spectra of the IR lamp used for irradiation, was taken in a HR4000 spectrograph for visible region and Red wave StellarNet for NIR region. The IR lamp used for irradiation in DCFH assay experiment, was of ~5000 lux intensity and 600 nm above wavelength.

3.1.18. Molecular Beam Epitaxy (MBE): In the late of 1960s, the Molecular beam epitaxy (MBE) technique was first invented at Bell Telephone Laboratories [6]. It is an ultrahigh vacuum (UHV; 10^{-8} to 10^{-12} Torr)-based technique for the high-quality epitaxial growth of compound semiconductor films or quantum structures. The process involves the reaction of one or more thermal molecular beams with a crystalline surface in UHV. The operating principles and development of MBE are explained in earlier literatures [7]. Foxon has reported very recently the major developments of this growth technology over the last three decades, including the understanding of the growth process and the application of MBE for the production of low-dimensional structures and devices [8]. All the self-assembled quantum confined nano-structures used in this study are grown in a Riber SYS14020 Epineat III-V MBE system. The three main components of an MBE system are the load-lock chamber, the buffer chamber, and the growth chamber.

A. Load-Lock Chamber: The load-lock chamber facilitates the insertion and removal of samples or wafers without disturbing the vacuum of the growth chamber. In other words, it separates the outside environment and the high-vacuum region of the MBE system.

B. Buffer Chamber: To avoid contamination, a major concern during growth and fabrication, the wafers were loaded into the buffer chamber, where they are heated to remove organic impurities.

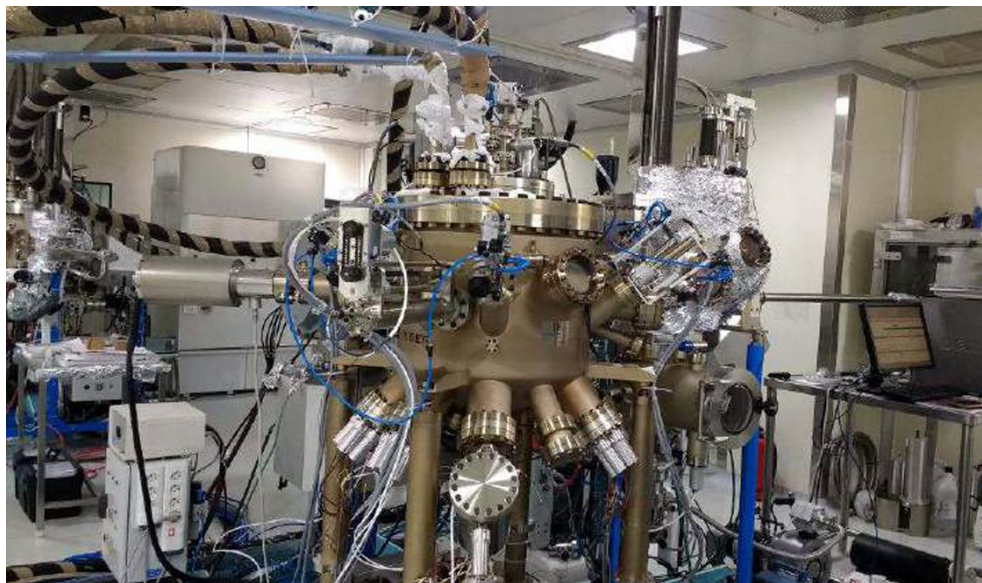


Figure 3.16. The ultrahigh vacuum (UHV) molecular beam epitaxy (MBE) system.

C. Growth Chamber: After heating in the buffer chamber for 1 h, the wafer becomes ready for deposition. Effusion cells in the growth chamber are the source of the molecular beams. In this chamber, the substrate is heated to a high temperature to avoid dislocations, and the samples are translated and rotated for uniform growth. The chamber also houses a reflection high-energy electron diffraction (RHEED) gun and a RHEED screen to monitor the growth of the structures. MBE systems use strong and reliable pumping systems to maintain the high vacuum inside the different chambers. The load-lock chamber uses a turbo pump and a roughing pump, the buffer chamber uses an ion pump and a titanium sublimation pump (TSP), and the growth chamber uses an ion pump, a TSP, and a cryopump.

Figure 3.16 illustrates image of the MBE system, used in our study for sample preparation. In MBE, a semiconductor element, such as gallium or arsenide, is heated using the effusion cell. The beams of atoms or molecules

ejected from the cell impinge on the substrate in a UHV environment. Consequently, adatoms nucleate, forming a single monolayer. During this growth process, RHEED is often used to monitor the growth of the crystal layers and to precisely control the layer thickness by monitoring the RHEED pattern (Figure 3.17).

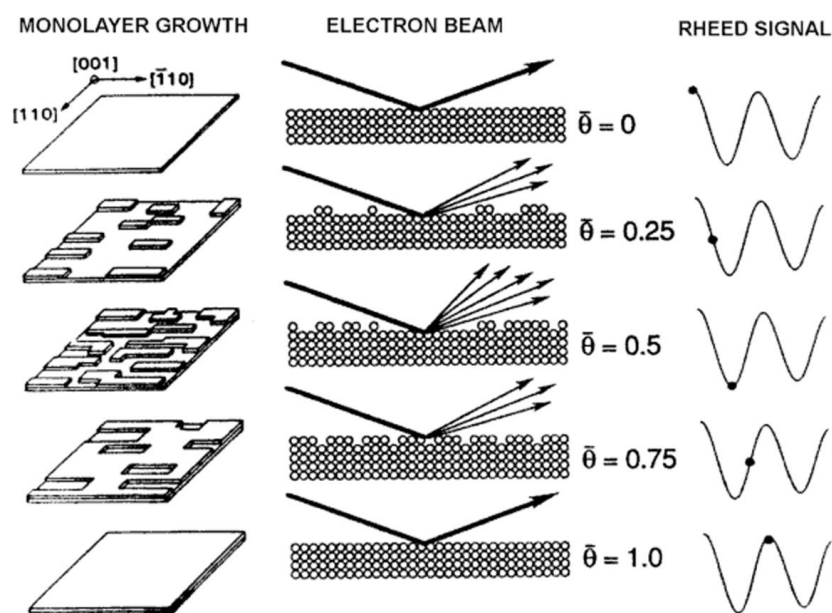


Fig. 3.17: Relationship between RHEED patterns and monolayer growth.

All types of quantum structures and a wide range of unique structures, such as quantum wells and quantum dots (QDs), superlattices, and lasers, can be grown through MBE with precise control of the growth parameters such as thickness, composition, and growth rate. Because of the high cleanliness of the growth environment and the precise composition control, MBE structures closely approximate the idealized models used in solid-state theory [9].

3.2. Sample Preparation: In this section the different sample preparation methods have been discussed.

3.2.1. Chemicals Used: The chemicals and spectroscopic probes were procured from the following sources. Analytical-grade chemicals were used for synthesis

without further purification. Deionized (DI) water, obtained from Millipore, was used to prepare all aqueous solutions. Among the other solvents used in this study, dimethyl sulfoxide (DMSO), toluene, chloroform, acetonitrile and ethanol ($\geq 99\%$) were purchased from Merck. The dyes and probes Protoporphyrin IX (Sigma Aldrich), Squaraine (SQ2) (Solaronix, Switzerland), N719 (Solaronix, Switzerland), Coumarin 343 (Sigma Aldrich), Phenothiazine (PTZ) (Sigma Aldrich), Dichlorofluorescein diacetate (DCFH-DA) (Calbiochem) were used without any further purification. The salts used in this work, Cobalt (II) chloride hexahydrate $[\text{CoCl}_2 \cdot 6\text{H}_2\text{O}]$ and Zinc (II) nitrate hexahydrate $[\text{Zn}(\text{NO}_3)_2 \cdot 6\text{H}_2\text{O}]$ were purchased from Sigma-Aldrich. The materials for solar cell fabrication, platinum chloride (H_2PtCl_6), lithium iodide (LiI), 4-tert-butylpyridine (TBP) and iodine (I_2) were purchased from Sigma-Aldrich. The conducting glass substrate with fluorine-doped tin oxide (FTO) and 60 μm thick Surlyn were bought from Solaronix. ZnO NPs (~ 30 nm), TiO_2 NPs (~ 21 nm), Al_2O_3 NPs (~ 40 nm) were purchased from Sigma Aldrich. PbS quantum dots were purchased from Evident Technology.

3.2.2. Preparation of the Cocktail-dye Solutions: 0.3 mM PPIX and 0.3 mM SQ2 solutions were prepared separately under constant stirring for 1 h, using dimethyl sulfoxide (DMSO) as solvent. DMSO is taken a solvent because both the dyes have good solubility in DMSO and it is an accepted biologically relevant solvent [10]. These two dye solutions were mixed at different molar ratios of the both such as (SQ2: PPIX) 8:2, 6:4, 4:6, 2:8 and the dye cocktails were named accordingly as S8P2, S6P4, S4P6, S2P8. The preparation of metalloporphyrins were done using the earlier reported literature [11]. For the preparation of the cobalt (II) ion metalated porphyrin [PP(Co)] solution an excess amount of (1:10 molar ratio) cobalt (II) chloride hexahydrate was added to 0.3 mM of the PP dye solution in DMSO and the mixture for overnight stirring. For the preparation of PP(Zn), the core metalation was done using the same procedure as cobalt (II) using the salt zinc (II)

nitrate hexahydrate. SQ2 and PP(Co) were mixed at 8:2 molar ratio for the preparation of another co-sensitizer solution and the SQ2 and PP (Zn) mixture was also prepared using the same molar ratio.

3.2.3. Synthesis of the Co-sensitized Nanohybrids: The ZnO NPs were sensitized with each of the above mentioned individual dyes and their respective dye cocktails by adding 20 mg of ZnO NPs to 10 ml of each dye solution with continuous stirring for 12 h, at room temperature. After sensitization, the solutions were centrifuged for a few times and the clear supernatants containing the unbound dyes were separated out. Then, the sensitized nanohybrids were washed with DMSO for several times to remove the possible unbound or loosely bound dyes from the surface of the nanoparticles. The nanohybrids were then dried by heating on a water bath and stored in dark.

3.2.4. Methods for Photocatalysis Test: The photocatalytic activity of the nanohybrids under visible light illumination was examined for photodecomposition of acridine orange (AO), a model pollutant having a nitrogen containing heterocyclic structure in aqueous solution. The photodegradation of AO (initial concentration $C_0 = 0.5 \times 10^{-4}$ M) was carried out in a 1 cm optical path quartz cell containing 3 mL of solution having 1 gL^{-1} concentration of each nanohybrid. The suspension was irradiated under light and appropriate amount of aliquots were taken out at certain time intervals. The percentage degradation (%DE) of AO in 1hr was calculated using equation 3.1:

$$\% \text{ DE} = \frac{I_0 - I}{I_0} \times 100 \quad (3.1)$$

where, I_0 is the initial absorption intensity of AO at $\lambda_{\text{max}} = 491 \text{ nm}$ and I is the absorption intensity after 1 h light irradiation.

3.2.5. Growth Technique of GaAs/Al_{0.27}Ga_{0.73}As Single Quantum Well (QW)

Structures: The GaAs/Al_{0.27}Ga_{0.73}As single quantum well structures, used in this study were grown using a Riber Sys 14020 Epineat a solid-source molecular beam epitaxy (MBE) furnished with Ga and Al effusion cells and As cracker. The sample was grown on a semi insulating GaAs (001) substrate layer at a growth temperature of 590 °C. Quantum structure were overgrown on 200 nm GaAs buffer layer The GaAs well layer of thickness (L_z) was sandwiched between 25 nm thick Al_{0.27}Ga_{0.73}As barrier layers and then capped with a 3 nm thick intrinsic GaAs layer on the top. The only structural difference between the two samples was the well width. For one sample it was 5.3 nm and for the other it was 16.5 nm.

3.2.6. Fabrication of Capacitive Devices using QW Heterostructures:

For studies regarding electronic properties, vapour deposition of Indium was done on both side of the sample to make the metallic contacts. The deposition chamber pressure was maintained at 5e -6 mbar throughout the process. On growth side a 250 nm layer of Indium was made while on bottom side of the sample the Indium layer thickness was 200 nm. An optical aperture was inserted on the growth side by using a circular shadow mask during deposition.

3.2.7. Determination of Energy Levels of Quantum Well (QW) by Simulation:

A MATLAB based quantum well simulation was carried out to calculate the first three energy level transitions which corresponds to the transitions between ground, first and second excited states of conduction band and valence band in quantum well. In the simulation we have used finite difference method for calculating the Hamiltonian matrix while taking into account the effective mass differences at the interfaces. We have discretized the position variable x into a lattice of points such that the spacing between the points is equal to 'a' which is the smallest unit of the cube mesh. The theoretical calculation becomes exact only in the limit a tending to 0 i.e. smaller the mesh more accurate is the result. For simulation purpose we have chosen $N_b = 25\text{nm}$ (AlGaAs width) and variable

GaAs width (N_w) though both of the parameters can be varied in the simulation. The value of ΔE_c was considered to be 0.2469 eV at 19 K and 0.2468 eV at 300 K. Also we have used infinite wall boundary conditions where the potential is infinitely large at the beginning and ending at a discrete point (Specific value of potential at the end point will not matter as long as the wave function is zero).

3.2.8. Growth of the DWELL and DDWELL Heterostructures: The samples were grown using solid state Molecular Beam Epitaxy method (MBE) with Stranski Krastanov being the growth mode. The three samples consist of the active layer of 10 layers of quantum dots with a subsequent capping/barrier. A 1000 nm n-type GaAs layer grown at 590 °C followed by intrinsic GaAs layer of 217 nm is deposited before active layer. In active region of all three samples, the bottom $\text{In}_{0.15}\text{Ga}_{0.85}\text{As}$ layer (Pseudomorphic layer) thickness is kept constant at 2 nm. The upper capping layer ($\text{In}_{0.15}\text{Ga}_{0.85}\text{As}$ - Strain reducing layer) thickness is varied by 4, 6 and 8 nm in samples A, B and C, respectively. In all samples 2.7 monolayer (ML) of InAs quantum dots were deposited at 490 °C and the whole active region was finally capped with 50 nm GaAs barrier to avoid coupling. A top n-type contact layer of 200 nm was deposited at 490 °C. The active region of the samples was grown at 500 °C. The growth rate was kept same for all.

3.2.9. Fabrication and Characterization of the Photodetector Devices: A standard two level lithography process was utilized for fabrication of the photodetectors. A Thermo Fisher Fourier transform infrared spectrometer was used for measuring the spectral response in which the fabricated devices were fixed and wire-bonded onto a 64-pin leadless chip carrier and mounted on a liquid nitrogen pour fill cryostat. A cold radiation shield was fitted in the cryostat for dark current and noise measurements. Temperature-dependent voltage vs. dark current, noise and spectral response were measured.

3.2.10. Synthesis of the PbS QD Based Hybrid Materials: The PbS QD-TiO₂ hybrid was prepared by constant stirring of 200 μ L stock colloidal PbS QDs and 15 mg TiO₂ NPs in the dark at room temperature in 5 mL toluene for 12 hr. The solution was centrifuged after the sensitization, for a few minutes and the clear supernatant solution was removed. Then, the hybrid material was collected after three-four times washing by the solvent toluene followed by drying in a water bath. The toluene-chloroform solvent mixture was used for the synthesis of the phenothiazine (PTZ) containing hybrids PbS QD-PTZ and PbS QD-TiO₂-PTZ (triohybrid). The synthesis procedure was similar to the PbS QD-TiO₂. The concentration of phenothiazine (PTZ) was kept to be 0.25 mM during the synthesis of the hybrids.

3.2.11. Preparation of Dichlorofluorescein and ROS Measurements: DCFH was prepared [12, 13] from DCFH-DA by mixing 0.5 mL of 1.0 mM DCFH-DA with 2.0 mL of 0.01 N NaOH in methanol. This deesterification reaction was continued at room temperature for 30 min, and the mixture was then neutralized with 10 mL of 25 mM NaH₂PO₄ at pH 7.4. This solution was stored in the dark in ice until further use. All the measurements were carried out in a total volume of 2.0 mL water that contained 10 μ L of DCFH solution and 2 mg of the hybrid material. The assay was performed for 20 mins under dark and then 60 mins under a IR lamp.

3.2.12. Fabrication of Dye-Sensitized Solar Cells: Fabrication of the photoanodes of DSSC are done using the earlier reported doctor blading method [14, 15]. TiO₂ pest coated FTO glass substrates were annealed at 450 $^{\circ}$ C for 1 hr, followed by a cooling to 80 $^{\circ}$ C and dipping into the dye solution for 24 hr. We used six different dye cocktails as sensitizers for the first work on photovoltaics, prepared by mixing different molar ratios of the two dyes, SQ2 and PPIX. Initially a 0.3 mM solution of SQ2 was prepared in ethanol and a PPIX solution of same concentration was prepared using DMSO as a solvent. Then these two solutions were mixed in different ratios maintaining the total volume to be 10 mL. The ratios of SQ2: PPIX

used are 10:0, 8:2, 6:4, 4:6, 2:8 and 0:10. For the one by one sensitization technique, the photoanodes were immersed in a single dye solution for 12 hr, followed by 12 hr dipping in the other dye. The one by one sensitized DSSCs are named as SQ2_PPIX and PPIX_SQ2 according to the sequence of dye used for sensitization. To ease the comparison, the total dipping time in dye solution was kept 24 hr in both cocktail dye sensitization and sequential one after another sensitization. The counter electrodes were prepared by depositing platinum on the FTO substrates via thermal decomposition of 5 mM platinum chloride (in isopropanol) at 385 °C for 30 min. 60 µm thick Surlyn was used as a spacer between the active and counter electrodes. I⁻/I₃⁻ redox couple was used as electrolyte which was prepared by mixing iodine crystal (I₂), lithium iodide (LiI), and 4-tert-butylpyridine (TBP) using acetonitrile as a solvent. The active area of all the devices were 0.64 cm².

For the second study on photovoltaics, the device fabrication strategy was similar as above. Before the fabrication of cells Fluorine-doped tin oxide (FTO) conducting glass substrates, were cleaned by successive sonication with double distilled water (DDW), acetone, and ethanol for 10 mins, each with adequate drying followed by annealing at 150 °C for 1hr. TiO₂ and ZnO pest coated FTO glass substrates were annealed at 400 °C for 1 hr, followed by a cooling to 80 °C. Then the photo-anodes were dipped into the dye solutions of C343 or N719 for 18 hrs. The solvent of the dyes was ethanol. The counter electrodes were prepared by depositing platinum on the FTO substrates via thermal decomposition of 5 mM platinum chloride (in isopropanol) at 385 °C for 30 min. 60 µm thick Surlyn was used as a spacer between the active and counter electrodes. I⁻/I₃⁻ redox couple was used as electrolyte which was prepared by mixing iodine crystal (I₂), 4-tert-butylpyridine (TBP) and lithium iodide (LiI) using acetonitrile as a solvent. The active area of all the devices were ~1 cm².

References

- [1] D.V. O'Conner, D. Philips, Time correlated single photon counting, *Academic Press*, London, 1984.
- [2] T. Khan, Chemical and physical strategies for modulation of excited state dynamics and consequent emission enhancement of schiff bases, (2017).
- [3] U. Megerle, I. Pugliesi, C. Schrieber, C.F. Sailer, E. Riedle, Sub-50 fs broadband absorption spectroscopy with tunable excitation: putting the analysis of ultrafast molecular dynamics on solid ground, *Appl. Phys. B*, 96 (2009) 215-231.
- [4] A. Maciejewski, R. Naskrecki, M. Lorenc, M. Ziolk, J. Karolczak, J. Kubicki, M. Matysiak, M. Szymanski, Transient absorption experimental set-up with femtosecond time resolution. Femto-and picosecond study of DCM molecule in cyclohexane and methanol solution, *J. Mol. Struct*, 555 (2000) 1-13.
- [5] S.S. Sinha, P.K. Verma, A. Makhal, S.K. Pal, A versatile fiber-optic coupled system for sensitive optical spectroscopy in strong ambient light, *Rev. Sci. Instrum.*, 80 (2009) 053109.
- [6] A.Y. Cho, J. Arthur, Molecular beam epitaxy, *Prog. Solid State Chem.*, 10 (1975) 157-191.
- [7] B. Joyce, Molecular beam epitaxy, *Rep. Prog. Phys*, 48 (1985) 1637.
- [8] C. Foxon, Three decades of molecular beam epitaxy, *J. Cryst. Growth*, 251 (2003) 1-8.
- [9] J.R. Arthur, Molecular beam epitaxy, *Surf. Sci.*, 500 (2002) 189-217.
- [10] M. Liong, J. Lu, M. Kovoichich, T. Xia, S.G. Ruehm, A.E. Nel, F. Tamanoi, J.I. Zink, Multifunctional inorganic nanoparticles for imaging, targeting, and drug delivery, *ACS nano*, 2 (2008) 889-896.
- [11] P. Kar, S. Sardar, E. Alarousu, J. Sun, Z.S. Seddigi, S.A. Ahmed, E.Y. Danish, O.F. Mohammed, S.K. Pal, Impact of metal ions in porphyrin-based applied materials for visible-light photocatalysis: Key information from ultrafast electronic spectroscopy, *Chem. Eur. J.*, 20 (2014) 10475-10483.

- [12] D. Bagchi, S. Chaudhuri, S. Sardar, S. Choudhury, N. Polley, P. Lemmens, S.K. Pal, Modulation of stability and functionality of a phyto-antioxidant by weakly interacting metal ions: curcumin in aqueous solution, *RSC Adv.*, 5 (2015) 102516-102524.
- [13] S. Sardar, P. Kar, S. Sarkar, P. Lemmens, S. Pal, Interfacial carrier dynamics in PbS-ZnO light harvesting assemblies and their potential implication in photovoltaic/photocatalysis application, *Sol. Energy Mater Sol. Cells*, 134 (2015) 400-406.
- [14] A.I. Kontos, A.G. Kontos, D.S. Tsoukleris, M.-C. Bernard, N. Spyrellis, P. Falaras, Nanostructured TiO₂ films for DSSCs prepared by combining doctor-blade and sol-gel techniques, *J. Mater. Process. Technol.*, 196 (2008) 243-248.
- [15] S. Gagliardi, L. Giorgi, R. Giorgi, N. Lisi, T.D. Makris, E. Salernitano, A. Rufoloni, Impedance analysis of nanocarbon DSSC electrodes, *Superlattice. Microst.*, 46 (2009) 205-208.

Chapter 4

Photophysical Studies on Light Harvesting Nanomaterials for Improved Photovoltaic Application

4.1. Introduction: The increasing demand to supply ratio of fossil fuel energy sources and the intensifying environmental pollution have promoted an extensive research for the development of efficient conversion technologies of clean and renewable energy sources. Solar energy has been considered to be the most promising sustainable and renewable energy source because of its quasi-unlimited supply. In the last decade, dye sensitized solar cells (DSSCs) have drawn significant attention as an alternative conversion technology for solar energy, besides conventional Si based solar cells, because of its simple and less expensive processing and a wide range of potential applications [1-3]. Since the first invention of DSSCs by O'Regan and Grätzel in 1991 [4], a plethora of designing strategies has been developed and reported in the literature in order to optimize the device performance and to minimize the effective costs [5-10].

A good spectral match between the absorption spectra of the sensitizer and the incident solar radiation is an essential requirement for efficient solar energy conversion [11]. So far, the most widely used photosensitizers are Ruthenium (Ru) based dyes (N719, N3, Black dye etc.) because of their good stability and efficient performance. However, the scarcity of the raw material, enormous purification cost, lower molar extinction coefficient (ϵ) of the metal to ligand charge transfer (MLCT) band, a poor absorption in the near infrared (NIR) range of the solar light and toxicity are well documented limitations of these Ru photosensitizers [12]. As an alternative to Ru dyes, relatively less toxic and less expensive organic dyes are

being used to sensitize the photoanodes [13]. Organic dyes are attractive as a photosensitizer because of their high molar extinction coefficient, tunable absorption wavelength, easy design and synthesis strategies. Still the efficiency of organic dye sensitized solar cells are not comparable to that of the metallo-organic dyes because of their narrow absorption spectra, shorter excited state lifetime and the problem of self-aggregation on the semiconductor surface [14]. For efficient organic dye sensitized solar cells, the appreciated techniques to achieve a broad absorption window are either using a sensitizer solution cocktail mixing one dye absorbing in the visible region with another dye absorbing in the NIR region or incorporating Förster resonance energy transfer (FRET) between two co-sensitizers [9, 15-19]. However, co-sensitization brings some additional complexity to the effective performance of the device [20, 21]. The control of the uptake of different dyes, the prevention of unwanted reactions and unfavorable electron-hole recombination [22] affect the device performance. FRET has been proposed to be a more useful tool to achieve strong light harvesting over a broad wavelength range without affecting the key parameters such as open circuit voltage (V_{oc}) or fill factor (FF) of the DSSC [23]. An enhancement in photocurrent due to efficient energy transfer from a quantum dot to the sensitizing dye has been reported earlier for quantum dot co-sensitized DSSC [24, 25]. But the study of energy transfer between two dyes in co-sensitized DSSCs is sparsely reported in the literature. Aggregation induced self-quenching of excited state electrons of NIR absorbing dyes is another limitation widely reported in co-sensitized DSSCs [26, 27]. The required use of high concentrations of co-adsorbent is unavoidable constrain on the co-sensitization of organic dyes [18, 28-30]. In order to avoid the co-adsorbent, one of the co-sensitizers can be used to counteract the aggregation of the other. Spectroscopic studies and excited state dynamics of the two dyes can help to optimize the co-sensitization procedure and to understand the complicated set of electron and energy transfer processes involved in co-sensitized DSSCs.

We have chosen squaraine (SQ2) and protoporphyrin IX (PPIX) to fabricate a co-sensitized DSSC and detail photo-physical studies have been carried out to explore the dynamical processes occurring between these two dyes after the attachment to the TiO₂ surface. PPIX is an environment friendly organic sensitizer which has a strong absorption in the visible region of the solar spectrum. Application of PPIX as a sensitizer in DSSC has been reported in the earlier publications of our group [31]. SQ2 is a commercially available NIR absorbing dye that has been receiving a growing attention in the field of DSSC due to its light harvesting ability in the NIR region [32, 33]. From the spectral overlap between the absorption of SQ2 and emission of PPIX and from the time resolved fluorescence decay of the mixture of SQ2 and PPIX, FRET from PPIX to SQ2 has been confirmed. DSSC was fabricated by co-sensitizing with different molar ratios of the two dyes where an optimum acceptor to donor ratio has been found to exhibit the highest efficiency. The FRET enhanced photocurrent and the anti-aggregating property of PPIX has been experimentally proven to be the major reasons for the enhanced light harvesting over the entire solar spectrum. The PPIX-SQ2 co-sensitized DSSCs was found to be more efficient compared to the SQ2 sensitized DSSCs prepared using optimum concentration of the well-known co-adsorbent chenodeoxycholic acid (CDCA). The wavelength dependent photocurrent measurements reveal that a small amount of PPIX can efficiently act as a co-adsorbent instead of CDCA. CDCA is more costly than PPIX and the required amount of CDCA to break the aggregations, is also much higher than PPIX. Thus, addition of PPIX as a co-sensitizer to SQ2 sensitized DSSC provides a simultaneous advantage of increased absorption window, FRET induced enhanced photocurrent and prevention of SQ2 aggregation.

Other than the sensitizer issue, extensive research has been going on since the last decade in the technological aspect of DSSCs [34, 35]. So far the widely known high efficiency DSSCs consist of a nanocrystalline TiO₂ photoanode

sensitized by a Ru based light absorbing dye, platinized conducting glass as counter electrode and redox couple I⁻/I₃⁻ as electrolyte [36, 37]. Another wide band gap semiconductor zinc oxide (ZnO) is a promising alternative to TiO₂ due to its higher bulk electron mobility and enormous diversity in probable nano-structures [38-40]. However, the achieved energy conversion efficiencies of ZnO-based DSSCs are usually lower than that of TiO₂. The probable reason behind the lower efficiency of ZnO has been a long lasting issue of extensive research [41-43]. The faster electron-transfer rate in TiO₂ than ZnO is predominantly responsible for the comparative efficiency. The higher density of states of the TiO₂ near the conduction band edge compared to ZnO causes the faster electron transfer [44]. Denser states in TiO₂ are able to provide additional efficient electron transfer channels which eventually increases the electron injection efficiency. The electron injection kinetics from different Ru based sensitizers to semiconductor materials are extensively studied using various spectroscopic techniques in earlier literatures [45, 46]. In an earlier report by Tachiya et al, the poor performance of ZnO cells for sensitizer N3 has been ascribed to partial dissolution of the ZnO and formation of N3-Zn²⁺ aggregates [47]. On the other hand, there are a few reports which reveal that ZnO cells perform better than TiO₂ upon sensitization by xanthene and acriflavine type organic dyes [48, 49]. Although the explanation of the higher efficiencies for ZnO cells upon these organic dye sensitization are not very clear in reported literature. Since the last decade, a large volume of research is done to increase the efficiency of ZnO based cells [50-52]. Nevertheless, a thorough understanding of the relative efficiency of ZnO and TiO₂ cells with organic sensitizer and ruthenium based sensitizer is still missing in the literature.

In the second part of the present work, we have done a comparative study using ultrafast dynamics and device characteristics to rationalize the efficiency inversion of ZnO and TiO₂ DSSC depending on the choice of sensitizer. We have chosen the organic sensitizer C343 and another ruthenium based sensitizer N719

for the comparative study. The electron injection efficiency from the sensitizer C343 to the semiconductors are obtained from picosecond resolved fluorescent transients. The transient absorption spectra of the sensitizer N719 and its conjugates with TiO₂ and ZnO provides a new insight into the dye conjugation and electron shuttling mechanism. Higher dye loading and slower back electron recombination (BER) in ZnO cells than TiO₂ is observed for both the sensitizers from absorption of photoanodes, open circuit potential decay and electro chemical impedance spectroscopy. All these observation justifies the ZnO to be a better photoanode material for both the sensitizers but still ruthenium based dye N719 is showing lower efficiency for the same. As a probable explanation of this anomaly, we have observed a signature of H-aggregate of N719 dye on ZnO photoanode surface through retro reflecting mode absorption of the photoanode. It is not possible to observe this aggregation signature by conventional method of dye desorption by basic solution. This type of aggregate is known to be non-harvesting in nature i.e. it can't inject electrons to the semiconductors. Additionally, we have observed from photocurrent versus wavelength response, that these aggregates retracts back the injected electrons from CB of the ZnO. This observation has been experimentally justified and correlated with the lower photocurrent in N719-ZnO DSSC. The present study provides a mechanistic explanation of the higher efficiency of ZnO cells than TiO₂ in case of an organic sensitizer C343 and the reversal of efficiency trend for the ruthenium based dye N719.

4.2. Results and Discussion:

4.2.1. Three in One Approach towards Efficient Organic Dye Sensitized Solar Cells: Aggregation Suppression, Panchromatic Absorption and Energy Transfer [53]: In the present study, the two organic dyes chosen for co-sensitization are protoporphyrin IX (PPIX) and squaraine (SQ2) because of their complementary absorption spectra. From the structure of PPIX shown in Figure 4.1a, it is evident that this sensitizer is a derivative of porphyrin, which is an integral part of many

naturally occurring and biologically active macrocyclic compounds, e.g. hemoglobin and chlorophyll. The absorption of PPIX in DMSO is shown in Figure 4.1c, where the highest intensity peak appearing at 407 nm is due to the Soret band and the other four lower intensity peaks at 509 nm, 542 nm, 578 nm and 630 nm are the Q-bands. The use of PPIX as a green alternative of the conventional toxic and expensive sensitizers has been reported earlier [31], but the so far reported efficiencies of PPIX sensitized DSSCs are poor from a point of commercialization.

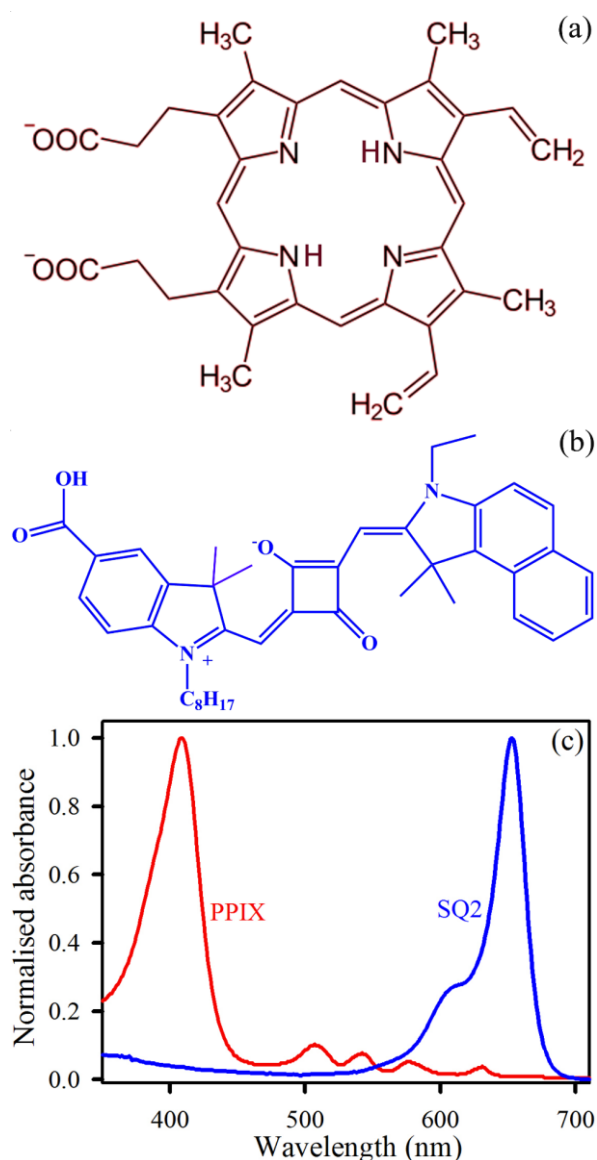


Figure 4.1. Structure of (a) PPIX and (b) SQ2; (c) normalized absorption spectra of PPIX in DMSO and SQ2 in ethanol.

In spite of having high molar extinction co-efficient in the visible region, PPIX shows a very low efficiency probably because of the inadequate absorbance in the NIR region. Squarines are widely known red/NIR absorbing synthesized organic dyes that can be used as a co-sensitizer with a visible absorbing dye to get a wide panchromatic absorption. From the structure of SQ2 shown in Figure 4.1b and the absorption spectra of SQ2 in ethanol shown in Figure 4.1c, it can be correlated that the highest intensity peak appearing at 651 nm corresponds to π - π^* charge-transfer (CT) transitions. A lower intensity peak at the blue end side (604 nm) of the spectra is a notable signature of dye aggregation [27]. It is evident from the combined absorption spectra shown in Figure 4.1c that by using PPIX and SQ2 as a co-sensitizers a wide range of solar spectra, starting from 360 nm to 680 nm, can be harvested.

Before going into the details of the co-sensitized DSSCs using PPIX and SQ2, the probable complexities and advantages of these dye mixtures were studied using ultrafast spectroscopic studies. A significant overlap between the absorption of SQ2 and the emission of PPIX was observed, as shown in Figure 4.2a. So, there is a possibility of energy transfer from the excited state of PPIX to SQ2 when the two dyes come to close proximity. To create this proximity between these two dyes, Al_2O_3 has been used. The excited state lifetime of PPIX (attached to Al_2O_3) was measured in presence and absence of SQ2 by fitting the time resolved fluorescence decays, as shown in Figure 4.2b. It can be noted from the lifetime components summarized in Table 4.1 that the average life time of the PPIX (attached to Al_2O_3) excited state is shortened from 13.20 ns to 5.47 ns when SQ2 is added to the solution. We propose FRET between the donor (PPIX) and the acceptor (SQ2) as the mechanistic explanation of the shortened lifetime of the excited state of the donor. The calculated distance between the donor and acceptor was found to be 4.9 nm with a 58% energy transfer efficiency. The confirmation of FRET from PPIX to SQ2 increases the possibility of getting enhanced photon to

current conversion in the visible region. Again because of the long life time of excited state of PPIX, both electron transfer to TiO_2 and energy transfer to SQ2 become feasible. Although these two processes will be competing with each other, the FRET from PPIX to SQ2 was observed to be efficient in terms of device performance and cost effectiveness, as discussed in the explanation of the device characteristics.

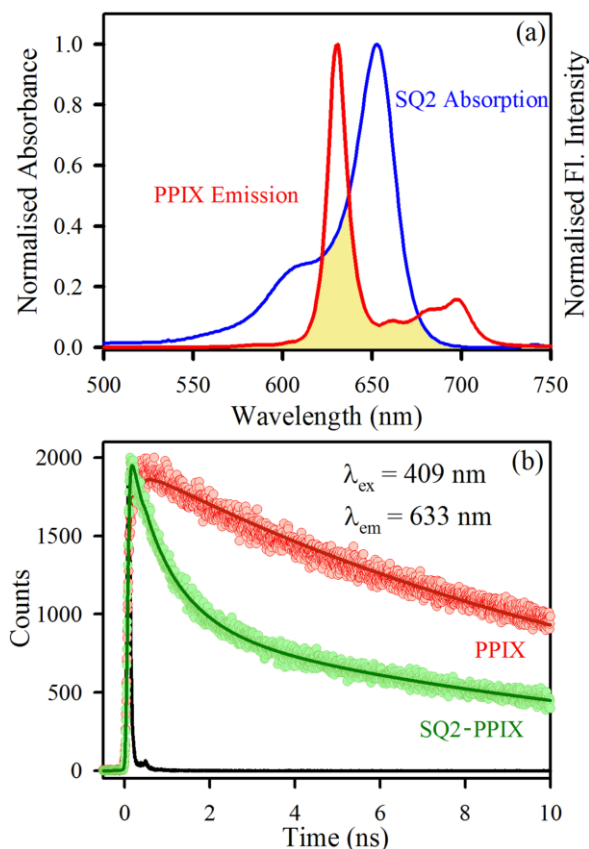


Figure 4.2. (a) Spectral overlap between the emission of PPIX and the absorption of SQ2, (b) the picosecond-resolved fluorescence decays of PPIX attached with Al_2O_3 in absence (red) and presence (green) of SQ2.

Table 4.1. Excited-state lifetime of the donor PPIX attached to Al_2O_3 in presence and absence of the acceptor SQ2.^a

Sample	Excitation Wavelength (nm)	Emission wavelength (nm)	τ_1 (ns)	τ_2 (ns)	τ_3 (ns)	τ_{avg} (ns)
PPIX	409	633	13.20 (100%)	-	-	13.20
PPIX-SQ2	409	633	0.25 (23%)	1.02 (39%)	13.20 (38%)	5.47

^a Numbers in the parenthesis indicate relative weightages.

The molar ratios of the two dyes SQ2/PPIX in the six cocktail mixtures used in this study were 10:0, 8:2, 6:4, 4:6, 2:8 and 0:10 and the sensitized DSSCs are named as S10P0, S8P2, S6P4, S4P6, S2P8 and S0P10, respectively. The different colours of the dye cocktails and the sensitized photoanodes are shown in Figure 4.3a. The solid state absorption spectra of the selective photoanodes are shown in Figure 4.3b as a function of the dye loading. The scattering correction in the solid state absorption spectra was done as reported literature [54, 55]. It is evident from the absorption spectra of S10P0 sensitized photoanode that the absorption of SQ2 has broadened after attaching to TiO₂ surface compared to the liquid phase absorption spectra of SQ2 (shown in Figure 4.1c). The broadening of the overall spectrum and increase in peak-intensity at the lower wavelength side signifies the increased aggregation after adsorption on a solid surface. The self-aggregation of squaraine based sensitizers is a familiar issue that decrease the efficiency of the device. In order to reduce the aggregation problem, the use of co-adsorbent is a common approach described in literature. From the absorption spectra of the photoanodes S8P2, S6P4, it can be observed that the simultaneous attachment of PPIX and SQ2 on TiO₂ surface can significantly reduce the aggregation of the SQ2 dye. It can be noted that after the addition of PPIX, the absorption region of SQ2 becomes narrower and the prominent peak around 600 nm, due the dimerization of SQ2 is almost absent in the photoanodes sensitized with the 8:2 and 6:4 cocktail dye mixtures. With the decreasing molar ratio of SQ2 in the mixture of dyes, the peak intensity also reduces around the red/NIR region. On the contrary, the peak intensity around 400 nm is not differing much with the varying molar ratios of the two dyes. The relative ratio of the dye loading is not exactly proportional to the ratio of the liquid cocktail in which the photoanodes were immersed. The most fascinating feature of this two particular dye is that PPIX is serving the purpose of a co-adsorbent and efficiently preventing the aggregation possibility of SQ2, which has been proved further from the device performances.

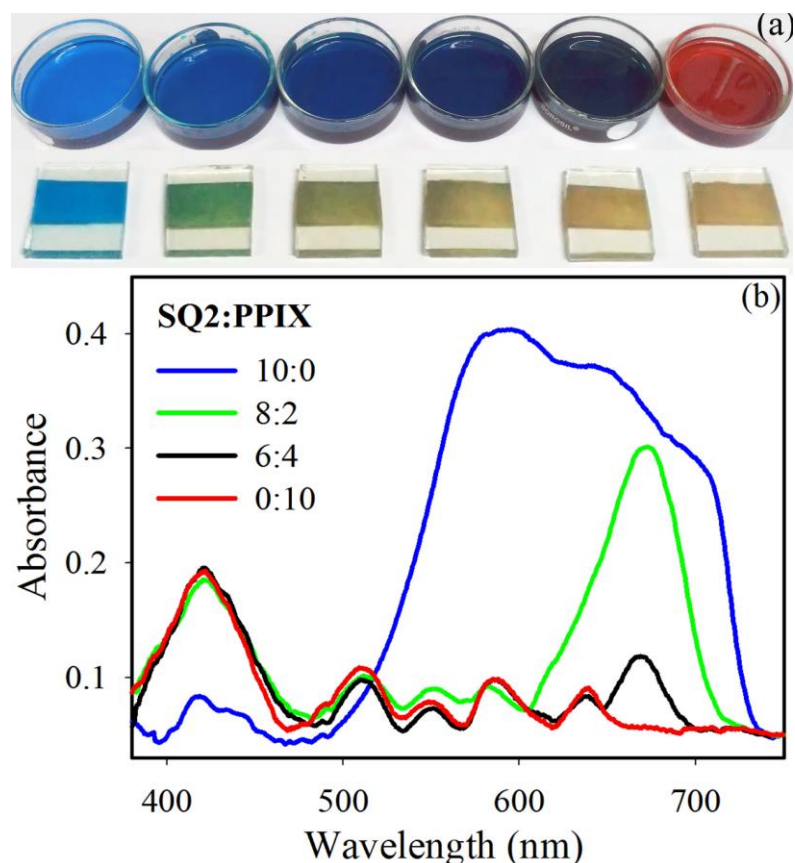


Figure 4.3. (a) Dye cocktail solutions and dye sensitized TiO₂ photoanodes with different molar ratios of SQ2 and PPIX. Starting from left to right the molar ratios of SQ2/PPIX are 10:0, 8:2, 6:4, 4:6, 2:8, 0:10. (b) Reflecting-mode absorption spectra of TiO₂ films sensitized by dyes with different molar ratio of SQ2/PPIX.

The electron injection efficiency from the dye to the semiconductor is one of the key factors that affects the efficiency of DSSCs. As shown in Figure 4.4a, time resolved fluorescence transients were measured for PPIX solution and PPIX-TiO₂ solution using DMSO as a solvent. A 409 nm laser was used as an excitation source and the emission decay was recorded at 633 nm. The decay of PPIX was single exponential with a time scale of 14 ns. For PPIX-TiO₂, a faster component of 130 ps (63%) was obtained which is ascribed to be the electron transfer time scale from the excited state of PPIX to the conduction band of TiO₂. Figure 4.4b shows that the decay of the excited state of SQ2 in ethanol was also a single exponential of 500 ps and a very fast electron transfer timescale of 60 ps (64%) was obtained after attachment of SQ2 on TiO₂ surface. All the lifetime components and their relative percentages are summarized in Table 4.2.

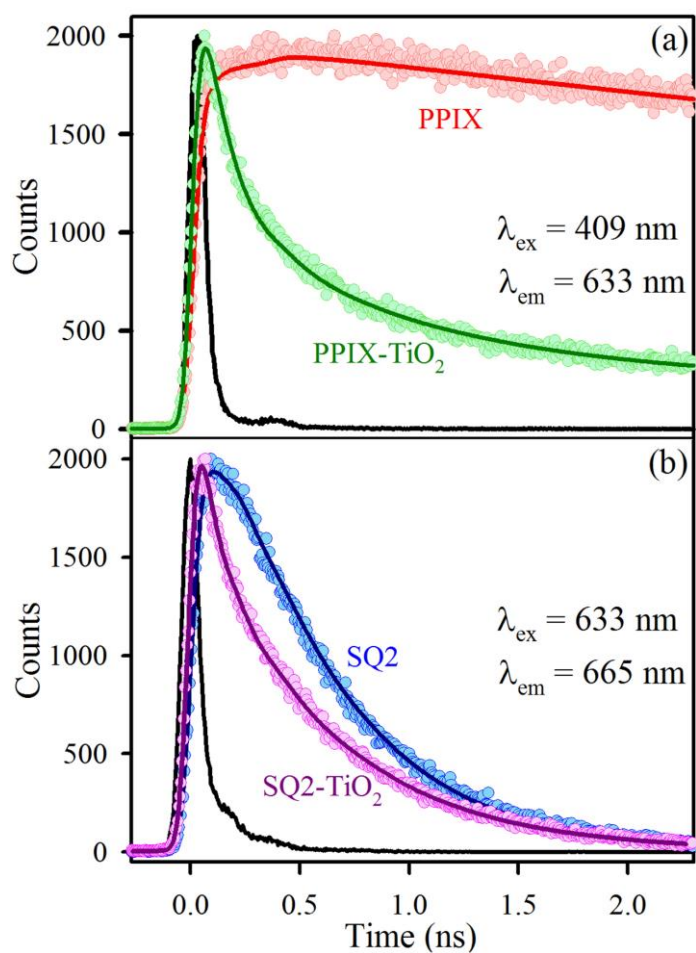


Figure 4.4. (a) Fluorescence decay profiles of PPIX (red) and PPIX attached to TiO₂ (green), (b) fluorescence decay patterns of SQ2 (blue) and SQ2 attached to TiO₂ (pink).

Table 4.2. Dynamics of picosecond-resolved fluorescence transients of the dyes PPIX, SQ2 and the nanohybrids^a

Sample	Excitation Wavelength (nm)	Emission wavelength (nm)	τ_1 (ns)	τ_2 (ns)	τ_3 (ns)
PPIX	409	633	14.00 (100%)		
PPIX-TiO ₂	409	633	0.13 (63%)	0.89 (26%)	14.00 (11%)
SQ2	633	665	0.50 (100%)		
SQ2-TiO ₂	633	665	0.06 (64%)	0.58 (36%)	

^a Numbers in the parenthesis indicate relative weightages.

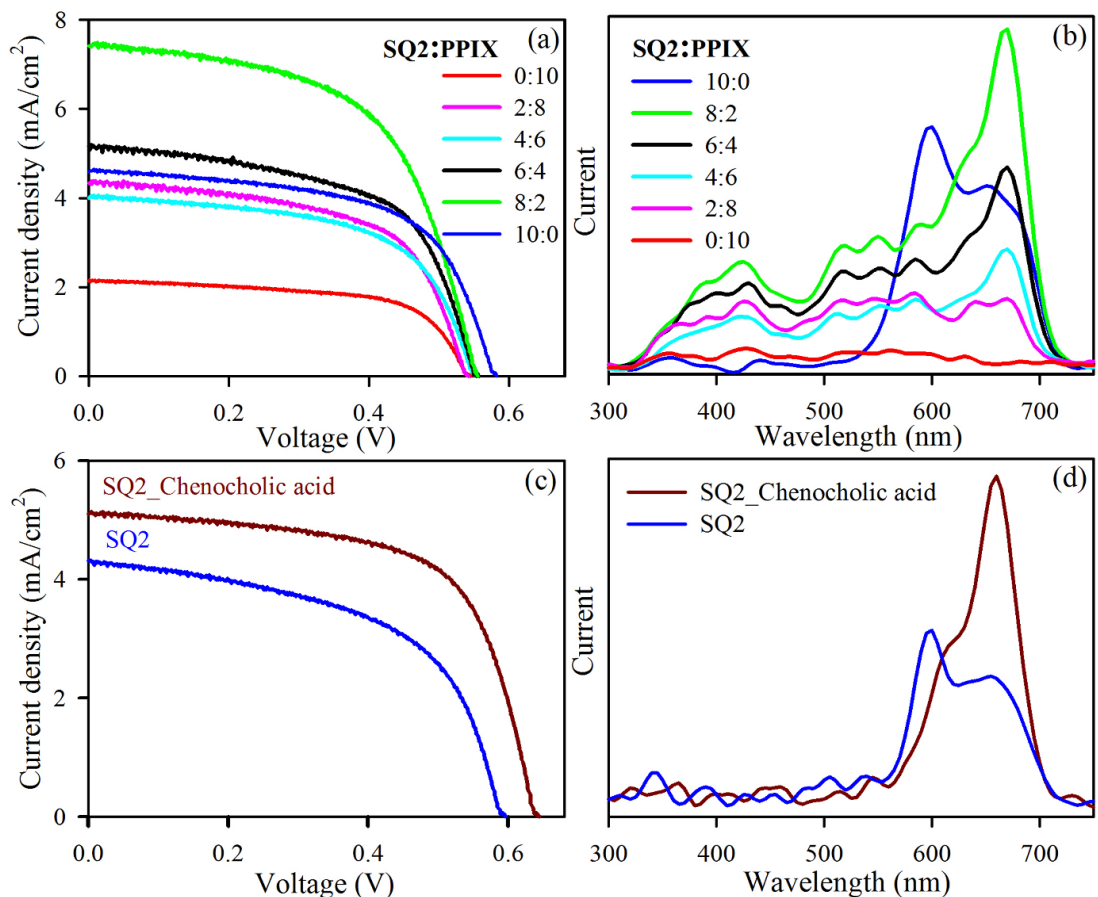


Figure 4.5. (a) I-V characteristics and (b) wavelength-dependent photocurrent for DSSCs sensitized by different ratios of SQ2 and PPIX. (c) I-V characteristics and (d) wavelength-dependent photocurrent for SQ2 and a mixture of SQ2 and 5mM chenodeoxycholic acid.

Table 4.3. Solar cell performances using different cocktail dyes with different molar ratios of SQ2 and PPIX as sensitizer.

SAMPLE SQ2/PPIX	FF (%)	V _{oc} (V)	J _{sc} (mA/cm ²)	η (%)
0:10	63	0.55	2.1	0.73
2:8	60	0.54	4.3	1.39
4:6	64	0.55	4.0	1.31
6:4	60	0.56	5.7	1.66
8:2	57	0.57	7.4	2.40
10:0	61	0.58	4.6	1.62

Table 4.4. Performances of SQ2 sensitized and a mixture of SQ2 and 5 mM chenodeoxycholic acid sensitized solar cells.

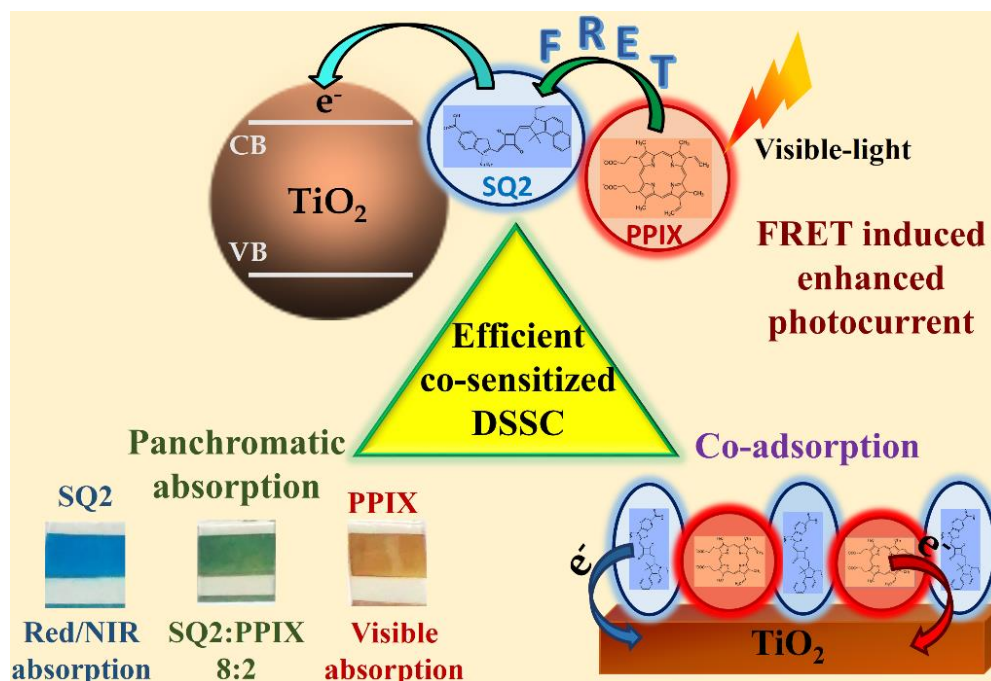
SAMPLE	FF (%)	V _{oc} (V)	J _{sc} (mA/cm ²)	η (%)
SQ2	54	0.60	4.3	1.38
SQ2-Chenocholic acid (5mM)	64	0.64	5.1	2.06

Figure 4.5a represents the current density (I) vs voltage (V) characteristics of the co-sensitized DSSCs. Sample S8P2 shows the highest efficiency (2.4 %) with much higher photocurrent than the cells sensitized by only one of the dyes. From Table 4.3, it can be noticed that we could reach an open circuit voltage (V_{oc}) of 0.58 V and an efficiency of 1.62 % for DSSC sensitized with only SQ2 (S10P0). For DSSC sensitized with only PPIX (S0P10) the efficiency was 0.73% and the V_{oc} was 0.55V. The V_{oc} values of the co-sensitized DSSCs were increasing from 0.55 V to 0.58 V with the increasing molar ratio of SQ2 dye as both the dyes have their contributions to the Fermi level of the photoanode. The current density was observed to increase with increasing relative concentration of SQ2. For molar ratio of SQ2/PPIX of 6:4 and 8:2, the DSSCs exhibit higher photocurrent and higher efficiency than the one sensitized with only SQ2. The highest efficiency (2.4%) was observed for S8P2 with a current density 7.4 mA/cm². Besides the increase in absorption window, the FRET from PPIX to SQ2 is responsible for the significant increase in photocurrent at that particular ratio of the two dyes which is evident from the photocurrent vs wavelength data of the DSSCs shown in Figure 4.5b. Even though the dye absorption in the visible region was shown to be almost the same for S8P2, S6P4 and S0P10 in the Figure 4.3b, the measured photocurrent was prominently higher in the visible range for the S8P2. It can be concluded that the optimum acceptor to donor ratio is 8:2 (SQ2/PPIX) and the excited state energy of PPIX is transferred to SQ2 followed by the injection from the excited state of SQ2 to conduction band of TiO₂. Thus, FRET causes an increased light harvesting in the visible region. Another notable feature in Figure 4.5b is the better harvesting in the NIR/ red region of S8P2 although there was lower concentration of SQ2 in S8P2 than the S10P0, as shown in Figure 4.3b. The reason behind this anomaly is the much better light harvesting ability of the monomer of SQ2 compared to the aggregated dye. The photocurrent around 600 nm is harvested mainly by SQ2 dimers, but the aggregation promotes a lack of directionality of excited state electrons of the dye. As a consequence the harvesting ability of the monomer

around 650 nm reduces significantly. This fact is clearly manifested in the wavelength dependent photocurrent measurement of S10P0 where a relatively higher photocurrent was observed at the absorption peak wavelength of the dimer of SQ2 than at that of the monomer. A noteworthy higher photon to current conversion in the absorption region of SQ2 was observed for the S8P2 as PPIX reduces the aggregation of SQ2. The harvesting in the absorption region of the SQ2 monomer is observed to be remarkably higher than in the dimer absorption region in the S8P2 sensitized DSSC which reduces the possibility of self-quenching and consequently increases the overall photocurrent output. In the earlier reports about SQ2 co-sensitized DSSCs, chenodeoxycholic acid (CDCA) was proposed as a co-adsorbent to diminish SQ2 aggregation [32, 33, 56]. A detailed characterization of the SQ2-CDCA sensitized DSSC was also carried out and the results are shown in Figure 4.5c and 4.5d. From the I-V values of the SQ2-CDCA sensitized DSSCs tabulated in Table 4.4, it can be noted that the efficiency was much lower than that of S8P2 sensitized DSSC. Comparing the ratio of the photocurrent at the dimer and monomer absorption region of SQ2 in Figure 4.5b and 4.5d it can be concluded S8P2 is the optimal composition. The value of V_{oc} of the CDCA-SQ2 sensitized DSSC was higher than that of S8P2 because CDCA does not contribute to the Fermi level unlike PPIX. The J_{sc} was strikingly higher in S8P2 than in the CDCA- SQ2 sensitized DSSC because of FRET from PPIX to SQ2. Thus, apart from getting a FRET induced higher photocurrent, the idea of using one of the co-sensitizers as a co-adsorbent of the other is interesting as it is reducing the effective cost of the device.

The enhancement in photocurrent due to dipole-dipole coupling is further verified by the sequential one by one sensitization of the two dyes where the first layer of the dye is supposed to be acting as the main electron injecting sensitizer and the second dye layer will prefer to form some π stacking attachment with the first dye layer as it would not get much vacancy on the TiO_2 surface to be attached

with directly. As shown in Figure 4.6a, the SQ2_PPIX is showing higher efficiency and higher photocurrent than PPIX_SQ2. The efficiency and other solar cell parameters are summarized in Table 4.5. In SQ2_PPIX the first active layer of sensitizer is SQ2. So, PPIX can absorb the visible light and transfer the energy to SQ2, followed by electron injection from SQ2 to TiO₂ in SQ2_PPIX which lead us to get an increased photocurrent. The process of FRET is not much facile in PPIX_SQ2 as the first active layer of sensitizer is the donor itself, in that case. It can also be demonstrated from the wavelength dependent photocurrent measurement of SQ2_PPIX and PPIX_SQ2 that the ratio of photocurrent in the absorption regions of the monomer and dimer of SQ2 is not comparable to that of S8P2. PPIX can efficiently perform as a co-adsorbent when it is in the cocktail mixture with the SQ2 unlike the one by one sensitization, as it could prevent the aggregation during the attachment of the sensitizers with TiO₂. The overall mechanism of this co-sensitization induced enhanced efficiency of DSSC is shown in Scheme 4.1.



Scheme 4.1. Choice of co-sensitizers leading to wide range absorption spectra, reduced aggregation of the NIR sensitizer and increased photocurrent due to dipole-dipole coupling. All these three events enhances the overall efficiency of the cell.

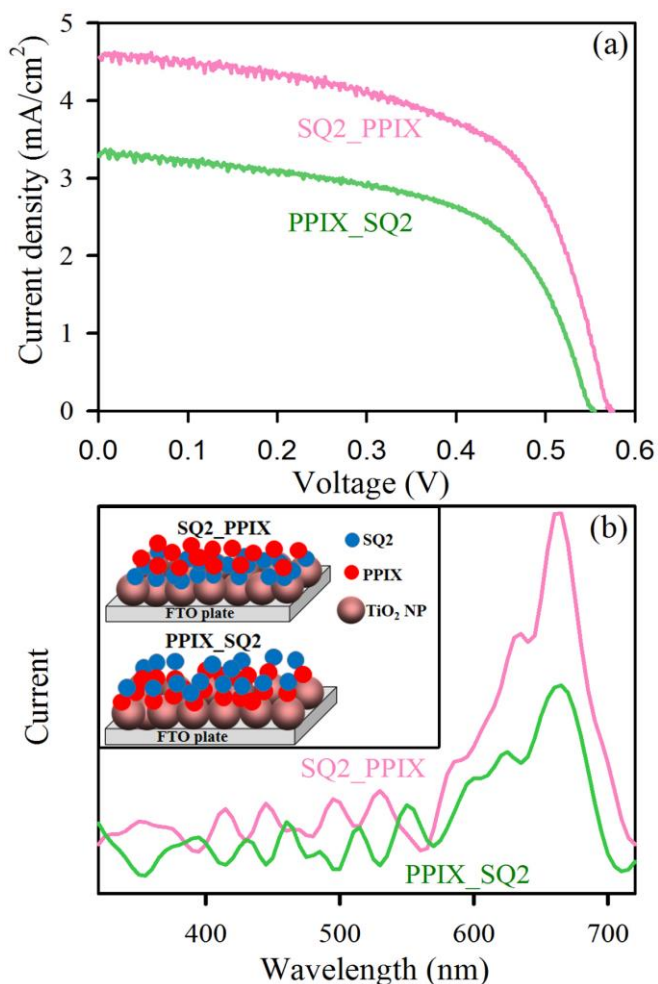


Figure 4.6. (a) I-V characteristics and (b) wavelength-dependent photocurrent response of the DSSCs for one-by-one dye sensitization. The inset shows the scheme of the sensitized photoanodes.

Table 4.5. Performances of DSSCs using one-by-one sensitization of SQ2 and PPIX.

SAMPLE	FF (%)	V _{oc} (V)	J _{sc} (mA/cm ²)	η (%)
SQ2 (12hrs)-PPIX (12hrs)	59	0.58	4.6	1.58
PPIX (12hrs) -SQ2 (12hrs)	59	0.55	3.3	1.09

4.2.2. Inversion of Activity in DSSC for TiO₂ and ZnO Photo-anodes Depending on the Choice of Sensitizer and Carrier Dynamics [57]: Figure 4.7a and 4.7b represents the absorption spectra of N719-ZnO, N719-TiO₂, C343-TiO₂ and C343-ZnO conjugates in solvent ethanol. For a comparison, the absorption spectra of the dyes, ZnO and TiO₂ nanoparticle in solvent ethanol are shown in the Figure 4.7a and 4.7b. It is evident from the absorption spectra that the band gap emission of

TiO₂ and ZnO in ethanol is observed at 330 nm and 363 nm respectively. In case of N719-ZnO the band gap absorption peak of ZnO absorbs at the same wavelength as that of bare ZnO. In the case of N719-TiO₂ hybrid the band gap absorption of TiO₂ appears at 337 nm. On the other hand, for C343-ZnO the band gap absorption of ZnO is observed to be at 357 nm. Due to the scattering of the TiO₂ and ZnO systems the 6-7 nm shift in peak position can't be concluded with some physical interpretation. Change in scattering may generate the pseudo shift in the peak position. The signature of the metal to ligand charge transfer (MLCT) peaks of the sensitizer N719 at 528 nm prominent in the absorption spectra of the N719-TiO₂ and N719-ZnO conjugates. Due to enhanced scattering in the conjugates the dye

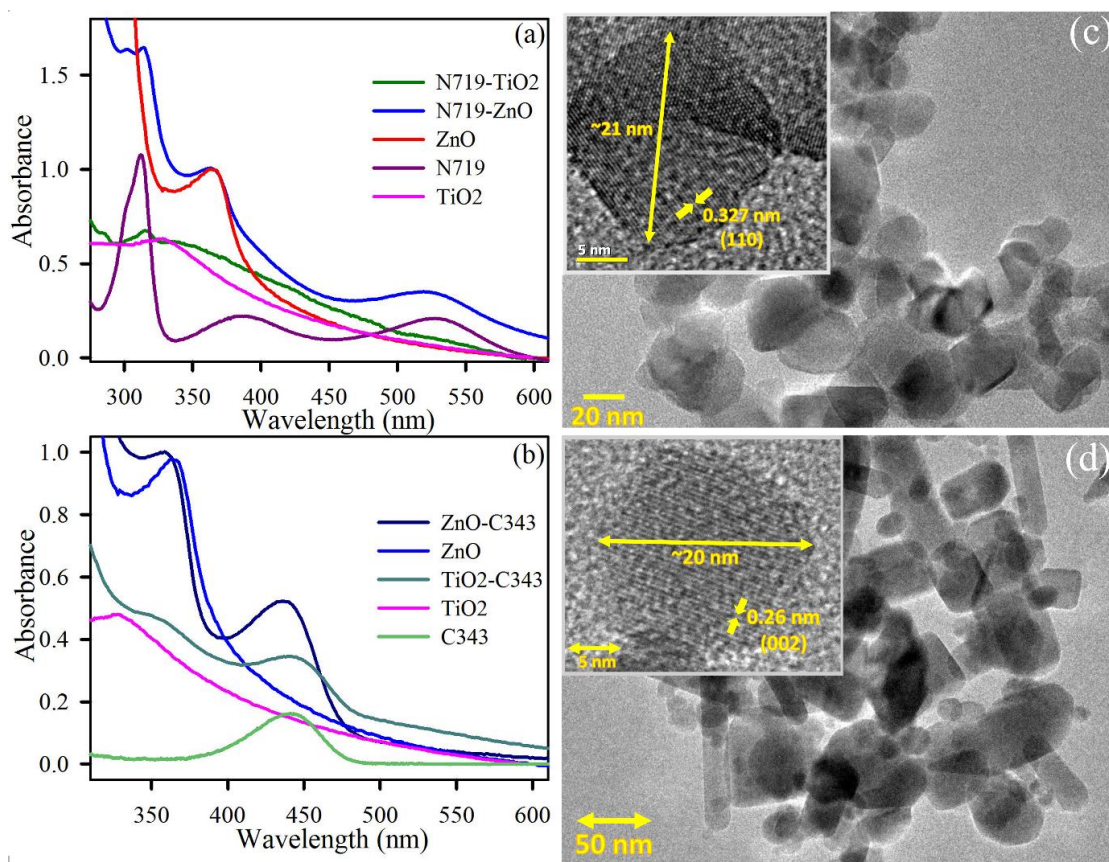


Figure 4.7. (a) Absorption spectra of N719 dye and the corresponding dye-semiconductor conjugates in the solvent ethanol, inset shows the N719 dye structure, (b) absorption spectra of C343 dye and the corresponding dye-semiconductor conjugates in solvent ethanol, inset shows the C343 dye structure, (c) TEM images of TiO₂ nanoparticles dispersed in ethanol. Inset shows the HRTEM image of TiO₂ nanoparticle, (d) TEM images of ZnO nanoparticles dispersed in ethanol. Inset shows the HRTEM image of ZnO nanoparticle.

peaks are not very prominent but comparing the absorption spectra of the conjugates with the only TiO₂ and ZnO nanoparticles the differences at the dye absorption positions are visible. The π - π^* absorption band of N719 in UV range at 311 nm with a shoulder at 300 nm is also present in the conjugates. Thus, in the N719-TiO₂ and N719-ZnO conjugate both the characteristic absorption peaks of the sensitizer and semiconductor are present. The same is true for the C343-ZnO and C343-TiO₂ conjugates also. In Figure 4.7c and 4.7d, the TEM images of the TiO₂ and ZnO nanoparticles are shown. The inset of each figure shows the HRTEM images of the TiO₂ and ZnO NP respectively. The average size of both the ZnO and TiO₂ NP is ~20 nm. The high crystallinity of the nanoparticles are evident from the HRTEM images. The inter-planar distance between the fringes of TiO₂ NP is found to be around 0.327 nm which represents the (110) plane of the crystal. The same for ZnO is observed to be around 0.26 nm which corresponds to the (002) plane of the crystal.

The quenching in the steady-state emission of the sensitizer C343 upon attachment to the semiconductors ZnO and TiO₂ are shown in Figure 4.8a. Both the emission peak of C343 at 480 nm and the excitation peak at 440 nm are observed to be decreased in intensity upon attachment to the semiconductor surface. As shown in the inset of Figure 4.7b, the sensitizer has a carboxylate (-COO⁻) functional group which gets attached to the oxygen vacancy centers of ZnO and TiO₂. Excited state electron transfer from the LUMO of the sensitizer to the CB of the semiconductor quenches the steady-state emission and excitation intensity of the semiconductor. The electron transfer process is further evident from the time resolved fluorescence decays of free C343, C343-ZnO and C343-TiO₂ conjugates as shown in Figure 4.8b. The summarized excited state lifetimes in the Table 4.6 reveals that the fluorescence timescale of the sensitizer C343 in ethanol is 3.8 ns. Upon attachment to ZnO, the excited state lifetime shows a two exponential decay pattern. The radiative lifetime of the C343-ZnO conjugate is 3.5 ns which is

almost the same as that of the free C343 in ethanol. Additionally, a 300 ps faster time constant is there for the C343-ZnO system which is responsible for the electron transfer from the sensitizer to the CB of ZnO. The similar two exponential decay pattern is observed for the C343-TiO₂ system as well. The electron transfer timescale is much faster (100 ps) in C343-TiO₂ than its ZnO counterpart. Although there are much controversy in the available literature regarding the explanation of physical origin for the delayed electron transfer time scale in ZnO than TiO₂ from other sensitizers [45, 51]. According to recent theoretical studies, the faster electron transfer from C343 to TiO₂ than ZnO can be ascribed to the higher density of states near the CB of TiO₂ than ZnO [44].

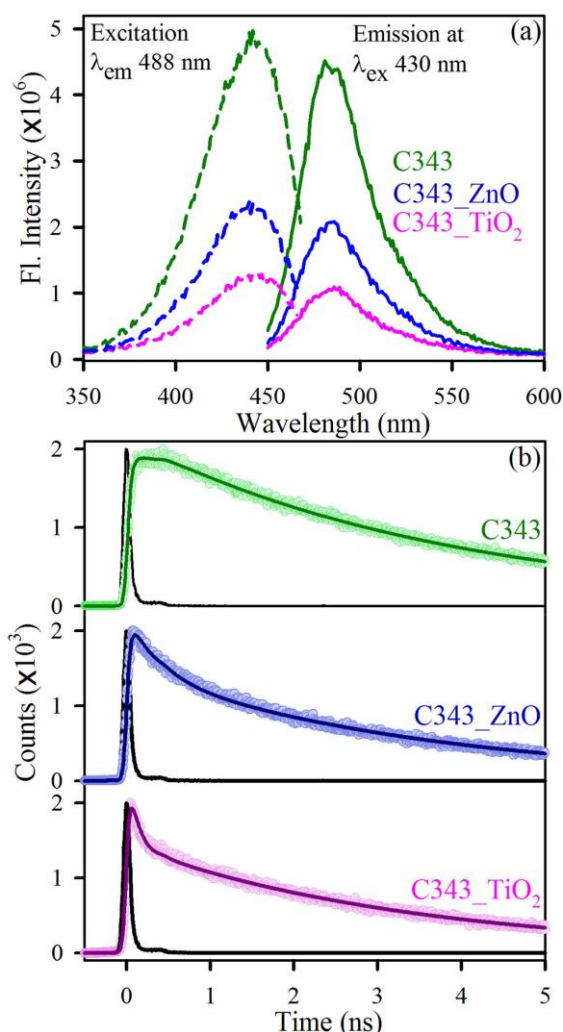


Figure 4.8: (a) Excitation and steady-state emission spectra of the dye C343, C343-ZnO and C343-TiO₂ conjugates in solvent ethanol, (b) picosecond-resolved fluorescence decays of C343 dye and corresponding dye-semiconductor conjugates in ethanol.

Table 4.6. Dynamics of picosecond-resolved fluorescence transients of the dye C343 and its conjugates with TiO₂ and ZnO in the solvent ethanol.^c

Sample	Excitation wavelength (nm)	Emission wavelength (nm)	τ_1 (ns)	τ_2 (ns)
C343	409	495	3.8 ± 0.10 (100%)	
C343-ZnO	409	495	3.5 ± 0.20 (60%)	0.3 ± 0.02 (40%)
C343-TiO ₂	409	495	3.5 ± 0.10 (47%)	0.3 ± 0.02 (53%)

^cNumbers in parentheses indicate relative weights.

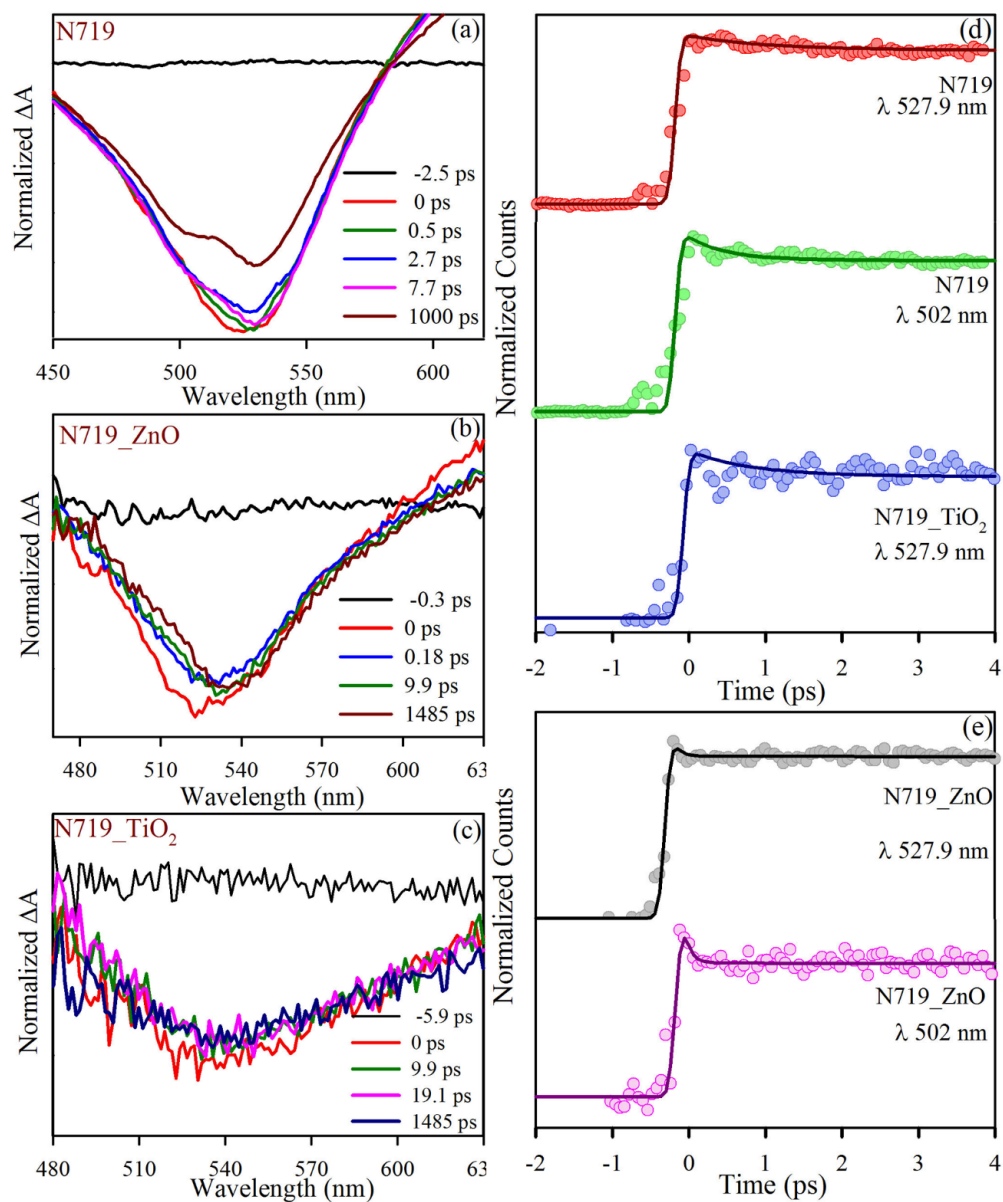


Figure 4.9. Transient absorption of (a) N719 dye, (b) N719-ZnO and (c) N719-TiO₂ conjugates in ethanol solution. (d) and (e) show the kinetics of the transient absorption data of the respective samples.

Table 4.7. Dynamics of femtosecond resolved transient absorption spectra of the dye N719 and its conjugates with TiO₂ and ZnO in the solvent ethanol.^c

Sample	Pump wavelength (nm)	Monitored wavelength (nm)	τ_1 (ps)	τ_2 (ps)
N719	400	527.9	1.00 (9%)	550 (91%)
N719	400	502	0.50 (18%)	550 (81%)
N719-ZnO	400	527.9	0.08 (23%)	1000 (77%)
N719-ZnO	400	502	0.08 (50%)	550 (50%)
N719-TiO ₂	400	527.9	0.80 (16%)	800 (84%)
N719	400	527.9	1.00 (9%)	550 (91%)

^cNumbers in parentheses indicate relative weights.

Figure 4.9 shows the transient absorption spectra of the sensitizer N719 in solvent ethanol along with its conjugates N719-TiO₂ and N719-ZnO at different delay time. The timescales of transient absorption kinetics at different wavelength for different samples are tabulated in Table 4.7. The longer time components for the ground state recovery of the three systems are consistent with earlier reported literature [58-60] and has been confirmed from a longer timescale fitting also. As shown in the Figure 4.9b and 4.9c, the signal to noise ratio of the N719-TiO₂ and N719-ZnO was poor than the only N719 system because of lower solubility of the dye-semiconductor system than only dye. The transient absorption kinetics at the absorption peak of the monomer at 527.9 nm shows that the faster time component of the ground state recovery of the dye N719 is ~1 ps where as that of the high energy aggregation peak around 502 nm is 500 fs. From this observation it is evident that the ground state recovery time scale of the aggregated N719 form is faster. Upon attachment to ZnO the ground state recovery of the monomer at 527.9 nm and the aggregated form at 502 nm both occurs at a much faster timescale of 80 fs which implies that after attachment on the ZnO surface the ground state recovery becomes faster. The N719-TiO₂ does not show any such faster time scale. This observation infers that the aggregated form of the sensitizer N719 on the ZnO surface are shuttling back the electrons to the ground state at a much faster rate. There is also a possibility that the aggregated form of N719

sensitizer is retracting back the electrons from the CB of ZnO followed by a recombination at the ground state of the monomer. Thus, the aggregates can pull back the injected electrons from the N719 monomer to ZnO which may lead to a lower light harvesting efficiency.

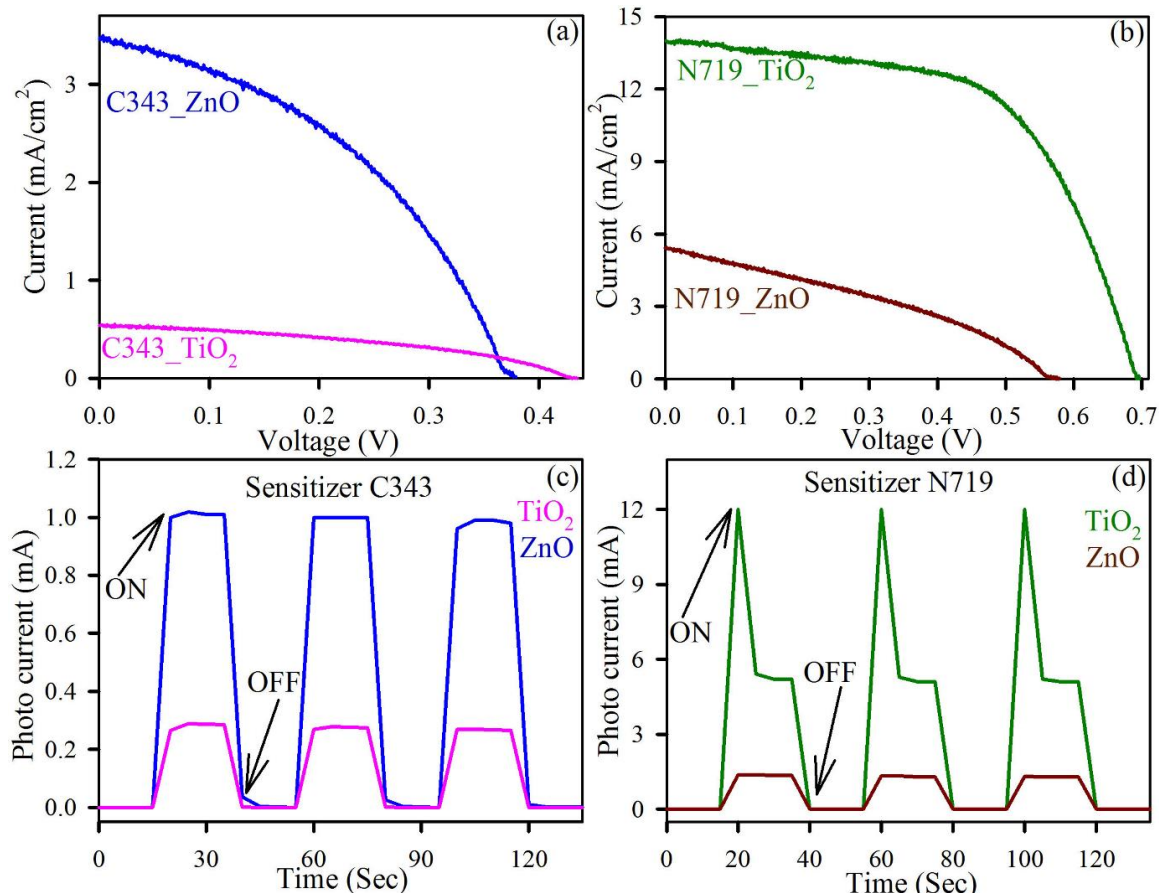


Figure 4.10. Current (I)-Voltage (V) characteristics for (a) C343 dye sensitized ZnO and TiO₂ photoanode based DSSCs, (b) N719 dye sensitized ZnO and TiO₂ photoanode based DSSCs, comparison of photocurrent vs time response for repeated light on and off for (c) C343 sensitized DSSCs and (d) N719 sensitized DSSCs with TiO₂ and ZnO photoanodes.

In order to investigate the performance of the fabricated DSSCs, the current (I)-voltage (V) characteristics of the cells are measured as shown in Figure 4.10a and Figure 4.10b. The I-V measurement details are summarized in Table 4.8 in details. It is evident that for the C343 sensitizer the ZnO photoanode shows a better efficiency than TiO₂. On the other hand, for the N719 sensitizer there is a reversal of efficiency trend for ZnO and TiO₂ photoanodes. The trend in the photocurrent response is consistent with the short circuit current of the

corresponding cell as shown in Figure 4.10c and 4.10d.

Table 4.8. Current (I)-voltage (V) characteristics of fabricated DSSCs.

Sensitizer	Photoanode material	FF (%)	V _{oc} (V)	J _{sc} (mA/cm ²)	η (%)
C343	TiO ₂	42 ± 1	0.44 ± 0.02	0.5 ± 0.1	0.1 ± 0.1
C343	ZnO	41 ± 2	0.38 ± 0.01	3.5 ± 0.2	0.5 ± 0.1
N719	TiO ₂	58 ± 1	0.70 ± 0.04	14.0 ± 0.4	5.6 ± 0.4
N719	ZnO	35 ± 1	0.58 ± 0.06	5.4 ± 0.3	1.1 ± 0.1

Numbers in parentheses indicate relative weights.

The photocurrent versus time response upon switching on and off the light source confirms the repeatability of the measurement and stability of the device. It can be observed from the Table 4.8 that for the C343 sensitizer the fill factor and open circuit potential (V_{oc}) of the cells are not much different from each other. The only difference is order of magnitude lower short circuit current (J_{sc}) density in case of TiO₂ photoanode. For the sensitizer N719 the fill factor and photocurrent both are much lower in ZnO than TiO₂. According to the earlier reports, the lower fill factor in ZnO-N719 is due to increased recombination rate with increasing applied potential [61]. Still, there has been much controversy in the available literature regarding the lower photocurrent in ZnO-N719 than the TiO₂-N719. The electron injection efficiency is known to be similar from N719 to ZnO and TiO₂. Thus, the investigation of the back electron transfer processes is impotent to infer some conclusion about the mechanism. The possible reasons for lower photocurrent in TiO₂-C343 are lower injection efficiency, poor dye loading or faster back electron recombination. All these possibilities are experimentally investigated in this study. From the time resolved fluorescence decays we have shown that the electron injection efficiency is better from C343 to TiO₂ than ZnO. Thus, unwanted back electron recombination and dye loading are the other two probable explanation which we have experimentally investigated and explained in the following section.

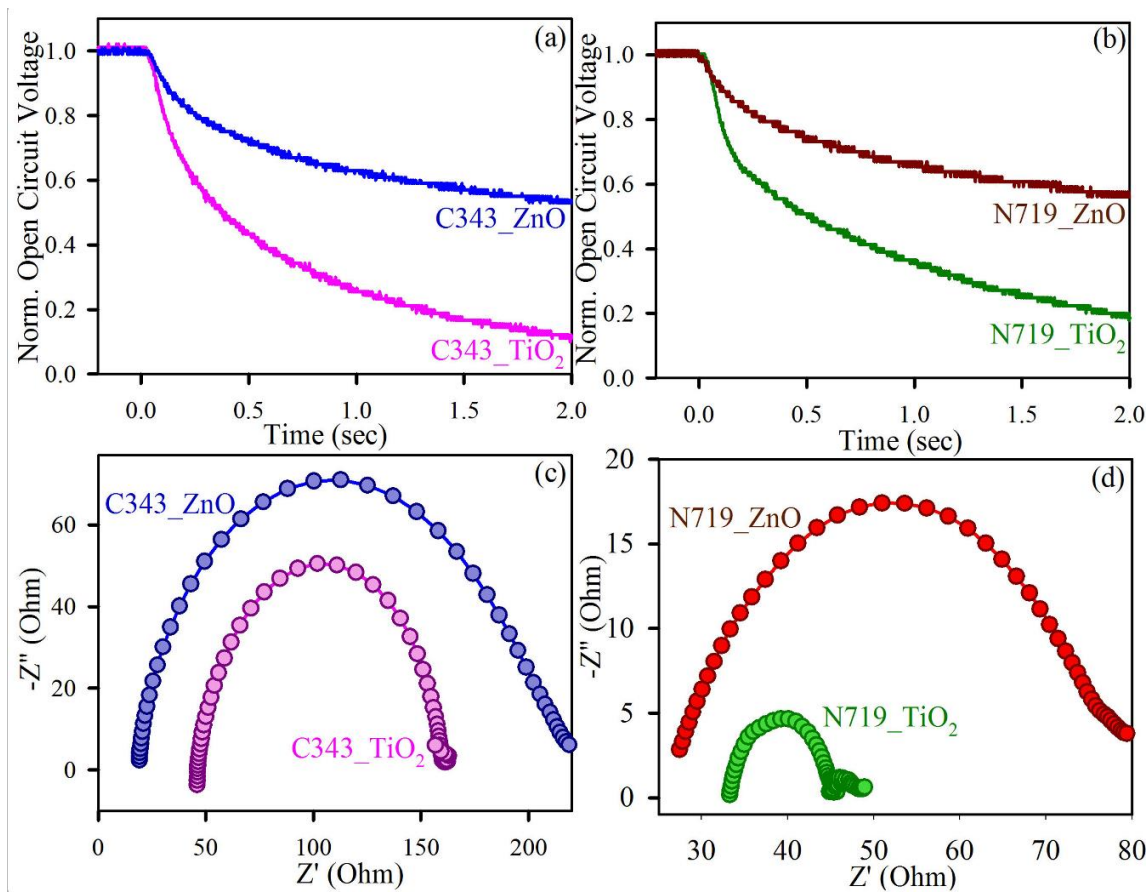


Figure 4.11. Normalized open circuit potential decay in (a) C343 sensitized DSSCs with TiO₂ and ZnO photoanodes, (b) N719 sensitized DSSCs with TiO₂ and ZnO photoanodes, (c) EIS of the devices (c) Nyquist plot for C343 sensitized DSSCs and (d) Nyquist plot for N719 sensitized DSSCs.

To investigate the rate of back electron recombination (BER) depending on the photoanode material and choice of sensitizer, we have performed the open circuit potential decay for different cells in the dark following an irradiation under 1 Sun. The results are represented in Figure 4.11a and 4.11b. Upon illumination, the photoexcited electrons are injected from the HOMO of the sensitizer to the conduction band of the semiconductor of the photoanode. The electrons accumulated into the CB of semiconductor drives the Fermi level towards negative potential which reflects in the enhancement of photovoltage. The forward electron injection process is terminated upon switching off the illumination. Then the electrons start discharging through the back electron recombination to the oxidized state of the electrolyte. The open circuit voltage decay reflects the

timescales for this recombination processes which usually occurs in second or millisecond time scale. Figure 4.11a and 4.11b show the decay profiles of different DSSCs fabricated using C343-ZnO, C343-TiO₂, N719-ZnO and N719-TiO₂ photoanodes. It is evident from the photovoltage decay profiles that for both the sensitizer C343 and N719 the ZnO photoanode show a slower decay profile than the TiO₂ counterpart. Thus, ZnO can be referred as a better photoanode material in terms of back electron recombination for both the sensitizers.

Table 4.9. EIS parameters of DSSCs fabricated using different active electrodes.

Active Electrode	R _s (Ω)	R ₁ (Ω)	R ₂ (Ω)
TiO ₂ -C343	45.5 ± 0.03	23.2 ± 0.03	94.6 ± 0.03
ZnO-C343	16.7 ± 0.04	82.5 ± 0.04	133.0 ± 0.04
TiO ₂ -N719	33.56 ± 0.01	4.2 ± 0.01	6.6 ± 0.01
ZnO-N719	23.9 ± 0.08	18.2 ± 0.08	41.3 ± 0.08

The similar trend of photovoltage decay can be observed in the electrochemical impedance spectroscopy (EIS) results as shown in Figure 4.11c and 4.11d. The details of the impedance spectra for DSSC and fitting circuits are shown in our earlier publication [62]. All the fitting parameters of the EIS data are summarized in Table 4.9. The R_s, R₁ and R₂ values correspond to the film resistance of photoanode, the charge transfer resistance at the counter electrode interface and interfacial resistance of electron recombination at semiconductor-electrolyte interface respectively. Both the R₁ and R₂ values are higher for the ZnO photoanodes than TiO₂ for sensitizers C343 and N719 which implies that the back electron recombination process at above mentioned interfaces are slower in case of ZnO. This observation is consistent with the open circuit potential decay trends. The film resistance is observed to be higher in case of TiO₂ than ZnO due to lower electron mobility in case of TiO₂. From the detail investigation of the back electron transfer process both from open circuit potential decay and EIS results, it is evident that the higher efficiency in ZnO cells than TiO₂ in case of C343 can be

referred as an effect of slower back electron recombination in the first one. But the mechanism of the reversal of efficiency trend in case of N719 sensitizer can't be explained from back electron recombination study because ZnO-N719 photoanode is better in terms of BER than TiO₂-N719.

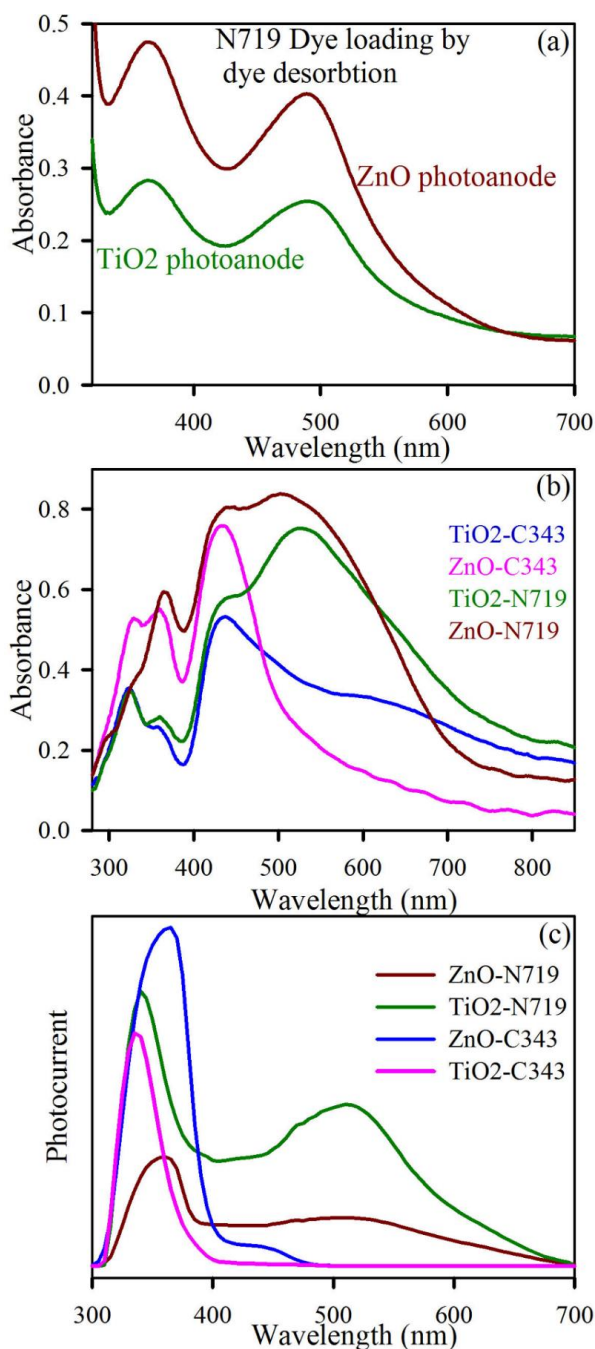
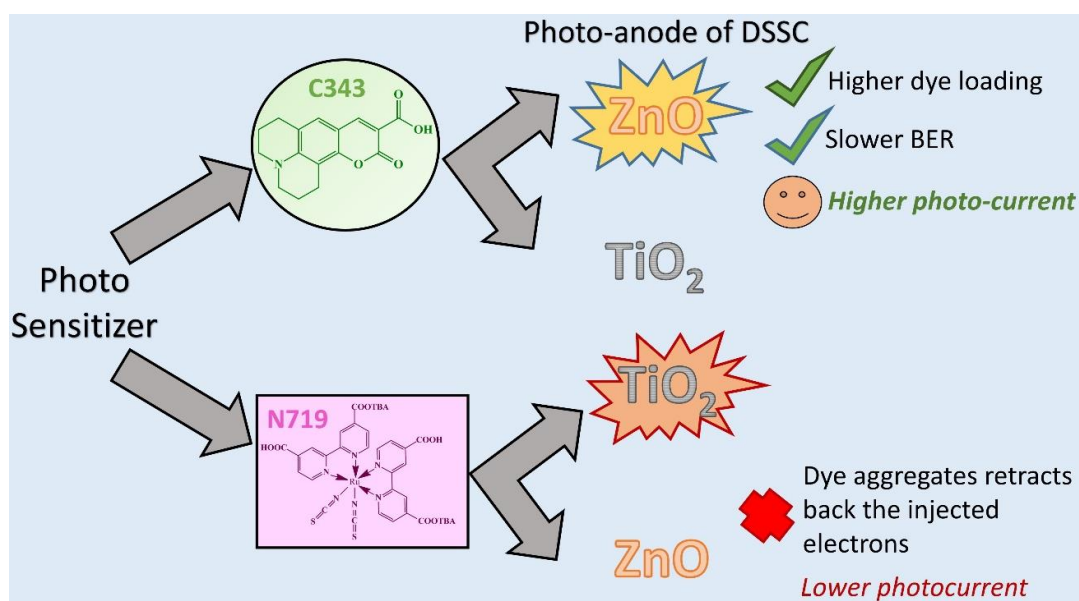


Figure 4.12. (a) Dye loading of N719 sensitized photoanodes by dye desorption with basic solution (pH 10). (b) Retro-reflecting mode absorption of the TiO₂ and ZnO photoanodes sensitized by C343 and N719 dyes. (c) Photocurrent vs wavelength of incident light for different devices.

To further explore the mechanism of efficiency trend in fabricated DSSCs, the dye loading experiment was performed initially in conventional dye desorption method using a NaOH solution of pH 10. N719 dye was completely desorbed from the TiO₂ and ZnO photoanodes and the absorption of the desorbed dye is shown in Figure 4.12a. It is clear that the dye loading in the ZnO photoanode is higher than that of TiO₂. However, the organic dye C343 could not be dissolved completely by the same basic solution. Thus, for the better comparison of dye loading, we have performed the retro reflecting mode absorption spectra of the photoanodes as shown in Figure 4.12b. The spectra represents that there is higher dye loading in ZnO for both the sensitizers than TiO₂. Thus, for sensitizer C343, the higher photocurrent in ZnO cells can be correlated with the higher dye loading. But the N719 dye absorption is observed to be broadened at blue side of the monomeric absorption peak for ZnO. The monomeric N719 peak is prominent on TiO₂ photoanodes at 527 nm. But on ZnO photoanode there are prominent absorption signature at 502 nm and 436 nm which can be ascribed to the formation of H-type aggregate of N719 dye on ZnO surface. The signature of high energy absorbing and less harvesting H-aggregates on the photoanode surface are widely reported for other dyes in the previously available literature [47, 63, 64]. H-aggregates are higher energy aggregates with lower electron injection efficiency. Additionally, these type of aggregates can shuttle back the injected electrons from the CB of ZnO to the ground state of the monomer as observed from the transient absorption spectra also. This phenomena is further confirmed from the wavelength dependent photocurrent spectra as shown in Figure 4.12c. The wavelength dependent photocurrent represents the similar response at TiO₂ band gap region (~340 nm) for TiO₂-C343 and TiO₂-N719 photoanodes. As the film thickness is same for both the photoanodes, the photocurrent at the band gap region should be same for both the sensitizers. But for ZnO photoanodes, significantly lower photocurrent is observed at the ZnO band gap region (~360 nm) for the N719 sensitizer than that of C343. Additionally,

the N719 dye monomer peak around 520 nm is observed to be harvesting in higher photocurrent while the peak positions in the aggregates on ZnO photoanodes are not observed to take part in the photocurrent generation as depicted in Figure 4.12c. Both this observation confirms that the unwanted aggregates on the ZnO surface of the photoanodes not only does not participate in light harvesting, these are capable of attracting back the injected electrons from the CB of the ZnO. Thus, photocurrent at the N719 dye monomer peak ~ 520 nm and at ZnO band gap region ~ 360 nm both are lower due to the formation of the H-type aggregates. It can be inferred that the H-type aggregate of the sensitizer N719 on the ZnO surface is responsible for the lower photocurrent than TiO₂ cells. We propose that the presence of Ru (II) in the dye can facilitate to form an aggregate at the ZnO surface because of the presence of the Zn (II) vacancy states. The entire mechanism has been depicted schematically in Scheme 4.2.



Scheme 4.2. Inversion in efficiency of TiO₂ and ZnO photo-anode based DSSC depending on the choice of sensitizer

4.3. Conclusion: Detailed studies of the dynamics between the organic dyes PPIX and SQ2 have been performed using ultrafast spectroscopy and FRET was observed from the donor PPIX to the acceptor SQ2. DSSCs have been fabricated by co-sensitizing the photoanodes with mixtures of these two dyes, to achieve a

reasonably good spectral match between the combined absorption of these two dyes and solar light. The I-V measurement data exhibit a higher efficiency for the co-sensitized DSSCs than the single dye sensitized DSSCs. A significantly enhanced photocurrent was obtained from the co-sensitized DSSCs at a particular ratio of the two sensitizers due to efficient dipole-dipole coupling. From the wavelength dependent photocurrent measurement, it has been observed that PPIX is successfully playing the role of an anti-aggregating agent of SQ2 in the co-sensitized DDSC and consequently increasing the light harvesting in the red/ NIR region compare to DSSC sensitized by the only SQ2. The use of any additional co-adsorbent is not needed in the proposed co-sensitization because PPIX is behaving simultaneously as a co-sensitizer and co-adsorbent. Thus, it can be asserted that PPIX has an impressive potential to increase the efficiency of a DDSC being a co-sensitizer with NIR absorbing SQ2 dye. Because the three essential requirements of efficient light harvesting i.e. FRET, increased absorption window and suppression of aggregation, are concurrently fulfilled by PPIX.

Additionally, we have established a mechanistic explanation for the higher efficiency in ZnO DSSC than TiO₂ for the organic sensitizer C343 and the reverse efficiency in Ru based dye N719. From the picosecond-resolved fluorescence decays it is observed that the forward electron injection efficiency is faster from C343 to TiO₂ than to ZnO. Thus, the slower back electron recombination (BER) and higher dye loading is responsible for the higher photocurrent in C343-ZnO cells which eventually increases the overall efficiency. The photovoltage decay, electro-chemical impedance spectroscopy (EIS), and absorption spectra of photoanode measurements reveal that slower BER and higher dye loading is applicable for N719-ZnO also compared to its TiO₂ counterpart. The retro reflecting mode absorption spectra of the ZnO photoanodes concludes the presence of a high energy absorbing H-type aggregate of N719 dye on ZnO photoanode surface. From transient absorption spectra and wavelength

dependent photocurrent measurement it was evident that this type of aggregate can't inject electrons to the CB of ZnO. Additionally, this aggregate has been observed to retract back the injected electrons from the ZnO CB which reduces the overall light harvesting at the absorption peak position of monomeric N719 and at the band gap absorption peak of ZnO as well. Thus, the formation of this H-type aggregate is mainly responsible for the lower efficiency in ZnO-N719 than that of TiO₂-N719 cells. In summary, this study provides a complete investigation of the inversion in efficiency for ZnO and TiO₂ photoanodes upon choice of sensitizer and the mechanism has been justified by ultrafast carrier dynamics and device characteristics as well.

References

- [1] S. Mathew, A. Yella, P. Gao, R. Humphry-Baker, B.F. Curchod, N. Ashari-Astani, I. Tavernelli, U. Rothlisberger, M.K. Nazeeruddin, M. Grätzel, Dye-sensitized solar cells with 13% efficiency achieved through the molecular engineering of porphyrin sensitizers, *Nat. Chem.*, 6 (2014) 242-247.
- [2] M. Grätzel, R.A. Janssen, D.B. Mitzi, E.H. Sargent, Materials interface engineering for solution-processed photovoltaics, *Nature*, 488 (2012) 304-312.
- [3] M. Grätzel, Recent advances in sensitized mesoscopic solar cells, *Acc. Chem. Res.*, 42 (2009) 1788-1798.
- [4] B. O'regan, M. Grätzel, A low-cost, high-efficiency solar cell based on dye-sensitized colloidal TiO₂ films, *Nature*, 353 (1991) 737-740.
- [5] H. Wang, B. Wang, J. Yu, Y. Hu, C. Xia, J. Zhang, R. Liu, Significant enhancement of power conversion efficiency for dye sensitized solar cell using 1D/3D network nanostructures as photoanodes, *Sci. Rep.*, 5 (2015) 9305.
- [6] X. Zhang, S.-T. Wang, Z.-S. Wang, Effect of metal-doping in TiO₂ on fill factor of dye-sensitized solar cells, *Appl. Phys. Lett.*, 99 (2011) 113503.
- [7] Y. Duan, N. Fu, Q. Liu, Y. Fang, X. Zhou, J. Zhang, Y. Lin, Sn-doped TiO₂ photoanode for dye-sensitized solar cells, *J. Phys. Chem. C*, 116 (2012) 8888-8893.
- [8] S.S. Mali, C.A. Betty, P.N. Bhosale, P.S. Patil, C.K. Hong, From nanocorals to nanorods to nanoflowers nanoarchitecture for efficient dye-sensitized solar cells at relatively low film thickness: All hydrothermal process, *Sci. Rep.*, 4 (2014) 5451.
- [9] J.-W. Shiu, Y.-C. Chang, C.-Y. Chan, H.-P. Wu, H.-Y. Hsu, C.-L. Wang, C.-Y. Lin, E.W.-G. Diau, Panchromatic co-sensitization of porphyrin-sensitized solar cells to harvest near-infrared light beyond 900 nm, *J. Mater. Chem. A*, 3 (2015) 1417-1420.
- [10] H.N. Tsao, C. Yi, T. Moehl, J.H. Yum, S.M. Zakeeruddin, M.K. Nazeeruddin, M. Grätzel, Cyclopentadithiophene bridged donor-acceptor dyes achieve high

power conversion efficiencies in dye-sensitized solar cells based on the tris-cobalt bipyridine redox couple, *ChemSusChem*, 4 (2011) 591-594.

[11] L.M. Gonçalves, V. de Zea Bermudez, H.A. Ribeiro, A.M. Mendes, Dye-sensitized solar cells: A safe bet for the future, *Energy Environ. Sci*, 1 (2008) 655-667.

[12] A. Connell, P.J. Holliman, M.L. Davies, C.D. Gwenin, S. Weiss, M.B. Pitak, P.N. Horton, S.J. Coles, G. Cooke, A study of dye anchoring points in half-squarylium dyes for dye-sensitized solar cells, *J. Mater. Chem. A*, 2 (2014) 4055-4066.

[13] R.Y.-Y. Lin, Y.-S. Yen, Y.-T. Cheng, C.-P. Lee, Y.-C. Hsu, H.-H. Chou, C.-Y. Hsu, Y.-C. Chen, J.T. Lin, K.-C. Ho, Dihydrophenanthrene-based metal-free dyes for highly efficient cosensitized solar cells, *Org. Lett.*, 14 (2012) 3612-3615.

[14] E. Stathatos, Dye sensitized solar cells as an alternative approach to the conventional photovoltaic technology based on silicon-recent developments in the field and large scale applications, Solar cells dye-sensitized devices, *InTech*, Rijeka, Croatia, 2011, 471-491.

[15] P.J. Holliman, M. Mohsen, A. Connell, M.L. Davies, K. Al-Salihi, M.B. Pitak, G.J. Tizzard, S.J. Coles, R.W. Harrington, W. Clegg, Ultra-fast co-sensitization and tri-sensitization of dye-sensitized solar cells with N719, SQ1 and triarylamine dyes, *J. Mater. Chem.*, 22 (2012) 13318-13327.

[16] L. Han, A. Islam, H. Chen, C. Malapaka, B. Chiranjeevi, S. Zhang, X. Yang, M. Yanagida, High-efficiency dye-sensitized solar cell with a novel co-adsorbent, *Energy Environ Sci*, 5 (2012) 6057-6060.

[17] M. Kimura, H. Nomoto, N. Masaki, S. Mori, Dye molecules for simple co-sensitization process: Fabrication of mixed-dye-sensitized solar cells, *Angew. Chem. Int. Ed.*, 51 (2012) 4371-4374.

[18] G. Sharma, M.K. Panda, M. Roy, J. Mikroyannidis, E. Gad, A. Coutsolelos, Significant enhancement in the power conversion efficiency of porphyrin based dye sensitized solar cell by co-sensitization with metal free dye, *J. Renew. Sustainable Energy*, 5 (2013) 023108.

- [19] C.H. Lee, S.A. Kim, M.R. Jung, K.-S. Ahn, Y.S. Han, J.H. Kim, Aggregation control of organic sensitizers for panchromatic dye co-sensitized solar cells, *Jpn. J. Appl. Phys.*, 53 (2014) 08NC04.
- [20] P.J. Holliman, M.L. Davies, A. Connell, B.V. Velasco, T.M. Watson, Ultra-fast dye sensitisation and co-sensitisation for dye sensitized solar cells, *Chem. Commun.*, 46 (2010) 7256-7258.
- [21] Z. Xue, L. Wang, B. Liu, Facile fabrication of co-sensitized plastic dye-sensitized solar cells using multiple electrophoretic deposition, *Nanoscale*, 5 (2013) 2269-2273.
- [22] B.E. Hardin, A. Sellinger, T. Moehl, R. Humphry-Baker, J.-E. Moser, P. Wang, S.M. Zakeeruddin, M. Grätzel, M.D. McGehee, Energy and hole transfer between dyes attached to titania in cosensitized dye-sensitized solar cells, *J. Amer. Chem. Soc.*, 133 (2011) 10662-10667.
- [23] J.I. Basham, G.K. Mor, C.A. Grimes, Förster resonance energy transfer in dye-sensitized solar cells, *ACS Nano*, 4 (2010) 1253-1258.
- [24] H. Choi, P.K. Santra, P.V. Kamat, Synchronized energy and electron transfer processes in covalently linked CdSe-squaraine dye-TiO₂ light harvesting assembly, *ACS nano*, 6 (2012) 5718-5726.
- [25] S. Sarkar, A. Makhil, K. Lakshman, T. Bora, J. Dutta, S. Kumar Pal, Dual-sensitization via electron and energy harvesting in CdTe quantum dots decorated ZnO nanorod-based dye-sensitized solar cells, *J. Phys. Chem. C*, 116 (2012) 14248-14256.
- [26] S. Das, T.L. Thanulingam, K.G. Thomas, P.V. Kamat, M. George, Photochemistry of squaraine dyes. 5. Aggregation of bis(2,4-dihydroxyphenyl) squaraine and bis(2,4,6-trihydroxyphenyl) squaraine and their photodissociation in acetonitrile solutions, *J. Phys. Chem.*, 97 (1993) 13620-13624.
- [27] S. Das, K.G. Thomas, K. Thomas, V. Madhavan, D. Liu, P.V. Kamat, M. George, Aggregation behavior of water soluble bis(benzothiazolylidene) squaraine derivatives in aqueous media, *J. Phys. Chem.*, 100 (1996) 17310-17315.

- [28] J.-H. Yum, P. Walter, S. Huber, D. Rentsch, T. Geiger, F. Nüesch, F. De Angelis, M. Grätzel, M.K. Nazeeruddin, Efficient far red sensitization of nanocrystalline TiO₂ films by an unsymmetrical squaraine dye, *J. Amer. Chem. Soc.*, 129 (2007) 10320-10321.
- [29] J. Li, W. Wu, J. Yang, J. Tang, Y. Long, J. Hua, Effect of chenodeoxycholic acid (CDCA) additive on phenothiazine dyes sensitized photovoltaic performance, *Sci China Chem*, 54 (2011) 699-706.
- [30] G.D. Sharma, R. Kurchania, R.J. Ball, M.S. Roy, J.A. Mikroyannidis, Effect of deoxycholic acid on the performance of liquid electrolyte dye-sensitized solar cells using a perylene monoimide derivative, *Int. J. Photoenergy*, 2012 (2012) 1-7.
- [31] P. Kar, T.K. Maji, P.K. Sarkar, S. Sardar, S.K. Pal, Direct observation of electronic transition-plasmon coupling for enhanced electron injection in dye-sensitized solar cells, *RSC Adv.*, 6 (2016) 98753-98760.
- [32] L.-Y. Lin, M.-H. Yeh, C.-P. Lee, J. Chang, A. Baheti, R. Vittal, K.J. Thomas, K.-C. Ho, Insights into the co-sensitizer adsorption kinetics for complementary organic dye-sensitized solar cells, *J. Power Sources*, 247 (2014) 906-914.
- [33] J. Chang, C.-P. Lee, D. Kumar, P.-W. Chen, L.-Y. Lin, K.J. Thomas, K.-C. Ho, Co-sensitization promoted light harvesting for organic dye-sensitized solar cells using unsymmetrical squaraine dye and novel pyrenoimidazole-based dye, *J. Power Sources*, 240 (2013) 779-785.
- [34] A. Yella, H.-W. Lee, H.N. Tsao, C. Yi, A.K. Chandiran, M.K. Nazeeruddin, E.W.-G. Diau, C.-Y. Yeh, S.M. Zakeeruddin, M. Grätzel, Porphyrin-sensitized solar cells with cobalt(II/III)-based redox electrolyte exceed 12 percent efficiency, *science*, 334 (2011) 629-634.
- [35] K. Lee, S.W. Park, M.J. Ko, K. Kim, N.-G. Park, Selective positioning of organic dyes in a mesoporous inorganic oxide film, *Nat. Mater.*, 8 (2009) 665.
- [36] M. Grätzel, Dye-sensitized solar cells, *J. Photochem. Photobiol. C*, 4 (2003) 145-153.

- [37] M. Grätzel, Recent advances in sensitized mesoscopic solar cells, *Acc. Chem. Res.*, 42 (2009) 1788-1798.
- [38] M. Borgwardt, M. Wilke, T. Kampen, S. Mähl, M. Xiao, L. Spiccia, K.M. Lange, I.Y. Kiyon, E.F. Aziz, Charge transfer dynamics at dye-sensitized ZnO and TiO₂ interfaces studied by ultrafast XUV photoelectron spectroscopy, *Sci. Rep.*, 6 (2016) 24422.
- [39] D.C. Look, D.C. Reynolds, J. Sizelove, R. Jones, C.W. Litton, G. Cantwell, W. Harsch, Electrical properties of bulk ZnO, *Solid State Commun.*, 105 (1998) 399-401.
- [40] Z.L. Wang, Nanostructures of zinc oxide, *Mater. Today*, 7 (2004) 26-33.
- [41] N. Memarian, I. Concina, A. Braga, S.M. Rozati, A. Vomiero, G. Sberveglieri, Hierarchically assembled ZnO nanocrystallites for high-efficiency dye-sensitized solar cells, *Angew. Chem.*, 123 (2011) 12529-12533.
- [42] D. Stockwell, Y. Yang, J. Huang, C. Anfuso, Z. Huang, T. Lian, Comparison of electron-transfer dynamics from coumarin 343 to TiO₂, SnO₂, and ZnO nanocrystalline thin films: Role of interface-bound charge-separated pairs, *J. Phys. Chem. C*, 114 (2010) 6560-6566.
- [43] C. Bauer, G. Boschloo, E. Mukhtar, A. Hagfeldt, Electron injection and recombination in Ru(dcbpy)₂(NCS)₂ sensitized nanostructured ZnO, *J. Phys. Chem. B*, 105 (2001) 5585-5588.
- [44] H. Wei, J.-W. Luo, S.-S. Li, L.-W. Wang, Revealing the origin of fast electron transfer in TiO₂-based dye-sensitized solar cells, *J. Am. Chem. Soc.*, 138 (2016) 8165-8174.
- [45] R. Katoh, A. Furube, T. Yoshihara, K. Hara, G. Fujihashi, S. Takano, S. Murata, H. Arakawa, M. Tachiya, Efficiencies of electron injection from excited N3 dye into nanocrystalline semiconductor (ZrO₂, TiO₂, ZnO, Nb₂O₅, SnO₂, In₂O₃) films, *J. Phys. Chem. B*, 108 (2004) 4818-4822.
- [46] R. Katoh, A. Furube, K. Hara, S. Murata, H. Sugihara, H. Arakawa, M. Tachiya, Efficiencies of electron injection from excited sensitizer dyes to

nanocrystalline ZnO films as studied by near-IR optical absorption of injected electrons, *J. Phys. Chem. B*, 106 (2002) 12957-12964.

[47] H. Horiuchi, R. Katoh, K. Hara, M. Yanagida, S. Murata, H. Arakawa, M. Tachiya, Electron injection efficiency from excited N₃ into nanocrystalline ZnO films: Effect of (N₃-Zn²⁺) aggregate formation, *J. Phys. Chem. B*, 107 (2003) 2570-2574.

[48] M. Giannouli, M. Fakis, Interfacial electron transfer dynamics and photovoltaic performance of TiO₂ and ZnO solar cells sensitized with Coumarin 343, *J. Photochem. Photobiol. A Chem.*, 226 (2011) 42-50.

[49] M. Senevirathne, P. Pitigala, V. Sivakumar, P. Jayaweera, A. Perera, K. Tennakone, Sensitization of TiO₂ and ZnO nanocrystalline films with acriflavine, *J. Photochem. Photobiol. A Chem.*, 195 (2008) 364-367.

[50] E. Guillén, F. Casanueva, J. Anta, A. Vega-Poot, G. Oskam, R. Alcántara, C. Fernández-Lorenzo, J. Martín-Calleja, Photovoltaic performance of nanostructured zinc oxide sensitised with xanthene dyes, *J. Photochem. Photobiol. A Chem.*, 200 (2008) 364-370.

[51] P. Tiwana, P. Docampo, M.B. Johnston, H.J. Snaith, L.M. Herz, Electron mobility and injection dynamics in mesoporous ZnO, SnO₂, and TiO₂ films used in dye-sensitized solar cells, *ACS nano*, 5 (2011) 5158-5166.

[52] Q. Zhang, T.P. Chou, B. Russo, S.A. Jenekhe, G. Cao, Aggregation of ZnO nanocrystallites for high conversion efficiency in dye-sensitized solar cells, *Angew. Chem.*, 120 (2008) 2436-2440.

[53] J. Patwari, S. Sardar, B. Liu, P. Lemmens, S.K. Pal, Three-in-one approach towards efficient organic dye-sensitized solar cells: aggregation suppression, panchromatic absorption and resonance energy transfer, *Beilstein J. Nanotechnol.*, 8 (2017) 1705-1713.

[54] P.K. Sarkar, N. Polley, S. Chakrabarti, P. Lemmens, S.K. Pal, Nano-surface energy transfer based highly selective and ultrasensitive "Turn on" fluorescence mercury sensor, *ACS Sensors*, 1 (2016) 789-797.

- [55] S. Leach, H. Scheraga, Effect of light scattering on ultraviolet difference spectra¹, *J. Amer. Chem. Soc.*, 82 (1960) 4790-4792.
- [56] X. Ren, Q. Feng, G. Zhou, C.-H. Huang, Z.-S. Wang, Effect of cations in coadsorbate on charge recombination and conduction band edge movement in dye-sensitized solar cells, *J. Phys. Chem. C*, 114 (2010) 7190-7195.
- [57] J. Patwari, S. Shyamal, T. Khan, H. Ghadi, C. Bhattacharya, S. Chakrabarti, S.K. Pal, Inversion of activity in DSSC for TiO₂ and ZnO photo-anodes depending on the choice of sensitizer and carrier dynamics, *J. Lumin.*, 207 (2019) 169-176.
- [58] L.-H. Yu, J.-Y. Xi, K.C. Lo, L.J. Antrobus, D.L. Phillips, W.K. Chan, Transient absorption of N719 and its electron transfer kinetics on ZnO nanoparticles surface, *J. Inorg. Organomet. Polym. Mater.*, 25 (2015) 169-175.
- [59] B. Pandit, T. Luitel, D.R. Cummins, A.K. Thapa, T. Druffel, F. Zamborini, J. Liu, Spectroscopic investigation of photoinduced charge-transfer processes in FTO/TiO₂/N719 photoanodes with and without covalent attachment through silane-based linkers, *J. Phys. Chem. A*, 117 (2013) 13513-13523.
- [60] I. Grądzka, M. Gierszewski, J. Karolczak, M. Ziółek, Comparison of charge transfer dynamics in polypyridyl ruthenium sensitizers for solar cells and water splitting systems, *Phys. Chem. Chem. Phys.*, 20 (2018) 7710-7720.
- [61] K. Kakiuchi, E. Hosono, S. Fujihara, Enhanced photoelectrochemical performance of ZnO electrodes sensitized with N719, *J. Photochem. Photobiol. A Chem.*, 179 (2006) 81-86.
- [62] S. Sardar, S. Ghosh, H. Remita, P. Kar, B. Liu, C. Bhattacharya, P. Lemmens, S.K. Pal, Enhanced photovoltage in DSSCs: Synergistic combination of a silver modified TiO₂ photoanode and a low cost counter electrode, *RSC Adv.*, 6 (2016) 33433-33442.
- [63] V. Shklover, Y.E. Ovchinnikov, L. Braginsky, S. Zakeeruddin, M. Grätzel, Structure of organic/inorganic interface in assembled materials comprising molecular components. Crystal structure of the sensitizer bis[(4,4'-carboxy-2,2'-bipyridine)(thiocyanato)]ruthenium(II), *Chem. Mater.*, 10 (1998) 2533-2541.

[64] L. Zhang, J.M. Cole, Dye aggregation in dye-sensitized solar cells, *J. Mater. Chem. A*, 5 (2017) 19541-19559.

Chapter 5

Photophysical Studies on Organic-Inorganic Hybrid Nanomaterials for Enhanced Photocatalytic Application

5.1. Introduction: The efficient conversion of solar light into chemical and electrical energy has been attracting expanding scientific and technological interest in order to address the scarcity of energy resources and enormous environmental pollution [1-4]. Photocatalysis is a technique to degrade toxic organic pollutants by formation of oxidizing free radicals, utilizing the renewable solar energy [5, 6]. Thus, development of novel materials with efficient photocatalytic activity, enough stability and a well matched absorption with the solar spectrum has been recognized as an essential step to combat environmental pollution through solar energy conversion [7-10]. Sensitization of wide bandgap semiconductor photocatalysts such as TiO_2 and ZnO with dyes to increase the photo response in the visible region is well documented in the literature but materials harvesting in the near infrared (NIR) region which constitutes 49% of the entire solar spectrum are still less explored [11, 12]. The use of organic dyes is favorable as a sensitizer when compare to the metal-based dyes as they are relatively cheap, less toxic and possess higher molar absorption coefficient [13, 14]. However, it is very difficult to emulate the solar spectra with a single organic dye sensitizer because of the characteristic narrow absorption band of most of the organic sensitizers [15]. To resolve this problem, co-sensitization of two dyes has been a well-known technique in case of dye sensitized solar cells (DSSCs) [16, 17]. However, co-sensitization using more than two sensitizers is less studied in case of photocatalysis [18, 19]. Co-sensitization may bring some additional difficulties to the system because of unwanted synergistic carrier mechanism and interactions

occurring between the sensitizers [20-22]. Hence, in order to achieve enhanced catalytic activity through co-sensitization, the choice of the sensitizers is supposed to be enough justified and the elucidation of photophysical properties and ultrafast carrier dynamics of the sensitizers is indispensable.

In our earlier work, Protoporphyrin IX (PPIX) sensitized ZnO has been proved to be a good visible light induced photocatalyst due to the appropriate alignment of the conduction band of ZnO and the highest occupied molecular orbital (HOMO) of the dye [23]. However, the main limitation of the porphyrin sensitized photocatalysts has been found to be poor absorbance in the red and NIR wavelength range. Recently, different squaraine dyes have stimulated a lot of attention as a NIR absorbing sensitizer in the field of DSSCs [24-26], organic solar cells [27, 28] and photocatalysis [29, 30] although they have a much reported self-aggregation problem [31, 32]. In the work explained in Chapter 4, we have successfully avoided the problem of sensitizer squaraine (SQ2) aggregation using PPIX as a co-sensitizer. Additionally, the increased absorption window due to co-sensitization and dipolar coupling between the sensitizer-co-sensitizer couple has been found to improve the efficiency in DSSCs [33]. It has to be noted that PPIX dye from natural resources has a metal ion at the central position of the dye. The impact of different metal ions in the porphyrin cavity on ultrafast photoinduced dynamics has been widely reported [34, 35] and their implications in photocatalysis are also studied in our previous publication [36]. However, role of different metal ions in porphyrin to determine the dipole-dipole coupling (FRET) with other organic dyes on a semiconductor surface and its implication in visible and NIR light harvesting is sparsely reported in the literature.

In the present study, we have co-sensitized ZnO nanoparticles with SQ2 (NIR absorbing dye) and PPIX (visible light absorbing dye). Förster resonance energy transfer (FRET) between the acceptor SQ2 and the donor PPIX has been observed from time resolved fluorescence measurements and it has been found to

play a beneficial role in providing enhanced catalytic activity apart from increasing the absorption window. For comparative studies, we have synthesized co-sensitized nanohybrids by impregnating PPIX moiety with different d-block metal ions (Zn and Co), which is expected to modulate the excited state lifetime of the energy donor at the surfaces of the host nanoparticles. Picosecond resolved fluorescence spectroscopy has been used to investigate the changes in FRET efficiency of PPIX upon metalation in presence of the acceptor dye SQ2. The effect of FRET between the two co-sensitizers has been correlated with the modulation of the visible light induced catalytic activity of their respective co-sensitized nanohybrid. We have also investigated NIR catalysis upon metalation of PPIX in the synthesized nanohybrid. In case of NIR catalysis, the suppression of aggregation of the SQ2 molecules due to co-sensitization is observed to enhance the catalytic activity of the PPIX-SQ2 co-sensitized nanohybrid. However, metalation of the PPIX co-sensitizer has reduced the efficacy of the NIR catalysis of the SQ2-sensitized nanohybrid. We have provided a mechanistic explanation for catalytic activity modulation of different co-sensitized nanohybrids under visible and NIR light irradiation by unraveling ultrafast excited state dynamic events.

5.2. Results and Discussion:

5.2.1. Ultrafast Dynamics in Co-sensitized Photocatalyst under Visible and NIR Light Irradiation [37]: Un-metalated protoporphyrin (PPIX) and squaraine (SQ2) are two commercially available dyes which have been chosen in this study as co-sensitizers. The other two dyes, cobalt (II) metalated protoporphyrin PP(Co) and zinc (II) metalated protoporphyrin PP(Zn), are synthesized by core metalation of the protoporphyrin moiety following the procedure mentioned in the Chapter 3, sample preparation section. Although, the acidic pKa value of the protonated imino nitrogens facilitates the reaction of core metalation, the process is highly selective upon the choice of metal ion. The absorption spectrum of PPIX (Figure 5.1a) in DMSO solvent shows the strongest intensity peak at 407 nm, which is due

to the Soret band transition (B band) and the other four lower intensity Q band peaks appear at 507 nm, 543 nm, 575 nm and 630 nm. Both the B and the Q bands arise from π - π^* transitions. The four Q bands are the X and Y components of the

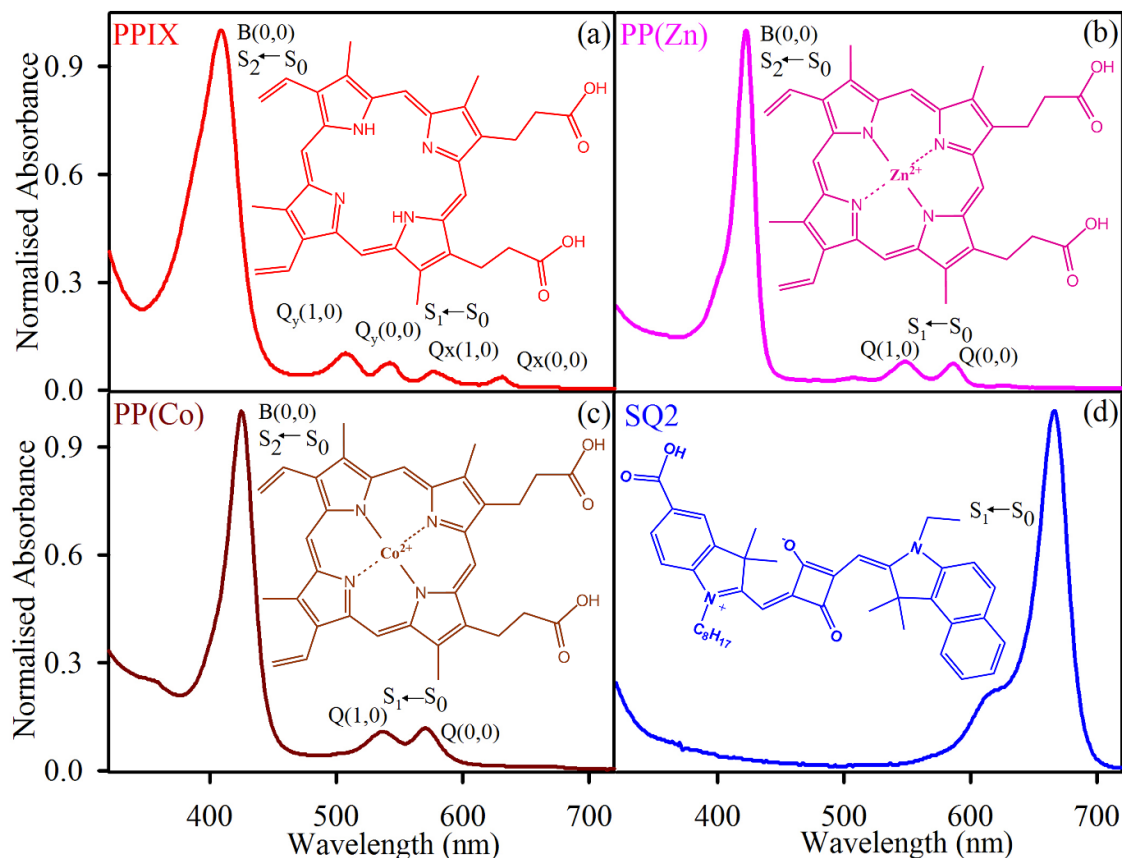


Figure 5.1. Molecular structure and normalised absorption spectra of (a) PPIX, (b) PP(Zn), (c) PP(Co) and (d) SQ2.

two vibronic transitions between $S_1 \leftarrow S_0$ electronic levels. The changes in absorption spectra in PP(Zn) (Figure 5.1b) and PP(Co) (Figure 5.1c) when compared to that of PPIX can be considered as evidence of metalation in the “pocket” of the porphyrin ligand. The red shifted Soret band and two vanished Q bands are typical signatures of the metal ion incorporation. For PP(Zn) the Soret band maxima appears at 421 nm and the two prominent Q bands appear at 547 nm and 584 nm. In case of PP(Co), the B band maxima is at 423 nm and the Q (1,0), Q (0,0) peaks are at 535 nm and 568 nm. The decrease in the number of Q bands

upon core metalation can be assigned to the increase in molecular symmetry from D_{2h} to D_{4h} . The Soret band ($S_2 \leftarrow S_0$) of PPIX is broader than the two metalated complexes probably due to the dimerization of the free ligands. As metal ion incorporation slightly reduces the possibility of aggregation, the B band became narrower. The structure and the absorption spectra of SQ2 in DMSO (Figure 5.1d) represents that the highest intensity peak appearing at 664 nm corresponds to the $\pi-\pi^*$ transitions while the lower intensity peak at 611 nm is a consequence of dye aggregation. From the absorption spectra of PPIX (Figure 5.1a) and SQ2 (Figure 5.1d) it is evident that if a mixture of these two sensitizers can be used in an appropriate ratio to sensitize a nanomaterial, the entire visible region of solar spectrum i.e. 400 nm-700 nm can be harvested. The combination of the absorption spectra of SQ2 with PP(Co) or PP(Zn) also emulates a wide range of solar spectra but the central metal ion of PP is observed to possess a very pronounced effect on the light harvesting efficiency as manifested by the catalysis results explained later.

Depending on the nature of central metal ion the metalloporphyrins are divided into two groups "Regular" and "Hypso" porphyrins where the first one consist of a closed shell central metal ion (d^{10} or d^0) and the second one consist of a metal ion which has a vacant d orbital (d^n , $n=6-9$) [38]. PP(Co) is a hypsoporphyrin with a d^7 central metal ion. From the emission spectra of PPIX and PP(Co) shown in Figure 5.2a, it can be observed that the fluorescence intensity is drastically reduced upon cobalt (II) ion incorporation in the porphyrin moiety. The intramolecular charge separation from the a_{2u} (π) of the ligand porphyrin to the vacant d_{z^2} orbital of the Co (II) metal ion is responsible for the reduction in fluorescence intensity. In hypsoporphyrins, there is a significant overlap between the π^* of porphyrin and the $d\pi$ (d_x and d_y) of the central metal ion which facilitate the metal to ligand back bonding and as a synergistic effect the a_{2u} (π) \rightarrow d_{z^2} charge transfer also become facile. From the similar excitation spectra of PPIX and PP(Co) shown in the inset of Figure 5.2a, it can be concluded that the very low emission

intensity at 630 nm of PP(Co) is attributed to the very small amount of free PP molecule left in the solution. Figure 5.2b shows the steady-state emission spectra of PP(Zn) where two prominent emission peaks are observed at 588 nm

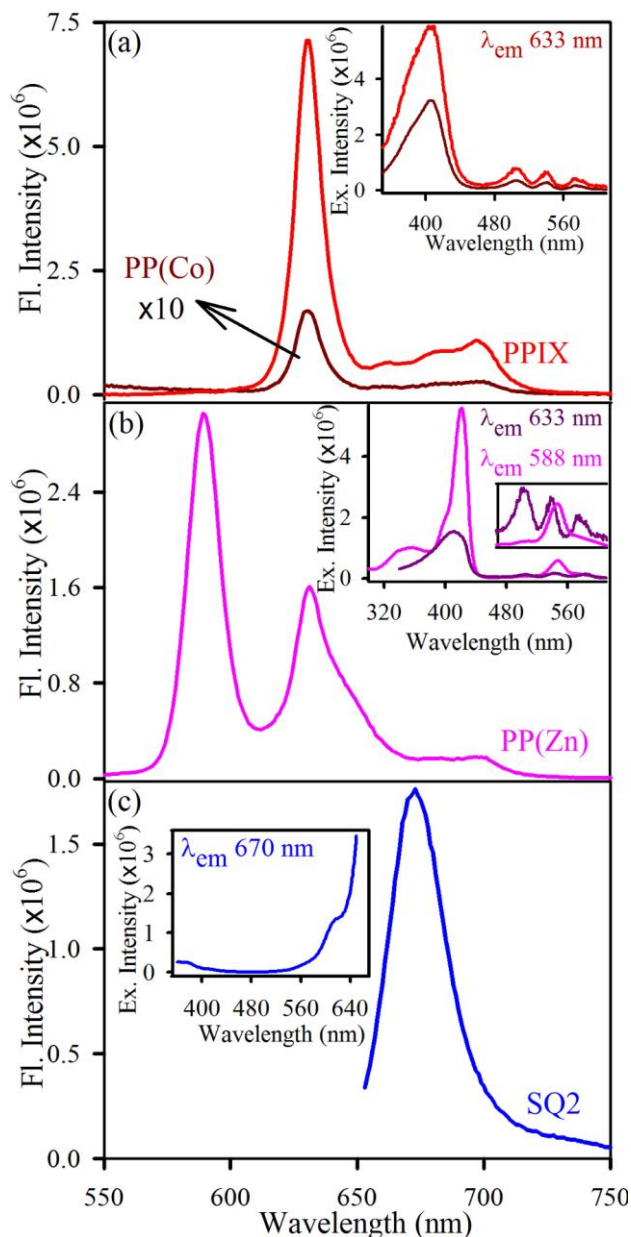


Figure 5.2. The steady state fluorescence emission spectra in solvent DMSO for (a) PPIX and PP(Co), (b) PP(Zn) and (c) SQ2. The insets of each show their respective excitation spectra.

and 631 nm which are due to Q(0,0) and Q(0,1) transitions, respectively. The emission peak positions are blue shifted in PP(Zn) from that of PPIX due to the

reorientation of the electronic levels and this is in good agreement with the absorption spectra of the dyes as discussed earlier. Higher energy gap is associated with the PP(Zn) for the increased molecular symmetry rather than PPIX. The intramolecular charge transfer process is not expected in case of the regular metaloporphyrin PP(Zn) as Zn (II) is a d^{10} system and it does not have any vacant d orbital to accept the electrons from the protoporphyrin ligand. Additionally, the metal based $d\pi$ orbitals are low lying in Zn (II), so the possibility of metal to ligand back bonding is also very less in case of PP(Zn). The excitation spectra of PP(Zn) in the inset of Figure 5.2b show two different spectral feature for two different emission wavelength. At 588 nm emission the excitation spectra resemble the absorption spectra of PP(Zn) whereas at 631 nm emission wavelength, the excitation spectra resemble the absorption spectra of PPIX. The emission maxima of the SQ2 are shown in Figure 5.2c, at 672 nm and the corresponding excitation spectra resembles the absorption spectra of SQ2 with an additional signature of $S_0 \rightarrow S_2$ transition around at 380 nm.

Figure 5.3a shows the absorption spectra of the sensitized nanohybrids along with the absorption spectra of the bare ZnO NP. The retention of the ZnO band gap peak after being sensitized by different sensitizers proves that sensitizers don't affect the stability of the ZnO nanoparticle. The absorption spectra of the ZnO NP shown in Figure 5.3a show a band gap of 3.4 eV. The HOMO-LUMO gap of the sensitizers used in this study is well reported in the literature in various theoretical and experimental studies [39]. The redox potential of PPIX, PP(Zn) and PP(Co) obtained from cyclic voltammetry (CV) are 0.46 V, 0.57 V, 0.67 V respectively, with respect to the saturated calomel electrode. [40] On the other hand, the reduction potential of squaraine obtained from CV is -0.78 V with reference to Normal Hydrogen Electrode (NHE) [41]. The TEM image of the ZnO NP shown in Figure 5.3b, shows an inter-planar distance of ~ 0.26 nm, corresponding to the spacing between two (002) planes. The ZnO NP (~ 30 nm)

used in this study, has a zeta potential (mV) / average agglomerate size (nm) of -3.00/1170 at pH 7.4 [42]. To obtain the details of attachment of the dyes on ZnO surface, we analyzed the FTIR spectra of SQ2_ZnO and PP_ZnO conjugates and compared them to that of free SQ2 and PPIX. As shown in Figure 5.4, the FTIR peaks corresponding to the carboxylic group stretching frequency of the free dyes were found to disappear and shift respectively for the two conjugate while the other peaks remained the same. This perturbation in stretching frequency at 1695 cm^{-1} in the case of PPIX and 1685 cm^{-1} in case of SQ2 proves their attachment to ZnO surface through carboxylic groups. The attachment of the carboxylic group of

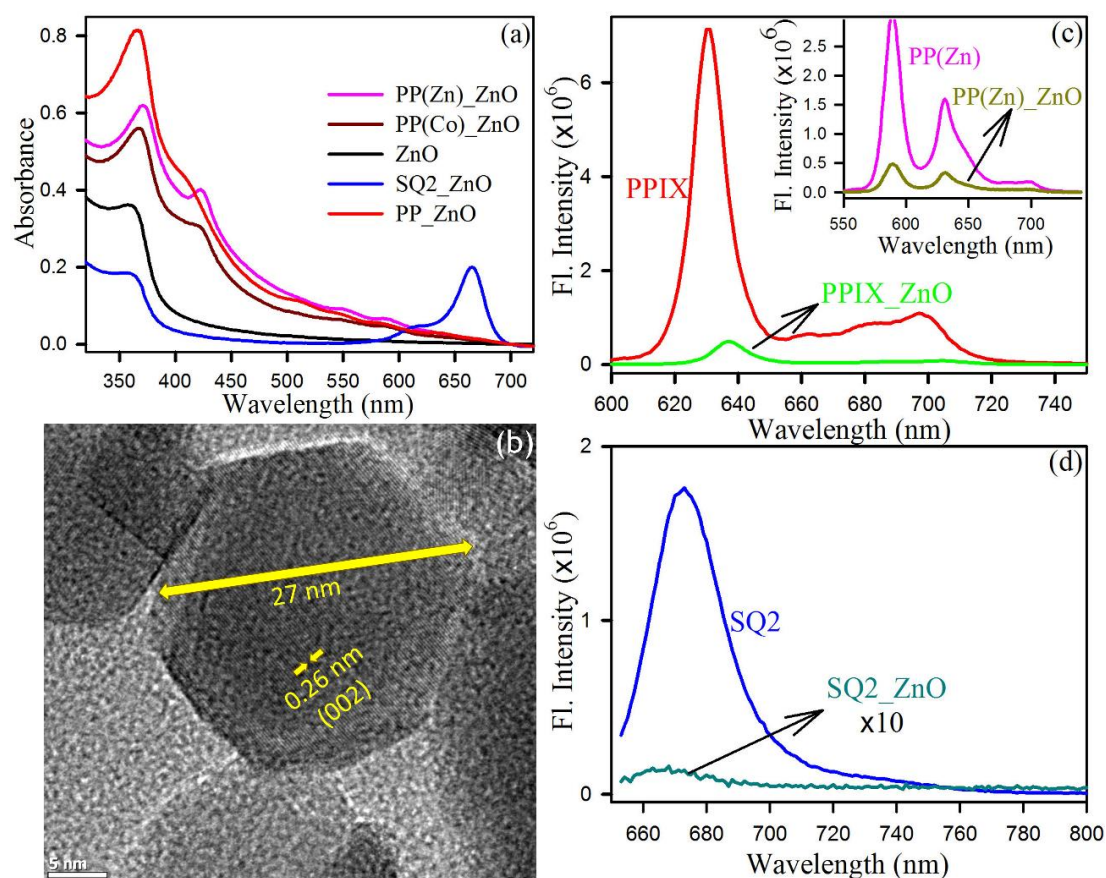


Figure 5.3: (a) Absorption spectra of PP(Zn)_ZnO (Pink), PP(Co)_ZnO (brown), ZnO NP (black), SQ2_ZnO (blue), PP_ZnO (Red), (b) TEM image of the ZnO nanoparticle, (c) emission spectra of the PPIX_ZnO compared to PPIX, inset shows the steady-state emission spectra of PP(Zn)_ZnO compared to that of PP(Zn) and (d) steady-state emission spectra of SQ2_ZnO compared to that of SQ2. The emission spectra of SQ2_ZnO is ten times multiplied to show the changes.

the sensitizer to Zn (II) located at the ZnO surface can further be proved from the Raman spectra of the functionalized nanohybrids as shown in our earlier publication [23]. From thermo gravimetric analysis and particle density of ~ 30 nm ZnO NP, we have estimated that ~ 15000 SQ2 and ~ 3500 PPIX were attached with one ZnO NP at 8:2 molar ratio of the SQ2: PPIX sensitizers. The estimated value is consistent with earlier reports [23]. Upon attachment to the ZnO NP surface the steady-state emission of the sensitizers is quenched as shown in Figures 5.3c and 5.3d. In addition, the steady-state emission peak of PPIX in the PPIX-ZnO nanohybrid is red-shifted by ~ 5 nm compared to the emission spectra of free PPIX. The observation indicates the electronic interaction between the singlet excited state of PPIX with the ZnO nanoparticle. The ~ 6 nm blue shift in the emission peak position of SQ2_ZnO with respect to that of free SQ2 is indicative of a probable aggregation.

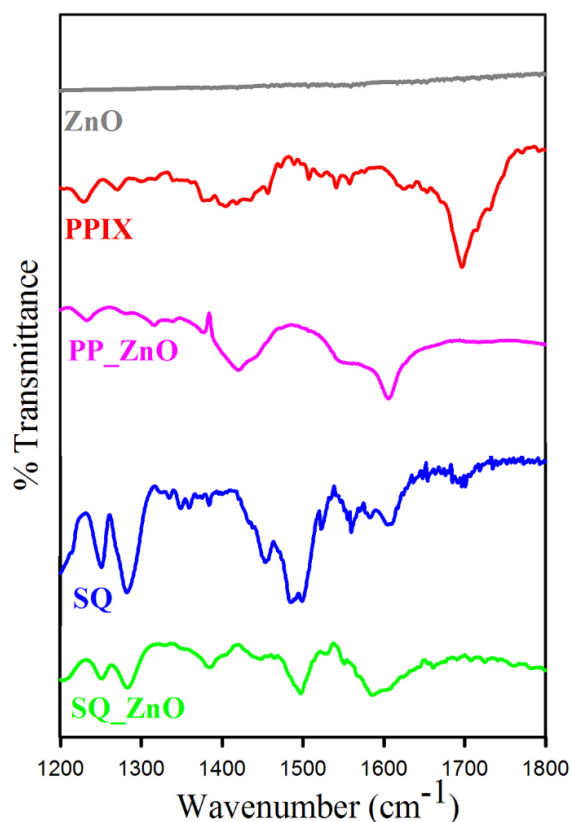


Figure 5.4: FTIR spectra of ZnO NP (Grey), PP (Red), PP-ZNO (Pink), SQ2 (Blue) and SQ2_ZnO (Green).

To analyze the photoinduced chemical and physical properties of the individual sensitizers and their respective nanohybrids with ZnO, the pico-second resolved fluorescence transients (Figure 5.5) were studied. The mechanistic explanation and dynamic behavior of the photo excited charge carriers are correlated with the excited state lifetimes summarized in Table 5.1. The ZnO NP (~30 nm) has no emission at the excitation wavelengths used in this study (409 nm and 633 nm). Thus, there is no possibility of interference in the decay patterns of the sensitizers from the ZnO defect state emission. In DMSO solvent, both PPIX and PP(Zn) show single exponential lifetimes of 16.50 ns and 2.24 ns, respectively. Kobayashi et al have reported earlier that the decay lifetime and quantum yield of

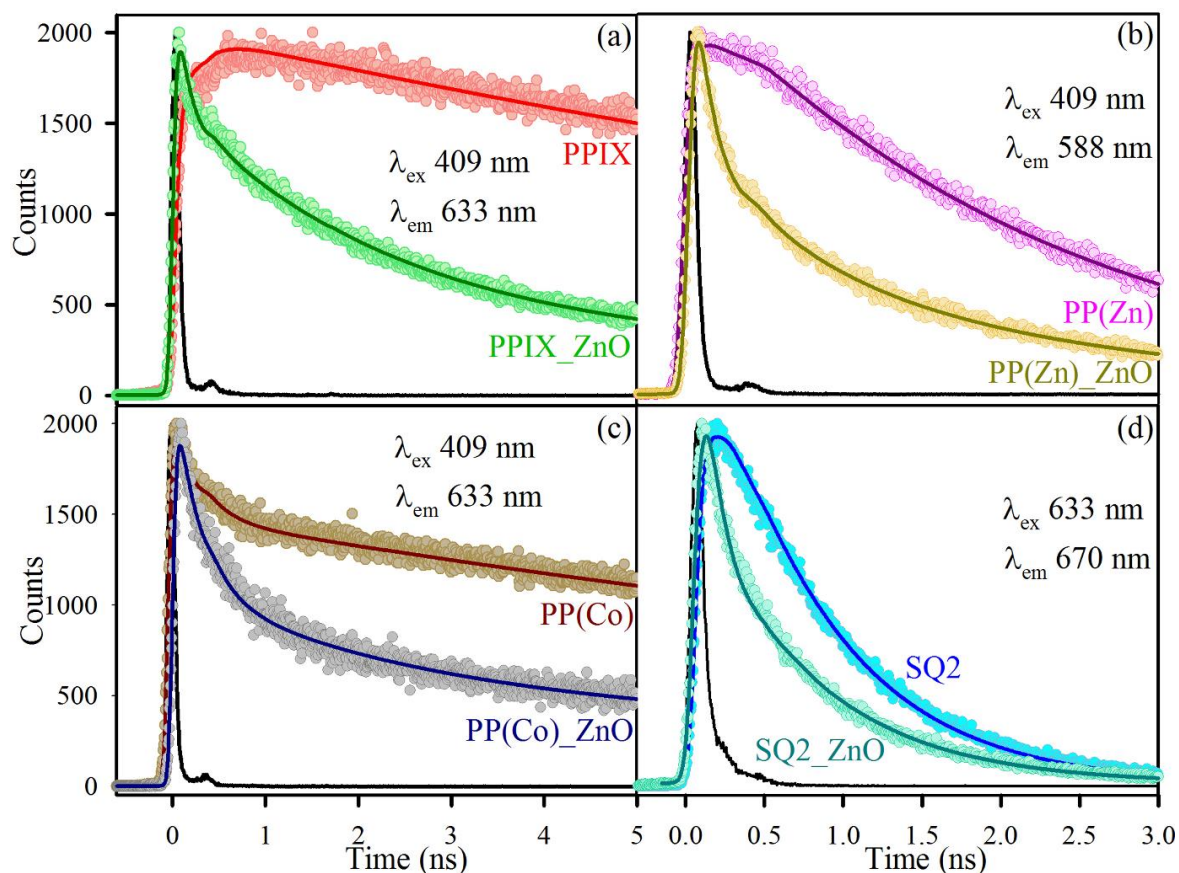


Figure 5.5: Pico-second resolved fluorescence decay profiles of (a) PPIX (red) and PPIX attached to ZnO (green), (b) PP(Zn) (pink) and PP(Zn) attached to ZnO (yellow), (c) PP(Co) (brown) and PP(Co) attached to ZnO (grey), (d) SQ2 (blue) and SQ2 attached to ZnO (Cyan). All the measurements were performed in DMSO as solvent.

Table 5.1. Dynamics of picosecond resolved fluorescence transients of the dyes PPIX, PP(Zn), PP(Co) and SQ2 and the respective nanohybrids with ZnO.^a

Sample	Excitation wavelength (nm)	Emission wavelength (nm)	τ_1 (ns)	τ_2 (ns)	τ_3 (ns)	τ_{avg} (ns)
PPIX	409	633	16.50 ± 0.10 (100%)			16.50
PPIX_ZnO	409	633	16.50 ± 0.10 (13%)	2.25 ± 0.05 (44%)	0.13 ± 0.03 (42%)	3.19
PP(Co)	409	633	16.50 ± 0.10 (62%)	0.24 ± 0.03 (38%)		10.32
PP(Co)_ZnO	409	633	16.50 ± 0.10 (23%)	2.17 ± 0.05 (22%)	0.24 ± 0.03 (55%)	4.40
PP(Zn)	409	588	2.24 ± 0.03 (100%)			2.24
PP(Zn)_ZnO	409	588	2.24 ± 0.03 (25%)	0.59 ± 0.02 (29%)	0.10 ± 0.03 (44%)	0.78
SQ2	633	670	0.73 ± 0.04 (100%)			0.73
SQ2_ZnO	409	670	0.73 ± 0.05 (34%)	0.08 ± 0.02 (66%)		0.30

^aNumbers in the parenthesis indicate relative weightages.

the S_1 state emission in porphyrin systems decrease with an increase in the atomic number of the central metal ion or the ligand as well due to enhanced spin-orbit coupling and acceleration of the intersystem crossing [43]. In the case of fluorescence decay lifetime of PP(Co), a fast component of 240 ps with 38% relative weightage is observed upon excitation at 409 nm because of the ligand to metal charge transfer. Regarding the excited state lifetime of the dye-ZnO complexes, both PPIX and PP(Zn) show efficient ligand to semiconductor electron transfer with timescales in hundreds of picosecond range. A very low extent of ligand to semiconductor charge transfer takes place in the PP(Co)_ZnO complex which is also evident from the reduced average lifetime of the complex compared

to the dye PP(Co) but the lifetime of that particular process is not much distinguishable from that of the ligand to metal charge transfer timescale. The fluorescence lifetime of the SQ2 dye is measured to be single exponential while upon attachment to the ZnO surface, an additional 80 ps faster component in lifetime appeared due to the electron transfer from SQ2 to ZnO. As there is no IRF like component in the decay pattern of SQ2_ZnO, there is no possibility of any predominant electron injection in sub-pico second time scales [44].

The steady-state quenching of donor emission for both PPIX and PP(Zn) after the addition of SQ2 has been shown in Figure 5.6. As shown in the insets of Figure 5.7a and 5.7b, there is a significant overlap between the absorption spectra of the NIR absorbing sensitizer SQ2 and the emissions of the visible absorbing sensitizers PPIX and PP(Zn). In order to investigate the possibility of resonance energy transfer between the donor PPIX or PP(Zn) and the acceptor SQ2, time resolved fluorescence decays are measured in a mimic of the proposed ZnO nanohybrid systems by attaching both the donor and acceptor on the surface of <50 nm Al₂O₃. The aim of attaching the donor and acceptor dyes to Al₂O₃ for investigation of FRET (Förster resonance energy transfer) is to bring them in enough proximity to each other enabling the possibility of intermolecular dipole-dipole coupling. As Al₂O₃ is an insulator, insignificant charge transfer possibility upon attachment of the dyes to the nanoparticle surface is evident in the literature [45]. Thus, all the three dyes PPIX, PP(Zn) and SQ2 have a single exponential lifetime even after being attached to the Al₂O₃ surface.

Figure 5.7a shows that the fluorescence of donor PPIX attached to Al₂O₃ decays at a single exponential lifetime and after addition of the acceptor SQ2 the average lifetime is observed to be quenched. The similar trend in the change of lifetime after addition of the acceptor SQ2 is observed for another donor molecule PP(Zn) also (Figure 5.7b). For the donor PP(Zn), we are able to capture the rise in the acceptor's decay profile in a solution mixture of PP(Zn) and SQ2 upon

excitation at 409 nm (Figure 5.7c) which provides a strong evidence of the FRET between these two dye pairs. In the inset of Figure 5.7c, the excitation spectra of only SQ2 and PP(Zn)-SQ2 FRET pair are compared at the emission wavelength of 675 nm. It is evident that in the FRET pair the acceptor's emission comes to some extent from the excitation at the absorption peak position of the donor PP(Zn). Due to resonance energy transfer from the excited state of the donor to that of acceptor, the decay lifetime of donor has been quenched. Additionally, FRET increases the carrier population in the excited state of the acceptor SQ2 which is responsible for the rise component in the acceptors decay profile upon exciting the donor PP(Zn). So, the average lifetime of the acceptor SQ2 is observed to be increased from 1.10 ns to 2.12 ns after FRET from the donor PP(Zn).

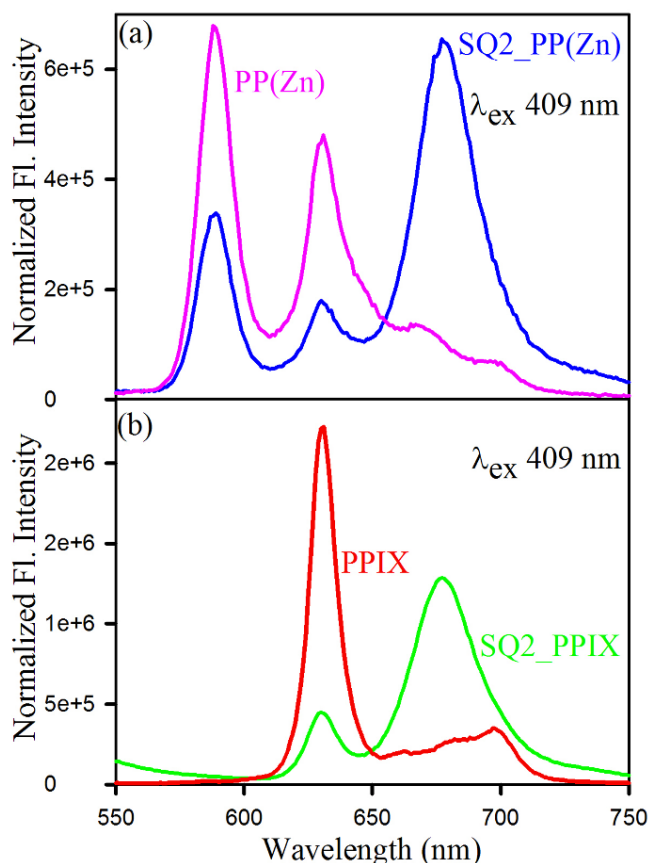


Figure 5.6: Steady-state PL spectra of (a) PP(Zn) and SQ2_PP(Zn) attached to Al_2O_3 . (b) PPIX and SQ2_PPIX attached to Al_2O_3 .

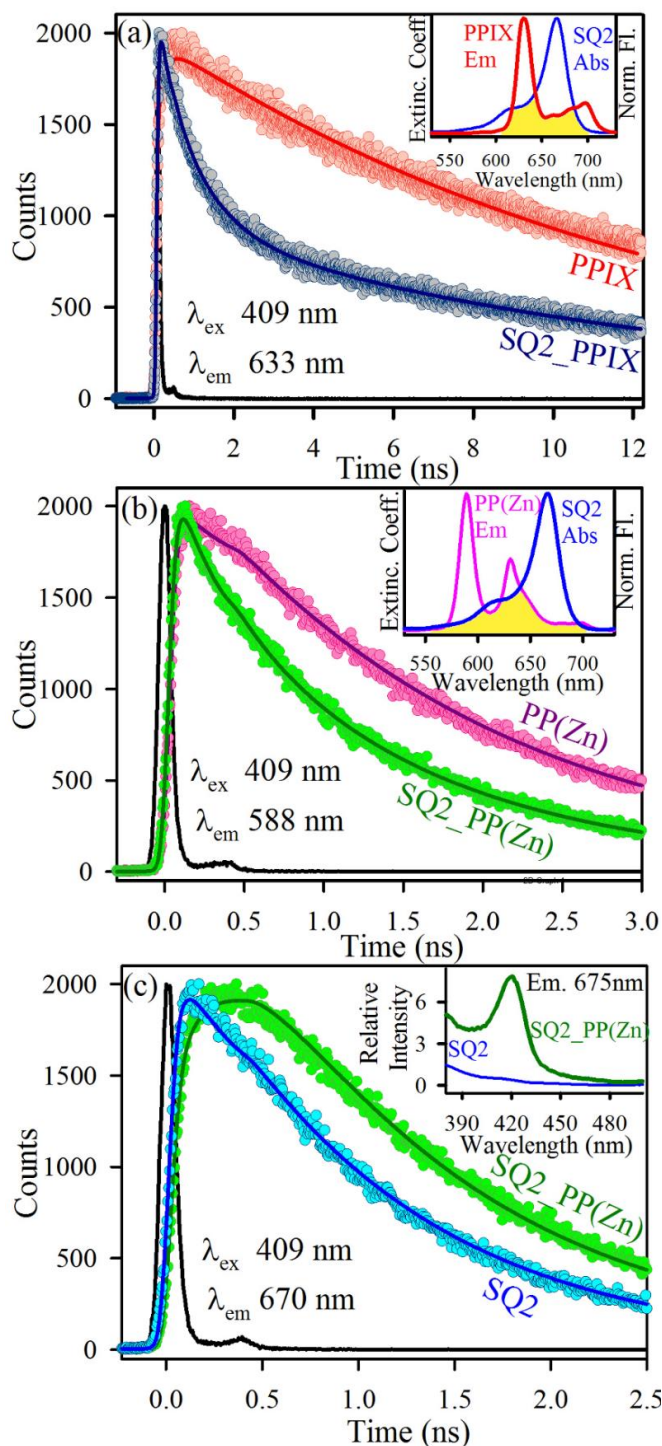


Figure 5.7: The picosecond resolved fluorescence decays of (a) PPIX attached to Al_2O_3 in the absence (red) and presence (grey) of SQ2. (b) PP(Zn) attached with Al_2O_3 in absence (pink) and presence (green) of SQ2. The inset shows spectral overlap between the emission of PP(Zn) and absorption of SQ2, (c) time resolved fluorescence decay of SQ2 attached to Al_2O_3 in absence (blue) and presence of PP(Zn). The inset shows the excitation spectra of SQ2 in the absence and presence of PP(Zn).

Table 5.2. Excited state lifetime of the donor PPIX and PP(Zn) attached to Al₂O₃ in presence and absence of the acceptor SQ2 and the excited state lifetime of the acceptor SQ2 attached to Al₂O₃ in presence and absence of the donor PP(Zn).^a

Sample	Excitation wavelength (nm)	Detection wavelength (nm)	τ_1 (ns)	τ_2 (ns)	τ_3 (ns)	τ_{avg} (ns)
PPIX	409	633	13.20 ± 0.10 (100%)			13.20
PPIX-SQ2	409	633	13.20 ± 0.10 (38%)	1.02 ± 0.05 (39%)	0.25 ± 0.01 (23%)	5.47
PP(Zn)	409	588	1.90 ± 0.06 (100%)			1.90
PP(Zn)-SQ2	409	588	1.90 ± 0.05 (26%)	1.10 ± 0.04 (45%)	0.25 ± 0.03 (28%)	1.06
SQ2	409	670	1.10 ± 0.10 (100%)			
PP(Zn)-SQ2	409	670	1.90 ± 0.10 (34%)	1.10 ± 0.04 (152%)	0.25 ± 0.03 (-86%)	2.12

^aNumbers in the parenthesis indicate relative weightages.

Table 5.3. FRET parameters.

System	J(λ)	R ₀ (nm)	E (%)	R _{DA} (nm)
SQ2_PPIX	1.8 × 10 ²³	4.5	58	4.2
SQ2_PP(Zn)	1.2 × 10 ²³	3.2	44	3.3

Comparing the excited state decay lifetimes of the PP(Zn)-SQ2 system at the emission peak position of PP(Zn) (588 nm) and the emission peak position of SQ2 (670 nm), it can be observed that both of them has the same three lifetime components. Only their relative weightage differs for different emission wavelengths. Both the faster decay lifetime at 588 nm and the rise lifetime at 670 nm are found to be same. So, the resonance energy transfer between the PP(Zn) and SQ2 is quite evident from all the above-mentioned observations. The rise in the decay profile of SQ2 is not distinguishable in the case of the PPIX- SQ2 pair, as the emission peak of PPIX (633 nm) is very close to the emission peak of the

acceptor SQ2 (670 nm), unlike the PP(Zn)-SQ2 pair. All the corresponding timescales and their relative percentage are summarized in Table 5.2. Using conventional methodologies, the FRET efficiencies between PPIX-SQ2 pair and PP(Zn)-SQ2 pair is calculated to be 58% and 44%, respectively. For both the pairs, the overlap integral between the donor emission and acceptor absorption $J(\lambda)$, donor-acceptor distances R_{DA} and other FRET parameters are arranged in Table 5.3. In time resolved measurements, no changes are found in the PP(Co) decay profile upon addition of SQ2. Thus, it can be concluded that the FRET is absent in case of PP(Co) and SQ2 pair due to the other ultrafast competing process of LMCT.

In order to investigate the effect of FRET in photo-catalytic activity, co-sensitized ZnO nanohybrids are prepared using the dyes PPIX and SQ2 at different molar ratios. Acridine orange (AO) is used as a model organic pollutant to degrade by the synthesized photocatalysts. Figure 5.8a represents the photocatalytic degradation profile of AO under visible light by co-sensitized photocatalyst. Hypso-chromic shift in the absorption peak of photodegraded AO and discolorations of the solution due to lower molar extinction coefficient of the photo-degraded products prove the photocatalysis of AO in the present study. The kinetics of the photodegradation of AO is shown in the inset of Figure 5.8a where the rate constant is found to be 0.04 min^{-1} . Figure 5.8b represents the photodegradation of AO under visible light illumination by the nanohybrids co-sensitized with different molar ratio of the two dyes PPIX and SQ2 along with the single dye sensitized nanohybrids i.e. PPIX_ZnO and SQ2_ZnO. From the photocatalytic degradation data of AO under visible light (above 395 nm) in 1hr summarized in Table 5.4, it can be observed that ZnO sensitized by 8:2 molar ratio of SQ2:PPIX shows much better visible light photocatalytic activity than the other molar ratios and the individual dye sensitized nanohybrids. The SQ2_ZnO shows

the lowest catalytic activity probably because of the extensive aggregation problem which may have reduced upon co-adsorption with PPIX. Control studies

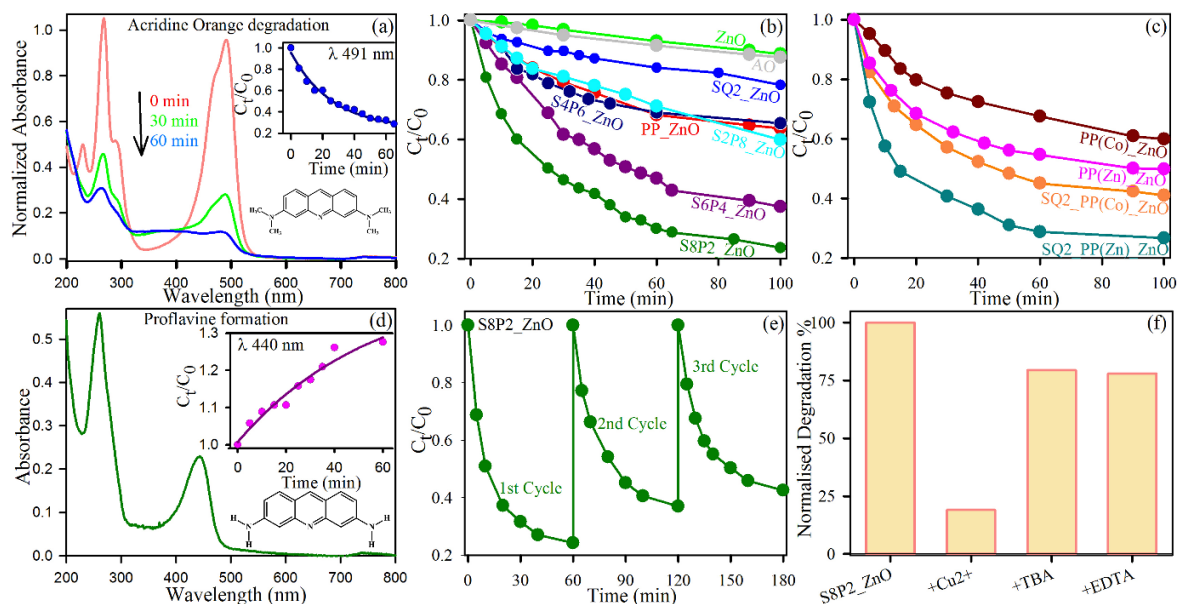


Figure 5.8: Photocatalysis under visible light irradiation (above 395 nm). (a) Photocatalytic degradation of acridine orange (AO) by the SQ2 and PPIX (8:2) co-sensitized ZnO, inset shows the kinetics at the absorption peak maxima of acridine orange, (b) comparison of catalytic activity for different co-sensitized ZnO sensitized by different ratios of SQ2 and PPIX, control ZnO and acridine orange. (c) Catalytic activity of ZnO sensitized by PP(Co), PP(Zn) and by their respective cocktail mixture with SQ2 at 8:2 molar ratio of SQ2 and the metalloporphyrins. (d) Absorption spectra the photo-degraded product Proflavine (PF), the inset shows the kinetics at the absorption peak maxima of PF during photocatalysis of AO obtained from a normalized absorption spectra of AO degradation. (e) Recyclability of the catalyst S8P2_ZnO i.e. ZnO sensitized by 8:2 molar ratio of SQ2 and PPIX. (f) Effect of Cu^{2+} , TBA and EDTA on the photocatalytic activity of S8P2_ZnO.

have been done with only AO or only ZnO under visible light illumination but its degradation is negligible. The 8:2 molar ratio of SQ2 and PPIX is found to have superior photocatalytic activity among the other molar ratios because at that particular ratio the probability of FRET is highest which is similar to an earlier observation in case of co-sensitized DSSC [33]. To check whether the extent of dipole-dipole coupling can control the catalytic activity, two more co-sensitized nanohybrids are prepared at the same best performing molar ratio of 8:2 of the SQ2 and the other visible absorbing metallo-porphyrin dye. These nanohybrids are named SQ2_PP(Co)_ZnO and SQ2_PP(Zn)_ZnO and their

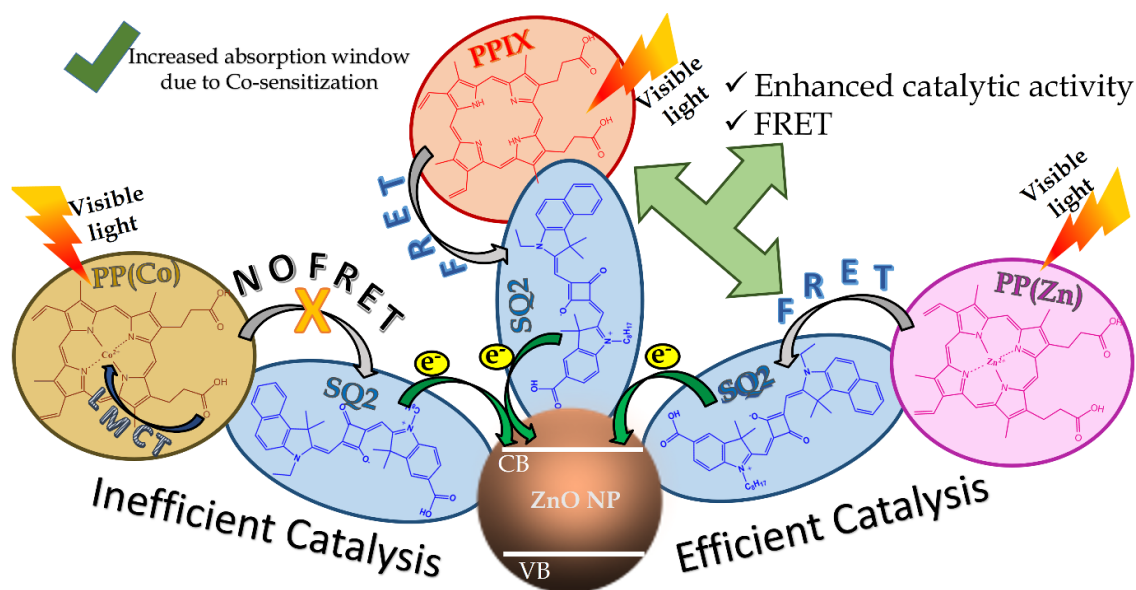
catalytic activities are compared to those of the single dye sensitized nano hybrids PP(Co)_ZnO and PP(Zn)_ZnO as shown in Figure 5.8c. The figure clearly depicts

Table 5.4. Percentage of photocatalytic degradation of acridine orange in the presence of different catalyst in 1hr.

Sample	Photocatalytic degradation (%) of AO in 1 hr
PP_ZnO	32 ± 2
SQ2_ZnO	16 ± 1
SQ2:PP (8:2)_ZnO	70 ± 3
SQ2:PP (6:4)_ZnO	54 ± 2
SQ2:PP (4:6)_ZnO	31 ± 2
SQ2:PP (2:8)_ZnO	29 ± 2
ZnO	8 ± 1
AO	9 ± 1
SQ2:PP(Co) (8:2)_ZnO	55 ± 2
SQ2:PP(Zn) (8:2)_ZnO	72 ± 3

that both the mixed dye hybrids show better activity than their respective control study of single dye sensitized nano hybrids because in both the cases the absorption window is increased due to co-sensitization. But the notable feature is that SQ2_PP(Zn)_ZnO shows a much higher activity than SQ2_PP(Co)_ZnO as in the latter the dipole -dipole coupling effect is absent. The activity of S8P2_ZnO and SQ2_PP(Zn)_ZnO is found to be similar as in both the cases, FRET is a photoinduced process which facilitates the enhanced radical generation and the pollutant degradation as well. The N-de-methylation process occurs during photodegradation of acridine orange (AO). The four N-methyl groups are removed from the original AO moiety during photodegradation [46]. 3, 6-diaminoacridine or proflavine has been the widely reported as the photodegraded product of acridine orange due to ROS mediated photocatalysis. Figure 5.8d shows the absorption spectra of the proflavine (PF) and the inset of Figure 5.8d shows the kinetics of formation of the product proflavine derived from a peak normalized degradation profile of AO. The formation of PF is taking place at a rate

constant of 0.018 min^{-1} which is slower than the degradation rate of AO due to the formation of several intermediate products. The comparison of the decay kinetics of AO and formation of proflavin further proves the photodegradation. The recyclability of the co-sensitized nanohybrid S8P2_ZnO has also been tested and Figure 5.8e shows that the catalyst is still 50% active after completion of three cycles. After consecutive cycles the activity decreases probably due to dye leaching process.



Scheme 5.1: FRET: The tuning tool for modulating catalytic activity of co-sensitized nanohybrids, under visible light illumination.

To explore the mechanism of catalytic activity of the SQ2 and PPIX co-sensitized nanohybrid, catalysis has been performed in the presence of excess radical scavengers and the results are represented in Figure 5.8f. Cu^{2+} is known as an electron scavenger because it accepts electron from the reaction media to yield Cu^+ . Tertiary butyl alcohol (TBA) acts as the scavenger of $\cdot\text{OH}$, and ethylenediaminetetraacetic acid (EDTA) is introduced as a hole (h^+) quencher. In all the three cases the catalytic activity decreases but Cu^{2+} has reduced the activity drastically to 20% which implies that among all the reactive species the negatively charged $\text{O}_2^{\cdot-}$ plays the most crucial role in photodegradation of the pollutant.

Comparing all the catalytic activities tabulated in Table 5.4, it can be inferred that in case of co-sensitized photocatalyst synthesis FRET is a dynamical event which has much pronounced influence in controlling the light harvesting activity and the nature of the specific metal ion in the porphyrin core plays a crucial role in the dipole-dipole coupling with the acceptor dye. The predominant mechanistic pathway under visible light catalysis of the nano hybrids is summarized in the set of equations 5.1 and Scheme 5.1.

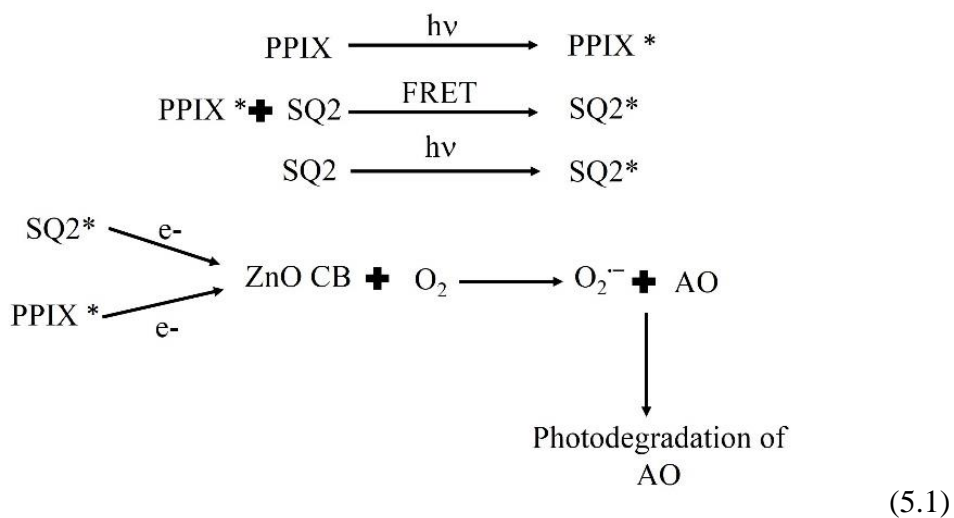


Figure 5.9a shows the NIR light induced photocatalysis by the co-sensitized nano hybrids. From the comparison of the dye degradation percentages summarized in Table 5.5, it is quite evident that the co-sensitized nano hybrids exhibit better catalytic activity under NIR light than the control SQ2-ZnO. However, the dye loading curve in Figure 5.9b shows that there is higher loading of SQ2 in the SQ2-ZnO hybrid rather than the other co-sensitized hybrids. This observation leads to the conclusion that higher loading causes a stronger aggregation which is clear from the monomer-dimer peak ratio of the SQ2-ZnO and the three co-sensitized photocatalyst. In the co-sensitized nano hybrids, aggregation is suppressed to some extent due to co-adsorption on the ZnO surface. The SQ2_PPIX_ZnO adduct is found to exhibit the best NIR catalysis with 69% dye degradation in 1 hr while activities of the SQ2_PP(Zn)_ZnO and

SQ2_PP(Co)_ZnO is show comparatively less activities due to the presence of the metal centre. The phenomenon is well explained in Scheme 5.2. The excited state electrons of SQ2 are trapped in the porphyrin core-metal through ZnO conduction band. It has been reported earlier that photoexcited carriers of the semiconductor conduction band move to the core metal of the metalloporphyrin photosensitizers [47, 48] and facilitate charge separation under UV irradiation but in the case of dual dye sensitization the same phenomenon is observed to diminish the NIR catalytic activity of the conjugate. As cobalt has vacant d orbital, the process is more facile in case of PP(Co) than PP(Zn). Thus, SQ2_PP(Co)_ZnO performs less efficiently than SQ2_PP(Zn)_ZnO. It can be inferred that for NIR catalysis the PPIX is proved to be a better co-adsorbent for SQ2_ZnO than the other two metalloporphyrins.

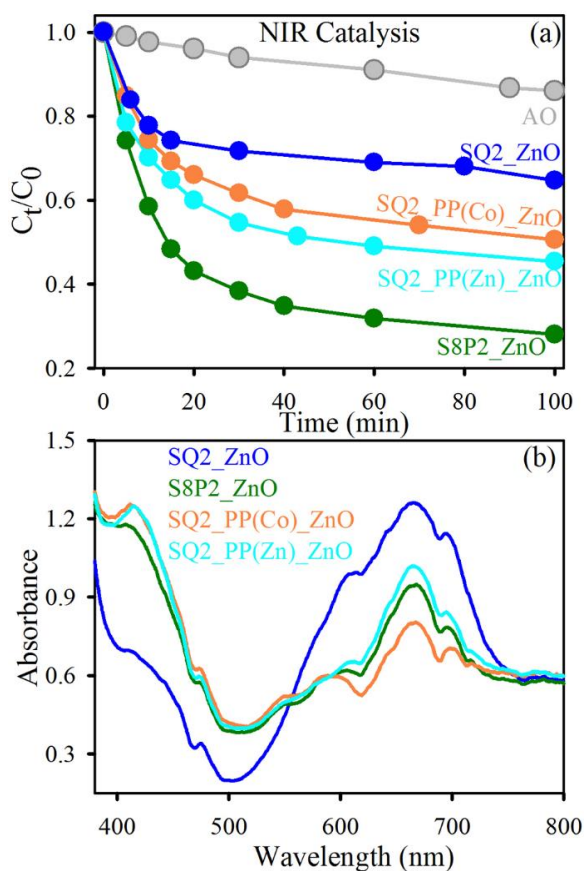
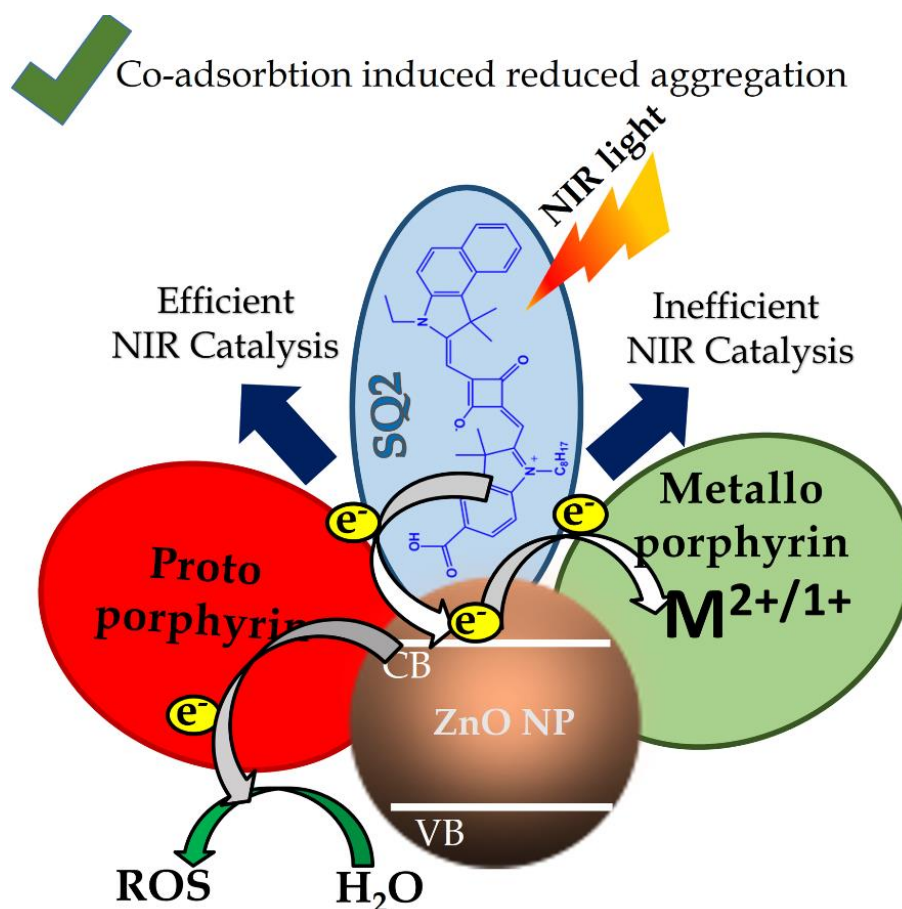


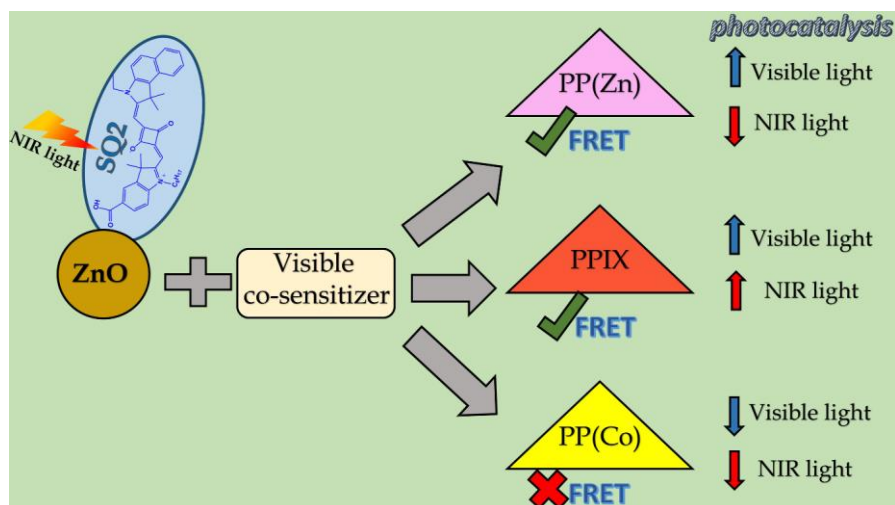
Figure 5.9. (a) Photocatalytic activities under NIR light irradiation (above 650 nm) using a tungsten-halogen light source, (b) dye loading in different nanohybrids from solid state absorption spectra collected in retro reflecting mode.

Table 5.5. Percentage of photocatalytic degradation of acridine orange in the presence of different catalyst in 1 h under NIR light irradiation (above 650 nm) using a tungsten-halogen light source.

Sample	Photocatalytic degradation (%) of AO in 1 h
AO	9 ± 1
SQ2_ZnO	31 ± 2
SQ2:PP (8:2)_ZnO	69 ± 2
SQ2:PP(Co) (8:2)_ZnO	45 ± 1
SQ2:PP(Zn) (8:2)_ZnO	51 ± 2
AO	9 ± 1
SQ2_ZnO	31 ± 2



Scheme 5.2: Photocatalysis under NIR light illumination by the three co-sensitized nanohybrids.



Scheme 5.3: Activity modulation of co-sensitized light harvesting nanohybrid through tuning the ultrafast carrier dynamics under visible and NIR light irradiation.

5.3. Conclusion: Our present study on the PPIX, PP(Co), PP(Zn) and SQ2 dyes provides an insight into their excited state dynamic behavior for their potential use as light harvesting photosensitizers. We have shown that the dipolar coupling or FRET from PPIX to SQ2 at the ZnO surface plays the key role to enhance the catalytic activity of the co-sensitized photocatalyst. Most importantly, the dipole-dipole coupling of PPIX and SQ2 pair is observed to be highly influenced by the core metalation of the donor PPIX and consequently affecting the catalytic activity of the co-sensitized ZnO nanohybrid under visible light. In case of PP(Co) the FRET is found to be absent due to ultrafast photoinduced ligand to metal charge transfer. At the same time PP(Zn)-SQ2 is observed to be a very efficient FRET pair. Photocatalytic efficiency is also conclusively correlated with the presence and absence of FRET. Additionally, the PPIX-SQ2 co-sensitized ZnO nanohybrid is observed to be an efficient NIR photocatalyst also due to the anti-aggregation effect of the PPIX on SQ2 molecule at the surface of ZnO. The entire correlation between the dynamics and catalysis efficiency under visible and NIR light has been represented in Scheme 5.3. Thus, different ultrafast phenomena has been proved to be the tuning tool of the visible light harvesting as well as NIR harvesting capacity of co-sensitized nanohybrids.

References

- [1] X. Guo, W. Song, C. Chen, W. Di, W. Qin, Near-infrared photocatalysis of β -NaYF₄: Yb³⁺, Tm³⁺@ZnO composites, *Phys. Chem. Chem. Phys.*, 15 (2013) 14681-14688.
- [2] J. Chen, S. Shen, P. Guo, M. Wang, J. Su, D. Zhao, L. Guo, Plasmonic Ag@SiO₂ core/shell structure modified g-C₃N₄ with enhanced visible light photocatalytic activity, *J Mater Res*, 29 (2014) 64-70.
- [3] S. Rajaambal, K. Sivaranjani, C.S. Gopinath, Recent developments in solar H₂ generation from water splitting, *J. Chem. Sci.*, 127 (2015) 33-47.
- [4] Q. Daniel, R.B. Ambre, B. Zhang, B. Philippe, H. Chen, F. Li, K. Fan, S. Ahmadi, H.k. Rensmo, L. Sun, Re-investigation of cobalt porphyrin for electrochemical water oxidation on FTO surface: formation of CoO_x as active species, *ACS Catal.*, 7 (2017) 1143-1149.
- [5] T. Bora, K.K. Lakshman, S. Sarkar, A. Makhal, S. Sardar, S.K. Pal, J. Dutta, Modulation of defect-mediated energy transfer from ZnO nanoparticles for the photocatalytic degradation of bilirubin, *Beilstein J. Nanotechnol.*, 4 (2013) 714.
- [6] S. Sardar, P. Kar, H. Remita, B. Liu, P. Lemmens, S.K. Pal, S. Ghosh, Enhanced charge separation and FRET at heterojunctions between semiconductor nanoparticles and conducting polymer nanofibers for efficient solar light harvesting, *Sci. Rep.*, 5 (2015) 17313.
- [7] S. Chu, A. Majumdar, Opportunities and challenges for a sustainable energy future, *Nature*, 488 (2012) 294.
- [8] X. Chen, C. Li, M. Grätzel, R. Kostecki, S.S. Mao, Nanomaterials for renewable energy production and storage, *Chem. Soc. Rev.*, 41 (2012) 7909-7937.
- [9] E. Kowalska, K. Yoshiiri, Z. Wei, S. Zheng, E. Kastl, H. Remita, B. Ohtani, S. Rau, Hybrid photocatalysts composed of titania modified with plasmonic nanoparticles and ruthenium complexes for decomposition of organic compounds, *Appl. Catal., B*, 178 (2015) 133-143.

- [10] M.D. Hernández-Alonso, F. Fresno, S. Suárez, J.M. Coronado, Development of alternative photocatalysts to TiO₂: Challenges and opportunities, *Energy Environ. Sci.*, 2 (2009) 1231-1257.
- [11] D. Pei, J. Luan, Development of visible light-responsive sensitized photocatalysts, *Int. J. photoenergy*, 2012 (2011) 262831.
- [12] M.J. Griffith, K. Sunahara, P. Wagner, K. Wagner, G.G. Wallace, D.L. Officer, A. Furube, R. Katoh, S. Mori, A.J. Mozer, Porphyrins for dye-sensitized solar cells: new insights into efficiency-determining electron transfer steps, *Chem. Commun.*, 48 (2012) 4145-4162.
- [13] L.M. Gonçalves, V. de Zea Bermudez, H.A. Ribeiro, A.M. Mendes, Dye-sensitized solar cells: A safe bet for the future, *Energy Environ. Sci.*, 1 (2008) 655-667.
- [14] R.Y.-Y. Lin, Y.-S. Yen, Y.-T. Cheng, C.-P. Lee, Y.-C. Hsu, H.-H. Chou, C.-Y. Hsu, Y.-C. Chen, J.T. Lin, K.-C. Ho, Dihydrophenanthrene-based metal-free dyes for highly efficient cosensitized solar cells, *Org. Lett.*, 14 (2012) 3612-3615.
- [15] E. Stathatos, Dye sensitized solar cells as an alternative approach to the conventional photovoltaic technology based on silicon-recent developments in the field and large scale applications, *Solar cells dye-sensitized devices*, InTech, Rijeka, Croatia, 2011, 471-491.
- [16] J. Chang, C.-P. Lee, D. Kumar, P.-W. Chen, L.-Y. Lin, K.J. Thomas, K.-C. Ho, Co-sensitization promoted light harvesting for organic dye-sensitized solar cells using unsymmetrical squaraine dye and novel pyrenoimidazole-based dye, *J. Power Sources*, 240 (2013) 779-785.
- [17] L.-Y. Lin, M.-H. Yeh, C.-P. Lee, J. Chang, A. Baheti, R. Vittal, K.J. Thomas, K.-C. Ho, Insights into the co-sensitizer adsorption kinetics for complementary organic dye-sensitized solar cells, *J. Power Sources*, 247 (2014) 906-914.
- [18] X. Zhang, T. Peng, L. Yu, R. Li, Q. Li, Z. Li, Visible/near-infrared-light-induced H₂ production over g-C₃N₄ co-sensitized by organic dye and zinc phthalocyanine derivative, *ACS Catal.*, 5 (2014) 504-510.

- [19] Z. Li, Y. Wu, G. Lu, Highly efficient hydrogen evolution over Co(OH)_2 nanoparticles modified g- C_3N_4 co-sensitized by eosin Y and rose bengal under visible light irradiation, *Appl. Catal., B.*, 188 (2016) 56-64.
- [20] Z. Xue, L. Wang, B. Liu, Facile fabrication of co-sensitized plastic dye-sensitized solar cells using multiple electrophoretic deposition, *Nanoscale*, 5 (2013) 2269-2273.
- [21] P.J. Holliman, M.L. Davies, A. Connell, B.V. Velasco, T.M. Watson, Ultra-fast dye sensitisation and co-sensitisation for dye sensitized solar cells, *Chem. Commun.*, 46 (2010) 7256-7258.
- [22] B.E. Hardin, A. Sellinger, T. Moehl, R. Humphry-Baker, J.-E. Moser, P. Wang, S.M. Zakeeruddin, M. Grätzel, M.D. McGehee, Energy and hole transfer between dyes attached to titania in cosensitized dye-sensitized solar cells, *J. Amer. Chem. Soc.*, 133 (2011) 10662-10667.
- [23] S. Sardar, S. Chaudhuri, P. Kar, S. Sarkar, P. Lemmens, S.K. Pal, Direct observation of key photoinduced dynamics in a potential nano-delivery vehicle of cancer drugs, *Phys. Chem. Chem. Phys.*, 17 (2015) 166-177.
- [24] H. Choi, I. Raabe, D. Kim, F. Teocoli, C. Kim, K. Song, J.H. Yum, J. Ko, M.K. Nazeeruddin, M. Grätzel, High molar extinction coefficient organic sensitizers for efficient dye-sensitized solar cells, *Chem. Eur. J.*, 16 (2010) 1193-1201.
- [25] Y. Shi, R. Hill, J.H. Yum, A. Dualeh, S. Barlow, M. Grätzel, S.R. Marder, M.K. Nazeeruddin, A high-efficiency panchromatic squaraine sensitizer for dye-sensitized solar cells, *Angew. Chem. Int. Ed.*, 123 (2011) 6749-6751.
- [26] S. Ito, H. Miura, S. Uchida, M. Takata, K. Sumioka, P. Liska, P. Comte, P. Péchy, M. Grätzel, High-conversion-efficiency organic dye-sensitized solar cells with a novel indoline dye, *Chem. Commun.*, 41 (2008) 5194-5196.
- [27] H. Choi, S.O. Kang, J. Ko, G. Gao, H.S. Kang, M.S. Kang, M.K. Nazeeruddin, M. Grätzel, An efficient dye-sensitized solar cell with an organic sensitizer encapsulated in a cyclodextrin cavity, *Angew. Chem. Int. Ed.*, 121 (2009) 6052-6055.

- [28] P. Ruankham, L. Macaraig, T. Sagawa, H. Nakazumi, S. Yoshikawa, Surface modification of ZnO nanorods with small organic molecular dyes for polymer-inorganic hybrid solar cells, *J. Phys. Chem. C*, 115 (2011) 23809-23816.
- [29] G. De Miguel, M. Marchena, B. Cohen, S. Pandey, S. Hayase, A. Douhal, Relating the photodynamics of squaraine-based dye-sensitized solar cells to the molecular structure of the sensitizers and to the presence of additives, *J. Phys. Chem. C*, 116 (2012) 22157-22168.
- [30] Y. Fang, Z. Li, B. Yang, S. Xu, X. Hu, Q. Liu, D. Han, D. Lu, Effect of dye structure on optical properties and photocatalytic behaviors of squaraine-sensitized TiO₂ nanocomposites, *J. Phys. Chem. C*, 118 (2014) 16113-16125.
- [31] S. Das, T.L. Thanulingam, K.G. Thomas, P.V. Kamat, M. George, Photochemistry of squaraine dyes. 5. Aggregation of bis(2,4-dihydroxyphenyl) squaraine and bis(2,4,6-trihydroxyphenyl) squaraine and their photodissociation in acetonitrile solutions, *J. Phys. Chem.*, 97 (1993) 13620-13624.
- [32] S. Das, K.G. Thomas, K. Thomas, V. Madhavan, D. Liu, P.V. Kamat, M. George, Aggregation behavior of water soluble bis(benzothiazolylidene) squaraine derivatives in aqueous media, *J. Phys. Chem.*, 100 (1996) 17310-17315.
- [33] J. Patwari, S. Sardar, B. Liu, P. Lemmens, S.K. Pal, Three-in-one approach towards efficient organic dye-sensitized solar cells: aggregation suppression, panchromatic absorption and resonance energy transfer, *Beilstein J. Nanotechnol.*, 8 (2017) 1705-1713.
- [34] H. Yu, J. Baskin, B. Steiger, C. Wan, F. Anson, A. Zewail, Femtosecond dynamics of metalloporphyrins: electron transfer and energy redistribution, *Chem. Phys. Lett.*, 293 (1998) 1-8.
- [35] H.-Z. Yu, J.S. Baskin, A.H. Zewail, Ultrafast dynamics of porphyrins in the condensed phase: II. Zinc tetraphenylporphyrin, *J. Phys. Chem. A*, 106 (2002) 9845-9854.
- [36] P. Kar, S. Sardar, E. Alarousu, J. Sun, Z.S. Seddigi, S.A. Ahmed, E.Y. Danish, O.F. Mohammed, S.K. Pal, Impact of metal ions in porphyrin-based applied

materials for visible-light photocatalysis: Key information from ultrafast electronic spectroscopy, *Chem. Eur. J.*, 20 (2014) 10475-10483.

[37] J. Patwari, A. Chatterjee, S. Sardar, P. Lemmens, S.K. Pal, Ultrafast dynamics in co-sensitized photocatalysts under visible and NIR light irradiation, *Phys. Chem. Chem. Phys.*, 20 (2018) 10418-10429.

[38] M. Prushan, Absorption and fluorescence spectroscopy of tetraphenylporphyrin and metallo-tetraphenylporphyrin, (2005). DOI: <http://www1.lasalle.edu/~prushan/Abs%20and%20Fluor%20of%20TPPH2.pdf>.

[39] S.P. de Visser, M.J. Stillman, Challenging density functional theory calculations with hemes and porphyrins, *Int. J. Mol. Sci.*, 17 (2016) 519.

[40] V. Narayanan, P. Natarajan, Photochemistry of macromolecular metal complexes. III. Synthesis, spectral and electrochemical properties of macromolecular bound protoporphyrin in aqueous solution, *J. Polym. Sci. A*, 30 (1992) 2475-2488.

[41] J.-H. Yum, P. Walter, S. Huber, D. Rentsch, T. Geiger, F. Nüesch, F. De Angelis, M. Grätzel, M.K. Nazeeruddin, Efficient far red sensitization of nanocrystalline TiO₂ films by an unsymmetrical squaraine dye, *J. Amer. Chem. Soc.*, 129 (2007) 10320-10321.

[42] J.M. Berg, A. Romoser, N. Banerjee, R. Zebda, C.M. Sayes, The relationship between pH and zeta potential of ~30 nm metal oxide nanoparticle suspensions relevant to in vitro toxicological evaluations, *Nanotoxicology*, 3 (2009) 276-283.

[43] O. Ohno, Y. Kaizu, H. Kobayashi, Luminescence of some metalloporphyrins including the complexes of the IIIb metal group, *J. Chem. Phys.*, 82 (1985) 1779-1787.

[44] J. Kallioinen, G. Benkö, V. Sundström, J.E. Korppi-Tommola, A.P. Yartsev, Electron transfer from the singlet and triplet excited states of Ru(dcbpy)₂(NCS)₂ into nanocrystalline TiO₂ thin films, *J. Phys. Chem. B*, 106 (2002) 4396-4404.

[45] C. Karunakaran, J. Jayabharathi, R. Sathishkumar, K. Jayamoorthy, Photoinduced electron transfer from phenanthroimidazole to nano WO₃, CuO

ZrO₂ and Al₂O₃. LUMO–CB energy binding efficiency relationship, *Measurement*, 46 (2013) 3261-3267.

[46] C.-S. Lu, C.-C. Chen, L.-K. Huang, P.-A. Tsai, H.-F. Lai, Photocatalytic degradation of acridine orange over NaBIO₃ driven by visible light irradiation, *Catalysts*, 3 (2013) 501-516.

[47] C. Wang, J. Li, G. Mele, G.-M. Yang, F.-X. Zhang, L. Palmisano, G. Vasapollo, Efficient degradation of 4-nitrophenol by using functionalized porphyrin-TiO₂ photocatalysts under visible irradiation, *Appl. Catal., B.*, 76 (2007) 218-226.

[48] H. Huang, X. Gu, J. Zhou, K. Ji, H. Liu, Y. Feng, Photocatalytic degradation of rhodamine B on TiO₂ nanoparticles modified with porphyrin and iron-porphyrin, *Catal. Commun.*, 11 (2009) 58-61.

Chapter 6

Photophysical Studies on NIR Light Harvesting Nanomaterials for Potential Device Application

6.1. Introduction: Before the 1970s the achievable band gaps in the field of semiconductor optoelectronics were fully dependent on the properties of common III-V materials like GaAs and its alloy materials e.g. AlGaAs, InGaAs etc. Discovery of quantum well (QW) and super lattice structures in the year of 1970 by *Esaki* and *Tsu* [1] lead to immense growth in this field. Since then a mammoth number of studies have been done to explore the basic physical properties of quantum confinement and their use in fabrication of optoelectronic devices such as light emitting diodes (LED) [2], diode lasers [3], quantum cascade lasers [4], solar cells [5], avalanche photodiode [6], inter-sub-band detectors [7], unipolar avalanche photodiode [8], modulators [9] and photodetector [10]. In QW samples, confinement energy (well width) offers an extra degree of freedom which helps to tune the emission wavelength. The fascinating features of QW structures are due to the quasi-2D carrier system which arises mainly due to the localization of excitons. There are lots of particle exchange processes involved in QW samples such as conversion of free electrons and holes from bound excitons, defect state trapping, recreation of photons due to the annihilation of electrons and holes etc [11]. Depending on the barrier height [12] and well width, the physical properties of QWs change widely due to the change in extent of confinement. The variations of physical properties depending on the change of well thickness were reported earlier but the approach to resolve physical processes is often oversimplified [13]. Despite the large number of reports on QW structures and about their physical properties, there are still uncertainties about various thermal escape [14], tunnelling [15], inter-

subband relaxation [16] and other non-radiative processes [17] and their relative importance specially in device application at room temperature.

In this study, we have mainly focused on the explanations of the large photo-induced capacitance observed in GaAs/AlGaAs single QW and the correlation of this phenomena with the excited state lifetime of the carriers. In recent literature this type of light induced unconventional capacitance generation is discussed in case of two dimensional electron systems (2DES) such as oxide-semiconductor interfaces [18], and QWs in III-V material heterojunctions [19]. The phenomena of light induced capacitance in 2DES has been used in fabricating capacitance based photodetectors [20-22]. The same structures can be used for resonant tunnel diodes [23] and charge coupled devices [24]. It was also reported recently that the density modulation of the light generated carriers can enhance the capacitance value [25] and the quantum mechanical description of the enhanced capacitance was given in terms of correlation and exchange energies in recent literature [22]. We have given experimental evidence to the explanations of enhanced light induced capacitance using spectroscopic tools and established a correlation between the optical and electronic properties. A lot of optical studies have been done on these systems in the literature but the excitonic behaviours i.e. lifetime and carrier holding capacities have never been correlated with photo-induced electrical phenomena. The picosecond time resolved photoluminescence (TRPL) studies for the QW samples have been done to get a convincing explanation of the carrier escape mechanism from the well and its dependence on the well thickness. Comparison between the photo-induced inbuilt capacitance and resistance of these undoped QW samples by Electrochemical Impedance Spectroscopy (EIS) implies that the charge accumulation capability of the insulating media is very much dependent on well thickness. By analysing this light induced capacitance we have given a proof of the well to barrier escape process to be the main nonradiative path of losing carriers. From the capacitance-voltage (C-V) measurement it was proven that the higher value of capacitance in the thicker well was due to the higher charge holding

capacity. The quantitative estimation of photocurrent generated from different samples with different width is convincingly correlated with the energy level distribution and escape mechanism of the electrons. Thus, in this present study we have successfully explained the two components of excitonic lifetime by correlating them with the light induced electronic phenomena which are solely dependent on the exciton generation, the carrier holding capacity of the confined structure and the loss mechanisms.

6.2. Results and Discussion:

6.2.1. Photo-induced Electronic Properties in Single Quantum Well System: Effect of Excitonic Lifetime [26]:

6.2.1.1 Material Characterization: The quantum well structures, used in this study, as shown in Figure 6.1a and the growth technique has been explained in Chapter 3. The only difference between the two samples of this study is the well thickness which is confirmed by the TEM images shown in Figure 6.1b and Figure 6.1c. It is clearly depicted in the TEM images that the well thicknesses are 5.3 nm and 16.5 nm, respectively while the barrier thicknesses are 25 nm in both the cases. Another notable feature which can be mentioned from Figures 6.1b and 6.1c is that the flat interfaces and good homogeneity. The barrier layer ($\text{Al}_x\text{Ga}_{(1-x)}\text{As}$) bandgap of 1.74 eV was calculated using Vegards law. The steady-state photoluminescence spectra measured at 19 K and 300 K temperatures are represented in Figures 6.2a and 6.2b for the thin and thick well sample, respectively. It is evident that the QW samples have only one prominent emission at lower temperature i.e. from first electronic ($n=1$) level to first heavy hole (HH1) level. The peak position of the 16.5 nm well is at ~ 45 nm higher wavelength than the ~ 5.3 nm well. This is because of the difference in confinement energy as explained by simulated results later. The peak positions are red shifted at 300 K temperature than that of 19 K temperature because of the decrease in band gap with increase in temperature according to Varshini's Law [27]. Notable difference between the spectra of 19 K and 300 K is the presence of a

shoulder at the higher energy side of the peak for the second case. This peak accounts for the $n=1$ electronic state to the light hole state of the confined structure [28-31]. This transition becomes visible only at higher temperature because at temperature below 100 K the light hole valence band level was not thermally populated and thermal equilibrium between the electrons and the light hole is a necessary condition for the transition to take place [32]. For 5.3 nm well sample,

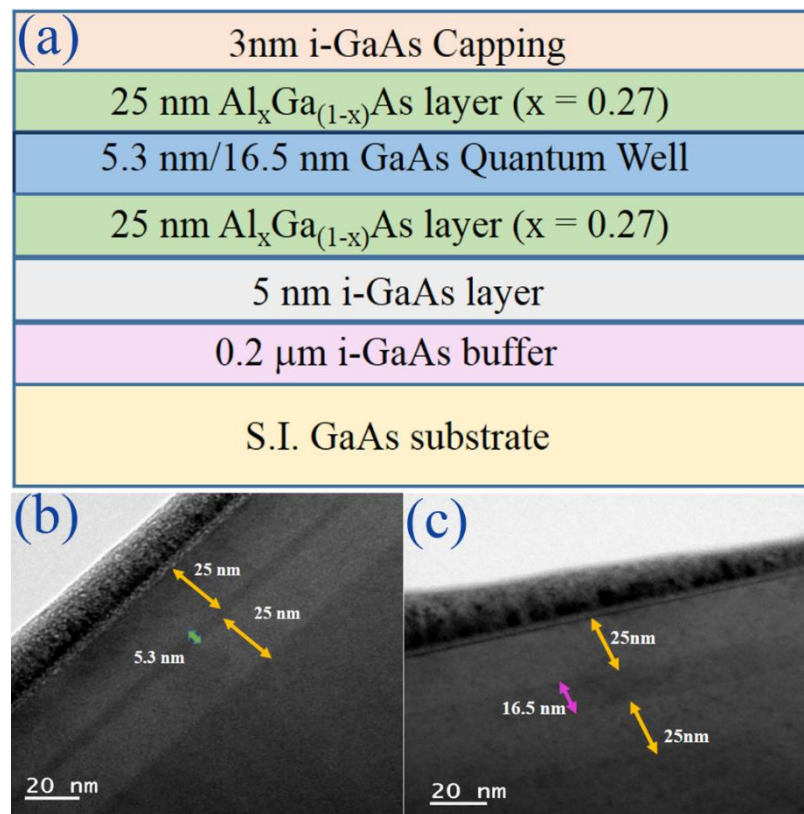


Figure 6.1: (a) Structure of QW samples with well width 5.3 nm and 16.5 nm, (b) TEM image of sample with 5.3 nm well width, (c) TEM image of sample with 16.5 nm well width.

the lower intensity peak at 870 nm is probably due to the GaAs substrate layer. In the case of the 16.5 nm well that substrate layer peak is masked by the peak from $n=1$ to heavy hole level transition. Activation energies (E_{a1}) from the first electronic state of the quantum well (QW) were calculated from the temperature dependent PL for both the samples. Using Gaussian fitting, the area under the curve was calculated and used in a double variable exponential decay function. Activation

energy for first electronic state was calculated at higher temperature where the equation became 1D and from the slope of linear fitting at high temperatures (equation 6.1). The reduced equation is given as,

$$I(T) = \frac{I(0)}{1+A\exp\left(-\frac{E_{a1}}{KT}\right)} \quad (6.1)$$

where $I(T)$ and $I(0)$ are the area under the curve fitted from Gaussian fitting at 19 K and 300 K, respectively. A is constant, k is the Boltzmann constant and E_{a1} is the activation energy for first electronic state. The magnitude of E_{a1} for the thinner well was found to be ~ 87.26 meV and that for the thicker one is ~ 191.6 meV.

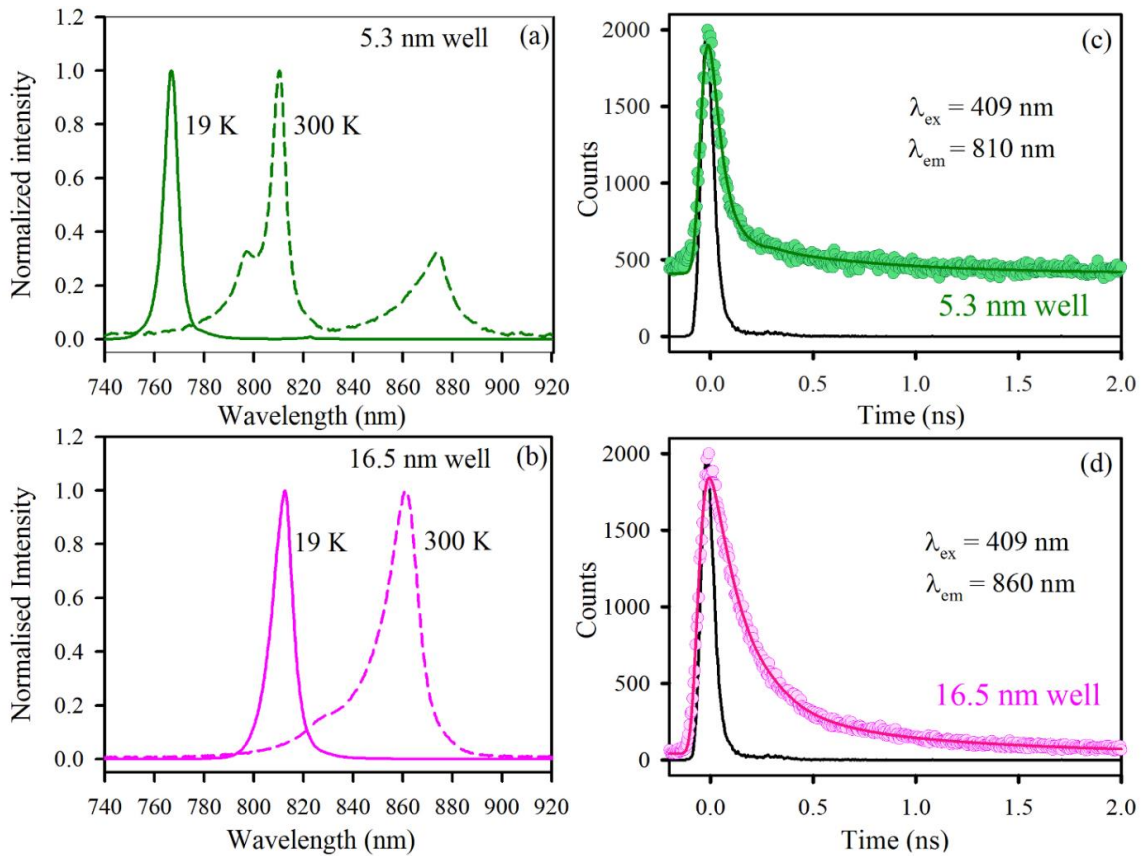


Figure 6.2: (a) and (b) Steady-state photoluminescence spectra of 5.3 nm well and 16.5 nm well, respectively, (c) and (d) time resolved photoluminescence spectra of 5.3 nm well and 16.5 nm well, respectively.

Figure 6.2c and 6.2d represents the picosecond resolved PL decay of the two samples. From the excited state carrier lifetimes mentioned in Table 6.1 it can be noted that both the QW samples have a faster time component due to the presence

of non radiative pathways. It is well documented in the literature that charge carriers in sufficiently narrow QWs have more than an order of magnitude shorter lifetime than those observed in bulk material of comparable quality [13, 33, 34]. The faster non radiative process occurring is due to a localization-induced reduction of radius in 2D exciton [13, 28, 33, 35]. At room temperature, recombination occurs between free carriers not between excitons [36]. The characteristic time of exciton formation from free carriers lies in the range from several tens to hundreds of picoseconds [37-41]. The exciton thermalization in the reservoir occurs approximately in the same time range [37, 42-44]. Width dependent study of the recombination dynamics were also done previously by various groups [13, 45] and the recombination time has been seen to decrease monotonically with the decreasing well thickness. In our study, the initial faster component of carrier lifetime was observed to be 45 ps for thinner well and 150 ps in case of thicker well. The relative percentage of the faster time component is nearly the same for both. The same non radiative mechanistic pathway is attributed to explain the faster component in both the cases. As a non-resonant excitation source has been used, non radiative recombination in GaAs channels as well as in AlGaAs barrier is equally probable [46]. We propose the thermal escape of the free carriers from the well towards the barrier is the predominant factor to monitor the faster time scale of PL decay which can also be correlated with the activation energy values. The energy difference between the well and the barrier is smaller in the case of the thinner well than that of the thicker as described by the energy level distribution earlier. As a consequence the τ_1 is much slower in case of the thicker well. PL and TRPL results are in coherence with each other and as expected high activation energy is required for the carriers to escape from the thicker well. Slower carrier lifetime indicates formation of loosely bound exciton in thicker well which can be applicable in charge migration based devices. Device characterization was carried out in presence of light to explore this charge migration possibility in current QW structures.

Table 6.1. Fitted decay time constant of QW and bulk samples from picosecond resolved PL experiments.^a

Sample	τ_1 (ps)	τ_2 (ps)	τ_{avg} (ps)
5.3 nm well	45 (93%)	650 (7%)	87.35
16.5 nm well	150 (87%)	846 (13%)	240.48

^aNumbers in the parenthesis indicate relative weightages.

6.2.1.2 Simulation Results: The energy level values calculated using MATLAB simulation for four different well widths are shown in Figure 6.3b. The model used for the calculation is shown in Figure 3a and the respective notations, terms and parameters are mentioned in Table 6.2 and Table 6.3. The energy levels calculated from the code is in good agreement with PL peak energies, as evident from Figure 6.3c. As explained from the experimental results the difference between ground state and excited state energies is higher in the thinner well which is evident from our simulation results. With increase in well thickness a reduction in energy spacing was observed which reduces resonant tunnelling effect. This higher spacing between the ground state and excited state energies in thinner well results in negative resistance which is further proved from current voltage characteristics in the device characterization section.

Table 6.2: Notations and terms used in simulation:

E_{gw}	Band gap of the well
E_{gb}	Band gap of the barrier
f	GaAs-AlGaAs band gap discontinuity percentage for electrons
N_b	Barrier width in terms of number of discrete points
N_w	Well width in terms of number of discrete points
x	Alluminum percentage in AlGaAs
m	Mass of electron in free space
m_{we}	Effective mass of electron in well
m_{be}	Effective mass of electron in barrier
m_{wh}	Effective mass of hole in the well
m_{bh}	Effective mass of hole in the barrier
T	Measurement temperature

Table 6.3: Material parameters as obtained from NSM archive:

E_{gw}	$1.519-5.405 \times 10^{-4} T^2 / (T+204)$
E_{gb}	$1.519+1.55x+0.37x^2-5.41 \times 10^{-4} T^2 / (T+204)$
f	0.65
m_{we}	0.063m
m_{be}	$(0.063+0.083x)m$
m_{wh}	0.51m
m_{bh}	$(0.51+0.25x)m$

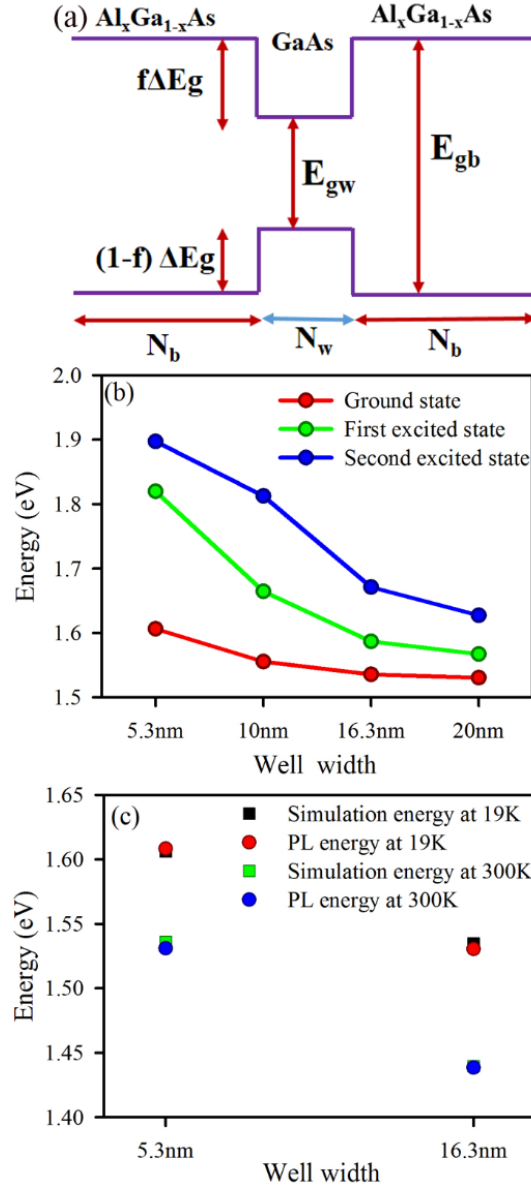


Figure 6.3. (a) Model used for simulation (terms and notations are described in table 6.2 and 6.3, (b) graphical representation of calculated energy values for different well widths. (c) Comparison of experimental and calculated energy values.

6.2.1.3. Device Characterization: The structure of the device is shown in Figure 6.4a and the fabrication technique has been explained in Chapter 3. A significant increase in capacitance for both the QW samples was observed upon light irradiation. The behaviour of the whole system can be considered as a metal-insulator-metal capacitor. Generation of light induced capacitance is due to charge separation forming exciton in presence of photons and the system behaves as a parallel plate capacitor with two different junctions. Semi insulating GaAs substrate to metal junction capacitance can be neglected as it is too thick and the carrier concentration is significantly low. To quantitatively measure the photo-induced capacitance for QW samples, the analysis of impedance spectra was carried out as shown in Figure 6.4b and fitted the data with an equivalent resistance-capacitance (RC) circuit which has one in-built geometric resistance (ohmic) and two RC circuits as shown in the inset of Figure 6.4b. The associated parameters are summarized in Table 6.4. The high frequency limit in Nyquist plot accounts for the geometric resistance in our study and that value is of the same order of magnitude for both the QW samples. It is clear from the Figure 6.4b that for both the samples there are two semi circles in which the higher frequency one is the characteristics of the interface of metal and capping GaAs layer. Resistance and capacitance values representing the semicircle at higher frequency side do not show significant variation. The associated resistance with the semicircle at lower frequency side differs by order of magnitude with the increase in the well thickness. This semicircle represents the junction of the well with the capping GaAs layer. As shown in Table 6.4, the capacitance (C_2) increases with increase in well width and correspondingly resistance (R_2) value decreases. The explanation behind the larger capacitance value is the better charge accumulation in case of the wider well, as proved earlier from the excited state lifetime measurements. Resistance (R_2) is greater in case of narrower well because decreasing well thickness results in increase in distribution of trapping states [47]. Capacitance-resistance characteristics obtained through

impedance spectroscopy can be useful in the field of capacitance-based photodetectors [20].

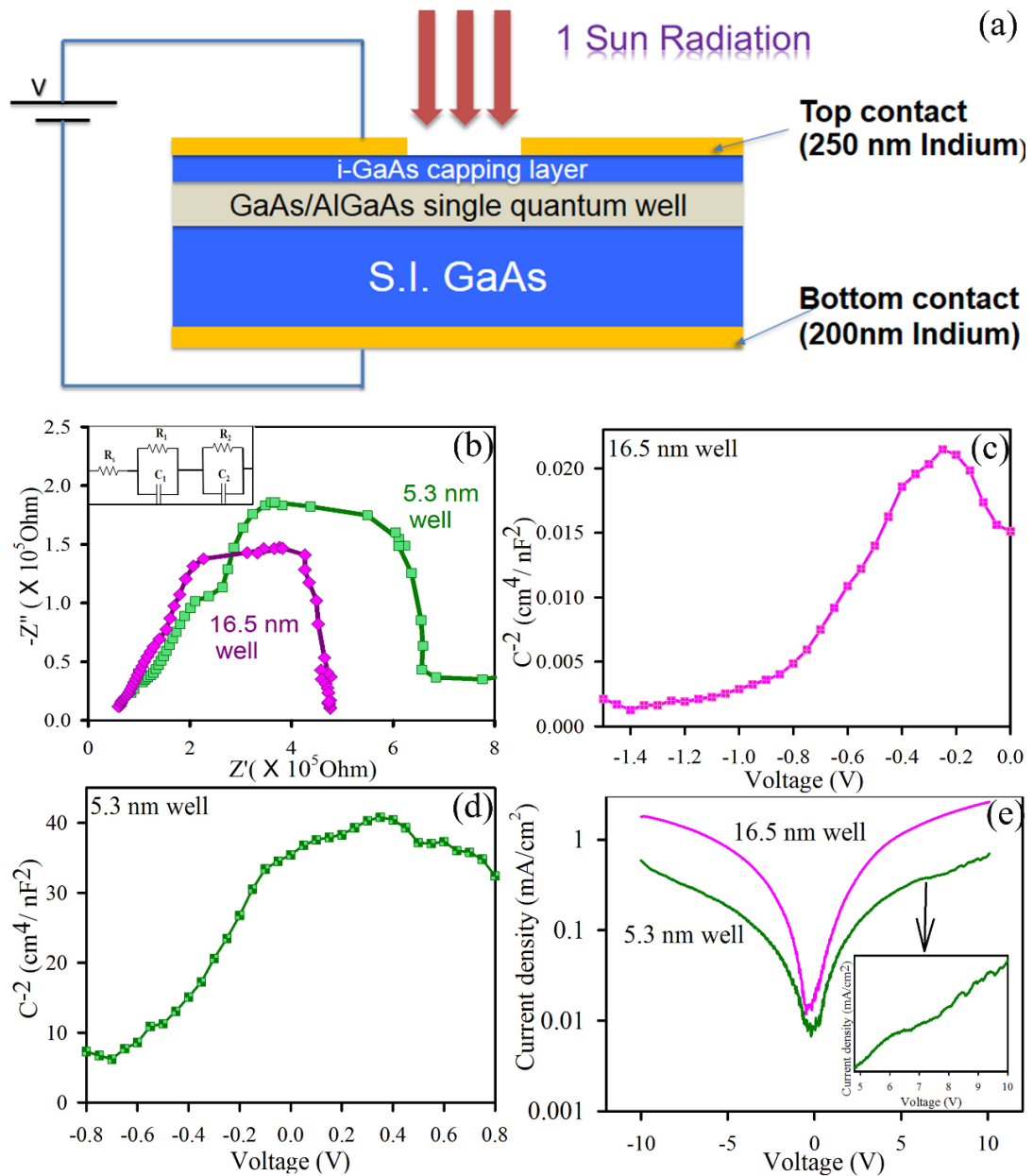


Figure 6.4: (a) Device structure, (b) Nyquist plots of different samples. Equivalent circuit model that was used to fit the EIS spectra is shown in the inset, (c) C-V characteristics of 5.3 nm well, (d) C-V characteristics of 16.5 nm well, (e) I-V characteristics of 5.3 nm well and 16.5 nm well. The inset shows the NDR effect for the 5.3 nm well.

To quantitatively measure the carrier concentration associated with the increased capacitance upon light irradiation the capacitance-voltage (C-V) characterization were performed. Figure 6.4c and 6.4d represents Mott-Schottky

plots for the thicker and thinner well respectively. The method used in this study for the quantitative estimation of carrier concentrations in QW sample was originally developed by K. Kreher in 1993 [48]. The carrier concentration at different junctions were measured by fitting the Mott-Schottkey data with the following equation,

$$\frac{1}{C^2} = \frac{2V}{\epsilon\epsilon_0 N_1 e} + \left(1 - \frac{N_w}{N_1}\right) \frac{(2d_2 + d)d}{(\epsilon\epsilon_0)^2} + \left(1 - \frac{N_2}{N_1}\right) \frac{d_2^2}{(\epsilon\epsilon_0)^2} \quad (6.2)$$

Where C is the total capacitance, V is the applied bias, ϵ and ϵ_0 is permittivity of well and free space. Permittivity constants for GaAs and AlGaAs are $12.9\epsilon_0$ and $12.19\epsilon_0$, respectively. Permittivity constant for the well was considered as an effective permittivity constant calculated from GaAs and AlGaAs. N_w is the total carrier concentration in the well, N_1 and N_2 are the carrier concentrations in the capping layer and semi-insulating substrate GaAs layer respectively, d_2 is the capping layer thickness and d is the thickness of the AlGaAs/GaAs/AlGaAs heterojunction. The capping layer is assumed to be of i-GaAs layer (3 nm) and total well thicknesses are (55.3 nm and 66.5 nm). The carrier concentration of the semi-insulating wafer (N_2) is much lower than capping layer (N_1) so the later part of the expression i.e. ratio of N_2/N_1 can be ignored. The simplified expression used in the calculation is given below,

$$\frac{1}{C^2} = \frac{2V}{\epsilon\epsilon_0 N_1 e} + \left(1 - \frac{N_w}{N_1}\right) \frac{(2d_2 + d)d}{(\epsilon\epsilon_0)^2} + \frac{d_2^2}{(\epsilon\epsilon_0)^2} \quad (6.3)$$

The associated carrier concentrations obtained for thicker well was 2 order higher than the thinner well which is consistent with the capacitance values obtained from the impedance spectroscopy and the trend in carrier escape phenomena observed in the time resolved PL measurements. The carrier concentrations values for different junctions of different samples extracted from the Mott-Schottky measurements are summarized in Table 6.5. In the thicker well these loosely bound excitons can be migrated from one terminal to another which has

potential applications in the field of charge coupled devices and photo-induced capacitive circuits. Current voltage characteristics will give further insights in photo generated charge transfer within QW structures which can be related to C-V results.

Table 6.4. EIS parameters of DSSCs fabricated using different active and counter electrodes.

Sample	R_s (Ohm)	R_1 (Ohm)	R_2 (Ohm)	C_1 (F)	C_2 (F)
5.3 nm well	9.27×10^4	5.7×10^5	1.09×10^5	3.34×10^{-8}	3.36×10^{-9}
16.5 nm well	6.45×10^4	3.4×10^5	5.6×10^4	4.5×10^{-8}	8.7×10^{-9}

Table 6.5. Carrier concentrations at different junction from C-V measurements.

Sample	N_1 (/cm ²)	N_w (/cm ²)
5.3 nm well	3.07×10^{11}	4.49×10^{11}
16.5 nm well	4.44×10^{13}	4.096×10^{13}

The current-voltage (I-V) characteristics of both QW samples is shown in Figure 6.4e. A noteworthy result was increase in output current with increasing well thickness. It can be concluded from the I-V data that the current coming out of the well is due to tunnelling so the whole device performs as a resonant tunnel diode. As the $n=1$ electronic state is lower in case of the thicker well, the ground electronic state becomes resonant with the emitter level for much lower bias than the thinner one. So, the thicker well is a better candidate for devices like resonant tunnel diode. For the thinner well sample an anomalous behaviour is observed in the IV curve nature at $\sim 6V$ applied voltage which is illustrated in the inset of Figure 6.4e. A negative differential resistance is observed in that region of applied bias as the tunnelling current is dropping due to the energy mismatch of the ground electronic levels and emitter levels and the second electronic level energy reduces due to band bending, then the thermionic emission becomes predominant. The reason behind the higher current associated with the thicker well is that the energy levels are such that thermionic emission current contribution is negligible compared to tunnelling

component at higher applied bias. The anomalous behaviour of having higher capacitance and higher current was observed in thicker well sample. It can be explained as the total capacitance in QW structures is a combination of diffusion and junction capacitances. Junction capacitance is inversely related to depletion width which can be assumed to be similar in both QW structures whereas the diffusion capacitance (C_d) is directly proportional to diffusion current (I_d) which is evident from the following equation [49],

$$C_d = \frac{\tau I_d}{\eta V} \quad (6.4)$$

Where τ is the average lifetime of the carrier which is also lower in case of thinner well and η is the generation-recombination co-efficient which is same for both the samples as the same excitation source is used for both the samples in all the studies. The higher tunnelling current for the thicker well is due to higher carrier diffusion which is consistent with the higher C_d achieved in the same sample. The average carrier lifetime for thicker well was comparatively higher than the thinner one which will result in more capacitive or charge accumulation with light irradiation and major component was contributed by diffusion capacitance. As diffusion capacitance is dependent on diffusing current, this capacitance can be used to modulate charge accumulation from one terminal of QW to another.

6.3. Conclusion: Dependence of the main nonradiative process on well thickness for GaAs/AlGaAs QW samples is revealed by steady-state and picosecond resolved PL studies. Temperature dependent PL results exhibit an increase in activation energy with increasing well width. Time resolved PL studies show that the narrower well exhibits faster decay lifetime compared to that of wider well due to the lower energy barrier which facilitates the thermal escape of the photo generated carriers from the well to barrier. EIS spectroscopy inflicted higher charge accumulation in thicker well which was modelled with 2 capacitive R-C circuits. The higher charge accumulation is further confirmed from the Mott-Schottky data which was found to be two order of magnitude higher in case of thicker well. The

higher photocurrent in the thicker well measured from I-V characteristics implies that the source of the current in the case of the thicker one is tunnelling not the thermionic emission. So the predominant nonradiative process is the thermal escape of carriers and that was proven both from electrical and optical signature of the systems. These huge photo-generated carriers could be used in future application of the QW samples in capacitance based photo-induced devices and photogenerated charge migration based devices like charge coupled devices and resonant tunnel diodes.

References

- [1] L. Esaki, R. Tsu, Superlattice and negative differential conductivity in semiconductors, *IBM J. Res. Dev.*, 14 (1970) 61-65.
- [2] M. Krames, J. Bhat, D. Collins, N. Gardner, W. Götz, C. Lowery, M. Ludowise, P. Martin, G. Mueller, R. Mueller-Mach, High-power III-nitride emitters for solid-state lighting, *Phys. Status Solidi A*, 192 (2002) 237-245.
- [3] E.P. O'Reilly, A.R. Adams, Band-structure engineering in strained semiconductor lasers, *IEEE J. Quant. Electron.*, 30 (1994) 366-379.
- [4] J. Faist, F. Capasso, D.L. Sivco, C. Sirtori, A.L. Hutchinson, A.Y. Cho, Quantum cascade laser, *Science*, 264 (1994) 553-556.
- [5] K. Barnham, I. Ballard, J. Barnes, J. Connolly, P. Griffin, B. Klufftinger, J. Nelson, E. Tsui, A. Zachariou, Quantum well solar cells, *Appl. Surf. Sci.*, 113 (1997) 722-733.
- [6] S. Asamira, Y. Atsushi, Y. Tatsuo, I. Ken, O. Yoshimasa, Dark current reduction of avalanche photodiode using optimized InGaAsP/InAlAs superlattice structure, *Jpn. J. Appl. Phys.*, 41 (2002) 1182.
- [7] D.G. Sarath, S. Gabby, S.P. Jin, L. True-Lon, F.L. Barry, Infrared detectors reach new lengths, *Phys. World*, 7 (1994) 35.
- [8] B. Levine, K. Choi, C. Bethea, J. Walker, R. Malik, Quantum well avalanche multiplication initiated by 10 μm intersubband absorption and photoexcited tunneling, *Appl. Phys. Lett.*, 51 (1987) 934-936.
- [9] J.S. Weiner, D.A. Miller, D.S. Chemla, Quadratic electro-optic effect due to the quantum-confined Stark effect in quantum wells, *Appl. Phys. Lett.*, 50 (1987) 842-844.
- [10] M. Horstmann, M. Marso, A. Fox, F. Rüdgers, M. Hollfelder, H. Hardtdegen, P. Kordos, H. Lüth, InP/InGaAs photodetector based on a high electron mobility transistor layer structure: Its response at 1.3 μm wavelength, *Appl. Phys. Lett.*, 67 (1995) 106-108.
- [11] D. Block, R. Romestain, P. Edel, S. Fränke, Exciton and free carrier dynamics in GaAs quantum wells: excitation density effects, *J. Lumin.*, 53 (1992) 339-344.

- [12] G.-B. Lin, D.-Y. Kim, Q. Shan, J. Cho, E.F. Schubert, H. Shim, C. Sone, J.K. Kim, Effect of quantum barrier thickness in the multiple-quantum-well active region of GaInN/GaN light-emitting diodes, *IEEE Photon. J.*, 5 (2013) 1600207-1600207.
- [13] E. Göbel, H. Jung, J. Kuhl, K. Ploog, Recombination enhancement due to carrier localization in quantum well structures, *Phys. Rev. Lett.*, 51 (1983) 1588.
- [14] M. Gurioli, J. Martinez-Pastor, M. Colocci, C. Deparis, B. Chastaingt, J. Massies, Thermal escape of carriers out of GaAs/Al_xGa_{1-x}As quantum-well structures, *Phys. Rev. B*, 46 (1992) 6922.
- [15] K. Leo, J. Shah, J. Gordon, T. Damen, D. Miller, C. Tu, J. Cunningham, Effect of collisions and relaxation on coherent resonant tunneling: Hole tunneling in GaAs/Al_xGa_{1-x}As double-quantum-well structures, *Phys. Rev. B*, 42 (1990) 7065.
- [16] A. Seilmeier, H.-J. Hübner, G. Abstreiter, G. Weimann, W. Schlapp, Intersubband relaxation in GaAs-Al_xGa_{1-x}As quantum well structures observed directly by an infrared bleaching technique, *Phys. Rev. Lett.*, 59 (1987) 1345.
- [17] H.-J. Polland, K. Leo, K. Ploog, J. Feldmann, G. Peter, E. Göbel, K. Fujiwara, T. Nakayama, Hot carrier trapping in GaAs/AlGaAs single quantum wells with different confinement structures, *Solid-State Electron.*, 31 (1988) 341-344.
- [18] L. Li, C. Richter, S. Paetel, T. Kopp, J. Mannhart, R. Ashoori, Very large capacitance enhancement in a two-dimensional electron system, *Science*, 332 (2011) 825-828.
- [19] X. Zhao, A. Cola, A. Tersigni, F. Quaranta, E. Gallo, J.E. Spanier, B. Nabet, Optically modulated high-sensitivity heterostructure varactor, *IEEE Electron Device Lett.*, 27 (2006) 710-712.
- [20] P. Dianat, R.W. Prusak, A. Persano, F. Quaranta, A. Cola, B. Nabet, Giant light-induced capacitance enhancements in an unconventional capacitor with two-dimensional hole gas, *Photonics Conference (IPC)*, Burlingame, CA, (2012) 792-793.
- [21] M. Horstmann, M. Marso, A. Fox, F. Rüdgers, M. Hollfelder, H. Hardtdegen, P. Kordos, H. Lüth, InP/InGaAs photodetector based on a high electron mobility

- transistor layer structure: Its response at 1.3 μm wavelength, *Appl. Phys. Lett*, 67 (1995) 106-108.
- [22] P. Dianat, A. Persano, F. Quaranta, A. Cola, B. Nabet, Anomalous capacitance enhancement triggered by light, *IEEE J. Sel. Top. Quantum Electron.*, 21 (2015) 228-232.
- [23] V. Sharma, R.P. Singh, Nano Scale Simulation of GaAs based Resonant Tunneling Diode, *Int. J. Eng. Comput. Sci*, 2 (2013) 3580-3583.
- [24] W. Goodhue, Using molecular-beam epitaxy to fabricate quantum-well devices, *Linc Lab J*, 2 (1989) 183-205.
- [25] P. Dianat, R. Prusak, E. Gallo, A. Cola, A. Persano, F. Quaranta, B. Nabet, A highly tunable heterostructure metal-semiconductor-metal capacitor utilizing embedded 2-dimensional charge, *Appl. Phys. Lett*, 100 (2012) 153505.
- [26] J. Patwari, H. Ghadi, S. Sardar, J. Singhal, B. Tongbram, S. Shyamal, C. Bhattacharya, S. Chakrabarti, S.K. Pal, Photo-induced electronic properties in single quantum well system: effect of excitonic lifetime, *Mater Res Express* 4 (2017) 016301.
- [27] Y.P. Varshni, Temperature dependence of the energy gap in semiconductors, *Physica*, 34 (1967) 149-154.
- [28] J. Christen, D. Bimberg, Recombination dynamics of carriers in GaAs-GaAlAs quantum well structures, *Surf. Sci.*, 174 (1986) 261-271.
- [29] J. Fouquet, A. Siegman, Room-temperature photoluminescence times in a GaAs/ $\text{Al}_x\text{Ga}_{1-x}\text{As}$ molecular beam epitaxy multiple quantum well structure, *Appl. Phys. Lett*, 46 (1985) 280-282.
- [30] J. Fouquet, A. Siegman, R. Burnham, T. Paoli, Carrier trapping in room-temperature, time-resolved photoluminescence of a GaAs/ $\text{Al}_x\text{Ga}_{1-x}\text{As}$ multiple quantum well structure grown by metalorganic chemical vapor deposition, *Appl. Phys. Lett*, 46 (1985) 374-376.
- [31] R. Miller, D. Kleinman, W. Tsang, A. Gossard, Observation of the excited level of excitons in GaAs quantum wells, *Phys. Rev. B*, 24 (1981) 1134.

- [32] H.-J. Polland, W. Rühle, J. Kuhl, K. Ploog, K. Fujiwara, T. Nakayama, Nonequilibrium cooling of thermalized electrons and holes in GaAs/Al_xGa_{1-x}As quantum wells, *Phys. Rev. B*, 35 (1987) 8273.
- [33] J. Christen, D. Bimberg, A. Steckenborn, G. Weimann, Localization induced electron-hole transition rate enhancement in GaAs quantum wells, *Appl. Phys. Lett*, 44 (1984) 84-86.
- [34] D. Bimberg, J. Christen, A. Steckenborn, G. Weimann, W. Schlapp, Injection, intersubband relaxation and recombination in GaAs multiple quantum wells, *J. Lumin.*, 30 (1985) 562-579.
- [35] G. Bastard, E. Mendez, L. Chang, L. Esaki, Exciton binding energy in quantum wells, *Phys. Rev. B*, 26 (1982) 1974.
- [36] J.E. Fouquet, R.D. Burnham, Recombination dynamics in GaAs/Al_xGa_{1-x}As quantum well structures, *IEEE J. Quant. Electron.*, 22 (1986) 1799-1810.
- [37] A. Trifonov, S. Korotan, A. Kurdyubov, I.Y. Gerlovin, I. Ignatiev, Y.P. Efimov, S. Eliseev, V. Petrov, Y.K. Dolgikh, V. Ovsyankin, Nontrivial relaxation dynamics of excitons in high-quality InGaAs/GaAs quantum wells, *Phys. Rev. B*, 91 (2015) 115307.
- [38] C. Piermarocchi, V. Savona, A. Quattropani, P. Schwendimann, F. Tassone, Photoluminescence and carrier dynamics in GaAs quantum wells, *Phys. Status Solidi A*, 164 (1997) 221-225.
- [39] D. Bajoni, P. Senellart, M. Perrin, A. Lemaitre, B. Sermage, J. Bloch, Exciton dynamics in the presence of an electron gas in GaAs quantum wells, *Phys Status Solidi B*, 243 (2006) 2384-2388.
- [40] J. Szczytko, L. Kappei, J. Berney, F. Morier-Genoud, M. Portella-Oberli, B. Deveaud, Determination of the exciton formation in quantum wells from time-resolved interband luminescence, *Phys. Rev. Lett.*, 93 (2004) 137401.
- [41] M. Portella-Oberli, J. Berney, L. Kappei, F. Morier-Genoud, J. Szczytko, B. Deveaud-Plédran, Dynamics of trion formation in In_xGa_{1-x}As quantum wells, *Phys. Rev. Lett.*, 102 (2009) 096402.

- [42] P. Basu, P. Ray, Energy relaxation of hot two-dimensional excitons in a GaAs quantum well by exciton-phonon interaction, *Phys. Rev. B*, 45 (1992) 1907.
- [43] C. Piermarocchi, F. Tassone, V. Savona, A. Quattropani, P. Schwendimann, Nonequilibrium dynamics of free quantum-well excitons in time-resolved photoluminescence, *Phys. Rev. B*, 53 (1996) 15834.
- [44] A. Ivanov, P. Littlewood, H. Haug, Bose-Einstein statistics in thermalization and photoluminescence of quantum-well excitons, *Phys. Rev. B*, 59 (1999) 5032.
- [45] A. Hariz, P.D. Dapkus, H. Lee, E. Menu, S. DenBaars, Minority-carrier lifetimes in undoped AlGaAs/GaAs multiple quantum wells, *Appl. Phys. Lett*, 54 (1989) 635-637.
- [46] Y. Fang, L. Wang, Q. Sun, T. Lu, Z. Deng, Z. Ma, Y. Jiang, H. Jia, W. Wang, J. Zhou, Investigation of temperature-dependent photoluminescence in multi-quantum wells, *Sci. Rep*, 5 (2015) 12718.
- [47] J. Bisquert, Beyond the quasistatic approximation: Impedance and capacitance of an exponential distribution of traps, *Phys. Rev. B*, 77 (2008) 235203.
- [48] K. Kreher, Capacitance-voltage characteristics of a quantum well within a Schottky layer, *Phys Status Solidi A*, 135 (1993) 597-603.
- [49] U. Bakshi, A. Godse, Analog electronics, *Technical Publications*, 2009.

Chapter 7

Temperature Dependent Photophysical Studies on NIR Light Harvesting Nanomaterials

7.1. Introduction: So far the efficiency of solar energy converting devices is largely limited by the poor photon to current conversion in the near-infrared or NIR spectral region [1-3]. The materials absorbing in the NIR spectral region are getting immense attention to the scientific and engineering community in recent years [2, 4-6]. The application of Infrared (IR) active materials in devices such as solar cells [7], photodetectors [8], photocapacitor [9], imaging devices [10, 11], photodiodes [12], light emitting devices (LEDs) [13] and light amplification by stimulated emission of radiation (LASERS) [14] is indispensable in this era of semiconductor technology. The widely used IR absorbing and emitting materials in device fabrication are thin film heterostructures of self-assembled quantum dots (InAs or InGaAs) [15], colloidal quantum dots (PbS or PbSe) [16], various IR emitting dyes [17] and up-converting nanomaterials [18]. The study of the unique photophysical properties for each of these IR sensitive materials is essential in order to optimize the device performance and to find out the perfect fabrication strategy. Picosecond time resolved photoluminescence (TRPL) study in the NIR spectral region (900 nm to 1700 nm) for these materials is a promising tool for detail investigation of the photoinduced carrier mechanism which would ultimately control the device phenomena [19, 20]. Although, there have been earlier reports in cryo assisted TRPL in the NIR region for quantum dots or quantum well samples, the commonly used technique is femtosecond resolved up-conversion [21, 22]. Eventually, the carrier mechanism occurring at sub diffusive time scale can't be captured in femtosecond resolved studies. Very often, the relaxation of the excited state carriers does not entirely complete within the measurement time window for femto-second resolved

studies. Again, most of the IR emitting QDs (PbS, PbSe) have radiative lifetime in the several hundreds of nanosecond or microsecond ranges depending on the size of the QD. Thus, a flexibility of operating time window starting from tens of picosecond to hundreds of nanosecond is needed to portray the excited state carrier dynamics with quantitative timescales for capture, migration and diffusion of carriers in these NIR emitting materials. Pico-second resolved NIR time correlated single photoncounting (TCSPC) can provide the variability to measure all the above-mentioned processes which is the motivation of the present customized NIR TCSPC instrument.

In the recent literatures, the picosecond time resolved dynamics of NIR emitting materials are receiving growing interest but to the best of our knowledge, TRPL study at NIR with widely varying temperature ranges for devices on action is really sparse in the contemporary literature [23]. Again, we are aware of the fact that TCSPC system for near infrared (NIR) spectral region is commercially available in market. But the commercial set up does not possess the features for in situ measurement of transient photoluminescence of device samples under tuneable bias voltages at liquid nitrogen temperature. Although the provision of temperature dependent TRPL can be managed by external attachment of the cryostat to the commercially available set up, some indigenous designing is essential to provide bias to the active device samples at widely varying temperatures during the measurement. Additionally, most of the thin film device samples have microscopic contacts. Thus, a microscope compatible sample holder is required to probe the contact of the device properly. Eventually, our customized system has been designed in such a way so that the external voltage dependent TRPL can be measured in situ for active device samples having microscopic contacts and the system has the flexibility to measure temperature dependent TRPL starting from -196 °C to 400 °C. To the best of our knowledge, this combination for the NIR TCSPC system having all the above mentioned features has not been reported so far. For

visible light emitting devices such as copper indium gallium selenide (CIGS) solar cells [24], GaN quantum dot light emitting diode (QLED) [25] and perovskite solar cell [26], the bias dependent TRPL study has recently been reported. Upon applying external bias to the active device the energy band diagram changes. Bias dependent TRPL provides necessary information to the band bending. The consequent changes at the interfaces affect the carrier dynamics and excited state lifetime as well. Another interesting point of bias dependent TRPL is to find out the optimum operability condition for the devices. For photo-detector or solar cell devices, the dominance of the thermionic current and tunnelling current at different applied bias could be easily correlated with the bias dependent TRPL results. Thus, the bias dependent TRPL is a must to conceptualize the proper dynamical behaviour of the majority and minority carriers in devices during their action. We believe that for NIR emitting devices the low temperature TRPL at varying bias can provide some exciting features of the active material which could be helpful to develop the device technology.

In the present work, we are reporting a customized system design for a liquid nitrogen cooled cryo assisted TCSPC for NIR (900 nm to 1700 nm) along with the provision of varying bias on a device sample with macroscopic and microscopic contacts. The sub hundred picosecond resolution of the system could allow us to study a variety of NIR emitting materials having lifetime from tens of picosecond to microsecond ranges. For the validation of the system, we have taken a molecular beam epitaxy (MBE) grown InAs/InGaAs/GaAs/AlGaAs dot in the dual well (DDWELL) heterostructure with top and bottom n-doped contacts as a model sample. The DDWELL structure has been reported to be ideal material for the multistack IR detector because of reduced strain per stack [27]. In the present study, the temperature dependent, emission energy dependent and bias dependent TRPL of the device sample have been carried out and the results are explained with a detail photophysical mechanism of the carriers. Carrier capture, thermal escape of

electrons, hole diffusion and carrier storage at the interfaces are the key features of the heterostructure which we have investigated in detail. In future, we would like to explore the carrier dynamics of IR sensitive quantum dot sensitized solar cell (QDSSC), quantum well infrared photodetector (QWIP), QLED and other devices using the indigenously developed system which might be helpful to design better material to achieve better device efficiencies.

Self-assembled InAs/GaAs quantum dots (QDs) have received considerable attention, due to their promising applications in opto-electronic devices [28-32]. The development of the InAs/GaAs QD based optical devices has progressed rapidly in last few years. However, the performance of such optical devices is still not satisfactory, due to their inability to tune the emission wavelength to certain desired values (3 to 5 and 8 to 14 μm) which are suitable for the optical fiber communication systems and infrared detectors. Hence, the dots-in-a-well (DWELL) structure has been widely investigated in the last decade as they provide tunability of emission wavelength [33-35]. InAs quantum dots are enclosed in asymmetric InGaAs wells and further capped with a GaAs barrier in a DWELL configuration. This DWELL design is based on optical transitions between dot and quantum well (QW) states and offers additional possibility to vary transition energy by adjusting QW width and composition. To optimize the operation of such devices it is essential to know their optical properties and electronic structures in detail [36]. Quantum dot infrared photodetectors (QDIPs) fabricated from DWELL are used to study the device properties as they offer low dark current and higher operating temperature with optimized quantum well thickness which consequently increases the quantum efficiency.

For DWELL structures the emission wavelength can be tuned by varying InGaAs strain-reducing layer (SRL) capping thickness. It causes the relaxation of the compressive strain around the QDs and In-Ga intermixing between the capping layer and the QDs is suppressed [36-38]. Also, the morphology and emission

wavelength can be varied by changing the InGaAs strained buffer layer (SBL) or pseudo-morphic layer [37-40]. Thus, in DWELL structures, growth parameters for the well layer, such as thickness and composition of the SBL and SRL, can be tuned to match the wavelength. While considerable efforts have been made to study the effect of composition of capping layer on the optical properties of the DWELL structure [41-43], very few studies have explored the effect of variation of the well thickness on its optical and electronic properties. It is a conventional approach to introduce ternary or quaternary capping over QDs to reduce interdiffusion and provide an additional energy level for inter-subband transition. Even though it is beneficial, these capping thickness and molar concentration have to be optimized. Almost every report in literature suggests increasing capping layer thickness benefits in QD formation and improves device performance [37-43]. A detailed analysis i.e. photophysics, structural, device characterization and correlation with theoretical simulation is yet to be reported. A higher quantum and optical efficiency can be obtained by changing the well thickness and deducing an optimized DWELL configuration.

In the second part of this work, we have studied the effect of variation of well thickness in three samples of InAs/InGaAs DWELL structure. The strain reducing layer is varied (4, 6 and 8 nm) keeping the pseudo-morphic layer fixed. The optical and device properties of three samples are compared. A concentration dependent strain model is developed to correlate our experimental results with the simulated results. The energy transitions obtained in the experimental model are compared with the peaks in the spectral response and thus the model is validated. This report is a detail study on DWELL systems by emphasizing on optical such as Photoluminescence (PL) and Time-resolved Photoluminescence (TRPL), structural e.g. Transmission electron microscopy (TEM) and simulated results to establish a good correlation with the fabricated device characteristics.

7.2. Results and Discussion:

7.2.1. *In Situ* Measurement of Temperature Dependent Picosecond Resolved Carrier Dynamics in Near Infrared (NIR) Sensitive Device on Action [44]: The multi-junction heterostructure of the dot in double well (DDWELL) structure is shown in Figure 7.1a. It has been represented that the sample is grown on a semi insulating GaAs substrate layer. 10 layers of the symmetric InAs/InGaAs/GaAs/AlGaAs DDWELL structure is grown on a 200 nm GaAs buffer layer for the device. Two n⁺ doped GaAs layers are put on top and bottom of the active layers for electrical contacts. The multiple layers are uncoupled due

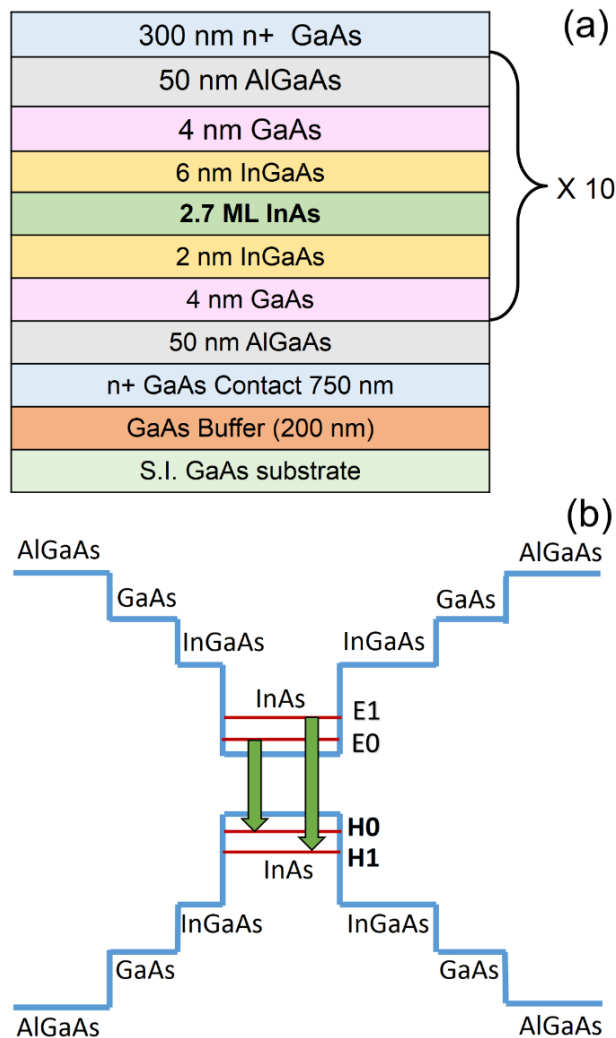


Figure 7.1. (a) Structure of the D-DWELL heterostructure and (b) the band diagram of the sample.

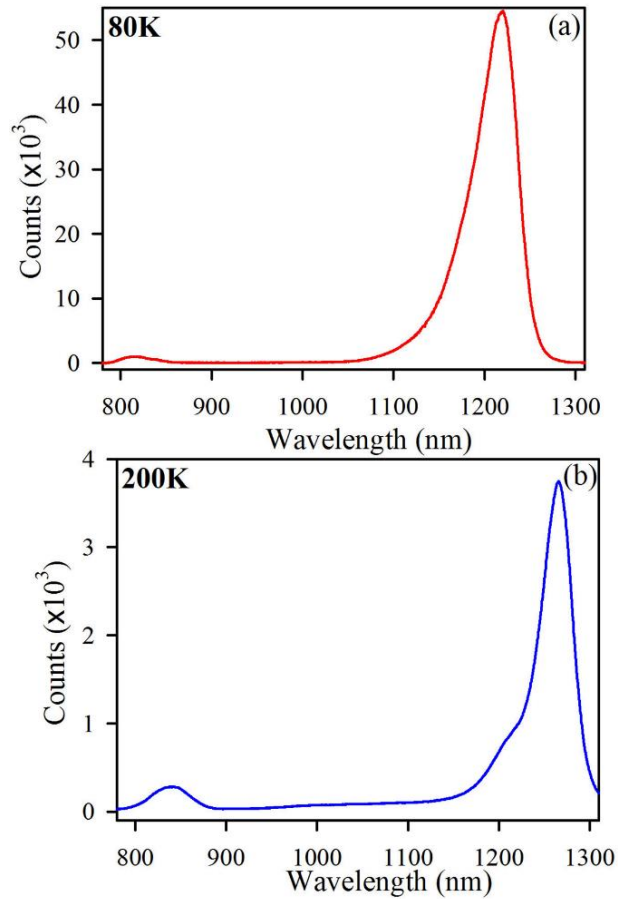


Figure 7.2. Photoluminescence spectra of the device at two different temperatures (a) 80 K and (b) 200 K.

to the presence of the thick 50 nm AlGaAs barrier. In earlier reports, the DDWELL heterostructure has been reported to be advantageous than the dot in the single well or simple dots due to reduced strain between the multiple stacks [27]. Thus, DDWELL structure is better in terms of device fabrication also and hence, is chosen as a model device sample in this study. The schematic band diagram of the active layer of the sample has been represented in Figure 7.1b. To confirm the number of energy states confined within the dot, a thorough simulation study is needed which is not the scope of the present work but at least the stepwise barrier is evident from the diagram. The energy levels embedded within the well can influence the dynamics of the carriers generated within the dots itself. The photoluminescence response of the sample at 80 K and 200 K has been shown in Figure 7.2a and 7.2b respectively. At 80K, the single emission peak at 1218 nm is due to the transition

from ground state of the conduction band (E_0) to the heavy hole level of the valance band (H_0) in the InAs QD. The small emission peak observed at 820 nm is due to transition in the bulk GaAs layer. At higher temperature, (200 K) the notable feature in the photoluminescence spectra is that both the peaks shift towards the red end (~ 40 nm) due to reduced band gap at elevated temperatures [45]. According to the earlier reports, the higher energy hump at 1200 nm is due to the prominence of the E_1 to H_1 transition [46]. The relative intensity of this particular transition is prominent compared to the main peak only at higher temperatures because at temperatures below 100 K, the light hole level of valence band is less thermally populated and thermal equilibrium between the electrons and the light hole is a necessary condition for the transition to take place.

To investigate the dynamics of photo generated carriers in DDWELL structure picosecond resolved photoluminescence study has been done at wide range of temperature starting from 80 K to 300 K upon non-resonant (510 nm) and resonant excitation (965 nm). The PL transients are shown in Figure 7.3a and 7.3b respectively. From the band gap of the materials it is evident that upon resonant excitation (965 nm) photo-induced carriers will be generated only within the dot. On the other hand, for non-resonant excitation (510 nm) all the barrier, two wells and the dot will be excited simultaneously. Thus, upon non resonant excitation, the carrier dynamics which contributes to the excited state life time are electron capture from barriers and well to the ground state of conduction band of the QD, thermionic emission from QD to the barrier, hole relaxation in the valance band etc. Thus, along with the excited state electrons created within the dot, the photo-generated carriers in the barriers and well also actively take part in determining the excited state lifetime upon non-resonant excitation. On the other hand for the resonant excitation, specifically the light induced excitons generated within the dot controls the entire carrier relaxation process. Radiative recombination from CB to VB of the QD, carrier escape from the QD and vibration relaxation are the possible carrier

mechanisms upon resonant excitation. The difference in photo

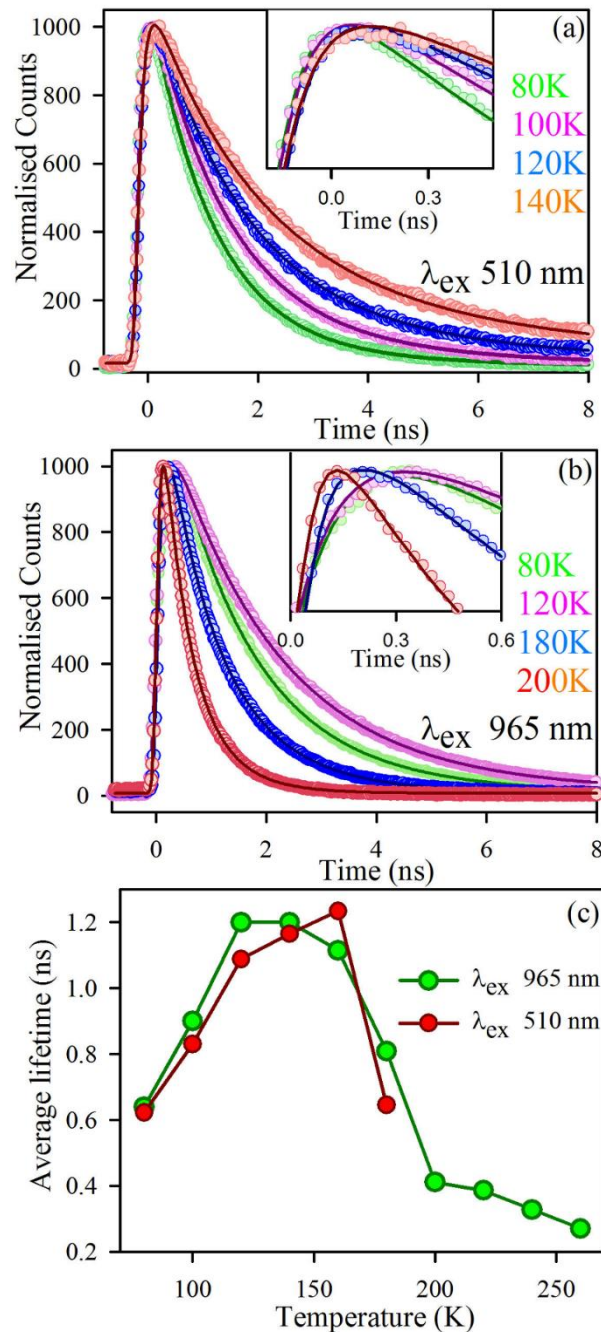


Figure 7.3. Temperature dependent TRPL for DDWELL sample at (a) nonresonant, (b) resonant excitation, the inset of (a) and (b) shows the rise times at a magnified scale and (c) dependence of average lifetime on temperature.

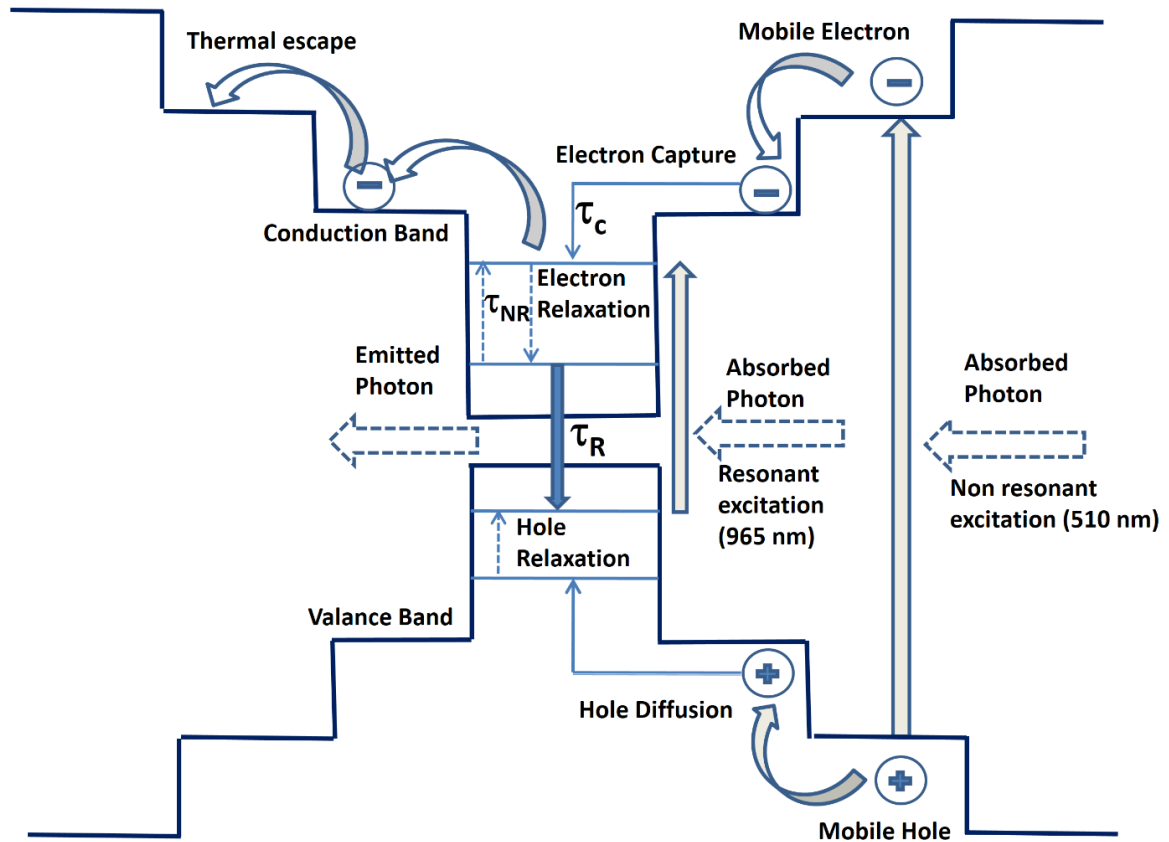


Figure 7.4. Photoexcited carrier dynamics in the DDWELL heterostructure studied from temperature dependent and wavelength dependent TRPL studies.

induced dynamical events upon resonant and non-resonant excitation is clearly depicted in Figure 7.4. Rise components in the decay patterns are responsible for the carrier capture processes to the ground state of the QD from all feasible transitions. The rise part is compared at a magnified scale in the insets of Figure 7.3a and 7.3b. On the other hand, the decay components are responsible for losing electrons from the particular excited state. It can be observed very clearly from Figure 7.3c that for both resonant excitation and non-resonant excitation, the average lifetime of the carriers at the ground state of conduction band increases upto a certain critical temperature (T_c) and then the lifetime sharply decreases. The critical temperature for the non-resonant excitation is found to be 160 K which is consistent with previously reported literature [47]. There has been a controversy in the available explanation of the increase in lifetime till the critical temperature (T_c). An increase in population of thermally excited carriers, redistribution of the carriers

between QDs and release of electrons from surface trap states are reported to be the factors affecting the average lifetime below critical temperature. Above critical temperature, non-radiative recombinations are claimed to be the predominant process. We propose that the migration of carriers from the InGaAs and GaAs well layers and the barrier as well to the ground state of the QD increases the average lifetime with increase in temperature. This carrier capture process is evident from the increasing rise component in the decay patterns with increasing temperature upto the critical temperature (T_c) as shown in the insets of Figure 7.3a and 7.3b. After T_c the thermal escape of carriers from well to the barrier is the predominant process which reduces the average lifetime sharply as evident from Figure 7.3c. It is evident from the PL decay at 200 K at Figure 7.3b that the rise component in the decay fitting also disappears gradually with increasing temperature after critical temperature (T_c) which proves the temperature dependent competition between the carrier capture and the thermal escape processes. Another noticeable fact is that the critical temperature is decreased (120 K) for the resonant excitation. As the carrier migration from the barrier and well is not present in case of the resonant excitation, the carriers starts flowing out at a lower temperature.

The competition between the carrier capture and the thermal escape process is further evident from the emission wavelength dependent transient photoluminescence at different temperatures as shown in Figure 7.5. It is evident from the tabulated timescales in Table 7.1 that at 80 K temperature, i.e. below the critical temperature the radiative decay lifetime is similar (~ 1.4 ns) at the three different emission wavelengths. Two representative TRPL data measured at two different emission wavelengths at 80 K temperature, are shown in Figure 7.5a. The three decays at 1130, 1210 and 1270 nm are all fitted in one rise component responsible for the carrier capture process and the longer decay component for the radiative recombination process. The rise component has been found to increase from blue end to red end of the emission peak due to increased carrier capture

process as shown in the inset of Figure 7.5a. Figure 7.5b represents that above the critical temperature (180 K) an additional decay component is generated along with one rise and one radiative decay timescale. This additional decay component appearing at elevated temperature is attributed to the thermal escape of carriers from the dots to the barrier. Consequently, the second decay component is observed to be much faster at the higher energy states than that of the lower one. The distinct difference of the decay pattern and the reduced rise component at the blue end of the emission spectra represented in the inset of Figure 7.5b proves the predominant carrier escape mechanism above the critical temperature. The entire carrier dynamics inferred from the temperature dependent and the wavelength dependent TRPL is demonstrated in Figure 7.4.

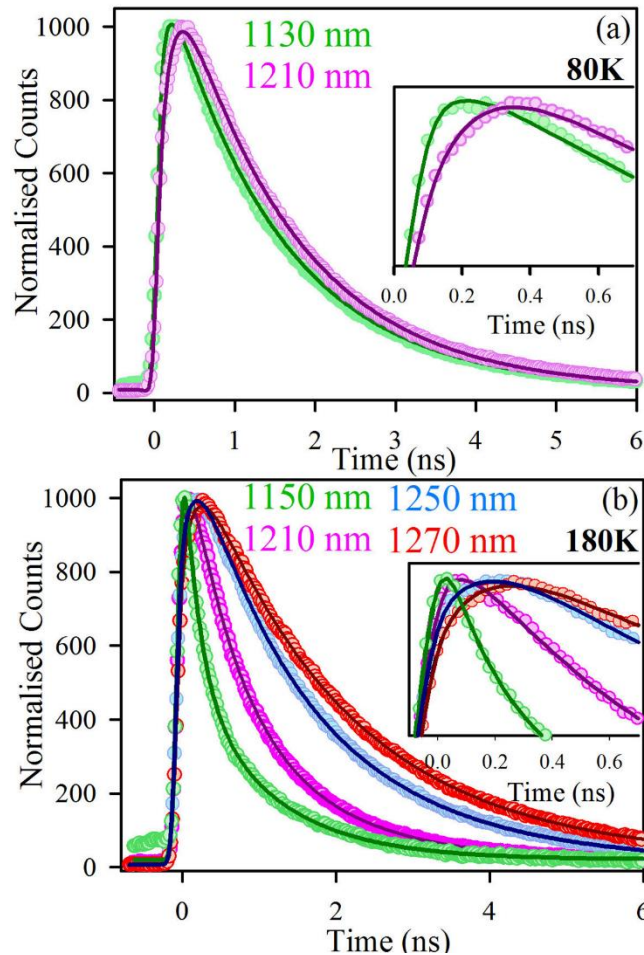


Figure 7.5. Wavelength dependent TRPL for DDWELL sample at (a) 80 K and (b) 180 K temperature upon resonant excitation. The inset of (a) and (b) shows the rise times at a magnified scale.

Table 7.1. Dynamics of picosecond resolved photo-luminescence transients of the DDWELL heterostructure at different emission wavelengths.^b

Emission wavelength (nm)	Temperature (K)	τ_1 (ns) (rise component)	τ_2 (ns) (decay component)	τ_3 (ns) (decay component)
1130	80	0.10 (-44%)		1.42 (144%)
1210	80	0.15 (-426%)		1.46 (526%)
1270	80	0.16 (-111%)		1.37 (211%)
1150	180		0.21 (60%)	1.06 (40%)
1210	180	0.10 (-73%)	0.64 (115%)	1.59 (58%)
1250	180	0.17 (-100%)	1.25 (123%)	2.20 (77%)
1270	180	0.18 (-119%)	1.84 (202%)	4.36 (17%)

^bNumbers in the parenthesis indicate relative weightages.

The structure of the fabricated device along with the proper position of the contacts have been represented in Figure 7.6a. The current (I)-voltage (V) characteristics of the device proves the authenticity of the device. The wavelength dependent photocurrent also show the response at the absorption region of AlGaAs (600 nm) and GaAs (800 nm). With the same device sample we performed a bias dependent TRPL using 510 nm excitation as shown in Figure 7.7a. The bias was provided from top to bottom contact and varied from 0 V to 15 V. All the decays are fitted in one rise and two decay components. It is shown in Figure 7.7b that the average lifetime of the carriers increases with increasing voltage up to 12 V and then decreases sharply. The similar phenomena has been reported earlier for InAs/GaAs Stranski-Krastanov (SK) dots in a charge-tunable heterostructure [23]. The phenomena have been explained as capture of photo generated holes near the interface of the nanostructure for a small range of external voltage and after a certain bias, the holes are transferred to the nanostructure in a controlled fashion reducing the average lifetime. We observe the similar phenomena applicable for the photo excited electrons as well. Upon increase in bias voltage till 12 V the rise timescale also increases as shown in the inset of Figure 7.7a, then there is a sudden decrease

in the rise timescale. This observation leads to a conclusion that the photogenerated electrons are getting trapped at the interface due to change in the band diagram and after 12 V, the carriers starts flowing out of the dot as a consequence of increased current. The dependence of the capture rate on applied voltage suggests the confinement potential of the system.

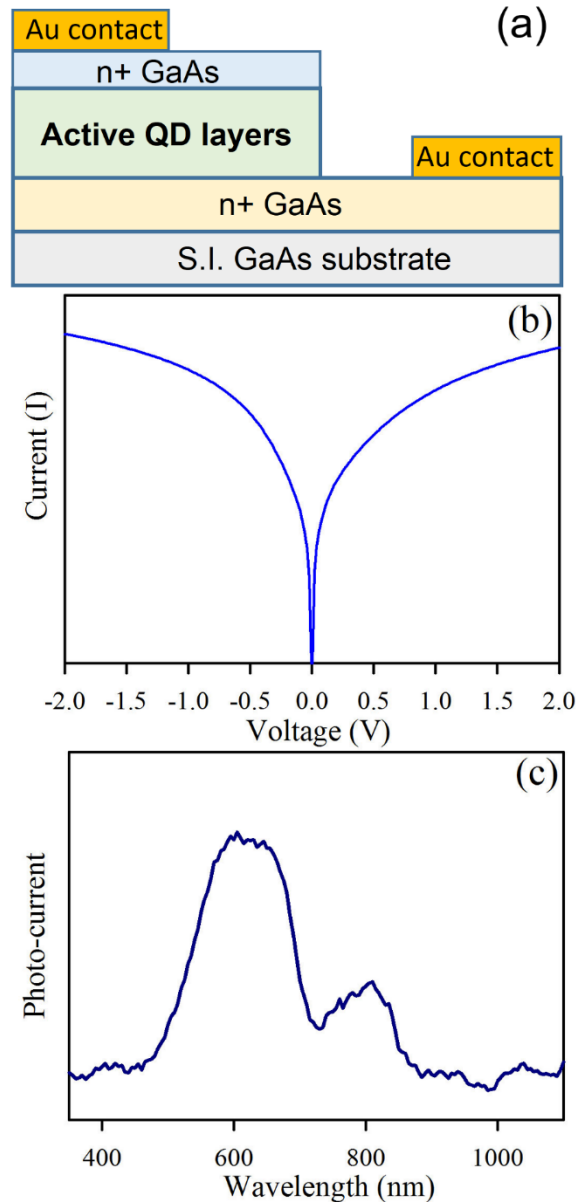


Figure 7.6. (a) Device structure, (b) IV characteristic of the device, (c) wavelength dependent photocurrent of the device.

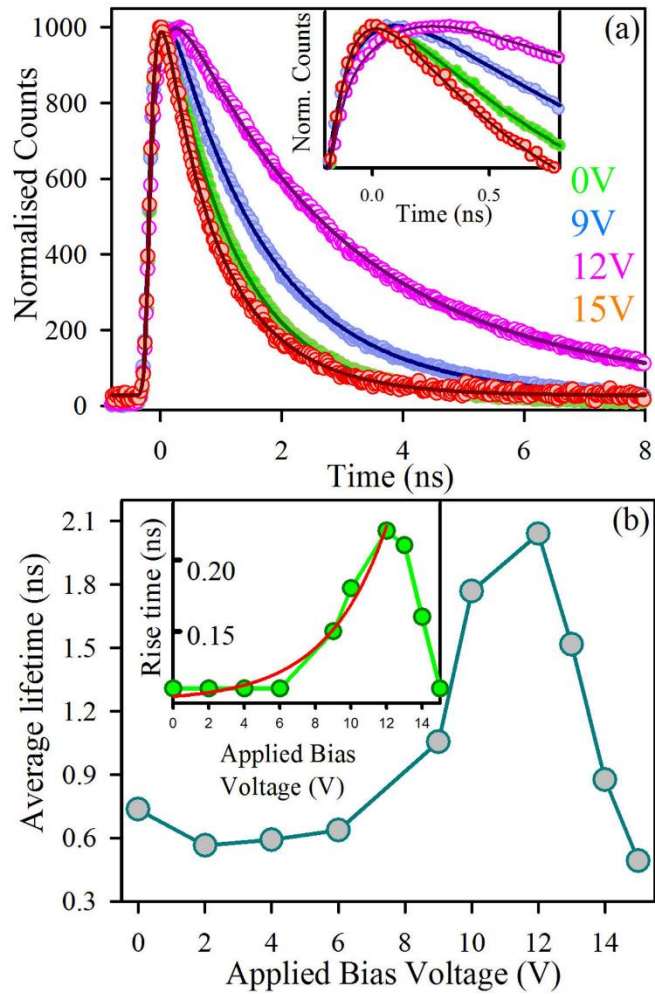


Figure 7.7. (a) Bias voltage dependent TRPL for DDWELL sample upon excitation at 510 nm, (b) dependence of average lifetime on applied bias.

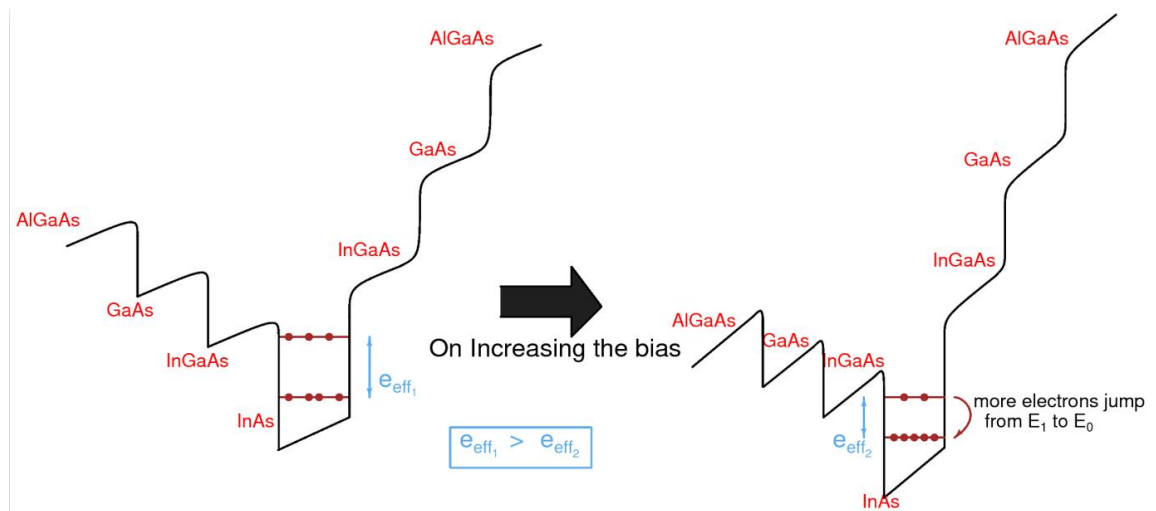


Figure 7.8. Energy relaxation dynamics upon increasing external bias voltage in voltage dependent TRPL study.

The bias dependent TRPL results can be explained using three different phenomena for three different applied bias voltage regions: (1) hole diffusion/injection (0 to 6 V), (2) energy relaxation of electrons (6 V to 12 V) and (3) breakdown (beyond 12 V). Hole diffusion or injection is responsible for the small decrease in carrier lifetimes with increasing bias voltage up to certain range (0 V-6 V). The hole diffusion mechanism is supposed to be dominant for p-type of detector structure where the majority carrier is hole. For the n-type or n-i-n diode, the contribution of hole diffusion exists to a very small extent due to the non-resonant excitation generated electron hole pair. At higher voltage, instead of diffusing in the dot layer, the hole carrier is lost in the continuum state. But for low bias/electric field the bands start bending in the lateral direction and holes start tunnelling through higher valence band states to the ground state of valence band in InAs QD [48]. This phenomena causes decrease in the average lifetime of the excited carriers. For bias values from 6 V to 12 V, the energy relaxation plays a major role to determining the carrier lifetime. We look upon the inter-subband energy level spacing i.e. energy gap between E_1 and E_0 to find a relation between lifetime, energy spacing and applied bias. The energy relaxation process can be modelled by [49],

$$\tau_{tr} = \tau_{tr0} e^{\left(\frac{\Delta E}{K_b T}\right)} \quad (7.1)$$

Here, τ_{tr} is the rise time or carrier capture time at applied bias V , τ_{tr0} is the carrier capture time in absence of any external bias, ΔE is the energy difference with external applied bias which can be written as $\Delta E = e(V - V_b)$, T is Temperature and K_b is the reduced Boltzmann constant. The fitting of the rise time is done using this formula with respect to the applied bias as shown in the inset of Figure 7.7b. After fitting V_b is found to be 11.6 V. For applied bias above 11.6 V the exponentially increasing carrier capture process does not exist anymore. At higher external bias, instead of going through radiative process the electrons stores at the thin triangular barrier or 2 dimensional electron gas (2D-GES) formed as shown in Figure 7.8 [23]. Starting bias for the carrier tunnelling is different for conduction and valence bands

since the offset is higher in the case of the conduction band as compared to valence band. The offset ratio i.e. $\frac{\Delta E_c}{\Delta E_v}$ in DDWELL heterostructures are reported in between $\frac{66}{34}$ to $\frac{70}{30}$ which validates our claim. The breakdown starts from 12 V but the maximum hole diffusion is observed at 6 V. It is evident that the carrier capture is prominent only after increasing the voltage beyond a specific value (6 V). With increasing bias the allowed energy levels come closer to each other which results in more jumps of carriers from high level to lower ones causing an increase in the rise time as shown in the inset of Figure 7.7b. For more increase in the bias, the energy levels finally collapse into one level; hence the structure collapses causing a breakdown. The band bending also plays a role here as the carriers directly go bypassing the dot instead of tunnelling through the energy levels. Breakdown occurs in a diode when a massive amount of current flows from the device from various modes like avalanche, zener etc. As we reach the breakdown, a steep drop in time constant is observed which is essentially from 12 V and above in our device. Thus, among all possible dynamical phenomena the carrier capture at the lowest energy level of conduction band is found to be the predominant in our experimental condition.

7.2.2. Optimizing Dot-in-a-well Infrared Detector Architecture for Achieving High Optical and Device Efficiency Corroborated with Theoretically Simulated Model [50]:

7.2.2.1. Optical Characterization: The three different DWELL samples used in this study are shown in Figure 7.9 and the details of the growth technique are described in Chapter 3. Low temperature (8 K) photoluminescence (PL) spectrum exhibits maximum peak intensity at 1142.74, 1166.93 and 1140.38 nm for the samples A, B and C, respectively as shown in Figure 7.10. A threefold increase in highest peak intensity was measured from sample B at 8 K. A red shift obtained in sample B can be attributed to formation of larger dots (increase in height of QD) with increase in capping layer thickness. This is due to reduction in the compressive strain on the

quantum dots layer which results in better vertical confinement [37-39]. Blue shift of around 24 nm with a decrease in intensity was obtained when the capping thickness was further increased from 6 to 8 nm. This is attributed to reduction in surface migration process with increasing strain reducing layer thickness. As the capping thickness increases another dominant process to hinder the growth is low surface transport of indium atoms. Reduced surface migration process leads to formation of QD in two possible scenarios. Firstly, the growth in vertical direction is restricted resulting in bigger dots with smaller height i.e. dots are laterally stretched and vertically squeezed. In second scenario, smaller InAs dots coalesce with one another and dissolve, giving rise to formation of InGaAs well with varying In concentration.

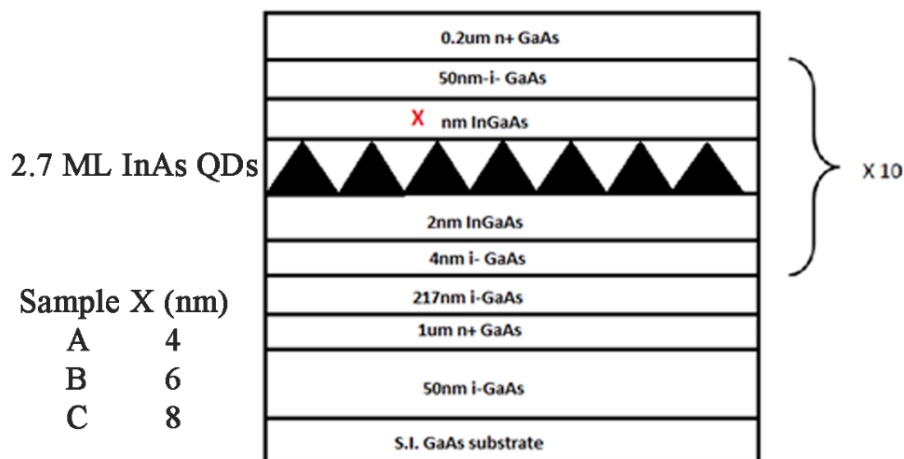


Figure 7.9. Schematic diagram of DWELL samples A , B and C.

For highest capping thickness, InAs dot layer between the strain reducing layer (SRL) and the pseudomorphic layer (bottom 2 nm InGaAs layer) dissolves. Thus forms an InGaAs well with non-linear In concentration. Consequently, the concentration of In gradually decreases from the center of the well to the edges. Subsidiary peaks obtained at 1080.86, 1104.84 and 1085.02 nm for samples A, B and C, respectively (Figure 7.10) were the ground state peaks of the InGaAs well structure.

Maximum absolute area was achieved from sample B. Also, the FWHM is the maximum for sample B. An increase in FWHM suggests non-uniform dot size distribution. The FWHM further decreases for sample C due to the dissolution of the quantum dots. In sample B, even though there is non-uniformity in QD size distribution a significantly high PL intensity was observed. Increase in intensity is achieved possibly because of increasing density of dots available for absorption. The SRL layer provides In gradient across the dot to reduce out-diffusion and also act as a strain reducing layer thus forming bigger dots. For thin capped samples, strain relaxation and out-diffusion processes are limited whereas increasing capping layer above an optimum thickness might result in dots sublimation. Hence, above a particular capping thickness (6 nm) a reduction in PL intensity with blue shift is observed [51-55].

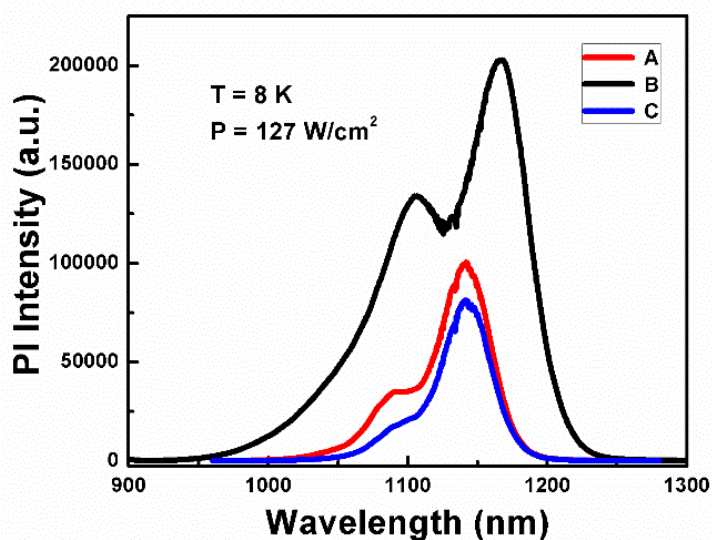


Figure 7.10. Photoluminescence intensity measured at 8 K. Power density 127 W/cm².

Temperature dependent PL measurement was carried out and thermal escape energy was calculated using standard process reported in our earlier work [51, 52]. Sample B exhibited highest thermal escape energy in comparison with others. The achieved activation energies for sample A, B and C were 201.46, 232.96 and 193.65 meV, respectively. High activation energy suggests better confinement with a possibility of improved device performance.

The photoluminescence excitation (PLE) spectra for all samples are shown in Figure 7.11. PLE measurement indicates the presence of first and second excited state at 1074.62 and 1006.11 nm for sample A (Figure 7.11a), 1098.55 and 1034.51 nm for sample B (Figure 7.11b) and 1062.98 and 1003.34 nm for sample C (Figure 7.11c). The observed first excited state values in sample A and B are within the range whereas in case of sample C the transition appeared to be from some other confinement.

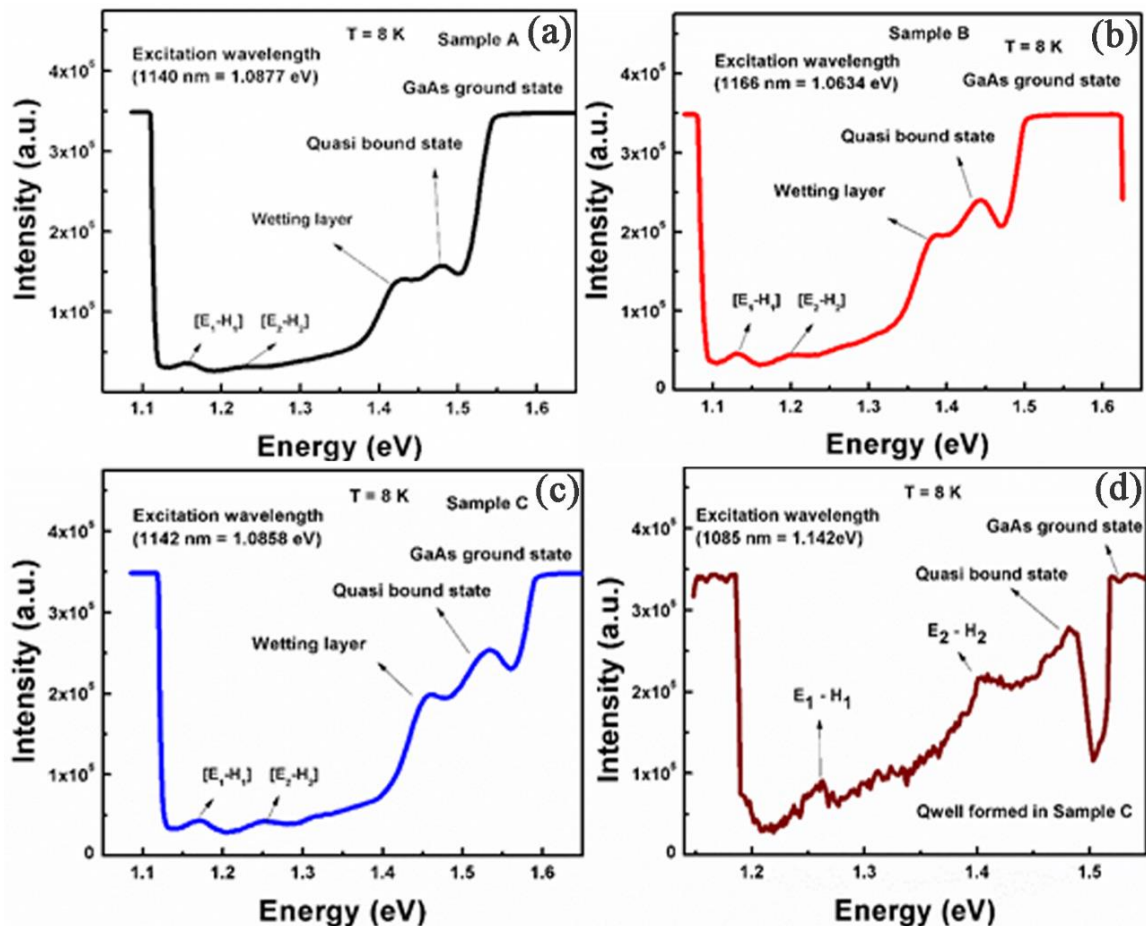


Figure 7.11. PLE Spectra measured at 8 K (a) at 1140 nm in sample A (b) at 1166 nm in sample B. (c) at 1142 nm (ground state) from sample C, (d) at 1085 nm in sample C.

To further investigate PLE spectra, keeping the emission wavelength fixed at 1085.02 nm for sample C measured first excited state peak was at 981.4 (1.2635 eV) nm and second excited state at 879.3 (1.412 eV), respectively. The PLE signature for Figure 7.11d is different from ground state PLE spectrum at Figure 7.11c. Hence, it

can be deduced here that owing to the dissolution of dots, there exists a gradient of In concentration in the space between two InGaAs layers (SRL and Pseudomorphic layer) forming a new confined structure. Increasing capping thickness arises the possibility of InGaAs quantum well formation thus lowering device performance in DWELL structures. The PLE spectra measured at lower wavelength for samples A and B exhibited a blue shift having similar response as shown in Figure 7.11c and 7.11d indicating the origin of spectrum from same source i.e. quantum dots.

It is evident from Figure 7.12 that the excited state PL decay lifetimes from the measured PL peaks (ground and excited states) are the signature of radiative recombination at different energy levels. The higher energy hump of the PL is associated with a radiative recombination within the capping layer where the excited state lifetime has one rise component and one decay component. As, the TRPL has been measured upon a non-resonant high energy excitation, the rise component of 220 ps can be assigned to the carrier migration timescale from barrier GaAs to the capping layer InGaAs while the radiative decay lifetime is 0.81 ns and 1 ns respectively for the 4 nm and 6 nm capping layer samples at 80 K temperature. The red-shifted higher intensity PL peak is most likely due to the ground state recombination (e_0-h_0) within the InAs QD having three components of lifetimes in both the cases of 4 nm capping (Table 7.2) and 6 nm capping (Table 7.3). The rise component at this state is higher in time scale i.e. 350 ps due to the carrier migration both from the GaAs barrier and the InGaAs capping layer. There have been two decay timescales associated with the excited state of the InAs QDs both in case of 4 nm and 6 nm samples. The longer one is the radiative recombination timescale and the shorter decay timescale can be ascribed to the non-radiative carrier loss mechanisms. The 8 nm capping (Table 7.4) sample is showing a different decay pattern with two exponential time scales at the 1150 nm PL peak position which is an additional proof of suppression of vertical growth of InAs QDs with increasing capping layer thickness and decreased QD confinement (or dissolved dots).

Comparing the decay patterns for three of the samples it can be concluded that with increasing capping layer thickness the carrier lifetimes at InAs QD are behaving similar. For the 8 nm samples, both the carrier lifetimes at ground and excited states are having single rise and single decay pattern unlike the other two samples.

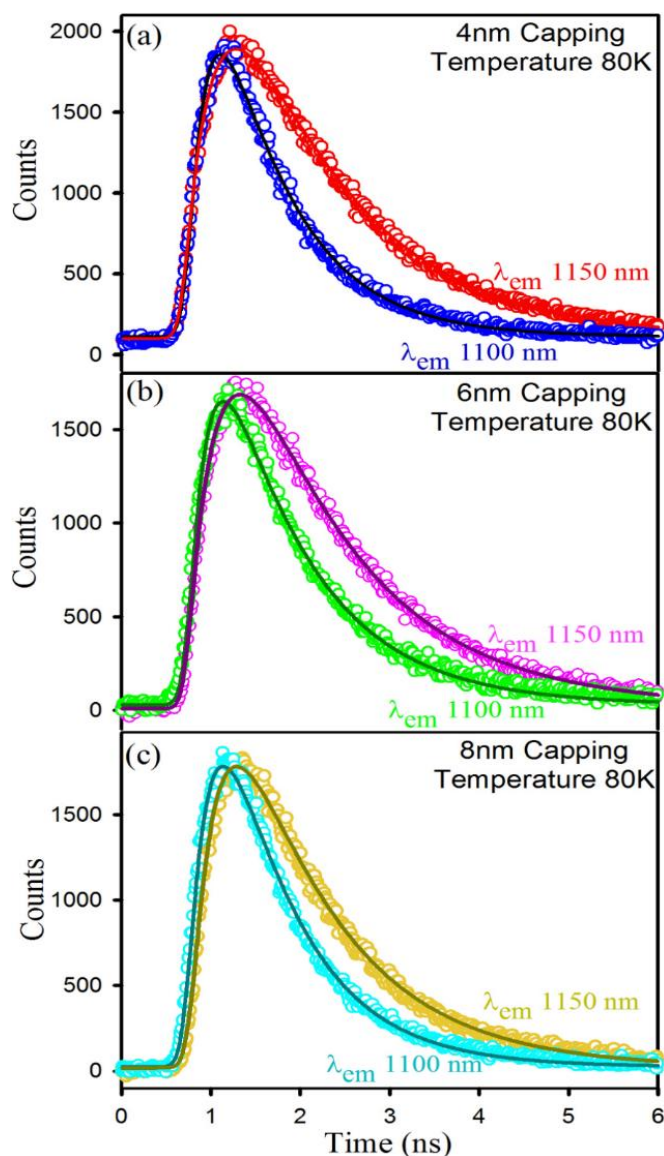


Figure 7.12. Picosecond-resolved photoluminescence transients of (a) 4 nm capping, (b) 6 nm capping, (c) 8 nm capping DWELL samples at different PL peak positions.

Figure 7.13 shows the temperature dependent nature of the PL transients, where it can be observed that for the 4 nm sample the excited state peak position is not much affected by temperature while for ground state peak the radiative

recombination timescale is gradually increasing with the increase in temperature [21, 56]. This particular observation is consistent with earlier reported literature [47, 57]. The probable reasons behind it is large carrier lifetime of the migrated electrons from barriers and capping layer to the QDs and thermally induced population of dark excitations. In case of the 8 nm sample, the carrier lifetimes at both the peak positions (ground state and other confined Qwell state) are found to be affected by temperature [58] and the overall carrier lifetime has increased with increasing temperature. Lesser QD confinement (or dot sublimation) to some extent leads to the similarity in behaviour of the PL transients at both the peak positions in case of the 8 nm capping sample unlike that with 4 nm which is in good agreement with the conclusions from other studies.

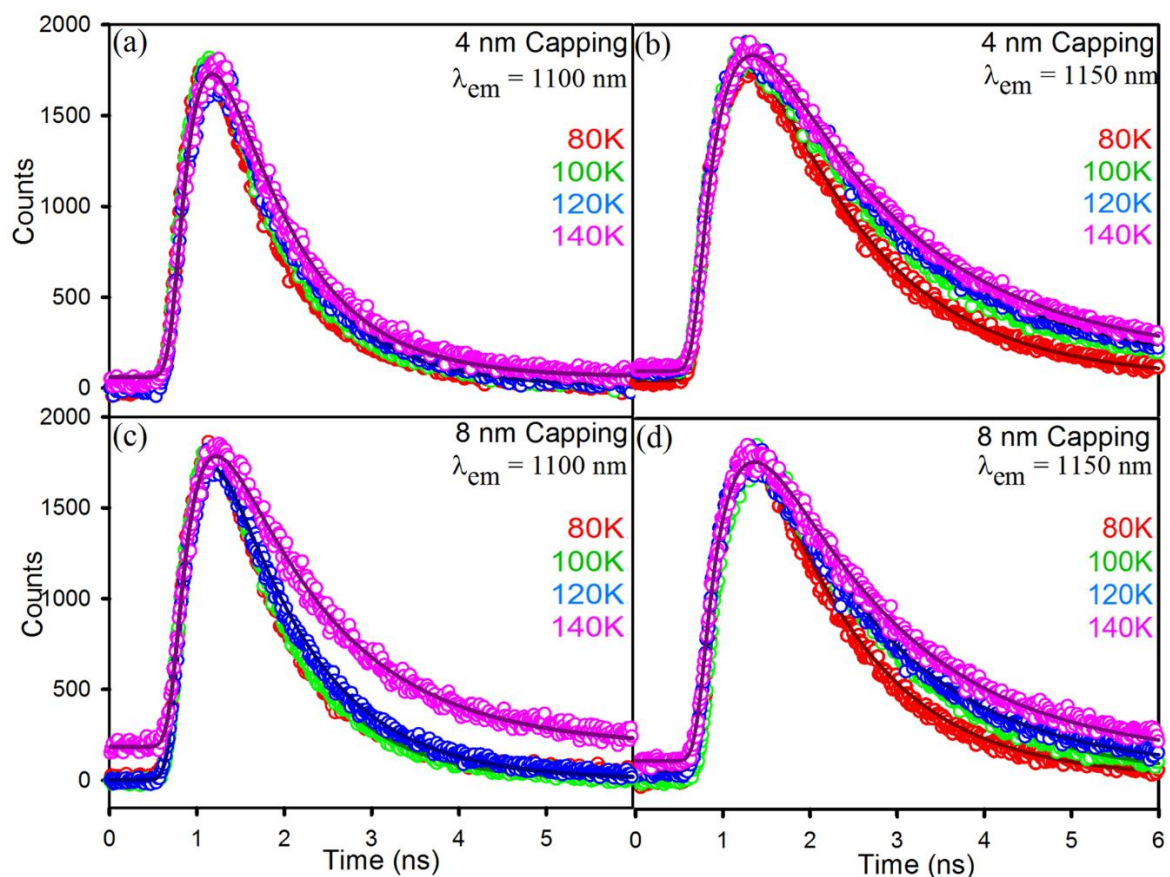


Figure 7.13. Temperature dependent time-resolved photoluminescence decay profiles of (a-b) 4 nm capping and (c-d) 8 nm capping DWELL samples at different emission wavelengths.

Table 7.2. Excited state lifetimes from the fitting details of TRPL data for sample A.^b

Emission wavelength (nm)	Temperature (K)	τ_1 (ns) (rise component)	τ_2 (ns) (decay component)	τ_3 (ns) (decay component)
1100	80	0.22 (50%)	0.81 (50%)	
1100	100	0.22 (49%)	0.85 (51%)	
1100	120	0.27 (50%)	0.85 (50%)	
1100	140	0.27 (50%)	0.85 (50%)	
1150	80	0.35 (46%)	1.52 (24%)	1.1 (30%)
1150	100	0.35 (47%)	1.97 (20%)	1.2 (33%)
1150	120	0.35 (46%)	2.18 (16%)	1.4 (38%)
1150	140	0.35 (47%)	2.67 (18%)	1.2 (34%)

^bNumbers in the parenthesis indicate relative weightages.**Table 7.3.** Excited state lifetimes from the fitting details of TRPL data for sample B.^b

Emission wavelength (nm)	Temperature (K)	τ_1 (ns) (rise component)	τ_2 (ns) (decay component)	τ_3 (ns) (decay component)
1100	80	0.22 (50%)	1.00 (50%)	
1100	100	0.24 (50%)	1.00 (50%)	
1170	80	0.27 (50%)	1.36 (16%)	1.00 (34%)
1170	100	0.35 (52%)	1.63 (21%)	1.00 (27%)

^bNumbers in the parenthesis indicate relative weightages.**Table 7.4.** Excited state lifetimes from the fitting details of TRPL data for sample C.

Emission wavelength (nm)	Temperature (K)	τ_1 (ns) (rise component)	τ_2 (ns) (decay component)	τ_3 (ns) (decay component)
1100	80	0.24 (50%)	0.84 (43%)	0.48 (7%)
1100	100	0.25 (49%)	0.84 (51%)	
1100	120	0.25 (50%)	0.97 (50%)	
1100	140	0.25 (50%)	1.27 (50%)	
1100	160	0.25 (50%)	1.15 (50%)	
1150	80	0.28 (50%)	1.2 (50%)	
1150	100	0.35 (47%)	1.4 (53%)	
1150	120	0.35 (46%)	1.5 (54%)	
1150	140	0.35 (45%)	1.6 (55%)	
1150	160	0.35 (44%)	1.6 (56%)	

^bNumbers in the parenthesis indicate relative weightages.

Lattice mismatch induced self-assembly in formation of InAs quantum dots over GaAs substrate leads to randomly configured dots having non uniform size distribution. Lack of controllability on the shape and density of formed QDs is evident from Figure 7.14a. All the grown structures were free from defect and dislocation. The pseudo-morphic ternary capping of 2 nm grown underneath of QDs has same lattice constant as that of GaAs. Addition of pseudo-morphic layer not only provides an additional energy level but also reduces In out-diffusion. High resolution TEM images of samples A, B and C are shown in Figure 7.14b, 7.14c and 7.14d, respectively. Increasing SRL capping thickness resulted in monotonic increase in lateral dimension of QD whereas the height of QD decreases. The measured dimensions are tabulated in Table 7.5 and further used for simulation.

The critical thickness for forming InAs QD reported in literatures is 1.7 ML. Similarly, for $\text{In}_{0.5}\text{Ga}_{0.5}\text{As}$ QD is 5.1 ML. Using the known experimental values, People-Bean model can be implemented and theoretically indium concentration versus critical thickness for forming InAs QDs can be calculated. The reduced form of the equation 7.2 is [59]:

$$h_c = \frac{(1-\gamma)}{(1+\gamma)} \frac{1}{16\pi\sqrt{2}} \frac{b^2}{a(x)} \left(\frac{1}{f^2}\right) \left(\ln \frac{h_c}{b}\right) \quad (7.2)$$

Here h_c is critical thickness, γ is Poisson's ratio, b is burgers vector (4.3 nm), $a(x)$ lattice constant of ternary alloy calculated using Vegard's law, f is lattice mismatch i.e. ratio of difference of lattice constants of alloy and GaAs to lattice constant of GaAs. From equation no. 7.2, a plot for critical thickness in monolayer versus indium concentration is depicted in Figure 7.15.

Ternary alloys reduces In-Ga inter-diffusion thus increasing the dot dimensions. But above a certain capping thickness there is a possibility of forming $\text{In}_x\text{Ga}_{1-x}\text{As}$ dots. For sample C, the total capping thickness including the pseudo-morphic layer (i.e. total thickness 8 nm + 2 nm) and sublimation of smaller dots

increases the possibility of InGaAs dot formation. Assuming 30% of indium (subsequently, this value we will confirm from theoretical simulation) to be present

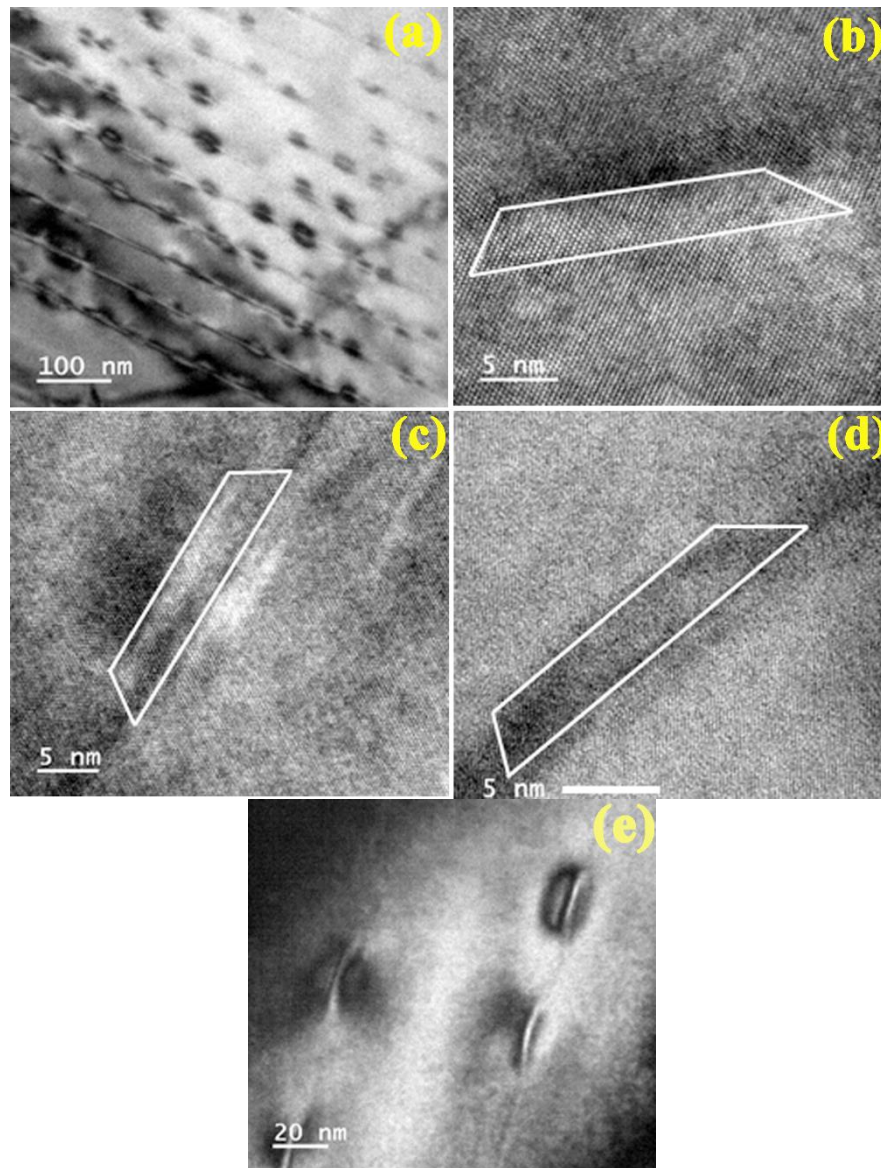


Figure 7.14. (a) TEM image of sample A exhibiting all 10 layers. High resolution TEM images of single QD in (b) sample A, (c) sample B, (d) sample C and (e) two layer TEM image of sample C exhibiting lateral stretching in horizontal direction.

in the QW structure formed, the calculated critical thickness in monolayer using People-Bean model is 41.37 ML (i.e. ~ 11.94 nm). Since, the indium concentration is non-uniform between the formed layer and the total thickness is near to the critical thickness (i.e. required for 2D to 3D transition) the 3D transition is withheld. So,

instead of forming an InGaAs dot a simultaneous InGaAs well is formed between the two GaAs interface. From low resolution TEM image of sample C in Figure 7.14e, it is visible that the lateral spacing between two QD in the same layer is minimum compared to other samples. It appears to be more like a Qwell structure.

Table 7.5. Average quantum dot dimension for different samples.

Sample	Base (a_2) (nm)	Top (a_1) (nm)	Height (h) (nm)
A (4 nm)	23.82	16.51	3.9
B (6 nm)	25.88	20.66	3.5
C (8 nm)	28.92	22.23	2.9
A (4 nm)	23.82	16.51	3.9

^bNumbers in the parenthesis indicate relative weightages.

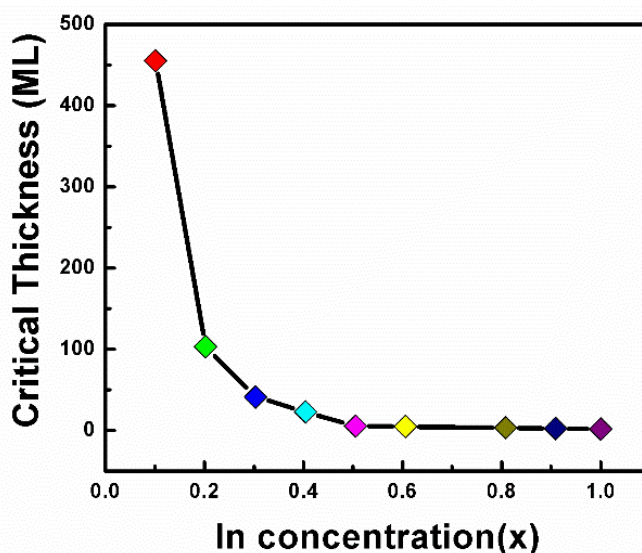


Figure 7.15. Critical thickness as a function of indium concentration from People-Bean relation.

7.2.2.2. Device Characterization: Single pixel detectors were fabricated and characterized. Dark current is an important parameter to judge detector performance. High temperature of operation and excellent figure of merits (i.e. high detectivity, low dark current density) are essential features of infrared detectors. Minimum dark current density was observed from sample B (Figure 7.16). The dominant sources of dark current are thermionic emission and field assisted

tunnelling. Another method to calculate thermal escape energy is from temperature dependent current voltage characteristics. The current density as a function of various parameters are specified in equation 7.3:

$$J_d = 2e\mu F \left(\frac{m^*kT}{2\pi\hbar^2} \right)^{1.5} \left(\left(1 + \left(\frac{\mu F}{v_s} \right)^2 \right)^{-0.5} \left(e^{\frac{E_0 - \beta F}{kT}} \right) \right) \quad (7.3)$$

Here J_d is the current density at different temperatures T , μ mobility of electron, m^* effective mass of electron, v_s saturation velocity, k and \hbar are boltzmann and reduced Planck's constant, F electric field, e charge of electron, β fitting parameter and E_0 is the thermal escape energy. β , μ and v_s are calculated by the fitting the equation with varying electric field and temperature. For sample B, the calculated values of various fitting parameters β , μ and v_s were 2.89×10^{-27} mC, 3965.24 cm²/V and 2.365×10^4 cm/s. The calculated values for other samples were slightly different ($\pm 10\%$) as compared to sample B but are similar to values reported in literatures. Based on the equation the measured thermal escape energy using current voltage characteristics for A, B and C were 210.69, 241.62 and 198.26 meV for sample A, B and C, respectively. Improved performance is attributed to enhanced optical properties in optimized capping thickness of 6 nm.

Similarly, other photodetectors figure of merits can be extracted by experimental results using specified equations given by *S. Wolde* et.al. Sample B exhibited maximum photoconductive gain (1.86) and highest electron capture probability (0.7) [60]. Higher photoconductive gain and better capture probability affirms improvement in device performance with optimized capping thickness (6 nm). Responsivity and detectivity are important figure of merits for an Infrared detector. High detectivity is essential for better device performance. Peak responsivity and detectivity calculation details are reported in our earlier work [28]. The measured values of responsivity at 80 K were 0.12, 0.33 and 0.075 A/W for samples A, B and C, respectively. Highest detectivity of 7.89×10^8 jones was measured from optimized sample B.

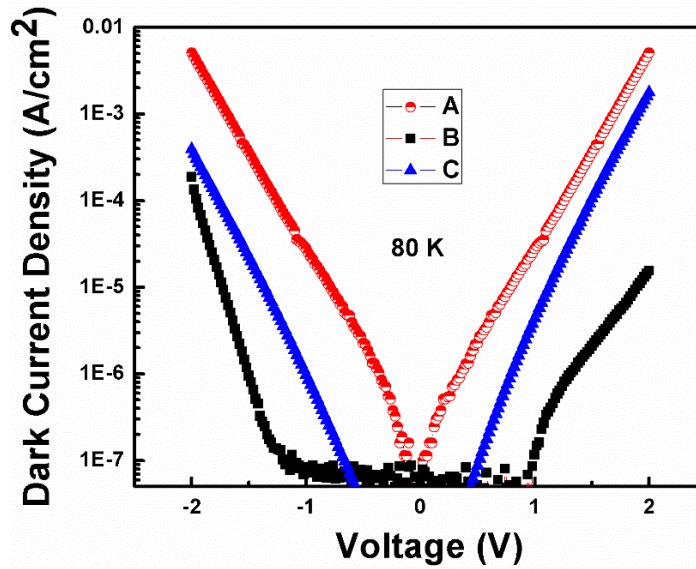


Figure 7.16. Dark current density as function of applied bias at 80 K.

The energy band diagram of InAs/InGaAs Dwell structure was obtained for samples A, B and C by simulating the theoretical model [51, 52]. Figure 7.17 represents the simulated energy levels for sample B. Specific transitions are highlighted in the band diagram.

The simulated thermal escape energies values for sample A, B and C were 203.2, 251.63 and 195.67 meV. The values are comparable to the experimentally calculated energies. The Energy level calculated for first three transitions and other important transitions are tabulated in Table 7.6. The decrement in the difference of the energy levels of the excited states as the order of transition increases ratifies the preciseness of the model and provides us with energy of the ground and higher excited states. The energy difference increases as the confinement reduces. The energy difference in sample C drastically increases as we consider higher energy level, phenomena exhibited by smaller dots. As the dot is laterally stretched and vertically suppressed it essentially affects the higher energy levels since the waveform overlap will be minimum.

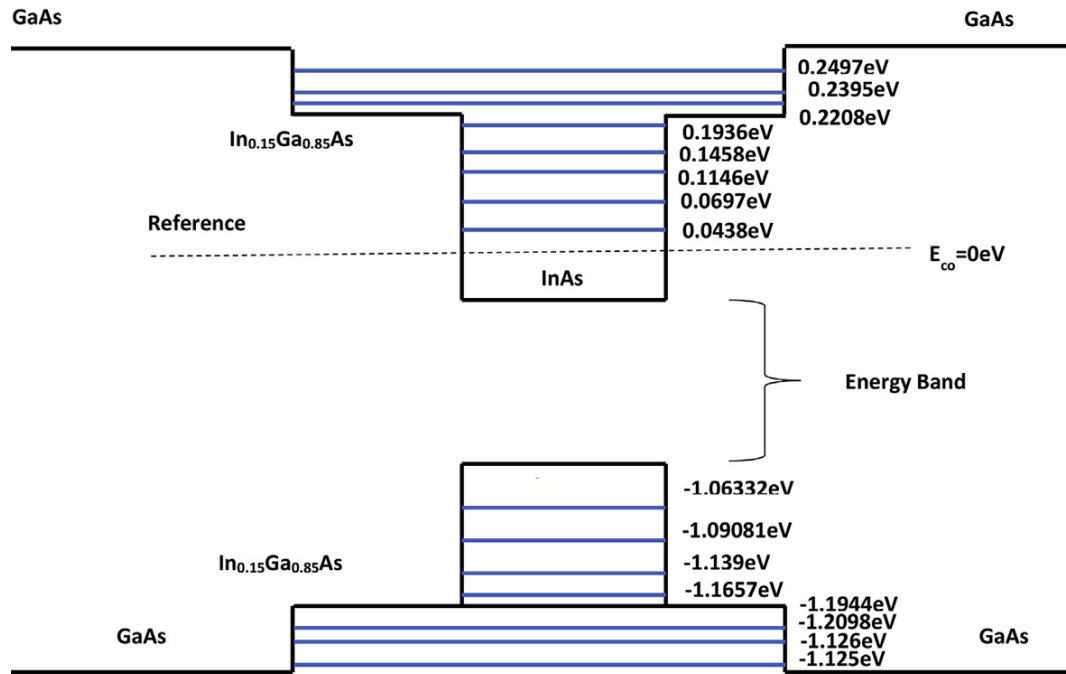


Figure 7.17. Energy Band diagram of InAs/InGaAs DWELL sample B from Simulation.

Table 7.6. Representation of the different energy levels measured and calculated from experimental and simulation results, respectively.

Transition	Sample A		Sample B		Sample C	
	PL & PLE (eV)	Simulated energy (eV)	PL & PLE (eV)	Simulated energy (eV)	PL & PLE (eV))	Simulated energy (eV)
E_0-h_0	1.0857	1.08653	1.0616	1.06332	1.086	1.08812
E_1-h_1	1.1569	1.156	1.1307	1.1346	1.173	1.1912
E_2-h_2	1.229	1.2312	1.198	1.1929	1.259	1.281
Wetting layer	1.41 - 1.45		1.37 - 1.40		1.44-1.48	
Quasi-bound states	1.45 - 1.51		1.41-1.47		1.48-1.51	

Figures 7.18a, 7.18b and 7.18c show the comparison of spectral response with the inter sub band energies obtained from the theoretical simulation. The different transitions have been highlighted. Spectral response peaks are comparable to the energy levels calculated from the simulation. The peak spectral response of all the samples was $7.56 \mu\text{m}$. The spectral response signal is Fourier transform of all the

possible transitions happening in conduction band for different sizes of QDs. The cumulative signal or the various optical results can be achieved by varying the input dot size in the proposed simulation. A dominant spectral response peak at 7.6 μm

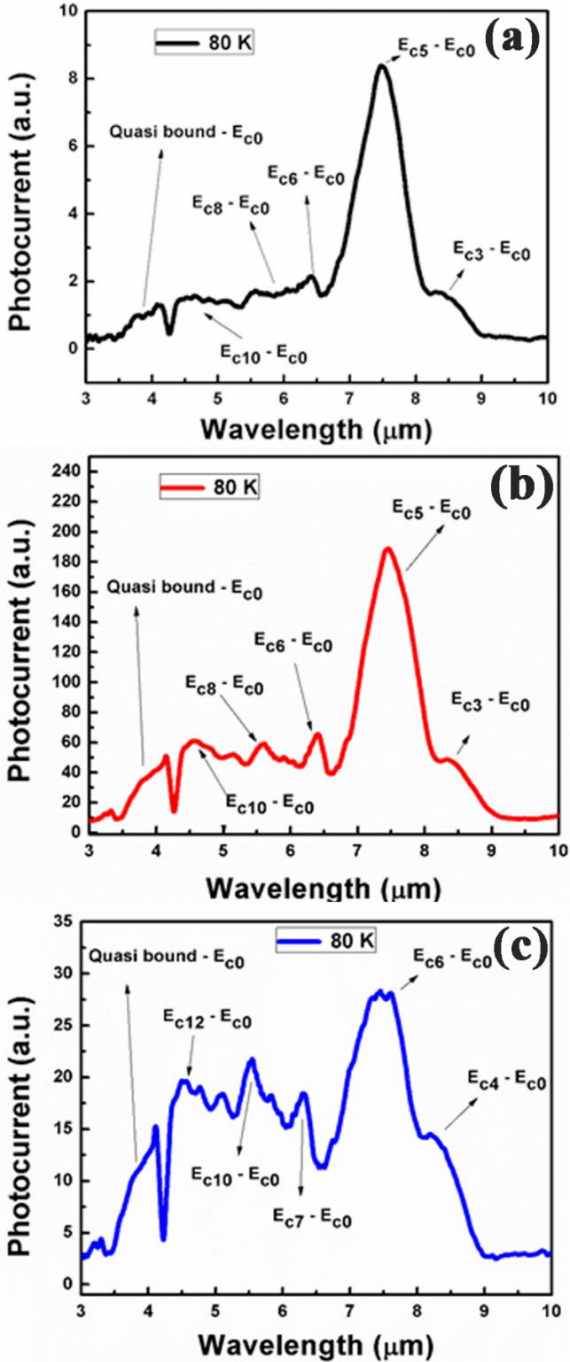


Figure 7.18. Comparison of Spectral response with the theoretical model for (a) Sample A, (b) Sample B, (c) Sample C.

was obtained from sample A and B whereas in case of sample C the peak value was shifted to 7.5 μm . Formation of bigger dots with higher confinement resulted in increased intensity or photocurrent in sample B whereas it decreases in sample C which is primarily due to formation of Qwell resulting in low absorption of normal incident light. A similar result i.e. decrease in responsivity and detectivity was observed from sample B to C.

All samples exhibited high photocurrent at reasonably high operating temperature of 90 K. Optimized sample B exhibited spectral response upto 100 K and blackbody signal lasting till 140 K. High temperature of operability with improved device performance was achieved in sample B with optimized capping thickness of 6 nm and beyond this thickness the dot sublimation process occurs along with lateral size increment.

7.2.2.3. Simulation results: Formation of quantum well with increasing capping thickness was confirm using various available optical and structural characterization. In this section, a reverse approach with known PL energy peak for claimed Qwell structure is simulated to roughly calculate the average indium concentration in GaAs/ $\text{In}_x\text{Ga}_{1-x}\text{As}$ /GaAs Qwell. In second part, the lateral and vertical size dependence of quantum dot is simulated and plotted. Confinement is affected by change in vertical dimension rather than that in lateral dimension. If we assume the formed Qwell has ground state peak near the first excited state peak obtained from PL spectra shown in Chapter 2. The ternary alloy thickness was considered as 10 nm and the ground state peak at 1085 nm. The average In concentration inside the Qwell structure was found to be 0.305 which matches with the predicted value from People-Bean relation.

The wave function solution till the n states can be calculated and the potential profile of the InGaAs well can be obtained using proposed simulation. Transition

energies corresponding to three excited states were 1.134, 1.262 and 1.419 eV. These energy levels are on par with PLE results in Figure 7.11d.

As we have observed, the energy spacing is primarily dependent on vertical height. In this section, we are simulating a QD and tabulating the first four energy levels by keeping one dimension constant and varying the other. Initiating parameter for dot simulation is assumed from TEM images obtained for sample B. In the first case, a_1 & a_2 values are assumed to be same as mention in TEM images of sample B while the height (h) of quantum dot is varied from 2.5 to 4.5 nm in steps of 0.5 nm each (Figure 7.19). In second case, height and top side length (a_1) are kept constant and lateral spacing (a_2) is varied. Similarly, a_1 can also be varied but the changes in energy level are insignificant. Hence the following simulation was performed in order to highlight the importance of vertical growth over lateral spreading through energy separation.

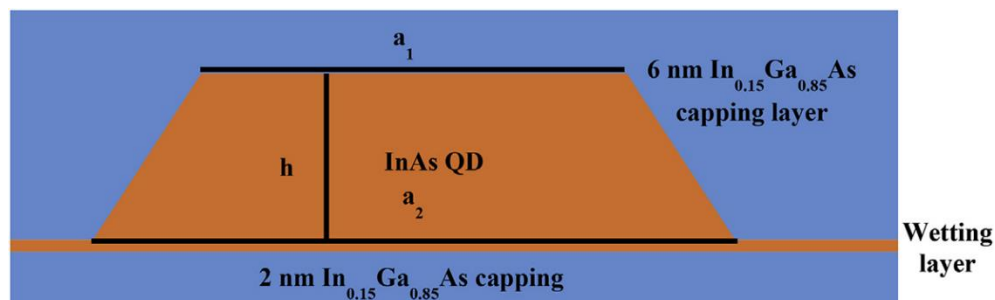


Figure 7.19. Comparison of spectral response with the theoretical model for (a) Sample A, (b) Sample B, (c) Sample C.

The calculated energy levels with varying height of QD is plotted in Figure 7.20a. The energy level spacing gradually increases as the thickness of the dot is reduced. Above 4.5 nm there is no significant change in ground state energy levels whereas the higher energy levels comes closer and closer thus increasing the electronics coupling in the structure. Varying lateral dimensions has insignificant effect on energy levels illustrated in Figure 7.20b. The QD confinement is essentially dependent on vertical growth rather than lateral stretching. After a certain height, the higher energy states are affected i.e. decrease in inter sub-band energy levels of

higher states. This simulation shows that the energy states are dependent on the vertical dimension rather than horizontal dimension. Similarly, if we change the shape of QD to hemispherical, pyramidal or conical geometry the energy states shows a variation of $\pm 3\%$ as compared to truncated pyramid.

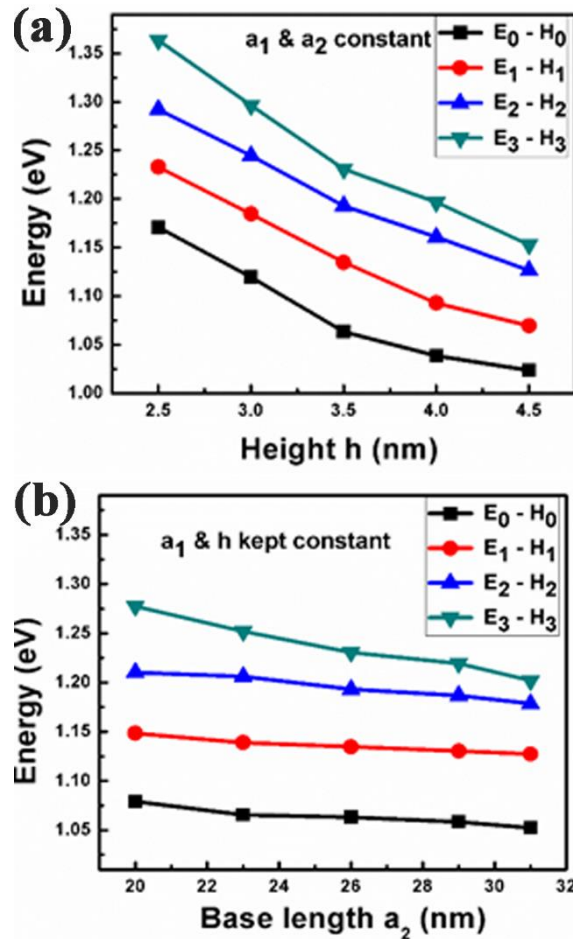


Figure 7.20. Simulated energy levels for (a) varying QDs height h and for (b) varying lateral length a_2 .

7.3. Conclusion: In summary, we have developed an indigenously designed NIR TCSPC system for the study of device samples on varying bias and temperature. We have studied the detail carrier dynamics of an InAs/InGaAs/GaAs/AlGaAs dot in double well (DDWELL) heterostructure through temperature dependent, bias dependent and emission wavelength dependent transient photoluminescence in the set up. We have obtained a critical temperature and a critical bias up to which the excited state carrier lifetime increases and after the critical value it decreases

sharply. The competition between carrier capture and thermal escape of carriers is observed to be the probable explanation of the critical temperature. The same phenomena has been proved from the emission energy dependent study as well. The critical bias phenomena has been explained through a carrier storage mechanism at the interface. At different ranges of applied bias, different carrier mechanism is found to be predominant such as hole diffusion, energy relaxation of electrons and breakdown. All the decay patterns at reasonably good time resolution ensures the future scope of studying other NIR devices using our system.

In conclusion of the second part of this work, we report that sample B (6 nm strain reducing layer of $\text{In}_{0.15}\text{Ga}_{0.85}\text{As}$) is an optimized configuration for achieving highest optical, structural and infrared detector characteristics. Sample B exhibited nearly threefold increase in low temperature PL intensity as compared to other samples. Increasing capping thickness above 6 nm resulted in dot sublimation and formation of undesirable quantum well having non-linear indium concentration confirmed using various characterization techniques. According to TRPL results, longer excited carrier lifetime was achieved in sample B. Minimum dark current density with improved figure of merits was achieved in infrared detector fabricated using sample B. The proposed theoretical model is on par with the experimental results for various dot-in-a-well detector structures. The energy levels calculated using the model matches with experimental peaks obtained in PL and PLE spectroscopy. The model specifically points out particular transitions observed in spectral response from all the detector samples. Theoretically, the effective indium concentration in QW formed was calculated using reverse approach and the observed value was around 30%.

References

- [1] P. Brogdon, H. Cheema, J.H. Delcamp, Near-infrared-absorbing metal-free organic, porphyrin, and phthalocyanine sensitizers for panchromatic dye-sensitized solar cells, *ChemSusChem*, 11 (2018) 86-103.
- [2] S. Lade, A. Zahedi, A revised ideal model for AlGaAs/GaAs quantum well solar cells, *Microelectron. J.*, 35 (2004) 401-410.
- [3] F. Tutu, P. Lam, J. Wu, N. Miyashita, Y. Okada, K.-H. Lee, N. Ekins-Daukes, J. Wilson, H. Liu, InAs/GaAs quantum dot solar cell with an AlAs cap layer, *Appl. Phys. Lett.*, 102 (2013) 163907.
- [4] N. Beattie, G. Zoppi, P. See, I. Farrer, M. Duchamp, D. Morrison, R. Miles, D.A. Ritchie, Analysis of InAs/GaAs quantum dot solar cells using Suns-Voc measurements, *Sol. Energy Mater. Sol. Cells*, 130 (2014) 241-245.
- [5] D. Araújo, M. Romero, F. Morier-Genoud, R. Garcia, Multiple quantum well GaAs/AlGaAs solar cells: transport and recombination properties by means of EBIC and cathodoluminescence, *Mater. Sci. Eng. B*, 66 (1999) 151-156.
- [6] L.M. Hernández, A. Contreras-Solorio, A. Enciso, C.I. Cabrera, M. Courel, J.P. Connolly, J.C. Rimada, Towards 50% efficiency in solar cells, Solar cells-new approaches and reviews, *InTech*, 2015.
- [7] U. Mayerhöffer, K. Deing, K. Größ, H. Braunschweig, K. Meerholz, F. Würthner, Outstanding short-circuit currents in BHJ solar cells based on NIR-absorbing acceptor-substituted squaraines, *Angew. Chem. Int. Ed.*, 48 (2009) 8776-8779.
- [8] A. Rogalski, Infrared detectors: an overview, *Infrared Phys. Technol.*, 43 (2002) 187-210.
- [9] L. Li, C. Richter, S. Paetel, T. Kopp, J. Mannhart, R. Ashoori, Very large capacitance enhancement in a two-dimensional electron system, *Science*, 332 (2011) 825-828.
- [10] A. Stiff-Roberts, S. Chakrabarti, S. Pradhan, B. Kochman, P. Bhattacharya, Raster-scan imaging with normal-incidence, midinfrared InAs/GaAs quantum dot infrared photodetectors, *Appl. Phys. Lett.*, 80 (2002) 3265-3267.

- [11] K. Kumari, H. Ghadi, D. Samudraiah, S. Chakrabarti, Indigenous development of 320 x 256 focal-plane array using InAs/InGaAs/GaAs quantum dots-in-a-well infrared detectors for thermal imaging, *Curr. Sci.*, 112 (2017).
- [12] B. Levine, K. Choi, C. Bethea, J. Walker, R. Malik, Quantum well avalanche multiplication initiated by 10 μm intersubband absorption and photoexcited tunneling, *Appl. Phys. Lett.*, 51 (1987) 934-936.
- [13] M. Krames, J. Bhat, D. Collins, N. Gardner, W. Götz, C. Lowery, M. Ludowise, P. Martin, G. Mueller, R. Mueller-Mach, High-power III-nitride emitters for solid-state lighting, *Phys. Status Solidi A*, 192 (2002) 237-245.
- [14] K. Barnham, I. Ballard, J. Barnes, J. Connolly, P. Griffin, B. Klufftinger, J. Nelson, E. Tsui, A. Zachariou, Quantum well solar cells, *Appl. Surf. Sci.*, 113 (1997) 722-733.
- [15] K. Tanabe, D. Guimard, D. Bordel, Y. Arakawa, High-efficiency InAs/GaAs quantum dot solar cells by metalorganic chemical vapor deposition, *Appl. Phys. Lett.*, 100 (2012) 193905.
- [16] K. Lu, Y. Wang, Z. Liu, L. Han, G. Shi, H. Fang, J. Chen, X. Ye, S. Chen, F. Yang, High-efficiency PbS quantum-dot solar cells with greatly simplified fabrication processing via "solvent-curing", *Adv. Mater.*, 30 (2018) 1707572.
- [17] A. Barbieri, E. Bandini, F. Monti, V.K. Praveen, N. Armaroli, The rise of near-infrared emitters: organic dyes, porphyrinoids, and transition metal complexes, *Photoluminescent materials and electroluminescent devices*, Springer, 2017, 269-307.
- [18] G. Chen, J. Seo, C. Yang, P.N. Prasad, Nanochemistry and nanomaterials for photovoltaics, *Chem. Soc. Rev.*, 42 (2013) 8304-8338.
- [19] H. Zhao, M. Chaker, N. Wu, D. Ma, Towards controlled synthesis and better understanding of highly luminescent PbS/CdS core/shell quantum dots, *J. Mater. Chem.*, 21 (2011) 8898-8904.
- [20] S. Miao, S.G. Hickey, B. Rellinghaus, C. Waurisch, A. Eychmüller, Synthesis and characterization of cadmium phosphide quantum dots emitting in the visible red to near-infrared, *J. Am. Chem. Soc.*, 132 (2010) 5613-5615.

- [21] T. Switański, U. Woggon, D.E.A. Angeles, A. Hoffmann, J.-H. Schulze, T.D. Germann, A. Strittmatter, U.W. Pohl, Carrier dynamics in InAs/GaAs submonolayer stacks coupled to Stranski-Krastanov quantum dots, *Phys. Rev. B*, 88 (2013) 035314.
- [22] K. Leo, J. Shah, J. Gordon, T. Damen, D. Miller, C. Tu, J. Cunningham, Effect of collisions and relaxation on coherent resonant tunneling: Hole tunneling in GaAs/Al_xGa_{1-x}As double-quantum-well structures, *Phys. Rev. B*, 42 (1990) 7065.
- [23] J. Smith, P. Dalgarno, B. Urbaszek, E. McGhee, G. Buller, G. Nott, R. Warburton, J. Garcia, W. Schoenfeld, P. Petroff, Carrier storage and capture dynamics in quantum-dot heterostructures, *Appl. Phys. Lett.*, 82 (2003) 3761-3763.
- [24] M. Maiberg, C. Spindler, E. Jarzembowski, R. Scheer, Electrical characterization of Cu(In,Ga)Se₂-solar cells by voltage dependent time-resolved photoluminescence, *Thin Solid Films*, 582 (2015) 379-382.
- [25] E. Sari, S. Nizamoglu, J.-H. Choi, S.-J. Lee, K.-H. Baik, I.-H. Lee, J.-H. Baek, S.-M. Hwang, H.V. Demir, Opposite carrier dynamics and optical absorption characteristics under external electric field in nonpolar vs. polar InGaN/GaN based quantum heterostructures, *Opt. Express*, 19 (2011) 5442-5450.
- [26] X. Deng, X. Wen, C.F.J. Lau, T. Young, J. Yun, M.A. Green, S. Huang, A.W. Ho-Baillie, Electric field induced reversible and irreversible photoluminescence responses in methylammonium lead iodide perovskite, *J. Mater. Chem. C*, 4 (2016) 9060-9068.
- [27] Y.D. Sharma, M. Kuttly, R. Sheno, A.V. Barve, S. Myers, J. Shao, E. Plis, S. Lee, S. Noh, S. Krishna, Investigation of multistack InAs/InGaAs/GaAs self-assembled quantum dots-in-double-well structures for infrared detectors, *J. Vac. Sci. Technol., B: Nanotechnol. Microelectron.: Mater., Process., Meas., Phenom.*, 28 (2010) C3G1-C3G7.
- [28] H. Ghadi, S. Sengupta, S. Shetty, A. Manohar, A. Balgarkashi, S. Chakrabarti, N.B. Pendyala, S.L. Prajapati, A. Kumar, Comparison of three design architectures for quantum dot infrared photodetectors: InGaAs-capped dots, dots-in-a-well, and submonolayer quantum dots, *IEEE T Nanotechnol*, 14 (2015) 603-607.

- [29] S. Lee, J. Park, J. Kim, S. Noh, J. Choe, Effects of a cap layer on the confined sublevels in near-surface InAs/GaAs quantum dots, *J. Korean Phys. Soc.*, 46 (2005) 985-989.
- [30] E. Ahn, Y. Lee, J. Kim, E. Yoon, Y. Kim, In-situ monitoring of InAs/GaAs QDs by using spectral reflectance, *J. Korean Phys. Soc.*, 49 (2006) 947-950.
- [31] Q. Xie, P. Chen, A. Madhukar, InAs island-induced-strain driven adatom migration during GaAs overlayer growth, *Appl. Phys. Lett.*, 65 (1994) 2051-2053.
- [32] S. Jung, H. Yeo, I. Yun, J. Leem, S. Cho, J. Kim, J. Lee, High potential barrier effects on self-assembled InAs quantum dots, *J. Korean Phys. Soc.*, 50 (2007) 767.
- [33] S. Krishna, Quantum dots-in-a-well infrared photodetectors, *J. Phys. D*, 38 (2005) 2142.
- [34] S. Sengupta, J. Kim, A. Barve, S. Adhikary, Y. Sharma, N. Gautam, S. Lee, S. Noh, S. Chakrabarti, S. Krishna, Sub-monolayer quantum dots in confinement enhanced dots-in-a-well heterostructure, *Appl. Phys. Lett.*, 100 (2012) 191111.
- [35] L. Höglund, C. Asplund, Q. Wang, S. Almqvist, H. Malm, E. Petrini, J.Y. Andersson, P.O. Holtz, H. Pettersson, Origin of photocurrent in lateral quantum dots-in-a-well infrared photodetectors, *Appl. Phys. Lett.*, 88 (2006) 213510.
- [36] R. Nedzinskas, B. Čechavičius, A. Rimkus, J. Kavaliauskas, G. Valušis, L. Li, E. Linfield, Optical features of InAs quantum dots-in-a-well structures, *LITH J Phys.*, 54 (2014).
- [37] K. Nishi, H. Saito, S. Sugou, J.-S. Lee, A narrow photoluminescence linewidth of 21 meV at 1.35 μm from strain-reduced InAs quantum dots covered by $\text{In}_{0.2}\text{Ga}_{0.8}\text{As}$ grown on GaAs substrates, *Appl. Phys. Lett.*, 74 (1999) 1111-1113.
- [38] H. Liu, X. Wang, J. Wu, B. Xu, Y. Wei, W. Jiang, D. Ding, X. Ye, F. Lin, J. Zhang, Structural and optical properties of self-assembled InAs/GaAs quantum dots covered by $\text{In}_x\text{Ga}_{1-x}\text{As}$ ($0 \leq x \leq 0.3$), *J. Appl. Phys.*, 88 (2000) 3392-3395.
- [39] J. Tatebayashi, M. Nishioka, Y. Arakawa, Over 1.5 μm light emission from InAs quantum dots embedded in InGaAs strain-reducing layer grown by metalorganic chemical vapor deposition, *Appl. Phys. Lett.*, 78 (2001) 3469-3471.

- [40] H. Liu, M. Hopkinson, C. Harrison, M. Steer, R. Frith, I. Sellers, D. Mowbray, M. Skolnick, Optimizing the growth of 1.3 μm InAs/InGaAs dots-in-a-well structure, *J. Appl. Phys.*, 93 (2003) 2931-2936.
- [41] J. Chen, U. Oesterle, A. Fiore, R. Stanley, M. Illegems, T. Todaro, Matrix effects on the structural and optical properties of InAs quantum dots, *Appl. Phys. Lett.*, 79 (2001) 3681-3683.
- [42] L. Seravalli, M. Minelli, P. Frigeri, P. Allegri, V. Avanzini, S. Franchi, The effect of strain on tuning of light emission energy of InAs/InGaAs quantum-dot nanostructures, *Appl. Phys. Lett.*, 82 (2003) 2341-2343.
- [43] J. Kim, C. Yang, U. Sim, E. Yoon, Y. Lee, W. Choi, Effects of the well layer on the emission wavelength of InAs/InGaAs dot-in-a-well structure, *J. Korean Phys. Soc.*, 52 (2008) 34.
- [44] J. Patwari, A. Chatterjee, H. Ghadi, H. Sharma, S. Chakrabarti, S.K. Pal, *In situ* measurement of temperature dependent picosecond resolved carrier dynamics in near infrared (NIR) sensitive device on action, *Rev. Sci. Instrum.*, 90 (2019) 043909.
- [45] Y.P. Varshni, Temperature dependence of the energy gap in semiconductors, *Physica*, 34 (1967) 149-154.
- [46] Z. Fang, Z. Gong, Z. Miao, L. Kong, X. Xu, H. Ni, Z. Niu, Effect of the InAlAs and InGaAs combination strain-reducing layer on 1.3 μm emission self-assembled InAs/GaAs quantum dots, *J. Phys. D*, 37 (2004) 1012.
- [47] L. Kong, Z.C. Feng, Z. Wu, W. Lu, Temperature dependent and time-resolved photoluminescence studies of InAs self-assembled quantum dots with InGaAs strain reducing layer structure, *J. Appl. Phys.*, 106 (2009) 013512.
- [48] O. Qasaimeh, Modulation bandwidth of inhomogeneously broadened InAs/GaAs quantum dot lasers, *Opt. Commun.*, 236 (2004) 387-394.
- [49] Z. Su, S. Xu, A generalized model for time-resolved luminescence of localized carriers and applications: Dispersive thermodynamics of localized carriers, *Sci. Rep.*, 7 (2017) 13.

- [50] H. Ghadi, J. Patwari, P. Murkute, D. Das, P. Singh, S. Dubey, M. Bhatt, A. Chatterjee, A. Balgarkashi, S. Pal, Optimizing dot-in-a-well infrared detector architecture for achieving high optical and device efficiency corroborated with theoretically simulated model, *J. Alloys Compd.*, 751 (2018) 337-348.
- [51] H. Ghadi, N. Sehara, P. Murkute, S. Chakrabarti, Minimization of material inter-diffusion for thermally stable quaternary-capped InAs quantum dot via strain modification, *Superlattice. Microst.*, 105 (2017) 117-131.
- [52] M. Srujan, K. Ghosh, S. Sengupta, S. Chakrabarti, Presentation and experimental validation of a model for the effect of thermal annealing on the photoluminescence of self-assembled InAs/GaAs quantum dots, *J. Appl. Phys.*, 107 (2010) 123107.
- [53] Z. Zaaboub, F. Hassen, M. Naffouti, H. Maaref, Temperature effect on the electronic transfer mechanism between InAs/GaAs quantum dots by the mean of time resolved photoluminescence spectroscopy, *J. Mater. Sci. Technol.*, 14 (2016) 1-17.
- [54] M.T. Man, H.S. Lee, Discrete states and carrier-phonon scattering in quantum dot population dynamics, *Sci. Rep.*, 5 (2015) 8267.
- [55] L. Bouzaiene, B. Ilahi, L. Sfaxi, F. Hassen, H. Maaref, O. Marty, J. Dazord, Tuning vertically stacked InAs/GaAs quantum dot properties under spacer thickness effects for 1.3 μm emission, *Appl. Phys. A*, 79 (2004) 587-591.
- [56] F. Pulizzi, A. Kent, A. Patanè, L. Eaves, M. Henini, Time-resolved photoluminescence of InAs quantum dots in a GaAs quantum well, *Appl. Phys. Lett.*, 84 (2004) 3046-3048.
- [57] L.Y. Karachinsky, S. Pellegrini, G. Buller, A. Shkolnik, N.Y. Gordeev, V. Evtikhiev, V. Novikov, Time-resolved photoluminescence measurements of InAs self-assembled quantum dots grown on misorientated substrates, *Appl. Phys. Lett.*, 84 (2004) 7-9.

- [58] J. Patwari, H. Ghadi, S. Sardar, J. Singhal, B. Tongbram, S. Shyamal, C. Bhattacharya, S. Chakrabarti, S.K. Pal, Photo-induced electronic properties in single quantum well system: effect of excitonic lifetime, *Mater Res Express* 4 (2017) 016301.
- [59] R. People, J. Bean, Calculation of critical layer thickness versus lattice mismatch for $\text{Ge}_x\text{Si}_{1-x}/\text{Si}$ strained-layer heterostructures, *Appl. Phys. Lett.*, 47 (1985) 322-324.
- [60] S. Wolde, Y.-F. Lao, A. Unil Perera, Y. Zhang, T. Wang, J. Kim, T. Schuler-Sandy, Z.-B. Tian, S. Krishna, Noise, gain, and capture probability of p-type InAs-GaAs quantum-dot and quantum dot-in-well infrared photodetectors, *J. Appl. Phys.*, 121 (2017) 244501.

Chapter 8

Photophysical Studies on Light Harvesting Hybrid Nanomaterials in the Near Infrared Region (NIR) of Solar Radiation for Potential Environmental Cleaning Applications

8.1. Introduction: The application of nanomaterials for light harvesting in the near infrared (NIR) region (> 700 nm) of the solar spectrum is an emerging area of scientific and technological interest [1-4]. The transparency of the widely reported light harvesting semiconductor materials and organic photosensitizers (PSs) towards the NIR region (800-2000 nm) leads to the wastage of nearly 51% of the total solar energy conversion to electrical or chemical energies [5-7]. The inefficiency in NIR light harvesting has been considered as the main limiting factor for the conventionally available solar energy conversion technologies such as photocatalysis and photovoltaic cells [8, 9]. Another important reason for the growing attention towards NIR absorbing and emitting materials is the augmenting biomedical technologies, such as photodynamic therapy (PDT) and *in vivo* imaging [10-12]. Reduced photon scattering and deeper skin penetration ability of NIR irradiation (900-1700 nm) have made the low band gap semiconductor nanocrystals (NCs) or quantumdots (QDs) a promising research subject to achieve higher biological activities.

Colloidal lead sulfide (PbS) quantum dots has recently been recognized as a potential NIR harvesting material owing to their wide spread applications including quantum dot sensitized solar cells (QDSSC) [13, 14], photocatalysis [15], biomedical labelling [10], light emitting diode [16] and IR light detection [17]. Additionally, the exceptional photophysical behavior of PbS QDs is highly

attractive to study various phenomena such as broad and tunable absorption extending from UV to the near-IR region [18], larger exciton Bohr radius (18 nm), long excited state lifetimes [19], multiple exciton generation probability (MEG) [20, 21], hot carrier extraction [22], and much higher extinction coefficient than the available PSs in NIR region [23]. However, inefficient photo-induced charge separation (PCS) [24], very slow electron transfer rate [25], trapping of charge carriers in surface defects of PbS QDs are reported to limit their energy conversion efficiency compared to the cadmium chalcogenide QDs. To resolve the unwanted exciton recombination problem within PbS QDs, several other groups have designed hybrids of low band gap PbS QDs assembling with wide band gap semiconductors such as TiO₂ [26, 27]. Nevertheless, the electron transfer time scale from the excited state of the PbS QD to the conduction band (CB) of the semiconductor is always reported to be an order of magnitude slower than that of Cd based nanostructures [24]. In addition to the slower electron transfer kinetics, the recombination of injected electrons from the CB of TiO₂ to the recombination centers (i.e. holes of valance band and surface trap states) of positively charged QDs eventually deteriorate the exciton separation process which turn out to be an inefficient charge separation. Instead of separating the electrons from the photoexcited QD, the separation of photoinduced holes is another possible way out of efficient exciton dissociation. Phenothiazine (PTZ) is a well reported hole transporting material used for charge separation in cadmium based quantum dots [28, 29]. Moreover, the charge separation efficiency of the QD can also be modulated by tuning the size of the QD and doping with other elements [1, 30]. Thus, the understanding of the typical energy levels, chemical and electronic nature of the QD and detailed carrier dynamics study of the interfaces is essential in order to design a hybrid material more rationally to achieve the desirable efficiency in NIR light harvesting. Although the significance of charge separation from the QD is well documented in literature, the simultaneous extraction of

electron and hole in a single hybrid and correlation of the dynamics to higher NIR harvesting activity are sparsely described in contemporary literature.

Considering all the photoinduced charge separation and back recombination processes at the interfaces of PbS QD_semiconductor conjugate, we propose that simultaneous dissociation of the electrons and holes could be the best possible way to increase the light conversion efficiency due to the suppression of unwanted back recombination. Thus, in the present work, we have employed a new hybrid material (PbS_TiO₂_PTZ) using three individual components: low band gap colloidal PbS QDs as sensitizer, high band gap semiconductor TiO₂ for electron transport and organic oxidizing molecule phenothiazine (PTZ) for hole transport. The activity of the trio hybrid has been measured in terms of reactive oxygen species (ROS) generation under IR light irradiation (>600 nm). The ROS generation ability of the trio hybrid is found to be much higher compared to the dual hybrids of PbS_TiO₂ and PbS_PTZ. All the individual components along with the hybrids have been characterized by spectroscopic (absorption, emission, TCSPC) and microscopic (HRTEM) techniques. The energy levels of the QDs are further verified using cyclic voltammetric (CV) analysis. To explore the variance of the activities between the hybrids, a rigorous interfacial dynamics study has been done for all composite materials using steady-state and time resolved photoluminescence (TRPL) techniques. The dissociation of exciton, separation of the photogenerated carries from the QD, reduced back recombination due to unavailability of the recombination center have been explicitly investigated from excited state lifetimes and probable energy level alignments. Along with the hole transfer, the feasibility of trap state passivation of the QD by the PTZ molecule has also been explored in the present work. Thus, the dynamical behavior of the composite has been mechanistically correlated to the higher ROS generation activity which could be useful to translate the idea of efficient exciton dissociation towards NIR catalysis or potential biomedical activities.

8.2. Results and Discussion:

8.2.1. Exciton Dissociation in an NIR-Active Trihybrid Nanocrystal Leading to Efficient Generation of Reactive Oxygen Species [31]: Figure 8.1 shows the characterization of oleic acid capped colloidal PbS QDs used in this study as a NIR light sensitizer. The absorption and emission spectra of the PbS QD are presented in Figure 8.1a. The first excitonic absorption and emission maxima appear at ~ 1365 nm and ~ 1465 nm respectively. Both absorption and emission peaks are attributed to the E_1 - H_1 transition (1S) of the QD. It is clearly mentioned in earlier literature that the emission of PbS QDs is always from the band edges and not from any defect state unlike the other semiconductor nanoparticles such as ZnO [25]. The band gap calculated from the 1S absorption of the QD in toluene is 0.9 eV. It is

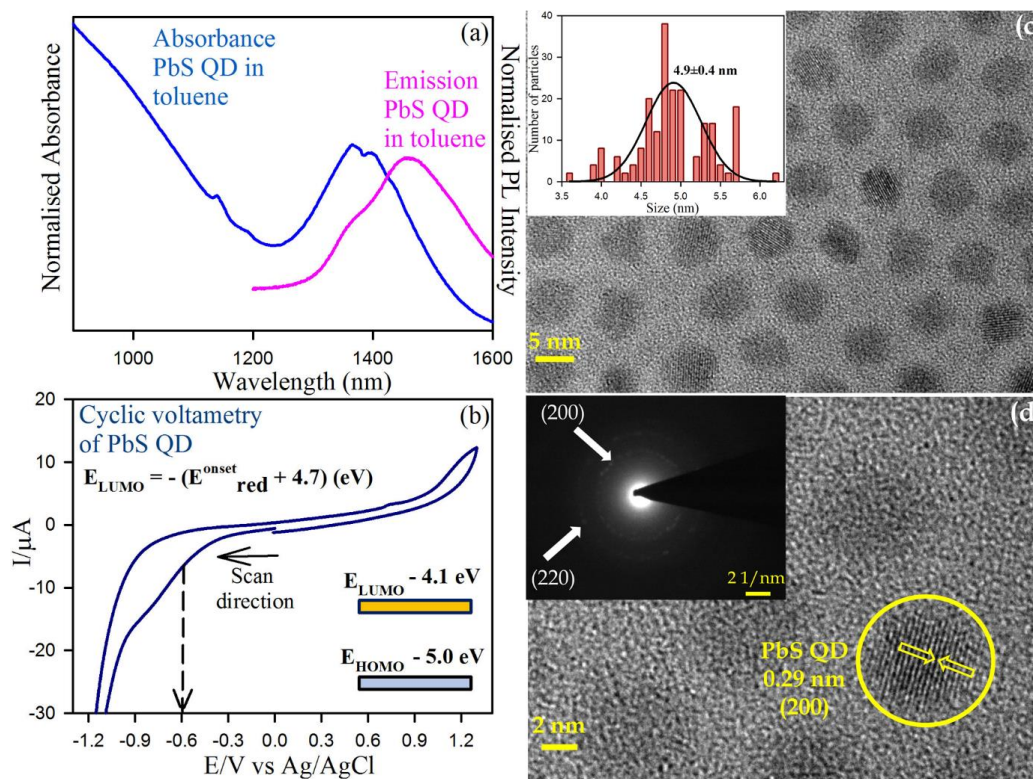


Figure 8.1. Characterization of PbS QD. (a) Absorption and emission spectra of PbS QD in solvent toluene, (b) cyclic voltammetry (CV) data, the dashed arrow denote the approximate onset of reduction step from which the LUMO level of the QD is obtained. The inset shows the approximate HOMO and LUMO levels of the nanocrystal, (c) TEM image of PbS QD. Inset: The size distribution of PbS QD. (d) HRTEM images of PbS QD. Inset: SAED pattern.

evident from the absorption spectra of the QD that it covers the entire NIR region of solar spectra up to 1600 nm wavelength. To measure the precise position of E_1 and H_1 levels of the QD, cyclic voltammetry was performed as shown in Figure 8.1b. The conduction band minimum or E_1 level of the QD is calculated with a precision of ± 0.1 eV from the onset potential value (-0.6 V *vs.* Ag/AgCl) of the first peak of initial cathodic scan. The reverse side peak in the anodic scan is not visible in the CV result probably because of the irreversible reduction of the under coordinated surface cations having a similar redox potential to the core state.

Table 8.1. Summary of the size distribution, absorption and electrochemical measurement of PbS QDs.

Avg. diameter ^a (nm)	Abs. max. ^b (nm)	E_g^c (eV)	E_{red}^d (V)	E_{HOMO}^e (eV)	E_{LUMO} (eV)
4.9 ± 0.4	1365 ± 2	0.9	-0.6 ± 0.05	-4.1	-5.0

^aThe average size of the QD is obtained from distribution curve for ~ 200 particles from TEM images. ^bPeak maxima of the first excitonic absorption of the QD in toluene. ^cEnergy gap is calculated from the 1S absorption peak. ^dOnset of the reduction potential in the cathodic scan of CV (*vs.* Ag/AgCl in saturated KCl). ^eDeduced from CV.

The equation for the energy level calculation and the obtained energy levels are mentioned in Figure 8.1b. The LUMO (E_1) energy level of the QD is calculated assuming the energy level of Ag/AgCl in saturated KCl is 4.7 eV below the vacuum level. Then the HOMO (H_1) (valance band maximum) level is obtained by subtracting the optical 1S energy gap of the QD. Corrections due to exciton binding energy are ignored. The E_1 and H_1 values of the QD are calculated to be -4.1 eV and -5 eV respectively, which are consistent with earlier reported literature [25]. Comparing the calculated energy levels of the QD with the reported conduction band level of TiO_2 at -4.2 eV [1] and PTZ HOMO level at -5.0 eV [32], the type II attachment probability is anticipated. The size distribution and uniform dispersion of the PbS QD are evident from the histogram and the TEM image as shown in Figure 8.1c. The average size of the QD is found to be 4.9 nm. The fringe distance deduced from the HRTEM image shown in Figure 8.1d is 0.29 nm which

corresponds to the (200) crystal plane of PbS. The Selected area (electron) diffraction (SAED) pattern represented in the inset of Figure 8.1c further proves the crystallinity of the QD showing two prominent rings corresponding to (200) and (220) planes of the PbS nanocrystal. A summary of the spectroscopic, electrochemical and microscopic measurements of the PbS QD material is presented in Table 8.1.

The HRTEM images of the QD_TiO₂ hybrid are shown in Figure 8.2a and 8.2b. In Figure 8.2a, the small spheres of darker spheres on the surface of bigger TiO₂ nanoparticle clearly depict the surface adsorption of the PbS QDs on the TiO₂ nanoparticle. The lattice fringes of TiO₂ NPs and PbS QDs in the PbS_TiO₂ hybrid are illustrated in Figure 8.2b, which represents the interplanar distances of 0.29 and 0.34 nm, corresponding to the spacing between two (200) planes of the PbS QD and (110) planes of the TiO₂ NP, respectively. The SAED pattern shown in the inset of Figure 8.2b further proves the crystallinity of the hybrid material and shows the spotty rings corresponding to the planes of the PbS QD [(220), (111)] and the TiO₂ NP [(110), (200)]. As our QDs are originally oleic acid capped, the two sided attachment is not feasible here as reported in some earlier studies for mercapto propionic acid (MPA), cysteine (Cys) or some similar ligands [33]. We propose surface adsorption of the QDs on the TiO₂ nanoparticle as the most probable attachment strategy. For QD_PTZ and QD_TiO₂_PTZ the TEM images are difficult to capture because of the burning issue of the organic PTZ ligand upon exposure to the electron beam. To determine the complex formation in QD_TiO₂, QD_PTZ and the QD_TiO₂_PTZ trio hybrid, the UV-VIS NIR absorption spectra were recorded for all the three. The visible side of the spectra (280-700 nm) is shown in Figure 8.2c and the NIR side (1000-1600 nm) is shown in Figure 8.2d. The absorption peak at 334 nm for the QD_TiO₂ hybrid corresponds to the band gap of the TiO₂ nanoparticle. On the other hand, the peaks at 318 nm for QD_PTZ and the trio hybrid correspond to the absorption maxima of the PTZ molecule. Due

to the scattering of TiO₂ NPs the peak for QD at the IR side is slightly blue shifted for QD_TiO₂ and QD_TiO₂_PTZ (triohybrid). The band gap absorption of the TiO₂ is not prominent in the trio hybrid because the corresponding signal is suppressed by the very high extinction coefficient of PTZ molecules. The prominent signal for all the individual components in the hybrids proves the formation of the assembly materials.

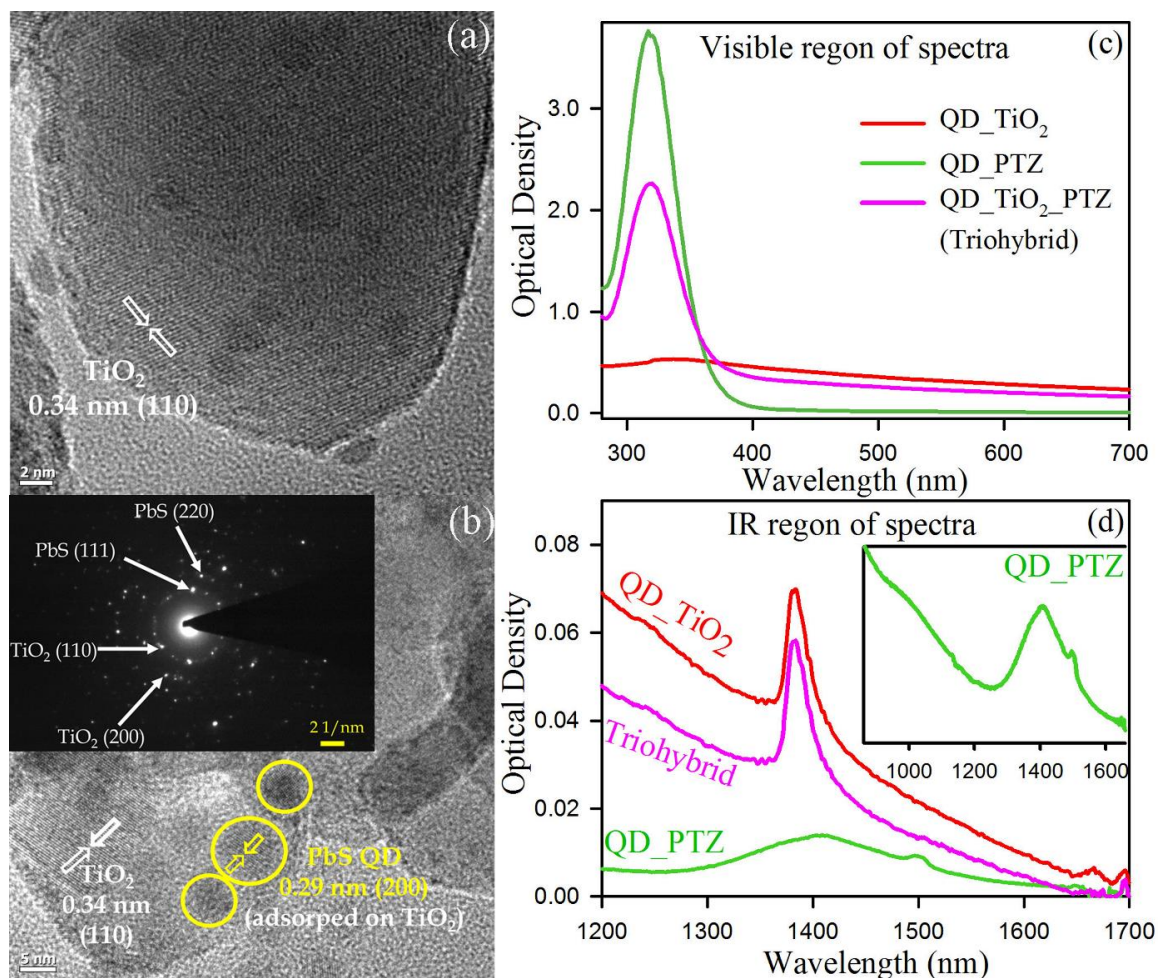


Figure 8.2. Characterization of the hybrids. (a)-(b) HRTEM images of the PbS QD_TiO₂ hybrid. Inset shows the SAED pattern of the PbS QD_TiO₂ hybrid. (c)-(d) Absorption spectra of the three different hybrids QD_TiO₂ (Red), QD_PTZ (Green) and QD_PTZ_TiO₂ (Pink). The inset shows the magnified spectra of QD_PTZ.

Phenothiazine (PTZ) having absorption at 320 nm is a well-documented hole transporting material (HTM) because of its very low oxidation potential. The positively charged oxidized PTZ molecule (PTZ⁺) absorbs at 520 nm, well

separated from that of the neutral PTZ molecule [34]. The absorption of the PTZ and QD_PTZ molecule is shown in Figure 8.3a which depicts a smaller hump at 500 nm for QD_PTZ which is not present in the absorption spectra of only the PTZ molecule. This is probably due to permanent irreversible oxidation of a smaller fraction of PTZ molecules upon attachment to the PbS QD surface. The quenching in the emission intensity of the PTZ molecule upon attachment to the PbS QD surface is further evident from the inset of Figure 8.3a where the emission spectra of the PTZ molecule are monitored at an excitation wavelength of 375 nm. The change in excited state lifetime of PTZ molecule is also shown through the picosecond resolved transient fluorescence data shown in Figure 8.3b.

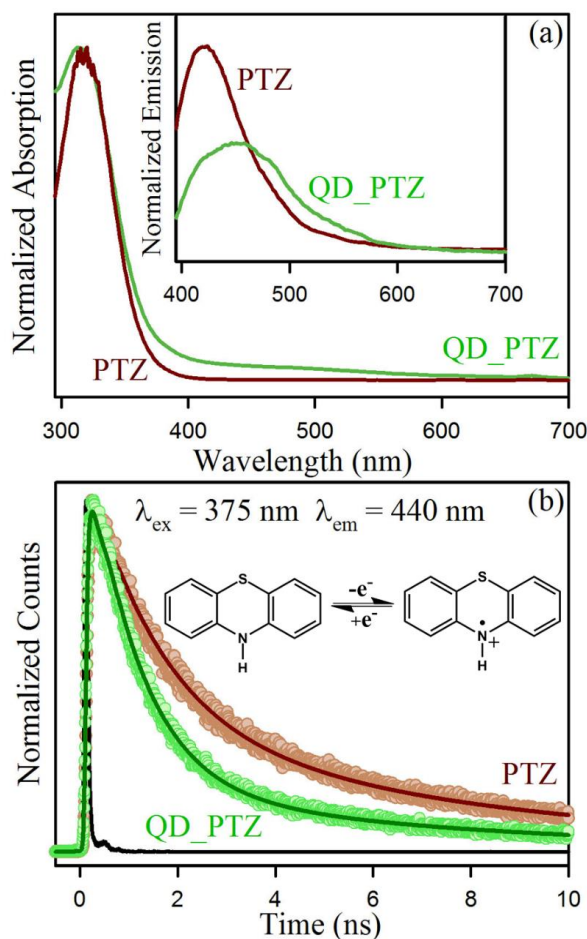


Figure 8.3. Changes in properties of phenothiazine (PTZ) after attachment to PbS QD. (a) Absorption, inset: emission spectra upon 375 nm excitation, (b) time resolved fluorescence decay profile of PTZ (Dark red) and QD_PTZ hybrid (Green).

Table 8.2. Dynamics of time resolved photoluminescence transients of phenothiazine (PTZ) and the PbS QD_PTZ composite in a chloroform-toluene solvent mixture.^a

Sample	Excitation wavelength (nm)	Emission wavelength (nm)	τ_1 (ns)	τ_2 (ns)	τ_{avg} (ns)
Phenothiazine (PTZ)	375	440	1.5 ± 0.1 (60%)	7.6 ± 0.1 (40%)	3.9
PbS QD_PTZ	375	440	1.0 ± 0.1 (71%)	7.0 ± 0.1 (15%)	1.8

^a Numbers in parentheses indicate relative contributions of the time components.

The excitation wavelength used in this study is 375 nm and the emission decay is monitored at 440 nm wavelength. As summarized in Table 8.2, the average lifetime of the PTZ molecule is decreased from 3.9 ns to 1.8 ns upon attachment to the PbS QD surface due to excited state photoinduced electron transfer (PET) from the LUMO of PTZ to the CB of PbS. The quenching in lifetime provides evidence of attachment of the PTZ molecule to the QD.

The photoinduced electron transfer (PET) from the PbS QD to TiO₂ under 965 nm excitation is shown in Figure 8.4a. The steady-state emission of the PbS QD at 1470 nm is gradually decreased with increasing concentration of TiO₂ nanoparticles due to electron transfer from the former to the later. The decrease in the steady-state emission of the QD is also observed with increasing concentration of PTZ molecule upon 965 nm excitation probably because of the photoinduced hole transfer (PHT) from the QD to PTZ. To further prove the PET and PHT phenomena, the excited state lifetime of the QD is measured upon addition of TiO₂ and PTZ individually. The transient photoluminescence data are shown in Figure 8.4c and the faster time scale region is represented at a magnified scale at Figure 8.4d to clarify the difference of the decays from the IRF. The fitted time scales of three of the decays are summarized in Table 8.3. As evident from the fitted results, the excited state lifetime of only QD has three different time components among which the shortest one might be due to the vibrational relaxation, auger recombination of the photo generated electrons or because of the

trapping of electrons to the defect state levels lying below the conduction band of PbS. As the fastest time scale is much longer than the IRF, it is definitely not due to the contribution of the IRF. The longest one (276 ns) is certainly due to the radiative recombination timescale from the CB to VB of PbS. After attachment to the TiO₂, the average lifetime of the QD is quenched from 88 ns to 36 ns. The fastest component of 1.1 ns has a relative contribution of 81% in the overall decay timescale of the PbS QD_TiO₂ hybrid. Although *Hyun et al* has reported [25] earlier that electron transfer is not energetically feasible for a PbS QD of diameter above 4.3 nm, we observed clear evidence of electron transfer for our system.

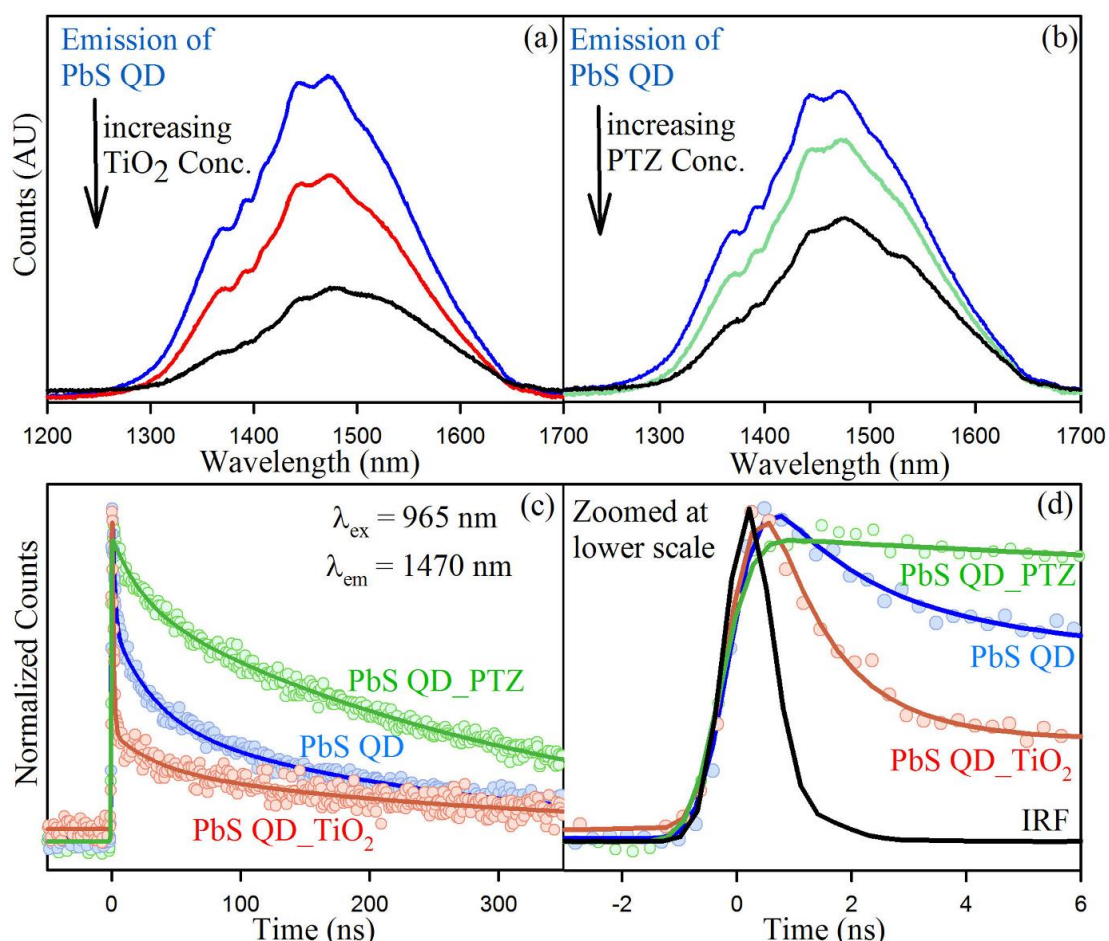


Figure 8.4. Quenching in steady-state emission counts upon addition of (a) electron quencher TiO₂ and (b) hole quencher phenothiazine (PTZ). (c) Time resolved photoluminescence for PbS QD (Blue) and the changes in decay profile upon addition of TiO₂ (Red) and PTZ (Green). (d) The faster PL decay profiles are represented at a magnified scale and compared with the instrument response function (IRF).

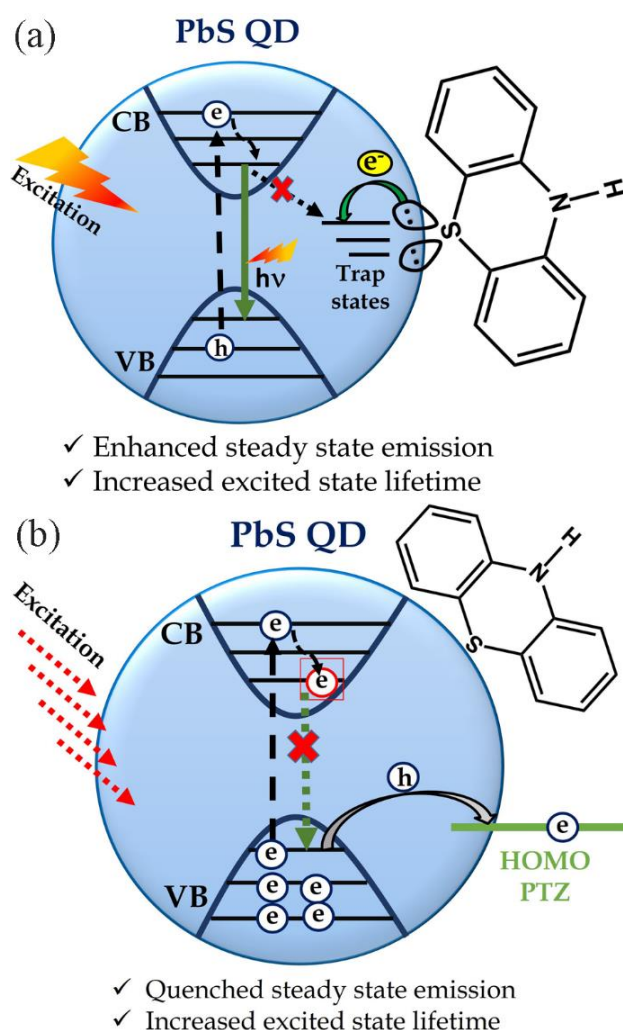
Table 8.3. Dynamics of time resolved photoluminescence transients of the PbS QD and the hybrids PbS QD_TiO₂ and PbS QD_PTZ (phenothiazine).^a

Sample	Excitation wavelength (nm)	Emission wavelength (nm)	τ_1 (ns)	τ_2 (ns)	τ_3 (ns)	τ_{avg} (ns)
PbS QD	965	1470	1.8 ± 0.2 (47%)	32 ± 1 (24%)	276 ± 4 (29%)	88
PbS QD_TiO ₂	965	1470	1.1 ± 0.1 (81%)	32 ± 1 (7%)	276 ± 4 (12%)	36
PbS QD_PTZ	965	1470		23 ± 2 (20%)	322 ± 4 (80%)	262

^aNumbers in the parenthesis indicate relative weightages.

On the other hand, the possibility of electron transfer from the 7 nm PbS QD to CB of TiO₂ is also reported for direct attachment of the QD to TiO₂ instead of attachment through bi-functionalized ligands which supports our experimental finding [13, 26]. As we have synthesized the hybrid by surface adsorption phenomena the electron transfer is most likely to happen even from the larger QDs available in the distribution. The radiative timescale for the QD_TiO₂ composite remains the same as that of the bare QDs. There is no spectral overlap between the absorption of PTZ or TiO₂ and the emission of quantum dot. Thus, the possibility of energy transfer can also be ruled out for both the QD_PTZ and QD_TiO₂ systems. The notable change in the PL lifetime of the QD_PTZ composite compared to the bare QD is that the faster component is vanished and the longest component of radiative recombination is lengthened from 276 ns to 322 ns. The significant change in excited state lifetime can be explained by two possible mechanisms which are depicted in Scheme 8.1. The most probable explanation for the disappearance of the faster time component of a few nanoseconds is the surface passivation of the PbS QD by the surface attached PTZ molecules as pictured in Scheme 8.1a. The electron rich sulfur atom of the PTZ ligand attaches to the surface vacancy states Pb²⁺ and eventually passivates the electron trap states energetically lying below the CB of the QD. Thus, the faster trapping of electrons is not favorable in the presence of PTZ. But this mechanism would lead to

enhancement in steady-state emission also which is not the case in the present study. Another probable mechanism is transfer of photo generated holes from the VB of the PbS QD to the HOMO of PTZ molecule which is energetically feasible according to the energy levels obtained from analyzing the CV data. The decrease in the steady-state emission of QD with increase in PTZ can be explained by this hole transport phenomena as depicted in Scheme 8.1b. The increase in the radiative lifetime of the excited state electron due to hole transfer from the valence band is very rarely reported in earlier literature [35]. We suggest that due to hole



Scheme 8.1. Possible mechanisms of interaction between Phenothiazine (PTZ) and single PbS QD. (a) Surface electron trap state passivation of the PbS QD by the PTZ molecule and consequent increase in excitonic lifetime. (b) Schematic of the probable hole transfer mechanism from the ground state of QD to the PTZ molecule.

separation to some other moiety the excited state electron doesn't have any vacant state to recombine anymore within the QD until some deep seated hole diffuse up to the H_1 level and allow the photoexcited electron to recombine radiatively. Thus, as an overall effect of hole transfer and trap state passivation, the excited state lifetime is observed to increase significantly. According to some earlier reports there is a possibility of very fast hole transfer occurring at a femtosecond time scale also but that is beyond the scope of our instrument to capture [29, 36]. But the increase in life time of cadmium based QDs (in several nanosecond range) upon addition of an efficient hole transport agent is also reported in some very recent studies by other groups [37]. So, from the entire mechanistic explanation it is evident that PTZ can act both as a surface passivator and as a hole acceptor efficiently. But up to a certain concentration range the hole transport phenomena is found to be predominant over the other. Nevertheless, both trap state passivation and hole separation are desired process to achieve better light harvesting.

In order to investigate the effect of simultaneous separation of photo generated electrons and holes in NIR light harvesting, the reactive oxygen species (ROS) generation has been monitored by DCFH assay using all the hybrids under IR light irradiation. However, the electron paramagnetic resonance (EPR) is a much confirmatory experiment of ROS generation and the specific nature of the reactive oxygen species can be identified (singlet, triplet or superoxide) from the EPR studies. But our aim in the present study was just to compare the activity of the different hybrids in terms of ROS generation. DCFH assay is a widely known technique to probe ROS generation in biological studies [38, 39]. Although the specific nature of ROS could not be confirmed from DCFH the oxidation of DCFH molecule at least confirms the generation of ROS within the media. ROS generation by different QD_TiO₂ systems are also well reported in earlier literature [27]. Thus, for the comparison of the activity of different hybrids, we

have avoided the rigorous EPR experiment and have used the probe DCFH.

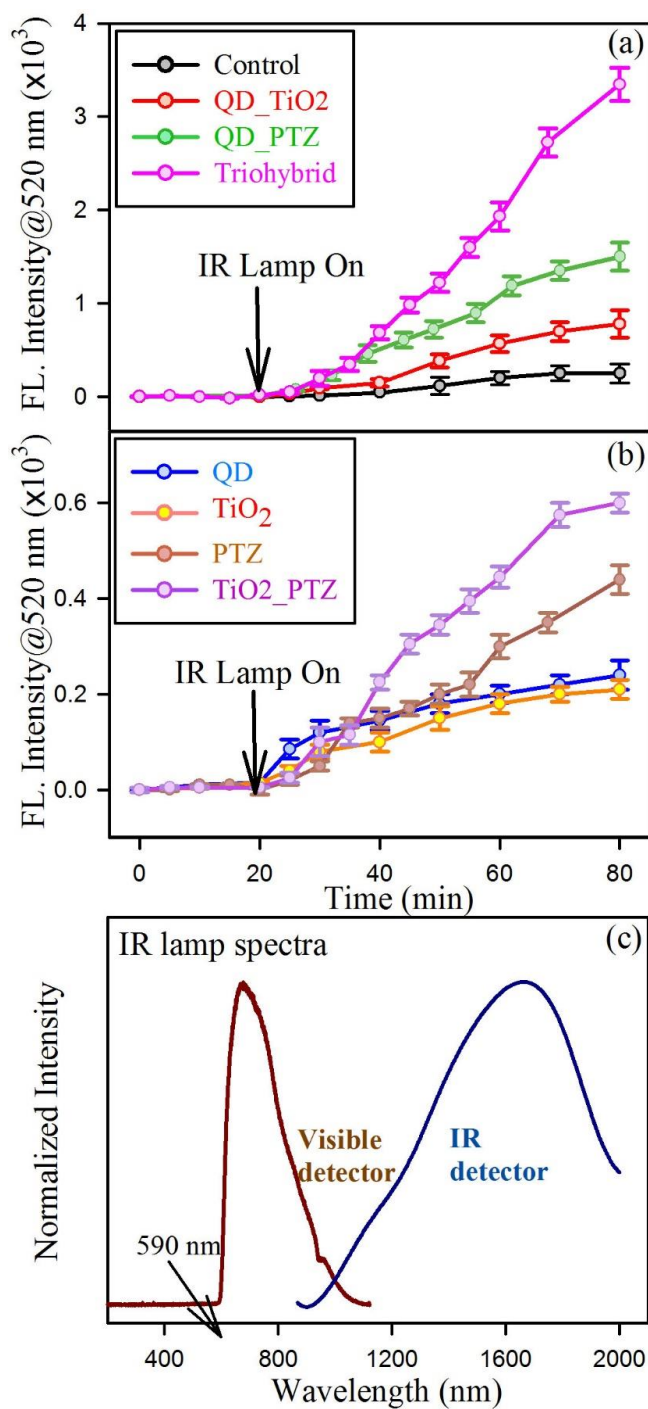
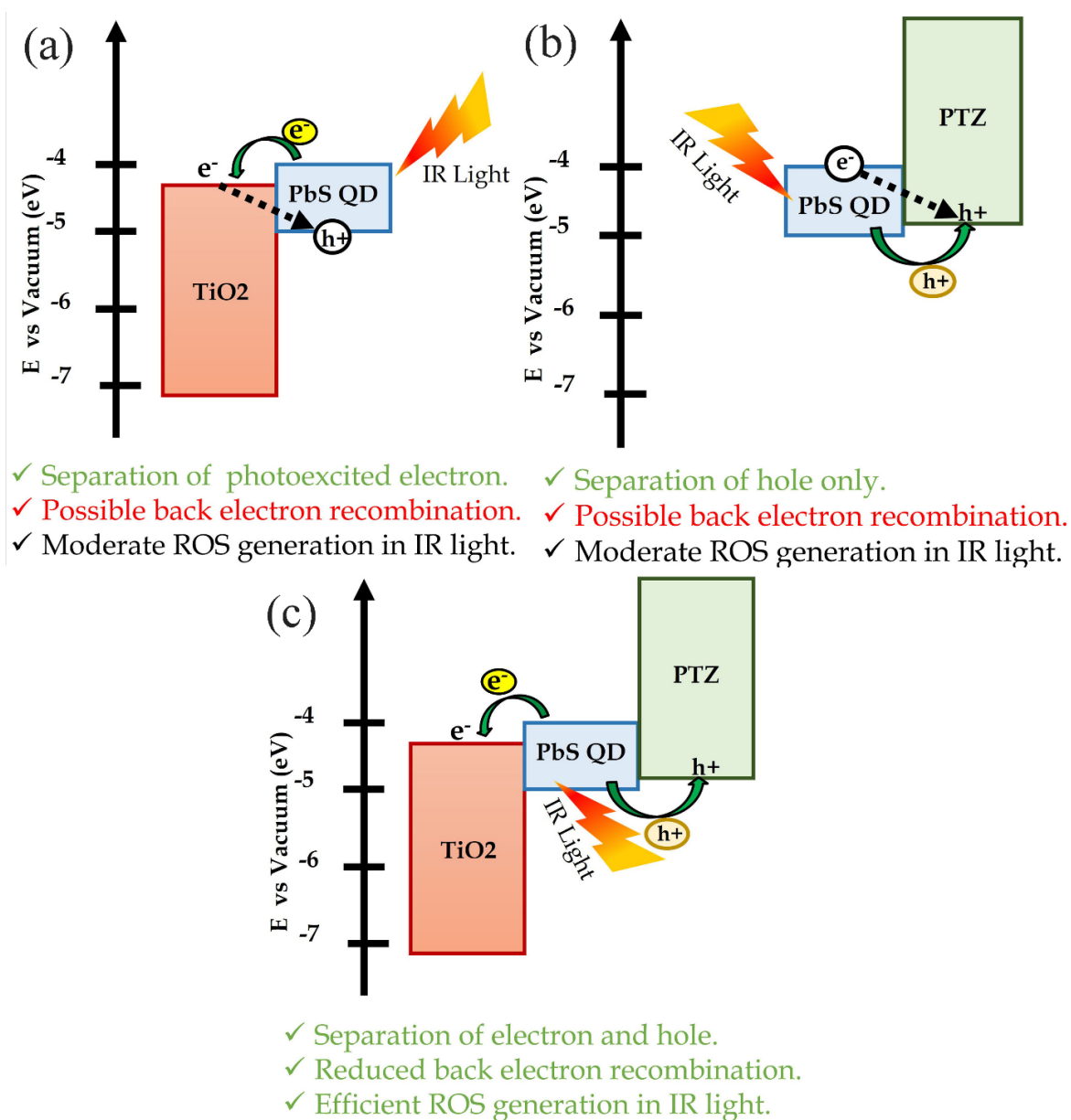


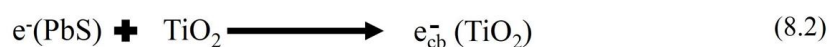
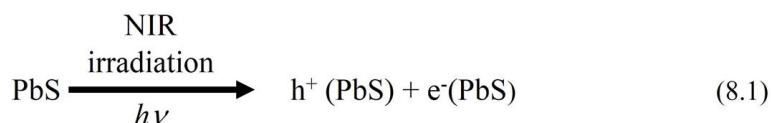
Figure 8.5. Time dependent oxidation of DCFH in water under IR light irradiation, monitored at 520 nm, in the presence of (a) QD_TiO₂_PTZ triohybrid (pink), QD_PTZ (green) and QD_TiO₂ (red) and DCFH only (black), (b) controls QD, TiO₂, PTZ and TiO₂_PTZ hybrid. The excitation was at 409 nm. (c) The spectra of the IR lamp which has been used for irradiation during DCFH assay experiment.



Scheme 8.2. Band structure, mechanism and application of the excitation-relaxation cycle in (a) PbS QD-TiO₂, (b) PbS QD-PTZ and (c) PbS QD-TiO₂-PTZ (triohybrid) under IR light irradiation.

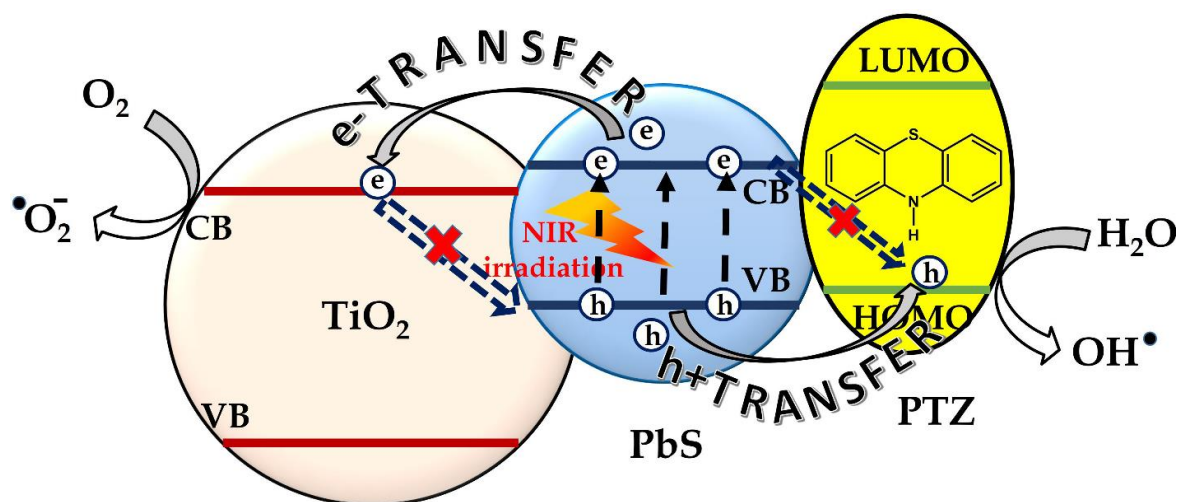
The results of the DCFH assay for the hybrids are shown in Figure 8.5a which reveals the much higher ROS generation activity of the trio hybrid than that of QD-TiO₂ and QD-PTZ where only electron transfer and hole transfer takes place separately. The activity of all the other controls including bare QD, bare TiO₂, only PTZ and TiO₂-PTZ has also been studied and ROS generation of an order of magnitude lower than that of the hybrids is observed as shown in Figure 8.5b. The

spectra of the IR lamp used for the irradiation in DCFH assay are also shown in Figure 8.5c which shows that the irradiation starts at 590 nm and extends up to 2000 nm. Under this specific region of irradiation only the QDs are expected to excite and the photo generated carriers within the QD only are supposed to take part in light harvesting. The mechanism of ROS generation using the trio hybrid in IR irradiation is shown below,



The higher ROS generation in the trio hybrid can be explained via the mechanism of the reduced back recombination process also which is shown in Scheme 8.2. For QD_TiO₂ hybrid although the excited state electron is well separated from the QD, the photogenerated hole is still present there in the VB. Thus, the separated electron has the vacancy to recombine back from the CB of TiO₂ to the VB of PbS. As a consequence, even after the separation, the entire population of excited electrons are not utilized to react with the dissolved oxygen in water and essentially does not produce ROS to a higher efficiency. The similar back recombination is feasible in the QD_PTZ hybrid also. The separated holes in the HOMO of the PTZ molecule can recombine with the electrons present in the conduction band of the PbS QD. Thus, the efficiency of hole mediated ROS generation is decreased in the QD_PTZ hybrid. In contrast, for the trio hybrid, the photoexcited electron and hole has been simultaneously separated by TiO₂ and PTZ respectively. The recombination center for the separated carriers is no longer

present within the QD. The entire mechanism of simultaneous dissociation of excitons is summarized in Scheme 8.3. Thus, all the electron and holes are enabled to interact with the dissolved oxygen molecules present in the water and generate reactive oxygen species at a much higher efficiency as a consequence of the suppressed back recombination.



Scheme 8.3. Exciton dissociation: The key factor in generating ROS under IR light irradiation.

8.3. Conclusion: The interfacial dynamics of the three NIR active hybrid materials PbS_TiO₂, PbS QD_Phenothiazine (PTZ) and triohybrid (PbS QD_TiO₂_PTZ) have been investigated in details and their activities have been compared in terms of reactive oxygen species (ROS) generation efficiency under IR light irradiation. The individual components and all the hybrids have been characterized by spectroscopic techniques and transmission electron microscopy (TEM). The attachment of the different components of the hybrids has been confirmed from absorption, quenching in steady-state emission and from the changes in the excited state photoluminescence decay lifetimes of the PbS QD. The photoinduced electron transfer from the E₁ of PbS QD to the CB of TiO₂ and hole transfer from the H₁ of the QD to the HOMO of the PTZ molecule inferred from the analysis of the transient PL timescales and energy level alignment obtained from the cyclic voltammetric analysis. The excited state life time of the PbS QD has

been observed to decrease upon attachment to TiO_2 due to photoinduced electron transfer (PET) from the QD of the conduction band of TiO_2 . On the contrary, the lifetime of the QD is observed to increase upon attachment to phenothiazine (PTZ) due to a combined effect of surface trap passivation and photoinduced hole transfer (PHT). Due to separation of both electrons and holes from the photoexcited QD in the trio hybrid, the back recombination centers of the carriers are abolished. Consequently, a higher ROS generation activity is being observed for the trio hybrid compared to the PbS_TiO_2 and PbS_PTZ hybrids where only electron separation and hole separation take place separately and the possibility of back recombination restricts the utilization of the photogenerated carriers. Thus, systematic investigation of the interfacial dynamics provide a mechanistic approach of comparison between consecutive separation of excitons and simultaneous separation of the same. The photophysical behavior at the interfaces of the hybrids has been interpreted rationally and correlated with the higher ROS generation activity under NIR light irradiation.

References

- [1] J.-W. Lee, D.-Y. Son, T.K. Ahn, H.-W. Shin, I.Y. Kim, S.-J. Hwang, M.J. Ko, S. Sul, H. Han, N.-G. Park, Quantum-dot-sensitized solar cell with unprecedentedly high photocurrent, *Sci. Rep.*, 3 (2013) 1050.
- [2] A.G. Arguinzoniz, E. Ruggiero, A. Habtemariam, J. Hernández-Gil, L. Salassa, J.C. Mareque-Rivas, Light harvesting and photoemission by nanoparticles for photodynamic therapy, *Part. Part. Syst. Character.*, 31 (2014) 46-75.
- [3] W. He, H. Jia, D. Yang, P. Xiao, X. Fan, Z. Zheng, H.-K. Kim, W.G. Wamer, J.-J. Yin, Composition directed generation of reactive oxygen species in irradiated mixed metal sulfides correlated with their photocatalytic activities, *ACS Appl. Mater. Interfaces*, 7 (2015) 16440-16449.
- [4] A. Braga, S. Giménez, I. Concina, A. Vomiero, I. Mora-Seró, Panchromatic sensitized solar cells based on metal sulfide quantum dots grown directly on nanostructured TiO₂ electrodes, *J. Phys. Chem. Lett.*, 2 (2011) 454-460.
- [5] J. Patwari, A. Chatterjee, S. Sardar, P. Lemmens, S.K. Pal, Ultrafast dynamics in co-sensitized photocatalysts under visible and NIR light irradiation, *Phys. Chem. Chem. Phys.*, 20 (2018) 10418-10429.
- [6] J. Patwari, S. Sardar, B. Liu, P. Lemmens, S.K. Pal, Three-in-one approach towards efficient organic dye-sensitized solar cells: Aggregation suppression, panchromatic absorption and resonance energy transfer, *Beilstein J. Nanotechnol.*, 8 (2017) 1705-1713.
- [7] G. Wang, B. Huang, X. Ma, Z. Wang, X. Qin, X. Zhang, Y. Dai, M.H. Whangbo, Cu₂(OH)PO₄, a near-infrared-activated photocatalyst, *Angew. Chem. Int. Ed.*, 52 (2013) 4810-4813.
- [8] M. García-Iglesias, J.-J. Cid, J.-H. Yum, A. Forneli, P. Vázquez, M.K. Nazeeruddin, E. Palomares, M. Grätzel, T. Torres, Increasing the efficiency of zinc-phthalocyanine based solar cells through modification of the anchoring ligand, *Energy Environ. Sci.*, 4 (2011) 189-194.

- [9] J. Tian, Y. Sang, G. Yu, H. Jiang, X. Mu, H. Liu, A Bi₂WO₆-based hybrid photocatalyst with broad spectrum photocatalytic properties under UV, visible, and near-infrared irradiation, *Adv. Mater.*, 25 (2013) 5075-5080.
- [10] M. Zhang, J. Yue, R. Cui, Z. Ma, H. Wan, F. Wang, S. Zhu, Y. Zhou, Y. Kuang, Y. Zhong, Bright quantum dots emitting at ~1,600 nm in the NIR-IIb window for deep tissue fluorescence imaging, *Proc. Natl. Acad. Sci. U.S.A.*, 115 (2018) 201806153.
- [11] J.-C. Boyer, M.-P. Manseau, J.I. Murray, F.C. van Veggel, Surface modification of upconverting NaYF₄ nanoparticles with PEG–phosphate ligands for NIR (800 nm) biolabeling within the biological window, *Langmuir*, 26 (2009) 1157-1164.
- [12] C. Wang, H. Tao, L. Cheng, Z. Liu, Near-infrared light induced in vivo photodynamic therapy of cancer based on upconversion nanoparticles, *Biomaterials*, 32 (2011) 6145-6154.
- [13] R. Plass, S. Pelet, J. Krueger, M. Grätzel, U. Bach, Quantum dot sensitization of organic–inorganic hybrid solar cells, *J. Phys. Chem. B*, 106 (2002) 7578-7580.
- [14] H. Lee, H.C. Leventis, S.J. Moon, P. Chen, S. Ito, S.A. Haque, T. Torres, F. Nüesch, T. Geiger, S.M. Zakeeruddin, PbS and CdS quantum dot-sensitized solid-state solar cells: “Old concepts, new results”, *Adv. Funct. Mater.*, 19 (2009) 2735-2742.
- [15] C. Ratanatawanate, Y. Tao, K.J. Balkus Jr, Photocatalytic activity of PbS quantum dot/TiO₂ nanotube composites, *J. Phys. Chem. C*, 113 (2009) 10755-10760.
- [16] L. Sun, J.J. Choi, D. Stachnik, A.C. Bartnik, B.-R. Hyun, G.G. Malliaras, T. Hanrath, F.W. Wise, Bright infrared quantum-dot light-emitting diodes through inter-dot spacing control, *Nat. Nanotechnol.*, 7 (2012) 369.
- [17] S.A. McDonald, G. Konstantatos, S. Zhang, P.W. Cyr, E.J. Klem, L. Levina, E.H. Sargent, Solution-processed PbS quantum dot infrared photodetectors and photovoltaics, *Nat. Mater.*, 4 (2005) 138.

- [18] V. Klimov, A. Mikhailovsky, S. Xu, A. Malko, J. Hollingsworth, A.C. Leatherdale, H.-J. Eisler, M. Bawendi, Optical gain and stimulated emission in nanocrystal quantum dots, *Science*, 290 (2000) 314-317.
- [19] H.C. Leventis, F. O'Mahony, J. Akhtar, M. Afzaal, P. O'Brien, S.A. Haque, Transient optical studies of interfacial charge transfer at nanostructured metal oxide/PbS quantum dot/organic hole conductor heterojunctions, *J. Am. Chem. Soc.*, 132 (2010) 2743-2750.
- [20] J.A. McGuire, M. Sykora, J. Joo, J.M. Pietryga, V.I. Klimov, Apparent versus true carrier multiplication yields in semiconductor nanocrystals, *Nano Lett.*, 10 (2010) 2049-2057.
- [21] A.A.O. El-Ballouli, E. Alarousu, A. Usman, J. Pan, O.M. Bakr, O.F. Mohammed, Real-time observation of ultrafast intraband relaxation and exciton multiplication in PbS quantum dots, *ACS Photonics*, 1 (2014) 285-292.
- [22] J. Pijpers, R. Ulbricht, K. Tielrooij, A. Osherov, Y. Golan, C. Delerue, G. Allan, M. Bonn, Assessment of carrier-multiplication efficiency in bulk PbSe and PbS, *Nat. Phys.*, 5 (2009) 811.
- [23] L. Cademartiri, E. Montanari, G. Calestani, A. Migliori, A. Guagliardi, G.A. Ozin, Size-dependent extinction coefficients of PbS quantum dots, *J. Am. Chem. Soc.*, 128 (2006) 10337-10346.
- [24] K.E. Knowles, M.D. Peterson, M.R. McPhail, E.A. Weiss, Exciton dissociation within quantum dot-organic complexes: Mechanisms, use as a probe of interfacial structure, and applications, *J. Phys. Chem. C*, 117 (2013) 10229-10243.
- [25] B.-R. Hyun, Y.-W. Zhong, A.C. Bartnik, L. Sun, H.D. Abruna, F.W. Wise, J.D. Goodreau, J.R. Matthews, T.M. Leslie, N.F. Borrelli, Electron injection from colloidal PbS quantum dots into titanium dioxide nanoparticles, *ACS nano*, 2 (2008) 2206-2212.
- [26] K.P. Acharya, N.N. Hewa-Kasakarage, T.R. Alabi, I. Nemitz, E. Khon, B. Ullrich, P. Anzenbacher, M. Zamkov, Synthesis of PbS/TiO₂ colloidal

heterostructures for photovoltaic applications, *J. Phys. Chem. C*, 114 (2010) 12496-12504.

[27] C. Ratanatawanate, A. Chyao, K.J. Balkus Jr, S-nitrosocysteine-decorated PbS QDs/TiO₂ nanotubes for enhanced production of singlet oxygen, *J. Am. Chem. Soc.*, 133 (2011) 3492-3497.

[28] K. Wu, Y. Du, H. Tang, Z. Chen, T. Lian, Efficient extraction of trapped holes from colloidal CdS nanorods, *J. Am. Chem. Soc.*, 137 (2015) 10224-10230.

[29] S. Lian, D.J. Weinberg, R.D. Harris, M.S. Kodaimati, E.A. Weiss, Subpicosecond photoinduced hole transfer from a CdS quantum dot to a molecular acceptor bound through an exciton-delocalizing ligand, *ACS nano*, 10 (2016) 6372-6382.

[30] G. Itskos, P. Papagiorgis, D. Tsokkou, A. Othonos, F. Hermerschmidt, S.P. Economopoulos, M. Yarema, W. Heiss, S. Choulis, Size-dependent charge transfer in blends of PbS quantum dots with a low-gap silicon-bridged copolymer, *Adv. Energy Mater.*, 3 (2013) 1490-1499.

[31] J. Patwari, H. Joshi, H. Mandal, L. Roy, C. Bhattacharya, P. Lemmens, S.K. Pal, Exciton dissociation in an NIR-active triohybrid nanocrystal leading to efficient generation of reactive oxygen species, *Phys. Chem. Chem. Phys.*, 21 (2019) 10667-10676

[32] L. Yang, J.-K. Feng, A.-M. Ren, Theoretical study on electronic structure and optical properties of phenothiazine-containing conjugated oligomers and polymers, *J. Org. Chem.*, 70 (2005) 5987-5996.

[33] J.B. Sambur, B.A. Parkinson, CdSe/ZnS core/shell quantum dot sensitization of low index TiO₂ single crystal surfaces, *J. Am. Chem. Soc.*, 132 (2010) 2130-2131.

[34] J. Huang, Z. Huang, S. Jin, T. Lian, Exciton dissociation in CdSe quantum dots by hole transfer to phenothiazine, *J. Phys. Chem. C*, 112 (2008) 19734-19738.

[35] C. Burda, S. Link, M. Mohamed, M. El-Sayed, The relaxation pathways of CdSe nanoparticles monitored with femtosecond time-resolution from the visible

to the IR: Assignment of the transient features by carrier quenching, *J. Phys. Chem. B*, 105 (2001) 12286-12292.

[36] S. Yu, X.-B. Fan, X. Wang, J. Li, Q. Zhang, A. Xia, S. Wei, L.-Z. Wu, Y. Zhou, G.R. Patzke, Efficient photocatalytic hydrogen evolution with ligand engineered all-inorganic InP and InP/ZnS colloidal quantum dots, *Nat. Commun.*, 9 (2018) 4009.

[37] X.B. Fan, S. Yu, X. Wang, Z.J. Li, F. Zhan, J.X. Li, Y.j. Gao, A.D. Xia, Y. Tao, X.B. Li, Susceptible surface sulfide regulates catalytic activity of CdSe quantum dots for hydrogen photogeneration, *Adv. Mater.*, 31 (2019) 1804872.

[38] D. Bagchi, S. Chaudhuri, S. Sardar, S. Choudhury, N. Polley, P. Lemmens, S.K. Pal, Modulation of stability and functionality of a phyto-antioxidant by weakly interacting metal ions: Curcumin in aqueous solution, *RSC Adv.*, 5 (2015) 102516-102524.

[39] S. Sardar, S. Chaudhuri, P. Kar, S. Sarkar, P. Lemmens, S.K. Pal, Direct observation of key photoinduced dynamics in a potential nano-delivery vehicle of cancer drugs, *Phys. Chem. Chem. Phys.*, 17 (2015) 166-177.

List of Publications

(Peer-reviewed journals)

1. **J. Patwari**, S. Sardar, B. Liu, P. Lemmens and S. K. Pal
"Three in one approach towards efficient organic dye sensitized solar cells: Aggregation suppression, panchromatic absorption and resonance energy transfer"
Beilstein J. Nanotechnol. 8 (2017) 1705-1713.
2. **J. Patwari**, S. Shyamal, T. Khan, H. Ghadi, C. Bhattacharya, S. Chakrabarti and S. K. Pal
"Inversion of activity in DSSC for TiO₂ and ZnO photo-anodes depending on the choice of sensitizer and carrier dynamics"
J. Luminescence. 207 (2019) 169-176.
3. **J. Patwari**, A. Chatterjee, S. Sardar, P. Lemmens and S. K. Pal
"Ultrafast dynamics in co-sensitized photocatalyst under visible and NIR light irradiation"
Phys. Chem. Chem. Phys. 20 (2018) 10418-10429.
4. **J. Patwari**, H. Ghadi, S. Sardar, J. Singhal, B. Tongbram, S. Shyamal, C. Bhattacharya, S. Chakrabarti and S. K. Pal
"Photo-induced electronic properties in single quantum well system: Effect of excitonic lifetime"
Mater. Res. Express. 4 (2017) 016301.
5. **J. Patwari**, A. Chatterjee, H. Ghadi, H. Sharma, S. Chakrabarti and S. K. Pal
"In Situ measurement of temperature dependent picosecond resolved carrier dynamics in near infrared (NIR) sensitive device on action"
Rev. Sci. Instrum. 90 (2019) 043909.
6. H. Ghadi, **J. Patwari**, P. Murkute, D. Das, P. K. Singh, S. Dubey, M. Bhatt, A. Chatterjee, A. Balgarkashi, S. K. Pal and S. Chakrabarti
"Optimizing dot-in-a-well infrared detector architecture for achieving high optical and device efficiency corroborated with theoretically simulated model"
J. Alloys Compd. 751 (2018) 337-348.

7. **J. Patwari**, H. Joshi, H. Mandal, L. Roy, C. Bhattacharya, P. Lemmens and S. K. Pal
“Exciton dissociation in an NIR-active trio hybrid nanocrystal leading to efficient generation of reactive oxygen species”
Phys. Chem. Chem. Phys. 21 (2019) 10667-10676.
- 8.* P. Kar, T. K. Maji, **J. Patwari** and S. K. Pal
“Can a light harvesting material be always common in photocatalysis and photovoltaic applications?”
Mater. Chem. Phys. 200 (2017) 70-77.
- 9.* A. Chatterjee, D. Das, **J. Patwari**, B. Tongbram, D. Panda, S. Chakrabarti and S. K. Pal
“Ultrafast electronic spectroscopy on the coupling of Stranski-Krastanov and submonolayer quantum dots for potential application in near infrared light harvesting”
Mater. Res. Express. 6 (2019) 085903.
- 10.* V. P. Deviprasad, H. J. Ghadi, D. Das, D. Panda, H. M. Rawool, V. Chavan, B. Tongbram, **J. Patwari**, S. K. Pal and S. Chakrabarti
“High performance short wave infrared photodetector using p-i-p quantum dots (InAs/GaAs) validated with theoretically simulated model”
J. Alloys Compd. 804 (2019) 18-26.
- 11.* A. Chatterjee, D. Panda, **J. Patwari**, B. Tongbram, S. Chakrabarti and S. K. Pal
“Strain relaxation in InAs quantum dots through capping layer variation and its impact on the ultrafast carrier dynamics”
Semicond. Sci. Technol. 2019 (in press).

* Not included in the thesis.

List of International/National Conferences

1. Presented poster and awarded **the best poster award** out of 53 posters in the DAE BRNS-Theme Meeting on “Ultrafast Science-2016 (**UFS- 2016**)” held at Bhaba Atomic Research Centre, Mumbai, India from 24th to 26th November, 2016.
2. Presented poster and awarded **the ACS best poster award** out of 135 posters in the **I2CAM-JNCASR** school on clean and renewable energy technologies via chemical route held at JNCASR, Bengaluru, India from 27th November to 2nd December, 2017.
3. Presented poster at 6th International Symposium on Integrated Functionalities (**ISIF-2017**), held at Shangri-La’s Eros, New Delhi, India from 10th to 13th December, 2017.
4. Presented poster at International Conference on Sustainable Chemistry for Health, Environment and Materials (**Su-Chem 2018**), held at CSIR-Indian Institute of Chemical Technology (CSIR-IICT), Hyderabad, India from 5th to 8th August, 2018.
5. Presented poster at International Conference on Complex and Functional Materials (**ICCFM 2018**) at Biswa Bangla Convention Centre, Kolkata, India from 13th to 16th December, 2018.
6. Presented poster at **EMRS Spring meeting 2019** held in Acropolis Congress Centre, Nice, France from 27th to 31st of May, 2019.
7. Delivered oral presentation at **EMRS Spring meeting 2019** held in Acropolis Congress Centre, Nice, France from 27th to 31st of May, 2019.
8. Presented poster at **GRC Photochemistry 2019** held at Stonehill College in Easton, MA, United States from 14th to 19th July, 2019.
9. Attended conference “Ultrafast Science- 2015 (**UFS- 2015**)” held at S. N. Bose National Centre for Basic Sciences, India from 19th to 21st November, 2015.
10. Attended the international conference named “Symposium on Advanced Biological inorganic Chemistry (**SABIC 2017**)” held at The Stadel, Kolkata, India from 7th to 11th January, 2017.
11. Attended the conference named **Industry Academia Meet 2018** held at S. N. Bose National Centre for Basic Sciences, Kolkata, India on 6th October 2018.